

UNCERTAINTY OF THE
COEFFICIENT OF BAND-TO-BAND ABSORPTION
OF CRYSTALLINE SILICON

Von der Fakultät für Mathematik und Physik
der Gottfried Wilhelm Leibniz Universität Hannover

zur Erlangung des Grades

Doktor der Naturwissenschaften

Dr. rer. nat.

genehmigte Dissertation

von

Dipl.-Phys. Carsten Jonathan Schinke

geboren am 31.05.1984 in Düsseldorf

Referent: Prof. Dr. Jan Schmidt
Korreferenten: Prof. Dr. Michael Oestreich
Prof. Dr. Daniel MacDonald
Tag der Promotion: 07.05.2015

Zusammenfassung

Kristallines Silizium ist ein wichtiges Halbleitermaterial für eine Vielzahl von Anwendungen, die aus dem Bereich der Energieerzeugung mit Solarzellen über Sensoren für bildgebende Verfahren bis hin zu physikalischer Grundlagenforschung reichen. Alle diese Anwendungen nutzen die Absorption oder Transmission von Licht in Silizium aus, die beide durch den Absorptionskoeffizienten beschrieben werden. Daher erstaunt es nicht, dass seit über 60 Jahren fortlaufend wissenschaftliche Arbeiten publiziert werden, die sich mit der Bestimmung des Absorptionskoeffizienten befassen. Dass die Bestimmung des Absorptionskoeffizienten von Silizium nach wie vor ein aktuelles Forschungsthema ist, hat verschiedene Gründe. Fast alle Arbeiten untersuchten den Absorptionskoeffizienten nur in einem Teil des Wellenlängenbereichs, der für praktische Anwendungen wie z.B. die photovoltaische Energieerzeugung interessant ist. Dabei kamen verschiedene Messverfahren zum Einsatz. Ein Blick auf die in der Literatur vorhandenen Datensätze zeigt, dass die Messdaten um bis zu 20 % voneinander abweichen. Es ist unklar, ob diese Abweichungen nur auf Eigenschaften der untersuchten Proben zurückzuführen sind oder auch auf systematische Abweichungen und Unsicherheiten aufgrund der eingesetzten Messverfahren. Die Genauigkeit der Literaturdaten lässt sich allerdings nicht bewerten, da Messunsicherheiten nicht systematisch ermittelt oder - zum größten Teil - überhaupt nicht angegeben wurden. Teilweise sind auch nur unvollständige Informationen über die Eigenschaften der untersuchten Proben oder Messbedingungen wie bspw. die Proben temperatur vorhanden. Dazu kommt, dass für viele der älteren Arbeiten die Datensätze nicht (mehr) in tabellarischer Form verfügbar sind. Für die Verwendung dieser Datensätze müssen Abbildungen digitalisiert werden, was zusätzliche Unsicherheiten unbekannter Größe verursacht.

Diese Arbeit befasst sich daher mit der erneuten, präzisen und nachvollziehbaren Bestimmung des Absorptionskoeffizienten von Silizium, genauer mit der Bestimmung des Koeffizienten der Inter-Band-Absorption, die zur Generation elektrischer Ladungsträger führt. Es werden verschiedene Messverfahren eingesetzt (spektroskopische Ellipsometrie, Reflexions- und Transmissionsmessungen, spektral aufgelöste Lumineszenzmessungen und Messungen der spektralen Bestrahlungsstärke-Empfindlichkeit), die den Wellenlängenbereich von 250 bis 1450 nm abdecken. In diesem Bereich variiert der Absorptionskoeffizient um mehr als 15 Größenordnungen. Für alle Messverfahren wird eine systematische Messunsicherheitsanalyse durchgeführt, die auf dem "Guide to the expression of uncertainty in measurement" (GUM) basiert. Damit ist es erstmals möglich, begründete Unsicherheiten für den so erhaltenen Datensatz des Absorptionskoeffizienten anzugeben. Darüber hinaus erfolgen Vergleichsmessungen mit der Physikalisch-Technischen Bundesanstalt in Braunschweig, Deutschland (PTB), sowie der Australian National University in Canberra, Australien (ANU), die die in dieser Arbeit erhaltenen Messdaten bestätigen. Die relative Unsicherheit des so bestimmten Absorptionskoeffizienten beträgt 0,3 % bei 300 nm, 10 % bei 600 nm, 1 % bei 900 nm, 10 % bei 1200 nm und 180 % bei 1450 nm. Da die Literaturdaten auf vergleichbaren Messungen beruhen, zeigt die in dieser Arbeit durchgeführte Analyse auch, dass die Abweichungen zwischen den Literaturdatensätzen nur zum Teil durch Messunsicherheiten erklärbar sind. Die Unsicherheit von Wirkungsgradsimulationen für Solarzellen aufgrund der Unsicherheit des ermittelten Absorptionskoeffizienten liegt in der Größenordnung von 0.1 % relativ und ist damit für die Genauigkeit solcher Simulationen nicht limitierend.

Schlagwörter: Kristallines Silizium, Absorptionskoeffizient, Messunsicherheitsanalyse

Abstract

Crystalline silicon is an important semiconductor material for a wide variety of applications, ranging from generation of electricity with solar cells to sensors for imaging methods or fundamental physical research. All of these applications make use of the absorption or transmission of light within silicon, which is described by the absorption coefficient. It is therefore no surprise that over the last 60 years, the determination of the absorption coefficient has been the subject of many scientific publications. Today, the determination of the absorption coefficient of crystalline silicon is still an ongoing research topic. There are several reasons for this. Almost all of the published studies investigate the absorption coefficient only in a part of the wavelength range that is of interest for a specific application, e.g., the photovoltaic generation of electricity. Moreover, different measurement methods were used. A comparison of literature data shows that there are deviations of up to 20 % between the different data. It is unclear whether the deviations are only due to the specific properties of the investigated samples or whether they can be explained by systematic deviations or uncertainties due to the measurement methods used. The accuracy of the literature data cannot be assessed since measurement uncertainties have not been determined systematically or, as for the major part of the studies, have not been indicated at all. Moreover, only incomplete information about the properties of the samples and measurement conditions as sample temperature is found in some of the studies. Another issue is that for most of the older work, tabulated data is not available (anymore). In order to use these data, figures must be digitized, which leads to additional uncertainties of unknown extent.

The subject of this work is thus the accurate and comprehensible redetermination of the absorption coefficient of crystalline silicon. More precisely, the work is concerned with the determination of the coefficient of inter-band absorption, which leads to the generation of electrical charge carriers. For this purpose, different measurement methods are used: spectroscopic ellipsometry, measurements of reflectance and transmittance, spectrally resolved luminescence measurements and measurements of the spectral responsivity of solar cells. These measurements cover the wavelength range from 250 to 1450 nm. In this region, the absorption coefficient varies by more than 15 orders of magnitude. For all methods, a systematic measurement uncertainty analysis is carried out based on the “Guide to the expression of uncertainty in measurement” (GUM). This allows to specify substantiated uncertainties for the data for the first time. Furthermore, the data is consolidated by comparison with data measured by the Physikalisch-Technische Bundesanstalt in Braunschweig, Germany (PTB) and the Australian National University in Canberra, Australia (ANU). The relative uncertainty of the absorption coefficient data determined in this work is 0.3% at 300 nm, 10% at 600 nm, 1% at 900 nm, 10% at 1200 nm and 180% at 1450 nm. Since the literature data result from comparable measurements, the analysis shows that the deviations between the data can only partly be explained by measurement uncertainties. The uncertainty of energy conversion efficiency simulations for solar cells due to the uncertainty of the absorption coefficient data determined in this work is of the order of 0.1% relative and does not limit the accuracy of such simulations.

Keywords: crystalline silicon, absorption coefficient, measurement uncertainty analysis

Contents

Einleitung	1
Introduction	5
1 Theoretical background	9
1.1 Electronic properties of crystalline silicon	9
1.2 Absorption of light within silicon	11
1.2.1 General definition of the absorption coefficient	12
1.2.2 Indirect band-to-band absorption	13
1.2.3 Direct band-to-band absorption	14
1.2.4 Free carrier absorption (FCA)	14
1.2.5 Temperature dependence of the band gap energy	14
1.2.6 Injection and doping dependence of the band gap energy	14
1.3 Systematical Measurement Uncertainty Analysis	15
1.3.1 Definition: Process equation	15
1.3.2 Definition: Uncertainty, error and correction	16
1.3.3 Type A and B uncertainties	17
1.3.4 Combined standard uncertainty	17
1.3.5 Expanded uncertainty	18
1.3.6 Conformity of measurement results	18
1.3.7 Combination of measurement results	19
2 Measuring the absorption coefficient	21
2.1 Measurements of reflectance and transmittance	22
2.1.1 Principle of measurement	22
2.1.2 Setup for measurements	23
2.1.3 Samples for measurements	24
2.1.4 Corrections of systematic effects	24
2.1.5 Uncertainty contributions	26
2.1.6 Results	33
2.2 Spectrally resolved luminescence measurements	37
2.2.1 Principle of measurement	37
2.2.2 Samples for measurements	38
2.2.3 Setup for measurements	39
2.2.4 In-house calibration of spectrometers	40
2.2.5 Procedure for measuring luminescence spectra	41
2.2.6 Correction of systematic effects	43
2.2.7 Uncertainty contributions	45
2.2.8 Performance of scanning vs. diode array spectrometer system	50
2.2.9 Electroluminescence vs. photoluminescence measurements	51

2.2.10	Results	53
2.3	Spectral responsivity measurements	58
2.3.1	Principle of measurements	58
2.3.2	Setup for measurements	58
2.3.3	Samples for measurements	59
2.3.4	Results and measurement uncertainty	59
2.4	Spectroscopic ellipsometry	61
2.4.1	Principle of measurements	61
2.4.2	Setup and samples for measurements	62
2.4.3	Evaluation procedure	62
2.4.4	Monte-Carlo simulation for the analysis of measurement uncertainty	63
2.4.5	Uncertainty contributions	64
2.4.6	Results	66
3	Analysis of measured data	69
3.1	Combined data of the coefficient of band-to-band absorption	70
3.1.1	Ellipsometry data	70
3.1.2	Reflectance/Transmittance data	70
3.1.3	Luminescence/Spectral responsivity data	72
3.2	Temperature dependence of the absorption coefficient	77
3.3	Final data of the coefficient of band-to-band absorption and its uncertainty at 295 K	78
4	Application of derived data for photovoltaics	83
4.1	Uncertainty of silicon solar cell energy conversion efficiency predictions	84
4.1.1	Ideal solar cells	84
4.1.2	Realistic solar cells	89
4.2	Impact of deviations between absorption coefficient data	90
4.3	Modeling luminescence spectra of silicon solar cells and wafers	91
4.3.1	General model of spectral luminescence emission	92
4.3.2	Review of models for the photon escape probability	93
4.3.3	Spectral luminescence emission of samples with a textured front surface and an arbitrary rough rear surface	95
4.3.4	Impact of absorption coefficient data set on modeled luminescence spectra	101
4.4	Determination of the rear surface reflectance of silicon solar cells from their luminescence spectrum	103
5	Summary and outlook	107
APPENDIXES		
A	Instability of nonlinearity corrections obtained by the superposition method	111
B	Impact of chuck reflectance on luminescence spectra	115
C	Derivations	119
C.1	Varian Cary 5000: Signal correction for reflectance/transmittance measurements with the PbS detector	119
C.2	Uncertainty contribution due to spectral bandwidth	124
C.3	Evaluation of luminescence and spectral responsivity measurements	125
C.3.1	Incorporation of FCA in the emitter of solar cells into the optical model	125
C.3.2	Effective rear surface reflectance of solar cells	125

C.3.3	Determination of the surface reflectance of solar cells from reference samples with highly doped layers on both sides	126
C.3.4	Impact of FCA on the scaling factor for EQE data of textured solar cells	127
C.4	Relation between absorptance and charge carrier generation rate	129
D	Tabulated data	131
D.1	Absorption coefficient	131
D.2	Temperature coefficient	139
E	Modeling of luminescence spectra	141
E.1	Photon escape probabilities	141
E.2	Effective path angle θ_n for lambertian diffused light	143
E.3	Derivation of $\Phi_{bb}(\lambda)$	144
E.4	Approximation of the photon generation rate r_{ph}	145
E.5	Derivation of the optical reciprocity theorem in terms of wavelengths and for a specific detection cone	146

Kristallines Silizium ist ein wichtiges Ausgangsmaterial für eine Vielzahl von Anwendungen. Die Mikroelektronikindustrie stellt daraus integrierte Schaltkreise her, die aus der modernen Telekommunikations- und Informationstechnologie nicht mehr wegzudenken sind. Auf kristallinem Silizium basieren die meisten Sensoren, die zur digitalen Bildgebung eingesetzt werden, oder Solarzellen, die Sonnenlicht direkt in elektrische Energie umwandeln. Seit einiger Zeit werden auf Silizium basierende photonische Technologien untersucht, die beispielsweise der optischen Datenübertragung dienen. Dadurch lässt sich der Datendurchsatz gegenüber einer elektronischen Übertragung und damit die Leistungsfähigkeit informationsverarbeitender Systeme steigern. Auch im Bereich der physikalischen Grundlagenforschung spielt Silizium eine wichtige Rolle. So wird beispielsweise daran gearbeitet, die Empfindlichkeit von Gravitationswellendetektoren durch die Verwendung von Testmassen aus Silizium weiter zu erhöhen, um damit die durch die allgemeine Relativitätstheorie vorhergesagten Gravitationswellen nachweisen zu können [1]. Alle diese Anwendungen nutzen die Absorption von Licht in Silizium oder die Transparenz für Licht großer Wellenlängen aus. Für ein Verständnis der physikalischen Vorgänge und darauf aufbauend die gezielte Optimierung der Bauteile ist eine genaue Kenntnis des Absorptionskoeffizienten erforderlich, der als fundamentale Materialkonstante die Absorption bei einer gegebenen Lichtwellenlänge quantifiziert. Der Absorptionskoeffizient von Silizium ist daher seit über 60 Jahren Gegenstand der Forschung, bereits 1955 wurden erste Messungen veröffentlicht. In der Folge haben sich eine Vielzahl wissenschaftlicher Arbeiten mit der Bestimmung des Absorptionskoeffizienten befasst, seit 1955 wurden fortlaufend neue Ergebnisse veröffentlicht [2–36]. Dass die Bestimmung des Absorptionskoeffizienten von Silizium nach wie vor ein aktuelles Forschungsthema ist, hat verschiedene Gründe. Da der Absorptionskoeffizient in dem für praktische Anwendungen wie z.B. die photovoltaische Energieerzeugung interessanten Wellenlängenbereich über mehr als 15 Größenordnungen variiert, untersuchten fast alle Arbeiten nur einen Teil dieses Wellenlängenbereichs, der mit dem jeweils verwendeten Messverfahren zugänglich ist. Aufbauend auf diesen Daten wurden kombinierte Datensätze erstellt, die den gesamten Wellenlängenbereich abdecken [32, 37]. Ein Blick auf die Literaturdaten (vgl. Abbildung 1) zeigt jedoch, dass die unterschiedlichen Datensätze teilweise um bis zu 20 % voneinander abweichen. Es ist unklar, ob diese Abweichungen nur auf Eigenschaften der untersuchten Proben zurückzuführen sind oder auch auf systematische Abweichungen und Unsicherheiten aufgrund der eingesetzten Messverfahren. Die Genauigkeit der Literaturdaten lässt sich nicht bewerten, da Messunsicherheiten nicht systematisch ermittelt oder - zum größten Teil - überhaupt nicht angegeben wurden. Teilweise sind auch nur unvollständige Informationen über die Eigenschaften der untersuchten Proben oder Messbedingungen wie beispielsweise die Proben temperatur vorhanden. Dazu kommt, dass für viele der älteren Arbeiten die Datensätze nicht (mehr) in tabellarischer Form verfügbar sind. Für die Verwendung dieser Datensätze müssen Abbildungen digitalisiert werden, was zusätzliche Unsicherheiten verursacht.

Diese Arbeit befasst sich mit der erneuten, präzisen und nachvollziehbaren Bestimmung des Absorptionskoeffizienten von Silizium, genauer mit der Bestimmung des Koeffizienten der Inter-Band-

Absorption, die zur Generation elektrischer Ladungsträger führt. Allerdings wird nicht nur ein Teil des für die Silizium-Photovoltaik interessanten Wellenlängenbereichs mit *einem* Verfahren untersucht, sondern es werden verschiedene Messverfahren eingesetzt (spektroskopische Ellipsometrie, Reflexions- und Transmissionsmessungen, spektral aufgelöste Lumineszenzmessungen und Messungen der spektralen Bestrahlungsstärkeempfindlichkeit), die insgesamt den Wellenlängenbereich von 250 bis 1450 nm abdecken. Für alle Messmethoden wird eine systematische Messunsicherheitsanalyse durchgeführt, die auf dem "Guide to the Expression of Uncertainty in Measurements" (GUM) basiert. Darüber hinaus erfolgen Vergleichsmessungen mit der Physikalisch-Technischen Bundesanstalt in Braunschweig, Deutschland (PTB), sowie der Australian National University in Canberra, Australien (ANU), die die in dieser Arbeit erhaltenen Messdaten bestätigen. Die Arbeit motiviert sich aus verschiedenen Interessen, die im Folgenden kurz skizziert werden.

Metrologisches Interesse Aufgrund des Fehlens systematisch ermittelter Messunsicherheiten für den Absorptionskoeffizienten ist es bislang nicht möglich, die Genauigkeit der Literaturdaten zu bewerten und die Abweichungen zwischen den Literaturdaten aufzuklären. So ist beispielsweise unklar, ob die Abweichungen auf systematische Unterschiede aufgrund der verschiedenen Messverfahren zurückzuführen sind. Aus metrologischer Sicht ist es daher von Interesse, den Absorptionskoeffizienten möglichst präzise zu messen und die damit verbundene Messunsicherheit systematisch zu ermitteln. Dies ermöglicht auch einen Vergleich der Ergebnisse der verschiedenen Messverfahren im Hinblick auf systematische Abweichungen, die im Messverfahren begründet sein könnten.

Finanzielles Interesse Allein in der Photovoltaik betrug das Marktvolumen im Jahr 2012 etwa 500 Milliarden Euro. Der Ertrag photovoltaischer Anlagen wird unter anderem durch den Wirkungsgrad bestimmt, mit dem sie Sonnenlicht in elektrische Energie umwandeln. Simulationen des Wirkungsgrads solcher Anlagen, anhand derer Investitionsentscheidungen getroffen werden, basieren unter anderem auf Materialkonstanten wie dem Absorptionskoeffizient. Bereits eine Unsicherheit in der Wirkungsgradvorhersage von 1 % führt bei dem erwähnten Marktvolumen zu einer finanziellen Unsicherheit von 500 Millionen Euro. Es ist wünschenswert, die tatsächliche finanzielle Unsicherheit abschätzen zu können, was die Kenntnis der Unsicherheit von Eingangsgrößen wie dem Absorptionskoeffizienten voraussetzt.

Ökologisches Interesse Die weltweite Energieversorgung beruht heute zum größten Teil auf fossilen Energieträgern. Die bei ihrer Verbrennung erzeugten Emissionen gelangen in die Umwelt, wo sie Klimaveränderungen, Luftverschmutzungen und Krankheiten beim Menschen hervorrufen. Das heutige Energiesystem schädigt also auf vielfältige Weise die natürliche Umwelt, beeinflusst massiv biogeochemische Kreisläufe und gefährdet die Gesundheit. Zudem sind die globalen Energieressourcen ungleich verteilt und begrenzt. Hieraus ergeben sich große geopolitische Konfliktpotentiale. Dies alles macht eine Änderung der Energieversorgung und eine Ausrichtung an nachhaltigen ökologischen und sozialen Kriterien dringend erforderlich. Dem erheblichen Auf- und Ausbau erneuerbarer Energien und insbesondere der Solarenergie kommt dabei eine Schlüsselrolle zu [38]. Um den Ausbau der Solarenergie voranzutreiben, müssen im Bereich der Photovoltaik unter anderem die flächenproportionalen Kosten für die Installation von Solarmodulen gesenkt werden. Dies lässt sich vor allem durch eine Steigerung des Wirkungsgrades der Solarzellen realisieren [39]. Eine wesentliche Voraussetzung für die Steigerung von Wirkungsgraden sind Charakterisierungs- und Simulationsverfahren, die eine genaue Analyse der Mechanismen ermöglichen, die in der Solarzelle zu Leistungsverlusten führen. Diese Verfahren benötigen einen genauen Datensatz des Absorptionskoeffizienten als Eingangsparameter.

Technisches Interesse Kristallines Silizium wird als gut verfügbares Halbleitermaterial für eine Vielzahl von Anwendungen in Industrie und Forschung eingesetzt. Für fundamentale Materialkonstanten wie den Absorptionskoeffizienten ist es wünschenswert, einen belastbaren Datensatz zur Verfügung zu haben, der auf nachvollziehbare Weise ermittelt wurde. Bei einer Vielzahl der Arbeiten zum Ab-

sorptionskoeffizienten wurden die Messdaten allerdings nur in grafischer Form publiziert und sind daher nicht unmittelbar für eine Weiterverwendung verfügbar. Aufgrund der Abweichungen zwischen den Datensätzen ist es darüber hinaus fraglich, welcher Datensatz verwendet werden soll. Im Rahmen dieser Arbeit erfolgten daher Vergleichsmessungen, die die Belastbarkeit der Daten sicherstellen. Darüber hinaus enthält die Arbeit die Daten in tabellarischer Form, um eine gute Verfügbarkeit zu gewährleisten.

Die Arbeit ist folgendermaßen aufgebaut: Kapitel 1 enthält eine kurze Zusammenfassung der wesentlichen physikalischen Grundlagen und Definitionen, auf denen die Arbeit aufbaut. Kapitel 2 beschreibt die verschiedenen Messverfahren, die zur Ermittlung des Absorptionskoeffizienten eingesetzt wurden. Dies beinhaltet jeweils eine Beschreibung der physikalischen Zusammenhänge zwischen dem Absorptionskoeffizienten und der Messgröße, eine Beschreibung des Messaufbaus und der verwendeten Proben sowie eine systematische Messunsicherheitsanalyse. Jedes dieser Verfahren deckt nur einen Teil des insgesamt untersuchten Wellenlängenbereichs ab. Im dritten Kapitel wird die Berechnung eines kombinierten Datensatzes des Absorptionskoeffizienten aus den verschiedenen Messdaten beschrieben. Da der Gegenstand dieser Arbeit die Bestimmung des Koeffizienten der Inter-Band-Absorption ist, wird an dieser Stelle auch die Notwendigkeit von Korrekturen bezüglich anderer Absorptionsmechanismen diskutiert. Kapitel 4 beschreibt Anwendungen des erhaltenen Datensatzes für die Photovoltaik. Es enthält eine Analyse des Einflusses der ermittelten Messunsicherheiten auf die Unsicherheit von simulationsgestützten Wirkungsgradvorhersagen und diskutiert den Einfluss der Abweichung der Daten von den bislang verwendeten Literaturdaten. Darüber hinaus wird ein analytisches Modell der spektralen Lumineszenzemission von Silizium-Solarzellen und -Wafeln vorgestellt. Dieses Modell erfordert einen Datensatz des Absorptionskoeffizienten als Eingangsparameter und ermöglicht unter anderem die Bestimmung der Rückseitenreflexion von Solarzellen aus dem Lumineszenzspektrum. In diesem Zusammenhang wird auch gezeigt, dass die bisher verwendeten Literaturdaten zu systematischen Abweichungen zwischen Modell und Messung von Lumineszenzspektren führen.

Crystalline silicon is an important feedstock for a wide variety of applications. For instance, it is used by the microelectronics industry for the fabrication of integrated circuits, which facilitate modern telecommunication and information technologies. Most of the sensors used for imaging purposes are based on crystalline silicon. For some time, there has been research on photonical technologies based on silicon, which might be used for optical data transfer and could increase the data transfer rate and thereby the capabilities of computational systems. Crystalline silicon is also important in the field of fundamental physical research. For instance, there are attempts to use silicon targets as test masses in order to increase the accuracy of interferometers used for the detection of gravitational waves, which are predicted by the theory of relativity [1]. All of these applications make use of the absorption of light within silicon or of the transparency for long-wavelength light. Detailed knowledge about the absorption coefficient, which is a fundamental material property and quantifies the absorption at a given wavelength, facilitates the understanding of physical processes and the subsequent optimization of the devices. It is for this reason that the absorption coefficient of silicon has been a subject of scientific research for more than 60 years. Already in 1955, first measurements were published. Thereafter, a variety of scientific studies on the determination of the absorption coefficient have been carried out. New data was published [2–36]. The absorption coefficient of crystalline silicon is still an ongoing subject of scientific research for several reasons. In the wavelength range that is interesting for practical applications such as the photovoltaic generation of electricity, the absorption coefficient varies by more than 15 orders of magnitude. Thus, almost all of the studies only investigated a part of this wavelength range, which is accessible by the measurement method used. Based on these data, combined data sets were created which cover the whole wavelength range [32, 37]. Figure 1 provides an overview of the most widely used data from literature. As can be seen, deviations between the different data of up to 20% are found. It is unclear whether the deviations are only due to the specific properties of the investigated samples or whether they can be explained by systematic deviations or uncertainties due to the measurement methods used. The accuracy of the literature data cannot be assessed since measurement uncertainties have not been determined systematically or, as for the major part of the studies, have not been indicated at all. Moreover, only incomplete information about the properties of the samples and measurement conditions as sample temperature is found in some of the studies. Another issue is that for most of the older work, tabulated data is not available (anymore). In order to use these data, figures must be digitized, which leads to additional uncertainties of unknown extend.

This work is concerned with the accurate and comprehensible redetermination of the absorption coefficient of crystalline silicon. More precisely, the work is concerned with the determination of the coefficient of inter-band absorption, which leads to the generation of electrical charge carriers. However, the investigation is not restricted to a part of the wavelength range which is of interest for silicon photovoltaics and to *one* measurement method. Different measurement methods are used (spectroscopic ellipsometry, measurements of reflectance and transmittance, spectrally resolved luminescence

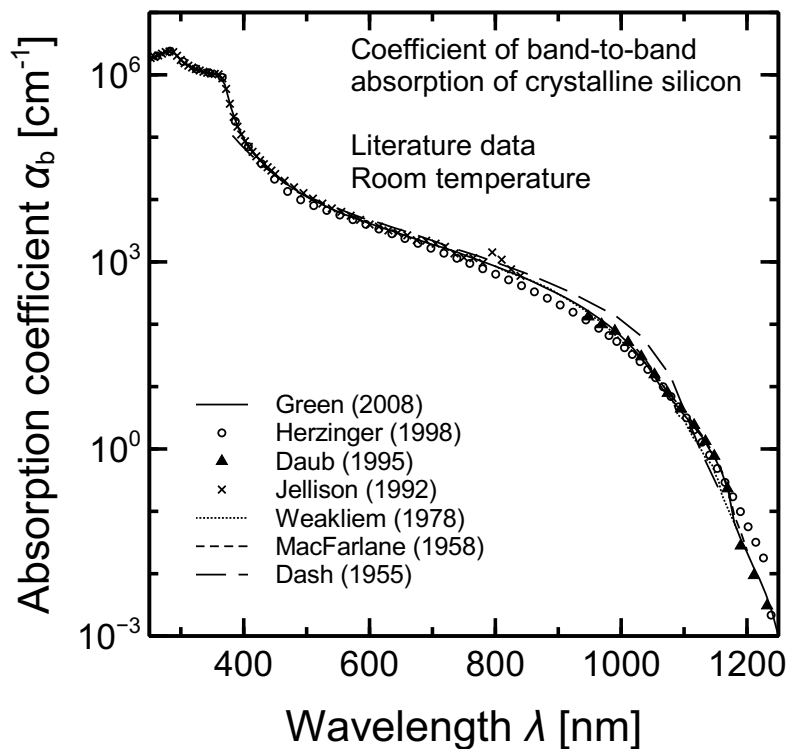


Figure 1: Overview of the most widely used literature data of the absorption coefficient of crystalline silicon at room temperature.

measurements and measurements of the spectral responsivity of solar cells) and cover the wavelength range from 250 to 1450 nm. For all methods, a systematic measurement uncertainty analysis is carried out based on the “Guide to the expression of uncertainty in measurements” (GUM). Furthermore, the data is consolidated by comparison with data measured by the Physikalisch-Technische Bundesanstalt in Braunschweig, Germany (PTB) and the Australian National University in Canberra, Australia (ANU). The work is motivated by different interests that are outlined in the following:

Metrological interest Due to the lack of systematically determined measurement uncertainties, to date it has not been possible to assess the accuracy of the literature data and to resolve the deviations between the data. For instance, it is unclear whether there are systematic deviations between the results of different measurement methods. From a metrological point of view, an accurate measurement of the absorption coefficient and a systematic determination of the measurement uncertainties is thus desirable. Such an analysis also enables a comparison of the different measurement methods with respect to systematic deviations between the results.

Financial interest The financial volume of the photovoltaic market was about 500 billion Euro in 2012. The yield of photovoltaic systems is determined, among others, by the efficiency of energy conversion from sunlight into electricity. Invest decisions are made based on the results of energy conversion efficiency simulations. Hence, an uncertainty of the simulation results of only 1% already corresponds to a financial uncertainty of 500 million Euro. An estimation of this uncertainty is thus desirable. For this purpose, the uncertainty of simulation input quantities such as the absorption coefficient must be known.

Environmental interest Today, the world’s energy supply is mostly based on fossil fuels. The combustion of these fuels leads to air pollution, climate changes and diseases. Hence, today’s energy

supply system endangers the preservation of nature and the living environment of all human beings. Moreover, the global energy resources are limited and unequally distributed. This urgently requires a transformation of the energy supply and a focus on sustainable, ecological and social criteria. The expansion of renewable energy supplies and especially the photovoltaics is a key part of this transformation [38]. The decrease of costs proportional to the area of photovoltaic devices is a promising way to further expedite the expansion of photovoltaics and can be achieved by increasing the energy conversion efficiency of photovoltaic devices [39]. The optimization of the energy conversion efficiency requires characterization and simulation methods that allow for a detailed analysis of power loss mechanisms. These methods require accurate data of the absorption coefficient as input.

Technical interest As a readily available feedstock, crystalline silicon is used for a variety of industrial or research applications. It is thus desirable to have accurate and reliable data for fundamental material constants such as the absorption coefficient. However, many of the publications on the absorption coefficient only contain the data in a graphical form. The data can thus not be used easily. Moreover, due to the deviations between the data, the question arises which data set should be used. In this work, the data is thus consolidated by comparison with measurement results obtained by other institutions. Additionally, tabulated data is given in order to ensure the availability and usability of the data.

The structure of this work is as follows: Chapter 1 provides a short review of the fundamental physical relations and definitions, on which the following work is based. Chapter 2 describes the different methods used for the determination of the absorption coefficient. For each method, the physical relation between the absorption coefficient and the measurand is outlined. The measurement setup and the samples are described and a systematical measurement uncertainty analysis is carried out. Each of the measurement methods only covers a part of the wavelength range which is investigated. Chapter 3 therefore describes the calculation of a combined data set of the absorption coefficient from the different data. As the purpose of this work is the determination of the coefficient of band-to-band absorption, the requirement of corrections for other absorption mechanisms is also discussed. Chapter 4 contains applications of the absorption coefficient data determined in this work for the field of silicon photovoltaics. In this chapter, the impact of the uncertainty of the absorption coefficient on the uncertainty of energy conversion efficiency predictions by means of device simulations is analyzed, as well as the impact of deviations from the literature data. Moreover, an analytical model of the spectral luminescence emission of silicon solar cells and wafers is presented. This model requires data of the absorption coefficient as input and facilitates the determination of the rear surface reflectance of solar cells from their luminescence spectrum. In this context, it is also shown that the most widely used literature data of the absorption coefficient lead to deviations between measured and modeled luminescence spectrum.

Theoretical background

This chapter presents a brief review of the electronic properties of crystalline silicon and the theory of light absorption within silicon devices. It is not the aim of this chapter to outline the fundamentals of semiconductor theory but to mention the important aspects that form the basis for this work. The chapter closes with a summary of the basic concepts and terminology used for the measurement uncertainty analysis presented in this work.

1.1 Electronic properties of crystalline silicon

The atomic arrangement found in crystalline silicon is referred to as the *diamond lattice*. The unit cell of this lattice is cubic. It is visualized in Fig. 1.1. The regular arrangement of the atoms within the crystal leads to the formation of bands of allowed energy states for the electrons, separated by bands of forbidden states. The most simple model of the band structure within a semiconductor consists of only two energy bands: The *valence band* and the *conduction band*, which are separated by the characteristic band gap energy E_G as shown in Fig. 1.2. Electrons which are excited from the valence to the conduction band are able to move within the crystal, i.e., they can contribute to a current flowing through the crystal. The excitation of an electron creates a vacant position in the valence band, which is commonly denoted as a *hole*. Holes are usually treated as (virtual) charge carriers with positive elementary charge instead of working with missing electrons in the valence band. Thus, the excitation of an electron into the conduction band creates an *electron-hole pair*. The minimum energy for the excitation of an electron is the band gap energy E_G . The inverse process (the transition of an electron from the conduction to the valence band) is denoted as *recombination*. Although this simple model is quite instructive, it neglects some important aspects of the band structure of crystalline silicon such as the separation of the band edges in momentum space or the fact that recombination requires both an electron and a hole to be at the same position in space.

The relation between energy E and momentum p of electrons and holes located in energy states near the band edges is given by the dispersion relations [40]

$$\begin{aligned} E - E_C &= \frac{(p - p_{0,c})^2}{2m_e^*}, \\ E - E_V &= -\frac{(p - p_{0,v})^2}{2m_h^*} \end{aligned} \quad (1.1)$$

where E_C and E_V denote the energy of the band edges according to Fig. 1.2 and m_e^* and m_h^* denote the

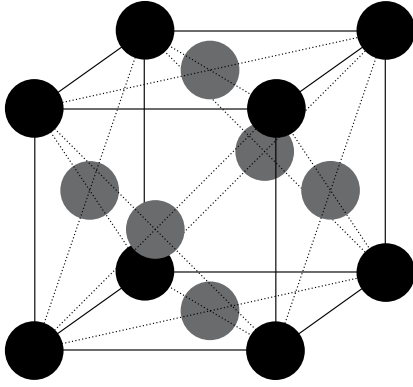


Figure 1.1: Unit cell of a diamond lattice.

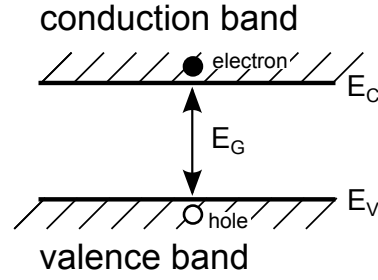


Figure 1.2: Simple representation of valence and conduction band.

effective masses of electrons and holes, respectively. $p_{0,c}$ and $p_{0,v}$ indicate the position of the energy band minima. If $p_{0,c} = p_{0,v}$, one speaks of a *direct band gap*. For silicon, $p_{0,c} \neq p_{0,v}$ which means that the minima of valence and conduction band are separated in momentum space. This is referred to as *indirect band gap*. Hence, a transition between the band minima requires a change of momentum of the electron. This change of momentum is achieved by an interaction with the crystal lattice, i.e., the absorption or emission of a phonon. Figure 1.3 shows the band structure of crystalline silicon according to Refs. 41 and 42.

Electrons are fermions, which means that each allowed energy level within the crystal can only be occupied by, at most, two electrons of opposite spin. In thermal equilibrium, the probability $f(E)$ for an energy state of energy E to be occupied by an electron is given by the *Fermi-Dirac distribution function*

$$f(E) dE = \frac{1}{1 + \exp((E - E_F)/(kT))} dE \quad (1.2)$$

where k is the Boltzmann constant, E_F is the Fermi energy and T is the absolute temperature. Note that $f(E)$ is a differential quantity in terms of energy as indicated by adding dE on both sides of the latter equation. Near the band edge, the density of allowed states for electrons in the conduction band N is given by

$$N_C(E) dE = \frac{8 \sqrt{2\pi} \sqrt[3]{m_e^*}}{h^3} \sqrt{E - E_C} dE \quad (1.3)$$

where h is the Planck constant. A similar expression follows for the density of states in the valence band:

$$N_V(E) dE = \frac{8 \sqrt{2\pi} \sqrt[3]{m_h^*}}{h^3} \sqrt{E_V - E} dE. \quad (1.4)$$

The density of electrons and holes, respectively, per energy interval dE is the product of the probability of occupancy $f(E)$ and the density of states $N(E)$. Figure 1.4 shows a qualitative sketch of the Fermi-Dirac distribution function, the density of states and the resulting charge carrier density D per energy interval dE .

Doping of the semiconductor introduces energy levels in the band gap, located either close to the edge of the valence band in case of acceptor dopants or close to the edge of the conduction band in case of donor dopants. At room temperature, nearly all dopants are ionized [43], which leads to an increased conductivity of the semiconductor crystal.

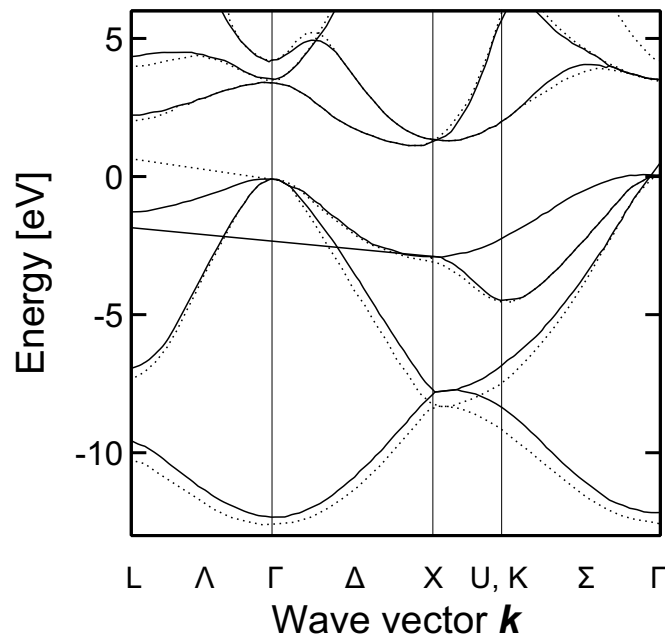


Figure 1.3: Band structure of crystalline silicon according to Refs. 41 and 42.

Optical or electrical injection of charge carriers leads to a deviation from thermal equilibrium. Under constant excitation, however, a static equilibrium between generation and recombination of charge carriers establishes. The distribution of electrons and holes in the conduction and valence band, respectively, can then be described by independent *Quasi-Fermi energy levels* for each band [44]. This is possible since the (intra-band) thermalization of charge carriers is much faster than the (inter-band) recombination or excitation. The rate of spontaneous radiative recombination, which is analyzed by luminescence measurements, depends on the splitting of the Quasi-Fermi energy levels ΔE_F (see chapter 2.2).

1.2 Absorption of light within silicon

Absorption of light is basically the annihilation of photons whose energy is transferred to an electron within the crystal, i.e., the electron is excited into a state of higher energy. Depending on the combination of initial and final states involved in the absorption process, different absorption mechanisms are distinguished.

The fundamental process in the ultraviolet, visible and near-infrared spectral range (wavelengths below 1100 nm) is the inter-band absorption where electrons from the valence band are excited into the conduction band. For photon energies above 3.4 eV, direct transitions are possible [8]. For lower photon energies, indirect transitions occur by the absorption or emission of phonons. Inter-band absorption creates free charge carriers that can contribute to a current flowing through the crystal. It is thus fundamental for all types of photovoltaic devices. In the following, this process will be referred to as *band-to-band absorption*. Photons may also be absorbed by either intra-band or band-impurity absorption. Intra-band absorption is caused by the excitation of an electron within the conduction band into a state of higher energy within the same band. This absorption process (also known as *free carrier absorption*, FCA) is often termed *parasitic absorption* as it does not generate additional free charge carriers but may hamper the functionality of photovoltaic devices. Band-impurity absorption denotes the excitation of an electron within the valence band into a state within the band gap which is induced by an impurity. Such transitions can also occur from an impurity state into the conduction

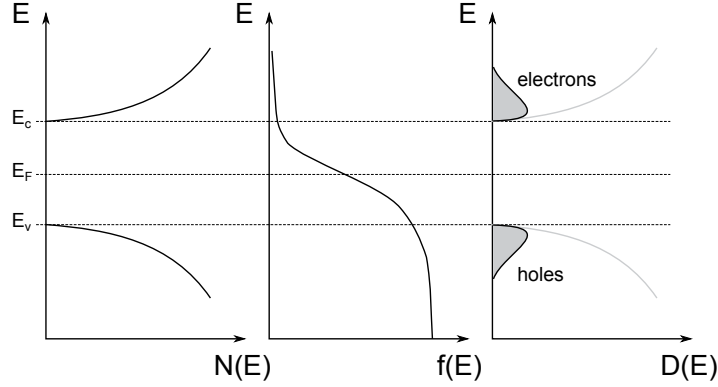


Figure 1.4: Qualitative sketch of the density of states $N(E)$, the Fermi-Dirac distribution function $f(E)$ and the resulting charge carrier density $D(E)$ per energy interval dE .

band.

This work focusses on the determination of the coefficient of band-to-band absorption α_{bb} , characterizing the fundamental absorption process for photovoltaic devices. Free carrier absorption is also briefly discussed since it may be the dominant absorption process at wavelengths around the band gap, which may impose restrictions on the methods used to measure α_{bb} . Band-impurity absorption is located at wavelengths far beyond the band gap and has virtually no significance for practical devices with low impurity concentrations. As it does not interfere with the measurements presented in this work, it is not discussed further here. Beside these main contributions to photon absorption, there are other processes such as lattice absorption, which contribute at very low photon energies only and are therefore not considered in the context of this work.

1.2.1 General definition of the absorption coefficient

Within a homogeneous silicon crystal, the rate of photon absorption is constant within each volume element. Mathematically, this is expressed as

$$-\text{div } \vec{\Phi}(\lambda) = \alpha(\lambda) |\vec{\Phi}(\lambda)| \quad (1.5)$$

where $\vec{\Phi}$ is the photon flux, λ is the photon wavelength and α is the absorption coefficient so defined. In silicon, absorption is isotropic. Equation (1.5) can thus be rewritten in a one-dimensional form,

$$-\frac{d^2}{dz^2} \Phi(\lambda, z) = \alpha(\lambda) \Phi(\lambda, z), \quad (1.6)$$

where the z -axis points in the direction of the photon flux. The solution of Eq. (1.6) is the common Lambert-Beer absorption law

$$\Phi(\lambda, z) = \Phi_0(\lambda) \exp(-\alpha(\lambda) z). \quad (1.7)$$

Here, Φ_0 denotes the initial intensity of the photon flux. The absorption coefficient contains all of the absorption processes mentioned above:

$$\alpha = \alpha_{bb} + \alpha_{fc} + \alpha_{imp}. \quad (1.8)$$

In the latter equation, α_{bb} , α_{fc} and α_{imp} represent the coefficients of band-to-band absorption, free carrier absorption and band-impurity absorption, respectively. The absorption coefficient α is related to the complex index of refraction

$$\hat{n} = n + i\kappa \quad (1.9)$$

by [45]

$$\alpha = \frac{4\pi\kappa}{\lambda}. \quad (1.10)$$

Real and imaginary part of the complex index of refraction are related by the Kramers-Kronig relations [45, 46]

$$n(E) = 1 + \frac{2}{\pi} P \int_0^{\infty} dE' \frac{E' \kappa(E')}{(E')^2 - E^2}, \quad (1.11)$$

$$\kappa(E) = 1 - \frac{2E}{\pi} P \int_0^{\infty} dE' \frac{n(E')}{(E')^2 - E^2}. \quad (1.12)$$

In the latter equations, $P \int_0^{\infty} \equiv \lim_{\delta \rightarrow 0} (\int_0^{E'-\delta} + \int_{E'+\delta}^{\infty})$ denotes the Cauchy principal value of the integral.

1.2.2 Indirect band-to-band absorption

Photons carry a large energy of $h\nu$ but only a small momentum of h/ν (ν being of the order of microns). In contrast, phonons carry a small energy E_{ph} of hd and a large momentum of h/d , the lattice constant d being of the order of Angstroms. Indirect band-to-band absorption thus requires the absorption or emission of a phonon due to conservation of momentum. The minimum photon energy required for the excitation of an electron to the conduction band is $h\nu = E_G - E_{\text{ph}}$. The absorption coefficient is proportional to the integral over all combinations of possible initial and final states and also to the probability of phonon interaction, which is described by Bose-Einstein statistics. Using the parabolic approximation of valence and conduction edges given in Eq. (1.1), it can be shown that the coefficient of indirect band-to-band absorption is expected to obey the relation [45]

$$\alpha_a(h\nu) \propto \frac{(h\nu - E_G + E_{\text{ph}})^2}{\exp(E_{\text{ph}}/kT) - 1} \quad (1.13)$$

for transitions where phonons are absorbed and

$$\alpha_e(h\nu) \propto \frac{(h\nu - E_G - E_{\text{ph}})^2}{1 - \exp(-E_{\text{ph}}/kT)} \quad (1.14)$$

when phonons are emitted. The overall coefficient of indirect band-to-band absorption α_{bb} is the sum of both processes:

$$\alpha_{\text{bb}}(h\nu) = \alpha_a(h\nu) + \alpha_e(h\nu) \propto (h\nu - E_G + E_{\text{ph}})^2 + (h\nu - E_G - E_{\text{ph}})^2. \quad (1.15)$$

Equation (1.15) suggests a method for the determination of the band gap energy E_G : Due to $E_{\text{ph}} \ll E_G$, a plot of $\sqrt{\alpha_{\text{bb}}}$ vs. photon energy $h\nu$ is expected to show a linear regime since

$$\sqrt{\alpha_{\text{bb}}} \propto (h\nu - E_G). \quad (1.16)$$

Extrapolation of the linear regime to $\alpha_{\text{bb}} = 0$ then yields the band gap energy E_G . This method, also known as *Tauc plot*, was first introduced by J. Tauc for the determination of the band gap energy of germanium [47].

1.2.3 Direct band-to-band absorption

Direct band-to-band absorption occurs when the photon energy exceeds the direct band gap energy of approximately 3.4 eV which corresponds to wavelengths below approximately 340 nm. The coefficient of direct band-to-band absorption is proportional to the density of associated states in the valence and conduction band as given by Eqs. (1.4) and (1.3). This leads to a square-root dependence of the absorption coefficient on photon energy [45]:

$$\alpha \propto \sqrt{h\nu - E_G} \quad (1.17)$$

According to the tabulated AM1.5G spectral distribution [48], about 1% of the photons in sunlight have enough energy to excite direct transitions. However, the absence of direct band-to-band absorption would not affect the functionality of practical photovoltaic devices, since photons of such energies would be absorbed by indirect processes anyway.

1.2.4 Free carrier absorption (FCA)

The coefficient of free carrier absorption α_{fc} depends on the concentration of free charge carriers in the conduction band and on the wavelength. Classical theory predicts a proportionality to the square of the wavelength and the charge carrier concentration [43]. Green [37] states an empirical expression for α_{fc} “for photon energies above 0.5 eV and carrier densities around 10^{18} cm^{-3} ”:

$$\alpha_{fc} [\text{cm}^{-1}] = n K_n \lambda^a + p K_p \lambda^b \quad (1.18)$$

where n and p are the densities of electrons and holes in units of cm^{-3} , λ is the wavelength in units of nm, $K_n = 2.6 \times 10^{-27}$, $K_p = 2.7 \times 10^{-24}$, $a = 3$ and $b = 2$. Figure 1.5 visualizes α_{fc} according to the parametrization of Green for different doping concentrations of a p -type wafer in comparison to α_{bb} as determined by Daub et al. [23]. As can be seen, FCA is important for highly doped layers and/or long wavelengths. Otherwise, the absorption is dominated by band-to-band absorption. Note that different FCA parametrizations were recently reviewed and experimentally validated by Baker-Finch et al. [36]. The parametrization of Green, which is used throughout this work, is shown to be generally consistent with the data obtained in their work.

1.2.5 Temperature dependence of the band gap energy

The band gap energy E_G decreases with increasing temperature, which implies an increasing absorption coefficient α_{bb} . The major contribution to this effect is caused by a temperature-dependent interaction of the electrons with the crystal lattice [49–54]. A second contribution results from a temperature-dependent dilatation of the crystal lattice [55, 56]. Several publications are concerned with the temperature dependence of E_G [57–63]. In the photovoltaic community, the parametrization of Palankovski [60], which is visualized in Fig. 1.6, is widely used:

$$E_G(T) = E_0 - \frac{aT^2}{T + b} \quad (1.19)$$

with $E_0 = 1.1695 \text{ eV}$, $a = 4.73 \times 10^{-4} \text{ eV/K}$, $b = 636 \text{ K}$ and the temperature T in units of K.

1.2.6 Injection and doping dependence of the band gap energy

The band gap energy E_G decreases with increasing charge carrier concentration. Reasons for the decrease of E_G are Coulomb screening and formation of band tails [64]. Schenk [65] developed an analytical model which calculates the band gap narrowing depending on doping concentration

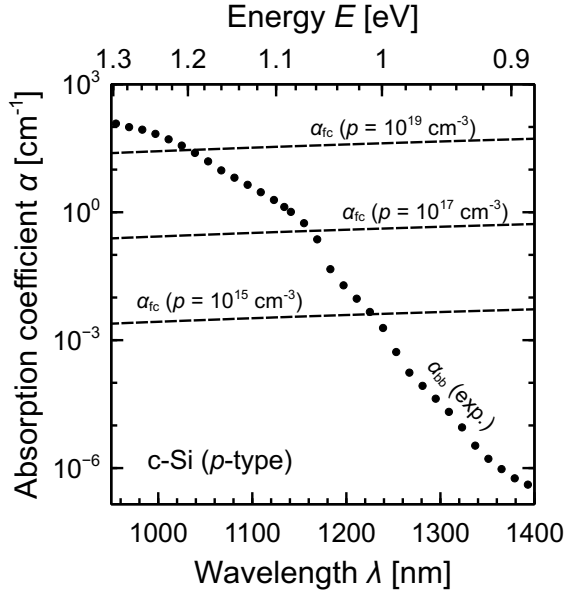


Figure 1.5: Coefficient of free carrier absorption α_{fc} according to the parametrization of Green [37] for different doping concentrations of a p -type silicon wafer in comparison to the coefficient of band-to-band absorption α_{bb} as determined by Daub et al. [23].

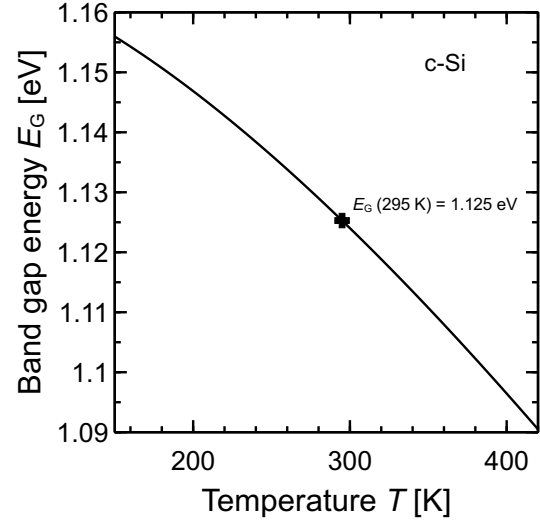


Figure 1.6: Temperature dependence of the band gap energy E_G as given in Ref. 60.

and charge carrier densities. The model is visualized in Fig. 1.7 for p -type silicon. The band gap narrowing in thermal equilibrium increases from -0.01 meV at acceptor concentrations of 10^{10} cm^{-3} to -100 meV at acceptor concentrations of 10^{20} cm^{-3} . Under low-level injection conditions, the band gap narrowing is dominated by the doping concentration. Under high-level injection conditions, the excess charge carrier concentration becomes dominant for the band gap narrowing.

1.3 Systematical Measurement Uncertainty Analysis

The objective of any measurement is to obtain an estimate of the *true value* of the measurand. In order to assess the quality of a measurement, it is necessary to evaluate the *uncertainty* of the measured value, which defines the interval around the measured value within which the true value is expected to lie with a given probability. The measurement uncertainty analysis presented in this work is based on the *Guide to the Expression of Uncertainty in Measurement* [66] (GUM). The GUM is the international standard for the systematic evaluation of measurement uncertainties. This section briefly summarizes the terminology and methodology used in the GUM and also in this work. For a definition of the metrological terms, the reader is referred to the *International vocabulary of metrology - Basic and general concepts and associated terms* (VIM) [67].

1.3.1 Definition: Process equation

In many experiments, a measurand Y is not measured directly but calculated from other quantities X_i whose values are determined in the experiment. The *process equation* describes the functional relationship

$$Y = f(X_1, \dots, X_N). \quad (1.20)$$

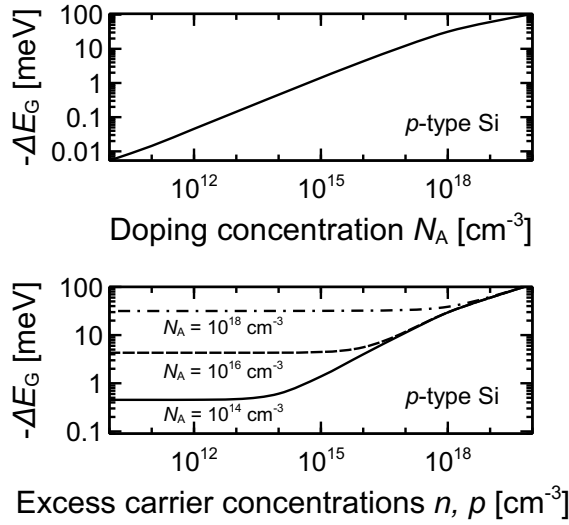


Figure 1.7: Visualization of band gap narrowing for p -type silicon as calculated with the model of Schenk [65]. Top: Dependence on acceptor concentration N_A in thermal equilibrium. Bottom: Injection dependence for different acceptor concentrations.

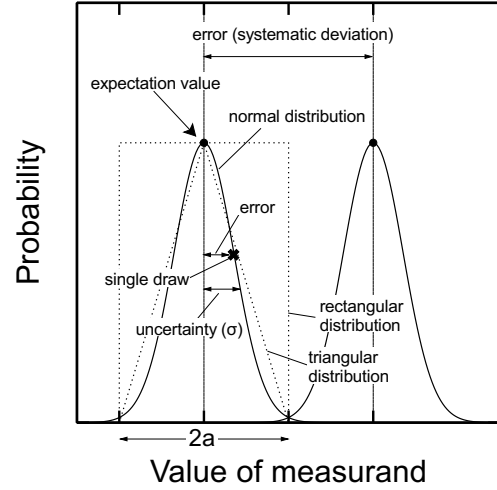


Figure 1.8: Visualization of the concepts of *uncertainty* and *error* in a measurement and recurrent probability distribution functions.

between the *input quantities* X_i and the *output quantity* Y . The values of the quantities are denoted by the corresponding lowercase letters, i.e., y and x_i . A common example for such an experiment is the determination of an electrical current (output quantity) by measuring the voltage drop over a calibrated measurement shunt (input quantities), where the process equation is given by Ohm's law.

1.3.2 Definition: Uncertainty, error and correction

In its basic sense, *measurement uncertainty* means “doubt about the validity of the result of a measurement” [66]. This doubt originates from unavoidable experimental imperfections such as fluctuations of output values due to measurement noise. The evaluation of the impact of such effects on the value of the output quantity leads to an interval, within which the true value is expected to lie with a given probability. In a practical sense, measurement uncertainty thus refers to this interval. From a statistical point of view, the uncertainty of a measured value is given by its probability distribution function, as visualized in Fig. 1.8. Recurrent probability distribution functions are the normal (gaussian) distribution, the rectangular distribution and the triangular distribution. These distributions are visualized in Fig. 1.8. The normal distribution is characterized by its standard deviation σ . For the rectangular distribution, the standard deviation σ_{rect} is given by [66]

$$\sigma_{\text{rect}} = a/\sqrt{3} \quad (1.21)$$

where a is the half width of the distribution (i.e., $2a$ is the difference between the bounds). For the triangular distribution, the standard deviation σ_{tri} is [66]

$$\sigma_{\text{tri}} = a/\sqrt{6}. \quad (1.22)$$

According to the VIM, an *error* is defined as the difference between the measured value and a reference value. Regarding the probability distribution of the measured value, the error of a single measurement (i.e., a single draw from the distribution) would thus be the difference between the measured value and the expectation value of the quantity. In practice, the term “error” is often also used

to describe the impact of systematic effects that change the expectation value of the measurand, as visualized in Fig. 1.8. In the context of the example of the current measurement mentioned above, such a “systematic error” could be a temperature variation of the measurement shunt which is not considered in the process equation. The example shows that this is actually not an error in the sense of the VIM definition, but rather an incomplete definition of the process equation. Thus, the systematic effect can be compensated by applying a *correction* to the measured value, which is actually an extension of the process equation to account for the effect.

It is important to note that the GUM assumes all systematic effects to have been identified and included in the process equation to the maximum extent possible, because the reported (expectation) value is usually assumed to coincide with the true value of the measurand. Only in case that the deviations caused by a systematic effect are negligible with respect to the uncertainty, a correction can be omitted. In this sense, applying corrections for systematic effects does not reduce the uncertainty of the measured value. The uncertainty of the correction itself is calculated by including the effect in the process equation and applying the standard formalism.

It should be noted that sometimes, known systematic deviations are taken into account by enlarging the uncertainty rather than including it in the process equation. In this case, applying a correction would indeed “reduce the uncertainty”. However, this approach gives misleading results and is deprecated by the GUM.

1.3.3 Type A and B uncertainties

The GUM distinguishes between *type A* and *type B* uncertainty components. This distinction refers to how the uncertainty component is determined. Type A uncertainties are determined by repeated observations of the measurand. The measured value is then the average of the single results. A familiar case of type A uncertainty evaluation is uncertainty due to statistically distributed noise. The type A uncertainty of the measured value is given by the standard deviation σ of the repeated observations,

$$\sigma = \sqrt{\frac{1}{1-N} \sum_{i=1}^N (\bar{x} - x_i)^2}, \quad (1.23)$$

divided by the square root of the number of results:

$$u_A(\bar{x}) = \frac{\sigma}{\sqrt{N}}. \quad (1.24)$$

In the latter equations, N is the number of observations, x_i are the single measurement results and \bar{x} is the average of the single results. Every other uncertainty component, which is not determined from repeated observations, is termed type B uncertainty. For instance, this includes uncertainties that are obtained from a calibration report, a technical reference, a physical model, separate measurements or scientific experience.

1.3.4 Combined standard uncertainty

The *combined standard uncertainty* $u_c(y)$ of the output quantity is the positive square root of the combined variance of the output quantity, given by

$$u_c^2(y) = \sum_{i=1}^N \left(\frac{\partial f}{\partial x_i} \right)^2 u^2(x_i) + 2 \sum_{i=1}^N \sum_{j=i+1}^N \frac{\partial f}{\partial x_i} \frac{\partial f}{\partial x_j} u(x_i) u(x_j) r(x_i, x_j). \quad (1.25)$$

The second summand in the latter equation is zero if all input quantities are uncorrelated, which means that the *correlation coefficients* $r(x_i, x_j)$ are zero. The correlation coefficient varies between 1 (correlated) and -1 (anticorrelated). The factors $(\partial f / \partial x_i)^2$ and $(\partial f / \partial x_i)(\partial f / \partial x_j)$ are denoted as *sensitivity coefficients* c_i^2 and $c_{i,j}$, respectively.

1.3.5 Expanded uncertainty

The *level of confidence* (also called *coverage probability*) for a given uncertainty indicates the probability that a measurement will yield a result which deviates from the expectation value of the measurement by not more than the specified uncertainty. The *expanded uncertainty* U for a desired level of confidence is obtained from the combined standard uncertainty u_c by multiplication with a *coverage factor* k :

$$U(y) = k u_c(y) . \quad (1.26)$$

The value of k for a given level of confidence is determined by the distribution function of the quantity. For a normal distribution, the combined standard uncertainty corresponds to a coverage probability of approximately 68%. The expanded uncertainty for $k = 2$, which is usually indicated by certified calibration laboratories, corresponds to a coverage probability of approximately 95%. The *central limit theorem* states that the distribution function of an output quantity which follows from the convolution of normal distribution functions of the input quantities is also a normal distribution. However, this holds approximately even if the input quantities are not described by normal distribution functions. In practice, the assumption of a normal distribution function for an output quantity which is calculated from several input quantities is usually justified as long as the uncertainty is not dominated by a non-normally distributed input quantity. The expanded uncertainty of an output quantity for $k = 2$ thus usually corresponds to a coverage probability of approximately 95%.

A more precise calculation of the coverage factor is enabled by recognizing that the distribution function of the output quantity can be approximated by a t-distribution with an *effective* degree of freedom ν_{eff} . The effective degree of freedom can be estimated by the Welch-Satterthwaite formula

$$\nu_{\text{eff}} = \frac{u_c^4(y)}{\sum_{i=1}^N \frac{(c(x_i)u(x_i))^4}{\nu_i}} \quad (1.27)$$

where ν_i is the degrees of freedom for the input quantity x_i . The expanded uncertainty

$$U(y) = t_p(\nu_{\text{eff}}) u_c(y) \quad (1.28)$$

then corresponds to a coverage probability p . The quantity $t_p(\nu)$ defines the fraction p of the t-distribution that is included in the interval $[-t_p(\nu), +t_p(\nu)]$. Values of $t_p(\nu)$ can be retrieved from tabulations.

If the quantity x_i is obtained by repeated observations (type A uncertainty), then ν_i is given by the number of observations minus the number of parameters that are determined from the set of data. For type B uncertainty components, $\nu_i = \infty$ can be assumed as the distribution function is assumed to be known completely. If the relative “uncertainty of the uncertainty” u_u can be estimated, it can be used to estimate the degrees of freedom of the type B uncertainty component by

$$\nu = \frac{1}{2} u_u^{-2} . \quad (1.29)$$

1.3.6 Conformity of measurement results

A measured value is assigned a certain probability distribution as outlined above. In this context, it is not meaningful to say that “two values match (or do not match) within their specified uncertainty”. Rather, a probability must be stated: How likely is it that the two measurements have the same result, i.e., the results are compatible? In order to answer this question, different concepts can be pursued. One option is to measure the similarity of the two normal distributions by using the *coefficient of overlap* (OVL) [68] . The OVL measures the ratio of the area covered by both distributions and

the total area covered by the two distributions. A OVL of 1 means that both distributions are equal, a OVL of 0 means no overlapping at all. However, the interpretation of the OVL when applied to probability distributions is difficult. Probability distributions f must satisfy the constraint $\int_{-\infty}^{\infty} f = 1$, i.e., they must be normalized such that the area covered by the distribution function is unity. Hence, two distribution functions with equal mean but different standard deviations actually look different and the OVL is smaller than 1. Therefore, the OVL is a useful measure only if the standard deviations of the two distribution functions are similar. Another approach, which is also pursued in this work, compares the difference of two measurement results $d = x_1 - x_2$ to the uncertainty of d in case of uncorrelated measurements, given by $U(d) = k \sqrt{u_c^2(x_1) + u_c^2(x_2)}$. This ratio, denoted as E_n -number

$$E_n = \frac{1}{k} \frac{|x_1 - x_2|}{\sqrt{u_c^2(x_1) + u_c^2(x_2)}}, \quad (1.30)$$

is also used in international key comparisons as a criterion for measurement compatibility [69]. In Eq. (1.30), k is the coverage factor defined above which must be equal for both measurements. Depending on the type of comparison, compatibility of the measurements is accepted for $E_n \leq 1/2$ or $E_n \leq 1$. In this work, compatibility is accepted if

$$E_n \leq 1 \quad (1.31)$$

holds, which means that the difference between the two measurement results, $|x_1 - x_2|$, is smaller than the expanded uncertainty of this difference for $k = 2$, $\sqrt{(2 u_c(x_1))^2 + (2 u_c(x_2))^2}$.

1.3.7 Combination of measurement results

If the same quantity is measured with different methods or by different institutions, the results y_i can be combined in order to obtain a best estimate \bar{y} for the true value of the quantity:

$$\bar{y} = \frac{\sum_{i=1}^N y_i / u^2(y_i)}{\sum_{i=1}^N 1 / u^2(y_i)}. \quad (1.32)$$

This formula calculates a weighted average of all results. The weights of the results y_i are given by their reciprocal squared uncertainty. The combined standard uncertainty of the weighted average is given by

$$u_c(\bar{y}) = \sqrt{\frac{1}{\sum_{i=1}^N 1 / u^2(y_i)}} \quad (1.33)$$

if the quantities y_i are uncorrelated. Equation (1.33) represents the lower limit of the uncertainty of the weighted average. For the case that all quantities are fully correlated, i.e., all correlation coefficients $r(x_i, x_j) = 1$, the uncertainty of the weighted average is [66]

$$u_c(\bar{y}) = \frac{\sum_{i=1}^N 1 / u(y_i)}{\sum_{i=1}^N 1 / u^2(y_i)}. \quad (1.34)$$

Equation (1.34) represents the upper limit of the uncertainty of the weighted average. In case that correlations with $0 < |r(x_i, x_j)| < 1$ are present, the uncertainty of the weighted average follows by applying Eq. (1.25) to Eq. (1.32).

In practice, there are situations where a weighted average is to be calculated from data which are suspected to be correlated, i.e., $r(x_i, x_j) \neq 0$ for at least some x_i, x_j , but the degree of correlation is unknown. Such a situation (also referred to as *hidden correlations*) may occur, for instance, if several data sets are measured using the same setup and one of the uncertainty contributions results

from a calibration of the setup with the same reference. In such a situation, using Eq. (1.33) risks to underestimate the uncertainty of the combined data, whereas assuming full correlation and using Eq. (1.34) would probably overestimate the uncertainty. Reference 70 proposes an effective approach for calculating the uncertainty of a weighted average \bar{y} in case of hidden correlations. The main idea of this approach is to use $\chi^2 = \sum_{i=1}^N (y_i - \bar{y})^2 / u^2(y_i)$ as an indicator for under- or overestimation of $u(\bar{y})$. The expectation value $\langle \chi^2 \rangle$ is equal to $N - 1$ if all y_i are uncorrelated. The case $\chi^2 < \langle \chi^2 \rangle$ can occur if positive correlations between the y_i are present, the case $\chi^2 > \langle \chi^2 \rangle$ can occur if the uncertainties $u(y_i)$ are underestimated. In both cases, the uncertainty of the weighted average $u(\bar{y})$ would be underestimated when using Eq. (1.33). Reference 70 proposes to calculate the uncertainty of the weighted average by

$$u^2(\bar{y}) = u_{\min}^2(\bar{y}) \times \begin{cases} N - \chi^2, & \chi^2 \leq N - 1 \\ \chi^2 / (N - 1), & \chi^2 > N - 1 \end{cases} \quad (1.35)$$

where $u_{\min}^2(\bar{y})$ is the minimum uncertainty of the weighted average given by Eq. (1.33) and N is the number of data. Application of Eq. (1.35) corresponds to assuming a common covariance for all y_i, y_j .

Measuring the absorption coefficient

This chapter describes the determination of the coefficient of band-to-band absorption of crystalline silicon by the different approaches used in this work, namely: Measurements of reflectance and transmittance, spectrally resolved luminescence measurements, spectral responsivity measurements and spectroscopic ellipsometry. For each method, the underlying theory is briefly reviewed. Based on an extensive characterization of the measurement setups, a systematic measurement uncertainty analysis is outlined. The resulting absorption coefficient data are reported.

Between the ultraviolet and infrared wavelength region, the absorption coefficient of silicon varies by more than fifteen orders of magnitude. No single measurement method is capable of covering this wavelength range completely. Thus, different methods need to be combined. An obvious approach for the determination of the absorption coefficient is the direct measurement of the absorptance of a silicon sample. Usually, planar (polished) samples are used for this purpose. For such samples, the relationship between the absorptance and the absorption coefficient is known, allowing to obtain absolute values of the absorption coefficient. Another possibility consists of the determination of reflectance and transmittance of the sample, from which the absorption coefficient can also be calculated. These measurements can be carried out in the wavelength range where the absorptance is not saturated. In the ultraviolet and visible spectral region, where the absorptance of silicon is large, very thin samples would be required. Although this is no restriction in general, the use of very thin samples may not only impose handling issues but also problems with optical interference effects and temperature control. In the infrared spectral region, the absorptance of silicon tends towards zero even for very thick samples, making the use of direct measurements of the absorptance impossible. In this work, measurements of reflectance and transmittance are used in the near-infrared region only, where reflectance and transmittance measurements can be carried out on samples with thicknesses of the order of several hundred microns with sufficient signal-to-noise ratio. The ultraviolet and visible spectral range is analyzed by spectroscopic ellipsometry. This technique measures the change of polarization of light that undergoes a reflection at a surface. An optical model of the sample allows the absorption coefficient to be determined from these data using the Kramers-Kronig relations. In the band gap and sub-band gap region, spectrally resolved measurements of luminescence emission are used. This approach makes use of the reciprocity between the absorption and emission of light [71]. The relation between the absorption coefficient and the luminescence spectrum is defined by the generalized Planck law for luminescence emission [72]. If either the charge carrier density within the sample is homogenous or the absorption coefficient is very low, the luminescence spectrum is proportional to the absorptance of the sample or the absorption coefficient, respectively. In these cases,

the absorption coefficient can be obtained from the luminescence spectrum by scaling the data to a previously determined absolute value of the absorptance or absorption coefficient, respectively. This approach has been demonstrated, for instance, in Refs. 23 and 31. Due to the scaling procedure, errors and uncertainties of the absolute values propagate into the data from luminescence. The availability of accurate absolute values is therefore crucial for the successful application of this method. Another approach, which is also pursued in this work, is the measurement of the spectral responsivity (SR) of silicon solar cells. An optical reciprocity theorem [73, 74] relates the spectral responsivity to the luminescence spectrum and thus the same theory applies. This approach has been demonstrated, for instance, in Ref. 25.

2.1 Measurements of reflectance and transmittance

Measuring the reflectance and transmittance of a sample allows for the determination of the absorption coefficient in absolute units. In this work, reflectance/transmittance (RT) measurements are applied in the wavelength range from 930 to 1160 nm.

2.1.1 Principle of measurement

For a planar sample, absorptance A and absorption coefficient α are related by

$$A = (1 - R_s) \frac{1 - \exp(-\alpha W)}{1 - R_s \exp(-\alpha W)} \quad (2.1)$$

where R_s is the reflectance of the surface, α is the absorption coefficient and W is the thickness of the sample. Equation (2.1) assumes normal incidence of light. It follows from the Lambert-Beer absorption law and takes an infinite number of internal reflections into account. The calculation of α using Eq. (2.1) requires knowledge about the reflectance of the surface R_s . This is circumvented by measuring the reflectance

$$R = R_s \left(1 + \frac{(1 - R_s)^2 \exp(-2\alpha W)}{1 - R_s^2 \exp(-2\alpha W)} \right) \quad (2.2)$$

and transmittance

$$T = \frac{(1 - R_s)^2 \exp(-\alpha W)}{1 - R_s^2 \exp(-2\alpha W)} \quad (2.3)$$

of the sample. The absorption coefficient then follows directly from R and T by

$$\alpha = -\frac{1}{W} \ln \left(\frac{C - R^2 + 2R + T^2 - 1}{2T} \right) \quad (2.4)$$

Additionally, R_s can be calculated by using the relation

$$R_s = \frac{C + R^2 - 2R - T^2 - 1}{2(R - 2)} \quad (2.5)$$

In the latter equations, the abbreviation

$$C = \sqrt{(R^2 - 2R - T^2 - 1)^2 - 4(2 - R)R} \quad (2.6)$$

is used.

The absorption coefficient α determined by RT measurements incorporates band-to-band absorption as well as free carrier absorption. However, for doping concentrations below 10^{16} cm^{-3} (corresponding to a resistivity $\geq 1 \text{ } \Omega\text{cm}$) and room temperature, as used in this work, the coefficient of free carrier absorption α_{fc} is some orders of magnitude below that of the coefficient of band-to-band absorption α_{bb} at wavelengths below 1150 nm (see Fig. 1.5), where data from RT measurements is used. Hence, $\alpha \approx \alpha_{bb}$ holds.

2.1.2 Setup for measurements

Reflectance/transmittance measurements in this work are carried out with a commercially available Varian Cary 5000 spectrophotometer equipped with an integrating sphere. Figure 2.1 shows a schematic drawing of the system. A halogen lamp in combination with a grating monochromator provides monochromatic light. Behind the exit port of the monochromator, a chopper wheel reflects the light either into the sample channel or the monitor channel. The monitor channel is used to compensate for variations of the irradiance over time and to adjust the detector pre-amplifier such that an optimal signal level is provided at the input of the A/D converter. A third position on the chopper wheel blocks the light. This position is used for the measurement of the internal dark signal of the detector. The chopper positions change with a fixed frequency of 30 Hz, corresponding to subsequent measurements every 33 ms. Depending on the configuration (reflectance or transmittance), the sample is mounted at the exit or entrance port of the integrating sphere, respectively. The reflected or transmitted light is collected by the integrating sphere and measured either by a photomultiplier (PM) or a lead sulfide (PbS) detector, depending on the wavelength. The calibration procedure depends on the measurand (reflectance or transmittance). For transmittance measurements, it consists of a measurement without sample (100% baseline) and a measurement with blocked sample beam (0% baseline). The 0% baseline is not subtracted since an internal dark signal correction is already performed, but used for correction purposes (see below). For reflectance measurements, measurements of a reference (100% baseline) and with open sample port (0% baseline) are required. The reference is a front-coated mirror which is primary calibrated by the German national metrology institute *Physikalisch-Technische Bundesanstalt* (PTB) in Braunschweig, Germany. The illumination intensity is low ($\leq 50 \text{ mW/cm}^2$) and sample heating due to illumination during the measurement is not observed. Luminescence emission of the samples under illumination is not observed either. For reflectance measurements, a depolarizer is inserted into the light beam at the entrance port of the integrating sphere.

The reflectance $R(\lambda)$ of the sample at wavelength λ is calculated by

$$R(\lambda) = \frac{S_{\text{sample}}(\lambda) - S_0(\lambda)}{S_{100}(\lambda) - S_0(\lambda)} \times R_{\text{ref}}(\lambda) \quad (2.7)$$

where S_{sample} is the detector signal while the sample channel is illuminated, S_{100} is the measured 100% baseline signal, S_0 is the measured 0% baseline signal and R_{ref} is the known reflectance of the reference. The transmittance $T(\lambda)$ is calculated by

$$T(\lambda) = \frac{S_{\text{sample}}(\lambda)}{S_{100}(\lambda)}. \quad (2.8)$$

Each of the quantities S_{sample} , S_{100} and S_0 is internally determined from the ratio of the detector signal during illumination of the sample channel Y_{sample} and monitor channel Y_{mon} , corrected with the internal dark signal Y_0 :

$$Y = \frac{Y_{\text{sample}} - Y_0}{Y_{\text{mon}} - Y_0}, \quad Y = \{S_{\text{sample}}, S_{100}, S_0\}. \quad (2.9)$$

Y_{sample} , Y_{mon} and Y_0 are not accessible to the operator.

For transmittance measurements, the acquisition of the 0% baseline is not required due to the internal dark signal subtraction (see Eq. (2.9)). For reflectance measurements, however, the 0% baseline must be acquired and subtracted due to light which is scattered at the exit port aperture of the integrating sphere and cannot be taken into account by the internal dark signal subtraction.

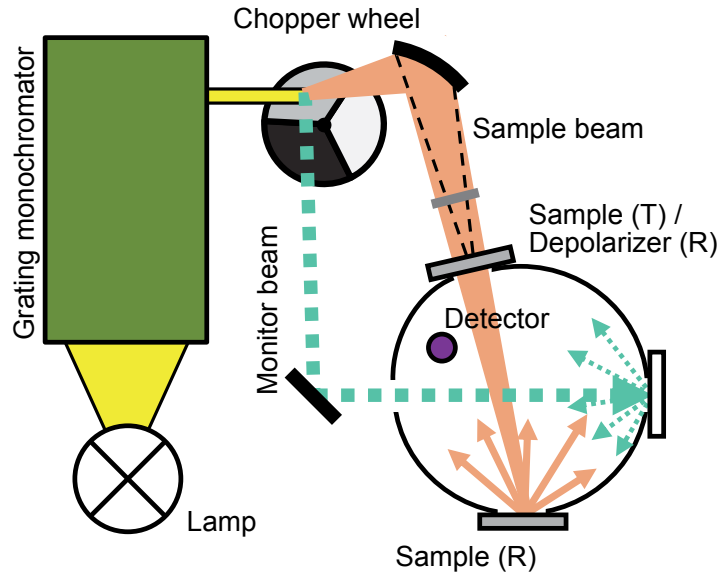


Figure 2.1: Schematic of the Varian Cary 5000 spectrophotometer used in this work.

2.1.3 Samples for measurements

RT measurements are carried out on two double side chemo-mechanically polished monocrystalline Czochralski grown p -type silicon wafers (supplied by Siltronic) with an area of $3 \times 3 \text{ cm}^2$ and a resistivity of 4 to 6 Ωcm . After polishing, the samples are RCA cleaned^a. The sample thickness is $(653.0 \pm 1.9) \mu\text{m}$ for sample RT-A and $(1284.0 \pm 1.5) \mu\text{m}$ for sample RT-B. The thickness is measured at four positions on the sample using a dial gauge. The sample temperature for the RT measurements is $(295 \pm 1) \text{ K}$.

2.1.4 Corrections of systematic effects

As outlined in section 1.3.2, it is important to identify effects which lead to a systematic deviation of the measured value, and to include them in the process equation. Another possibility is the application of corrections to the input quantities, from which the output quantity is then calculated using the original (unchanged) process equations. Both approaches are equivalent. In this work, the second option is chosen in order to keep the process equation simple.

A systematic deviation is identified for the PbS detector: The system alternately illuminates the monitor channel and the sample channel in order to determine the signal levels Y_{mon} and Y_{sample} . Afterwards, the light beam is blocked in order to acquire the internal dark signal Y_0 . This leads to a variation of the irradiance and the detector signal over time, as shown qualitatively in Fig. 2.2. The measurements of Y_{mon} , Y_{sample} and Y_0 are taken at the points t_{mon} , t_{sample} and t_0 , respectively. The cycle is repeated with a fixed frequency of $1/3\tau$. If the detector or the measurement amplifier cannot follow the irradiance variations immediately, as visualized by the dotted line, the signal levels Y'_{mon} , Y'_{sample} and Y'_0 would be determined instead. This corresponds to an underestimation of Y_{mon} , whereas Y_{sample} and Y_0 would be overestimated. Overall, this would lead to an overestimation of the measured and calculated according to the process equations (2.7) or (2.8). This also holds in case that the signal is integrated over the decay period instead of being measured at a single point in time, as shown in appendix C.1. The occurrence of this effect can be tested by setting up the system for transmittance

^aThis wet chemical cleaning process was developed on behalf of the *Radio Corporation of America* (RCA) [75] and is routinely used for the cleaning of silicon wafers.

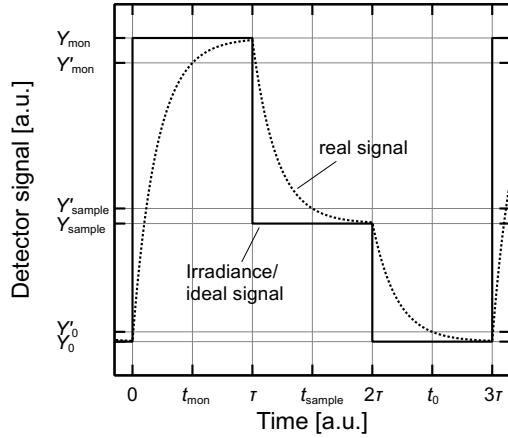


Figure 2.2: Qualitative sketch of the irradiance on the detector and its output signal as a function of time.

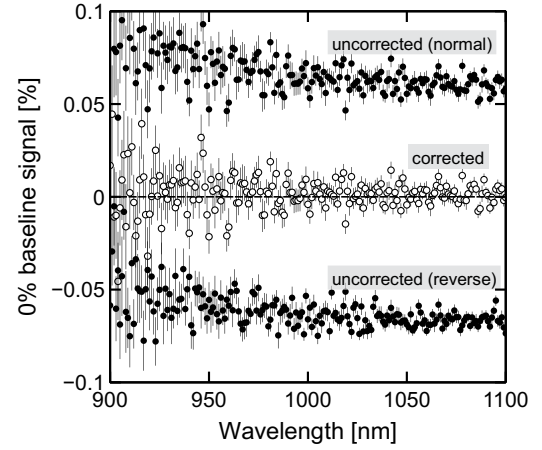


Figure 2.3: Measurements of the 0% baseline S_0 for transmittance in normal and reverse mode and corrected values.

measurements and blocking the sample beam with a beam trap. This corresponds to a measurement of the 0% baseline (S_0) for transmittance. In this configuration, Y_{sample} and Y_0 should be equal and $S_0 = 0$. Inertia of the detector signal would lead to $Y_{\text{sample}} > Y_0$ and $S_0 > 0$. This should be independent from the wavelength. The result $S_0 > 0$ could also be due to stray light. Stray light effects are excluded by operating the system in reverse mode, i.e., toggling sample and monitor channel. If stray light is present, S_0 is expected to change in amplitude as stray light is expected to affect both channels in a different manner. In absence of stray light, channel toggling should change the sign but not the amplitude of the measured 0% baseline signal. Under the described testing conditions, the PbS detector shows a baseline signal $S_0 > 0$ which changes in sign when toggling sample and monitor channel, as shown in Fig. 2.3. Moreover, a dependence of S_0 on the amplification level g_{amp} of the measurement amplifier is observed, as shown in Fig. 2.4. Both findings point towards inertia of the measurement amplifier as described above. The effect results in a systematic deviation of the measurand and requires a correction. Comprehensive modeling of the measurement procedure leads to the correction formula

$$Y = \frac{Y' - S_0}{1 + S_0(Y' - 1)} \quad (2.10)$$

where Y is the corrected value of the measurand to be used in Eq. (2.7) or (2.8) and Y' is its value actually measured. This correction makes use of the dependence of the measurable 0% baseline signal S_0 on the time constant of the signal decay. The 0% baseline S_0 is not measured each time but calculated from the amplification factor g_{amp} , which is recorded during the measurement, using the relation shown in Fig. 2.4. For the determination of the relation $S_0(g_{\text{amp}})$, long measurement times are used in order to improve the signal-to-noise ratio. The calculation of the correction is outlined in detail in appendix C.1. Figure 2.5 visualizes the effect of the correction for a transmittance measurement. For comparison, the transmittance measured with the PM, which is not affected by the inertia effect, is indicated as the solid line. For the measurements presented in this work, the PbS detector is used for wavelengths above 960 nm. For the PM detector, inertia behaviour is not detected. Note that this issue could in general be resolved if the chopper frequency could be reduced, which is not possible for the Cary 5000 system.

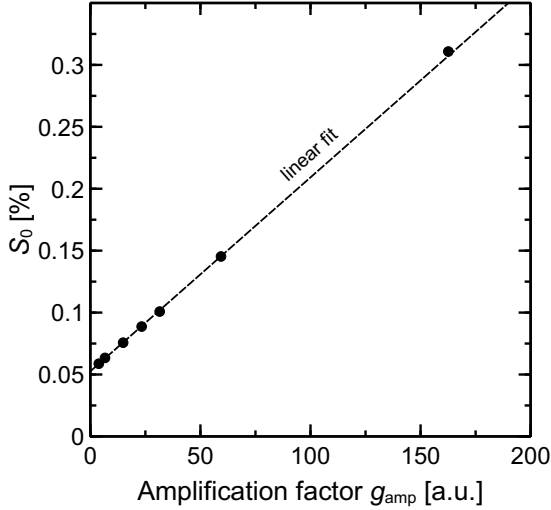


Figure 2.4: Dependence of the measured 0% baseline signal S_0 on the amplification factor.

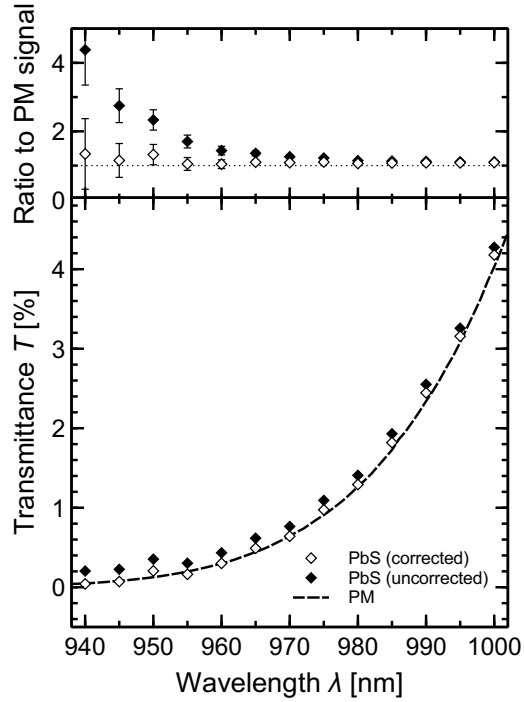


Figure 2.5: Comparison of inertia-corrected and uncorrected detector signal.

2.1.5 Uncertainty contributions

Various effects introduce uncertainties into the measurements of reflectance and transmittance. First of all, the repeatability and reproducibility of measurements must be taken into account. Further contributions of uncertainty arise from nonlinearities of the detectors and amplifiers, limited spectral bandwidth and wavelength accuracy of the monochromator, stray light, sample alignment, polarization of light and the uncertainty of the reference (if applicable). In this section, the single uncertainty contributions are described and quantified.

Repeatability (type A): The results of repeated measurements are statistically distributed due to noise of the incident photons, thermal noise of the generated electrons within the detector and noise of the amplifier electronics. This is verified by calculating the autocorrelation coefficient for 400 subsequent measurements of the detector's dark signal. The autocorrelation coefficient is ≈ 0 , indicating that subsequent measurements are not correlated. The type A uncertainty u_{stat}^2 of the average \bar{M} of the single results is then given by Eq. (1.24):

$$u_{\text{stat}}^2 = \frac{\sigma^2}{N}, \quad (2.11)$$

where σ is the standard deviation of the N single results. Eqs. (1.23) and (1.24) may only be used if the number of repetitions is large enough. In practice, this is usually accepted when $N \geq 25$. Figure 2.6a shows the evolution of the standard deviation of an exemplary 0% baseline measurement (calculated using Eq. (1.23)) when increasing the number of repeated measurements. As can be seen, the standard deviation of 25 repeated measurements already approaches the standard deviation of a large number of measurements within $\pm 10\%$ rel. Figure 2.6b shows normalized histograms for 25 and 400 repetitions together with the corresponding normal distributions which are obtained by a fit of the data. The histogram also shows that the standard deviations of both distributions are similar, which is underlined by a large OVL of 0.87 (see section 1.3.6). In this work, the uncertainty contribution

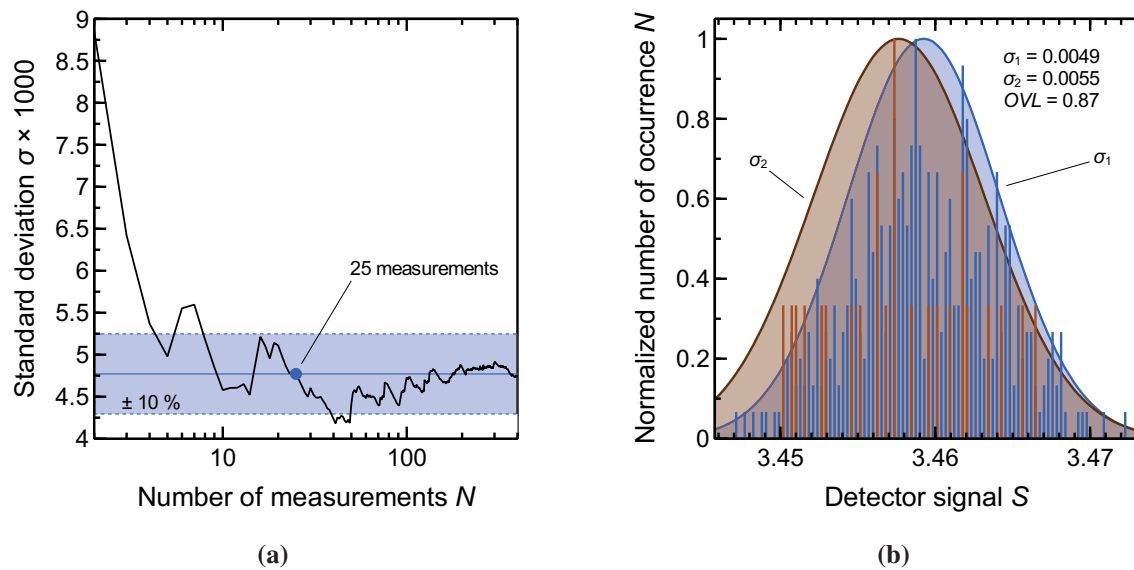


Figure 2.6: Determination of the type A uncertainty component due to repeatability of the measurement. Figure a shows the evolution of the standard deviation of N repeated measurements. Figure b shows normalized histograms of 25 and 400 repeated measurements together with the corresponding normal distributions.

u_{stat}^2 is thus calculated using the standard deviation of 25 repeated measurements in order to achieve acceptable measurement times.

Nonlinearity of the detectors (type B): The calibration of the system consists of baseline measurements with full signal (100% baseline) and zero signal (0% baseline). For a correct determination of the sample reflectance or transmittance, a linear characteristic of the detector between these two irradiance levels is essential. Nonlinearities can be determined most accurately by the superposition method, e.g., using two stable light sources, as demonstrated in section 2.2.7. However, this method cannot be applied for the Cary 5000 since the system is not prepared for such measurements. Alternatively, nonlinearities could be determined by a series of transmittance measurements on calibrated neutral density filters with known attenuation. However, such measurements are subject to uncertainties due to possible internal reflections within the filters. Thus, apertures with a large number of small pinholes are fabricated from 50 μm thick aluminium foils. These apertures serve as neutral density filters, which do not have the problem of possible internal reflections. The calibration of such apertures with respect to transmittance is challenging, since the measured transmittance may depend on the angle of acceptance of the detection system and may therefore be different for different setups. However, in Ref. 76 it is shown that different nonlinearity characteristics are expected even for different photodetectors of the same type. In order to examine the nonlinearity of the detectors, it is therefore assumed that deviations between the values of the aperture transmittance measured by both PM and PbS detector are due to nonlinearities. Figure 2.7 shows the ratio of the transmittance measured by the PM and PbS detector at 850 and 1100 nm (T_{PM} and T_{PbS} , respectively) as a function of T_{PM} . The values measured by the PbS detector are corrected as outlined in section 2.1.4. The uncertainty of the ratio is dominated by noise of the PbS detector. The solid line visualizes a weighted fit of a second order polynome to the data. At very low transmittances, the measurement of the ratio is disturbed by noise of the PbS detector, which is reflected by the large error bars. For $0.1 \leq T \leq 1$, however, the plot shows that the results of both detectors do not deviate by more than 0.25%. This estimation of nonlinearity cannot be used for correction purposes but yields an upper limit for the expected uncertainty contribution due to nonlinearity. It is globally taken into account

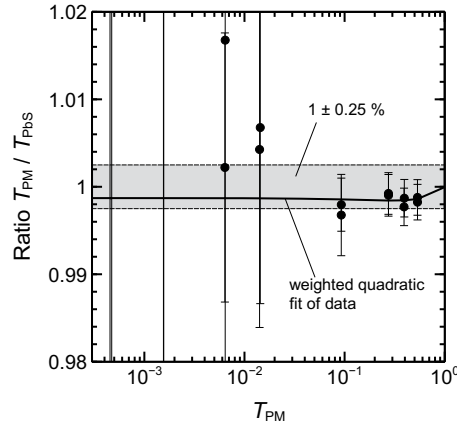


Figure 2.7: Examination of detector nonlinearity with respect to irradiance.

by a rectangularly distributed uncertainty contribution

$$u_{\text{lin},i}^2 = \frac{(0.0025 M)^2}{3}, \quad (2.12)$$

where M is the measurand (R or T).

Spectral bandwidth (type B): The finite bandwidth $\Delta\lambda$ of light provided by the monochromator may cause a deviation between the true value of reflectance or transmittance and the measured value, especially in regions where the slope of the curve varies. The uncertainty of the measured value introduced by this effect is estimated by assuming a rectangular light peak (which is a worst case estimation) and using a second-order Taylor approximation of the spectrum. Calculation (see appendix C.2) leads to

$$u_{\text{bw}}^2 = \frac{\left(M(\lambda - \frac{\Delta\lambda}{2}) - 2M(\lambda) + M(\lambda + \frac{\Delta\lambda}{2})\right)^2}{108} \quad (2.13)$$

where λ is the nominal wavelength, $\Delta\lambda$ is the spectral bandwidth and M the measurand. $M(\lambda \pm \Delta\lambda/2)$ is obtained by interpolation of the measured curve.

Wavelength accuracy (type B): Inaccuracy of the wavelength calibration leads to a wrong assignment of measurand and wavelength. This effect is especially important in regions where the measurand varies strongly over wavelength. The uncertainty of the measurand introduced by this effect is estimated by

$$u_{\text{wl}}^2 = \frac{1}{3} \left[\max \left\{ |M(\lambda - \delta\lambda/2) - M(\lambda)|, |M(\lambda + \delta\lambda/2) - M(\lambda)| \right\} \right]^2 \quad (2.14)$$

where $\delta\lambda$ is the distance between true and nominal wavelength and the other symbols have the same meaning as introduced above.

Tilt of the sample / angular incidence of light (type B): When measuring transmittance, the sample is mounted perpendicular to the optical axis as shown in Fig. 2.1. However, deviations from normal incidence arise from the divergence of the light beam. The angle of divergence is 3.7° at most. Reflectance measurements are taken under an average angle of incidence of 8° . This is necessary in order to ensure that the incident light is not completely reflected back into the entrance port of the integrating sphere in case of specular reflection. For reflectance measurements, the maximum angle of incidence is thus 11.7° . Under non-normal incidence, the optical path within the sample is

enlarged, which increases absorption. Moreover, the surface reflectance can be affected since polarization of the incident light must now be taken into account by using the general form of the Fresnel equations [77]. Both effects may cause a deviation between transmittance and reflectance actually measured and the corresponding values under normal incidence.

Transmittance measurements are not affected by polarization effects because the transmitted light is effectively unpolarized. This is visualized in Fig. 2.8. The optical axis coincides with the surface normal. For light incident vertically above or under the optical axis, the p-polarized component is parallel to the vertical plane of incidence. However, this direction is the direction of the s-polarized component for light incident horizontally beside the optical axis. This means that s- and p-polarization cancel out completely. Deviations of the measured transmittance thus result only from an increased absorption within the sample. An upper limit for this deviation is found by the following consideration: The transmittance T of a planar sample is given by Eq. (2.3). Under non-normal incidence, the thickness W must be replaced by the effective thickness $W_{\text{eff}} = W / \cos \theta$. The angle θ of the optical path within the sample is given by Snell's law with the refractive index of silicon n_{Si} and that of the surrounding medium, which is air for all measurements in this work. In the wavelength range of interest (950-1150 nm), $n_{\text{Si}} \geq 3.5$ (see section 2.4.6 and Ref. 32) and $n_{\text{air}} \approx 1.002$ [78] holds. Thus, $\theta \leq 1.057^\circ$ and the factor $\cos \theta$ follows to be

$$\cos \theta \geq 0.9998 . \quad (2.15)$$

A lower limit for the surface reflectance R_s is $R_s = 0.3$. Using these values, the absolute deviation to the transmittance for $\theta = 0$ can be calculated. This is shown in Fig. 2.9 as a function of the absorption coefficient and for different sample thicknesses as used in this work. According to Fig. 2.9, the transmittance is underestimated by a factor of 3.2×10^{-5} at most even under the worst-case assumption that all light is incident under the maximum angle of 3.7° . This deviation is so small that a correction is not necessary. Because it is also small compared to other uncertainty contributions, it is globally included into the uncertainty budget by assuming a rectangular distribution of width 3.2×10^{-5} , yielding

$$u_{\text{angle,T}}^2 = \frac{(3.2 \times 10^{-5})^2}{3} . \quad (2.16)$$

When measuring reflectance, the light beam is incident under an average angle of 8° , which adds to the angle of divergence. An upper limit for the deviation of the measured reflectance due to angular incidence is obtained by the following consideration: The reflectance R of a planar sample is given by Eq. (2.2). Again, the thickness W must be replaced by the effective thickness $W / \cos \theta$. For the reflection at the surfaces, the polarization of the incident light must be considered. The surface reflectance R_s is given by

$$R_s = p |r_s|^2 + (1 - p) |r_p|^2 , \quad (2.17)$$

where p is defined as the fraction of s-polarized light within the light beam, i.e., $p = 1$ for fully s-polarized light, $p = 0.5$ for unpolarized light and $p = 0$ for fully p-polarized light. r_s and r_p denote the reflection coefficients for perpendicular and parallel polarization, respectively. They are given by the Fresnel equations

$$r_p = \frac{\hat{n}_2 \cos \theta_1 - \hat{n}_1 \cos \theta_2}{\hat{n}_2 \cos \theta_1 + \hat{n}_1 \cos \theta_2} , \quad (2.18)$$

$$r_s = \frac{\hat{n}_1 \cos \theta_1 - \hat{n}_2 \cos \theta_2}{\hat{n}_1 \cos \theta_1 + \hat{n}_2 \cos \theta_2} . \quad (2.19)$$

In the latter equation, \hat{n} denotes the complex index of refraction and θ_1 the angle of incidence, from which the angle inside the sample θ_2 is obtained using Snell's law. Figure 2.10 shows the measured

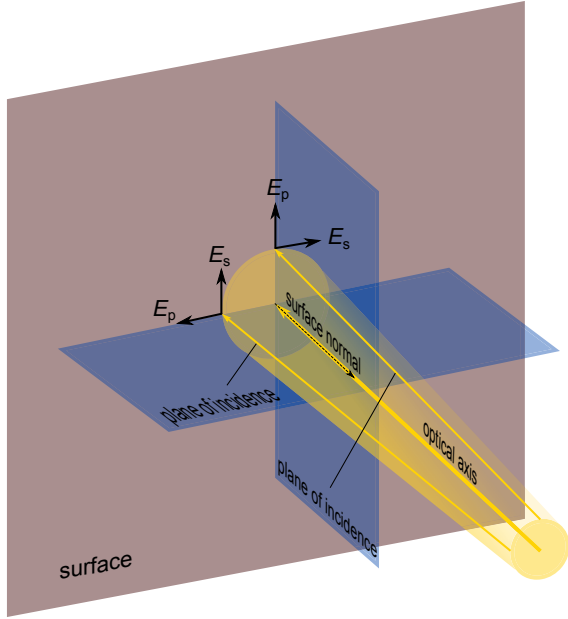


Figure 2.8: Visualization of polarization for divergent light incident around the surface normal.

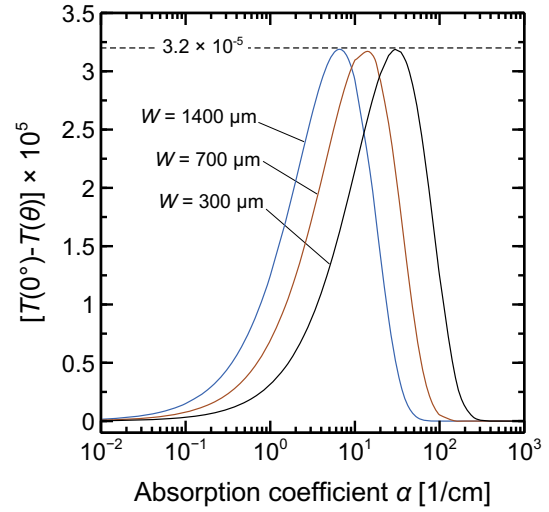


Figure 2.9: Absolute deviation $T(0^\circ) - T(1.057^\circ)$ as a function of the absorption coefficient.

degree of polarization p as a function of wavelength in the wavelength range of interest. The degree of polarization varies between 35 and 50%. The measurement with depolarizer (which is used for reflectance measurements) varies around 46% and shows some interference effects. The setup actually does not allow for precise mounting of depolarizer and analyzer at the same time. The curve with depolarizer is therefore likely to vary around 50% instead of 46%, the systematic offset and the interference effects being due to alignment issues. It is thus assumed that the degree of polarization varies between 46 and 54%, i.e., $0.46 \leq p \leq 0.54$. The complex index of refraction for air is $\hat{n}_1 \approx n_{\text{air}}$. An upper limit for the angle of incidence is $\theta_1 \leq 11.7^\circ$. With these values, the deviation between the reflectance R measured under normal incidence and R_{angle} measured under an angle of incidence of 11.7° is calculated. Figure 2.11 shows the relative deviation to the reflectance under normal incidence $(R_{\text{angle}} - R)/R$ as a function of the absorption coefficient for different waver thicknesses. The deviation does not exceed $\pm 0.2\%$ relative. Again, this deviation is so small that it is not corrected. It is taken into account by a rectangularly distributed uncertainty component

$$u_{\text{angle}}^2 = \frac{(2 \times 10^{-3} R)^2}{3}. \quad (2.20)$$

The reflectance of the reference is calibrated under an angle of 8° . Moreover, the reference is a front-coated mirror and internal reflections do not occur. Hence, non-normal incidence is taken into account by the calibration and does not need to be considered for the uncertainty budget.

Scattering of light within the sample (type B): Angular incidence of the light beam or non-parallel orientated surfaces may cause a lateral scattering of light inside the sample due to multiple internal reflections, as exemplarily shown in Fig. 2.12 for a reflectance measurement. This may cause a portion of light to be blocked at the port of the integrating sphere. During the baseline measurements, this effect cannot occur since for transmittance measurements, no reference is used. For reflectance measurements, the reference is a front-coated mirror which reflects all light at the front surface. Scattering of light within the sample thus results in an underestimation of the measurand (R or T).

The lateral displacement d of the internally reflected light can be estimated from Snell's law and

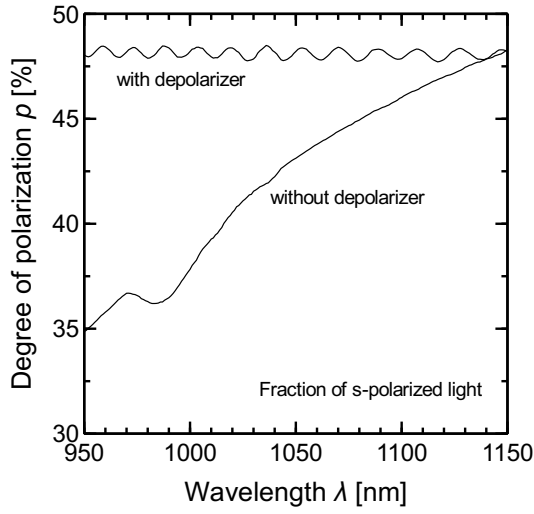


Figure 2.10: Degree of polarization p of the monochromatic light beam in the Cary 5000 system. p is defined as the fraction of s-polarized light within the light beam.

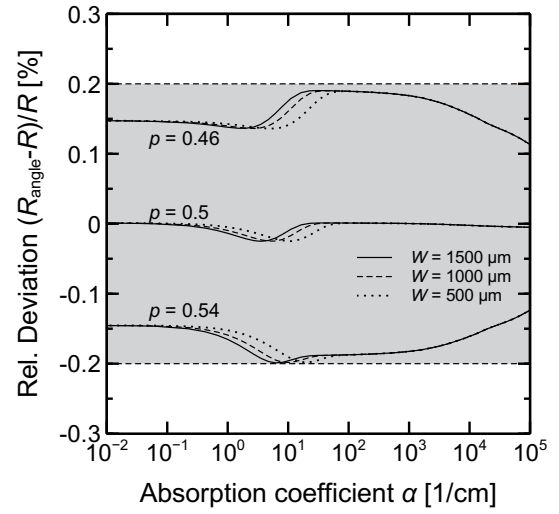


Figure 2.11: Relative deviation between reflectance R measured under normal incidence and R_{angle} measured under an angle of incidence of 11.7° as a function of the absorption coefficient.

geometrical relations as

$$d = 2W \tan\left(\arcsin\left(\frac{\sin(\theta)}{n_{\text{Si}}}\right)\right) \quad (2.21)$$

where W is the thickness of the sample, θ is the angle of incidence and n_{Si} is the refractive index of silicon. For the purpose of simplicity, the refractive index of air is assumed to be unity, as using the more precise value $n_{\text{air}} = 1.002$ leads to the same conclusions. At each internal reflection at the surfaces, only a fraction f of the light is reflected. Hence, after n internal reflections, the remaining intensity is $I_0 \times f^n$ (n odd) if absorption within the sample can be neglected, otherwise even smaller. I_0 is the intensity of the incident light. For polished silicon surfaces and relevant angles θ , $f \leq 0.32$ holds. The diameter of the aperture used for the measurements is 24 mm and the light beam is adjusted such that it hits the sample in the center of the aperture. The lateral displacement must be at least 1 mm until the internally reflected light is blocked at the port of the integrating sphere. From Eq. (2.21), the number of required internal reflections n (n odd) for this case is found. Considering a sample thickness of $1400 \mu\text{m}$ and zero absorption, the fraction of light blocked at the port due to internal reflections follows to be smaller than 0.0004% for $\theta < 11.7^\circ$, which follows from the divergence of the light beam. For thinner samples, the effect is even less pronounced as more reflections at the surfaces are required for the light ray in order to reach the edge of the aperture. Since this is a small value, a correction is not required. The fraction of blocked light is taken into account as a rectangularly distributed uncertainty contribution

$$u_{\text{disp}}^2 = \frac{(M f^n)^2}{3} \quad (2.22)$$

where M is the measurand (R or T), $f = 0.32$ and n follows from Eq. (2.21) with $d \geq 1$ mm.

Uncertainty of the standard (type B, reflectance measurements only): The uncertainty of the standard u_{std}^2 is given by the uncertainty of the primary calibration at the PTB, which is specified in the calibration certificate.

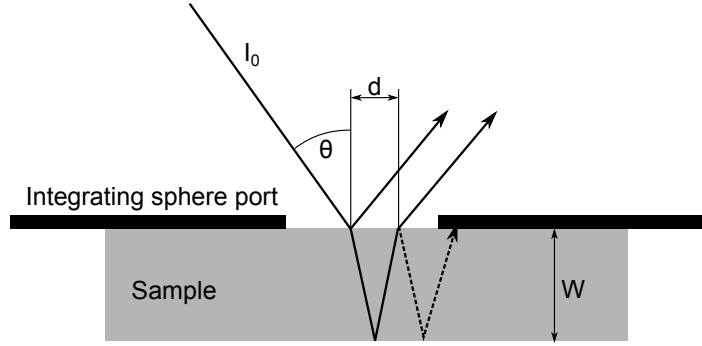


Figure 2.12: Schematic of lateral scattering of light due to multiple reflections inside the sample.

Uncertainty of the 0% baseline (type B, transmittance measurements only): According to Eq. (2.8), the transmittance is determined without measuring the 0% baseline (S_0). This is possible since the dark signal of the detectors is automatically measured and subtracted and has the advantage of speeding up the measurement and not having to deal with a noisy 0% baseline measurement. However, the 0% baseline measurement can only be omitted if the absence of systematic offsets that are not corrected by the internal dark signal measurement (e.g., stray light) is ensured. Figure 2.13 shows measurements of S_0 for transmittance (with the sample beam blocked by a beam trap) and histograms of the data. The measurements are carried out separately for both detectors. For the PM detector, small systematic deviations of S_0 from 0 are visible. According to Fig. 2.13, an upper limit for the deviation from 0 of over 95% of the data is 2×10^{-5} . This maximum deviation is taken into account as a rectangularly distributed uncertainty component u_0^2 . For the PbS detector, the measurement is dominated by measurement noise and systematic deviations of S_0 from 0 are not observed. The average of the S_0 data shown in Fig. 2.13 (867 values) is $6 \times 10^{-7} \approx 0$. The distribution of the data is approximately normal. The normal (statistical) distribution of the measurement results is already included in the uncertainty budget by the type A uncertainty component u_{stat}^2 . Hence, the uncertainty contribution due to deviations of S_0 from 0 is estimated as

$$u_0^2 = \begin{cases} (2 \times 10^{-5})^2 / 3 & \text{for the PM detector,} \\ 0 & \text{for the PbS detector.} \end{cases} \quad (2.23)$$

Inertia of the measurement amplifier (type B, PbS detector only): The correction of the inertia effect may lead to a small residual uncertainty, as shown in appendix C.1. However, this uncertainty is experimentally taken into account during the evaluation of detector nonlinearities, as corrected data is used for the PbS detector (see above). Hence, it is not necessary to include an additional contribution in the uncertainty budget.

Long-term reproducibility (type B): Other (unknown) effects than the ones listed so far may affect the long-term reproducibility of measurements. In order to quantify this effect, measurements of a test sample were carried out over the course of several months. From these measurements, the reproducibility was found to be $\pm 0.25\%$ rel. independent from the wavelength. This is taken into account as a rectangularly distributed uncertainty component

$$u_{\text{rep}}^2 = \frac{(0.0025M)^2}{3} \quad (2.24)$$

where M is the measurand.

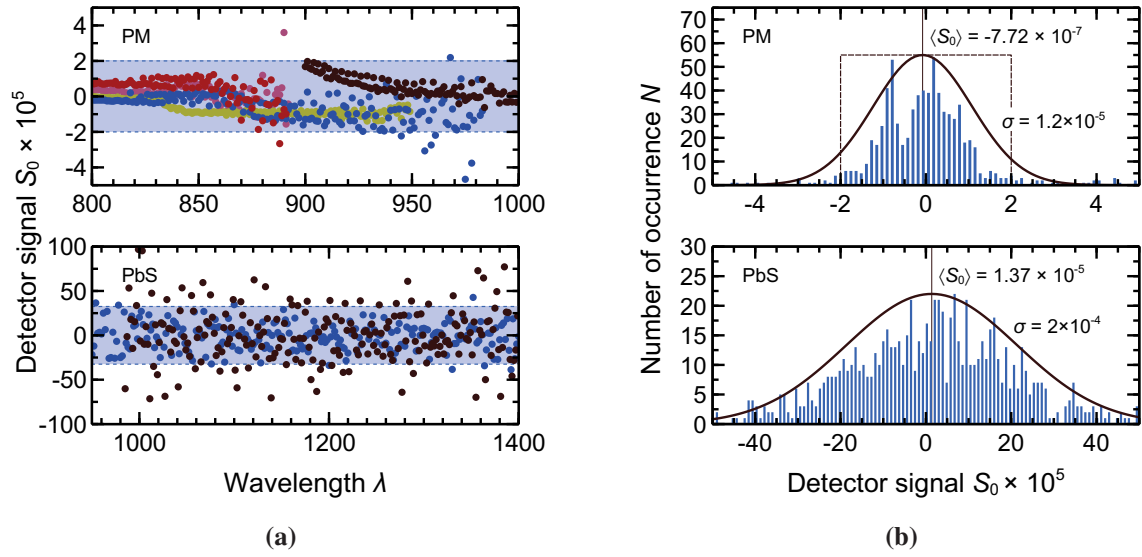


Figure 2.13: Measurements of the 0% baseline for transmittance for both PM and PbS detector (a) and histograms of the data (b).

2.1.6 Results

Reflectance and transmittance of the two samples investigated in this work are calculated from the measured data (i.e., baselines and sample measurement) and reference data using Eqs. (2.7) and (2.8). The uncertainty is determined by the uncertainty contributions listed in the preceding section. The sensitivity coefficients follow from Eqs. (2.7) and (2.8). For transmittance measurements, the overall uncertainty is

$$u^2(T) = \frac{u^2(S_{\text{sample}})}{(S_{100})^2} + \frac{S_{\text{sample}}^2 u^2(S_{100})}{(S_{100})^4} + u_{\text{lin,i}}^2 + u_{\text{wl}}^2 + u_{\text{angle,T}}^2 + u_{\text{disp}}^2 + u_{\text{rep}}^2 + u_0^2 \quad (2.25)$$

with

$$u^2(S_{\text{sample}}) = u_{\text{stat}}^2 + u_{\text{bw}}^2 \quad (2.26)$$

and

$$u^2(S_{100}) = u_{\text{stat}}^2 + u_{\text{bw}}^2. \quad (2.27)$$

For reflectance measurements, the overall uncertainty is

$$\begin{aligned} u^2(R) &= \left(\frac{R_{\text{ref}}}{S_{100} - S_0} \right)^2 u^2(S_{\text{sample}}) + \left(\frac{S_{\text{sample}} - S_0}{(S_{100} - S_0)^2} R_{\text{ref}} \right)^2 u^2(S_{100}) \\ &+ \left(\frac{S_{\text{sample}} - S_{100}}{(S_{100} - S_0)^2} R_{\text{ref}} \right)^2 u^2(S_0) + \left(\frac{S_{\text{sample}} - S_0}{S_{100} - S_0} \right)^2 u^2(R_{\text{ref}}) \\ &+ u_{\text{rep}}^2 + u_{\text{lin,i}}^2 + u_{\text{angle}}^2 + u_{\text{wl}}^2 + u_{\text{disp}}^2 \end{aligned} \quad (2.28)$$

with

$$u^2(S_{\text{sample}}) = u_{\text{stat}}^2 + u_{\text{bw}}^2, \quad (2.29)$$

$$u^2(S_{100}) = u_{\text{stat}}^2 + u_{\text{bw}}^2 \quad (2.30)$$

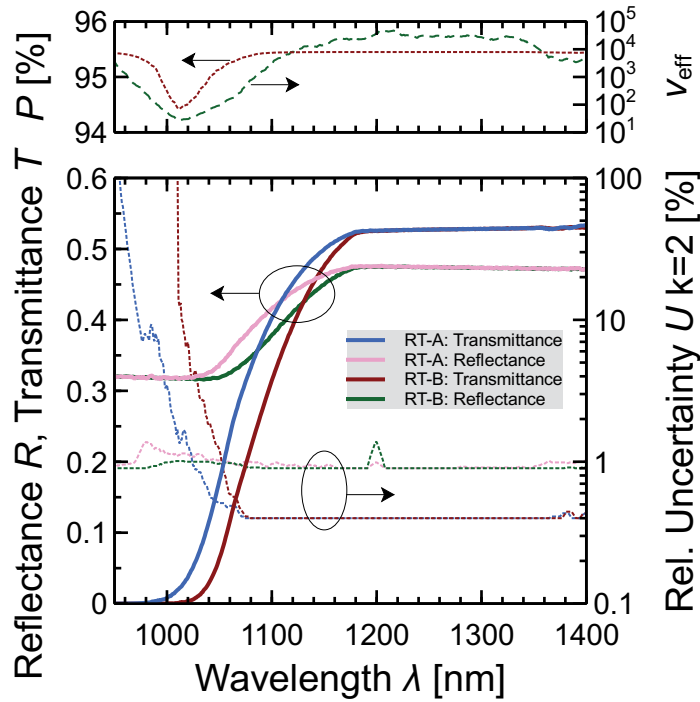


Figure 2.14: Measured reflectance and transmittance of the two samples investigated in this work (RT-A: $W = (653 \pm 1.9) \mu\text{m}$, RT-B: $W = (1284 \pm 1.5) \mu\text{m}$) and relative uncertainty of the data (dashed lines with corresponding color). The top graph shows the effective degrees of freedom for the t-distribution and the corresponding coverage probability.

and

$$u^2(S_0) = u_{\text{stat}}^2. \quad (2.31)$$

Note that the 0% baseline (resulting from light reflected at the exit port of the integrating sphere) is approximately constant for all wavelengths. Uncertainty due to spectral bandwidth thus needs not be considered.

Figure 2.14 shows the resulting values for both samples (represented by the solid lines). The dashed lines indicate the relative expanded uncertainty of the values for a coverage factor $k = 2$. The top graph of the figure shows the corresponding coverage probability P for a t-distribution with an effective degrees of freedom ν_{eff} (see section 1.3.5) following from the uncertainty analysis. In the region around 1000 nm, where the overall uncertainty is dominated by the type A component for measurement noise, the coverage probability for $k = 2$ is about 1% abs. below the value of 95.44%, which holds for a normal distribution. This is due to the limited number of repetitions (25) which is used. In order to obtain a coverage probability of 95.44%, a coverage factor of about 2.1 must be chosen in this region.

The uncertainty analysis allows to evaluate the impact of the different uncertainty contributions on the resulting uncertainty of R and T . Figure 2.15 exemplarily shows the relative contributions to the overall uncertainty at 1050 and 1250 nm. The evaluation shows that major uncertainty contributions for transmittance measurements are due to long term reproducibility and nonlinearity as well as measurement noise. At 1050 nm, where the transmittance varies strongly with wavelength, major contributions also result from spectral bandwidth and wavelength accuracy. A more precise investigation of detector nonlinearities would probably allow to decrease the overall uncertainty. Decreasing the slit width of the monochromator would result in a smaller uncertainty contribution due to spectral

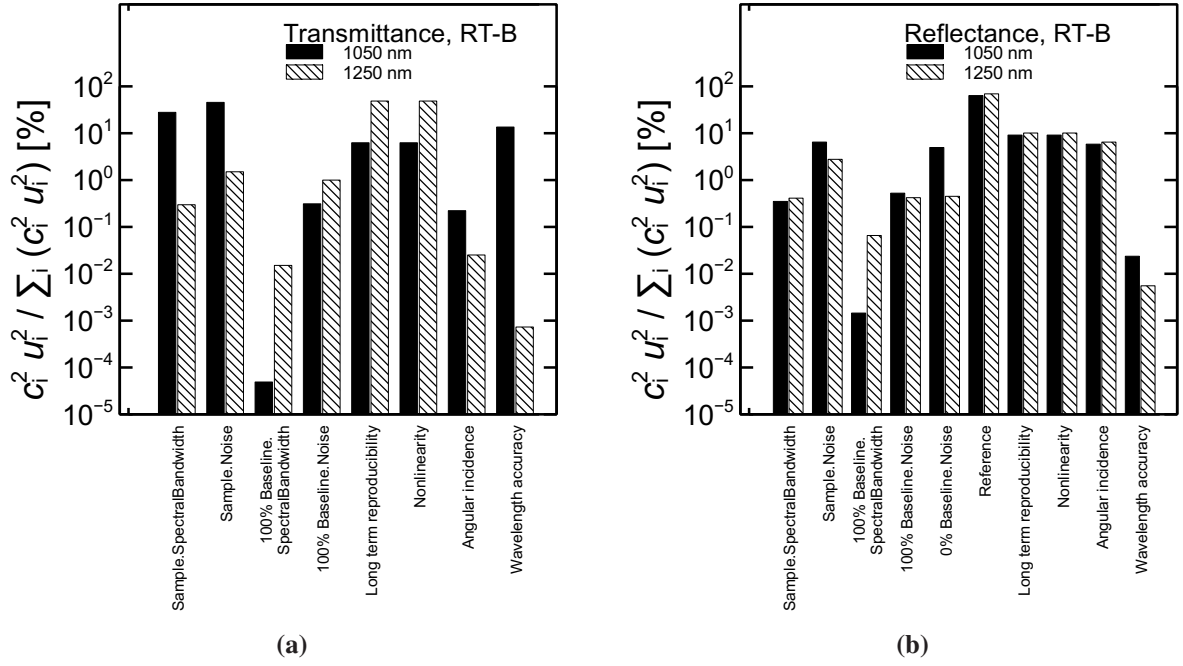


Figure 2.15: Uncertainty budget for transmittance (a) and reflectance (b) for sample RT-B at 1050 and 1200 nm.

bandwidth. However, doing so would also decrease the intensity of the monochromatic light and thus increase the uncertainty contribution due to measurement noise. The uncertainty of reflectance measurements is dominated by the uncertainty of the reference data.

From the RT data, the absorption coefficient α is calculated using Eq. (2.4). For the RT measurements, the sample temperature cannot be controlled actively and may slightly deviate from 295 K (deviations are of the order of ± 0.5 K). The sample temperature during the measurements is therefore recorded and a temperature correction (of the order of 0.5% to 1% rel.) is applied to the resulting absorption coefficient data using the temperature coefficients given in section 3.2. The uncertainty of the resulting absorption coefficient is given by the uncertainty of R and T as well as the uncertainty of the thickness W . This uncertainty component takes lateral variations of the thickness of four measurements at different positions and the uncertainty of the calibration of the dial gauge into account. It is estimated by

$$u_W^2 = \sigma^2(W_1, W_2, W_3, W_4) + 1/3 \mu\text{m}^2 \quad (2.32)$$

where $\sigma(W_1, W_2, W_3, W_4)$ is the standard deviation of the thickness measured at positions 1 to 4. The factor $1/3 \mu\text{m}^2$ follows from assuming a rectangular distribution of width $\pm 1 \mu\text{m}$ for the uncertainty of the calibration of the dial gauge. The sensitivity coefficients are

$$c_R^2 = \left[\frac{2(R-1)}{W \sqrt{(T^2 - R^2 + 2R + 1)^2 + 4(R-2)R}} \right]^2, \quad (2.33)$$

$$c_T^2 = \left[\frac{2R - R^2 - T^2 - 1}{T W \sqrt{(T^2 - R^2 + 2R + 1)^2 + 4(R-2)R}} \right]^2, \quad (2.34)$$

$$c_W^2 = \left[\frac{\alpha}{W} \right]^2. \quad (2.35)$$

The uncertainty contribution due to uncertainty of the sample temperature is considered in section 3.2.

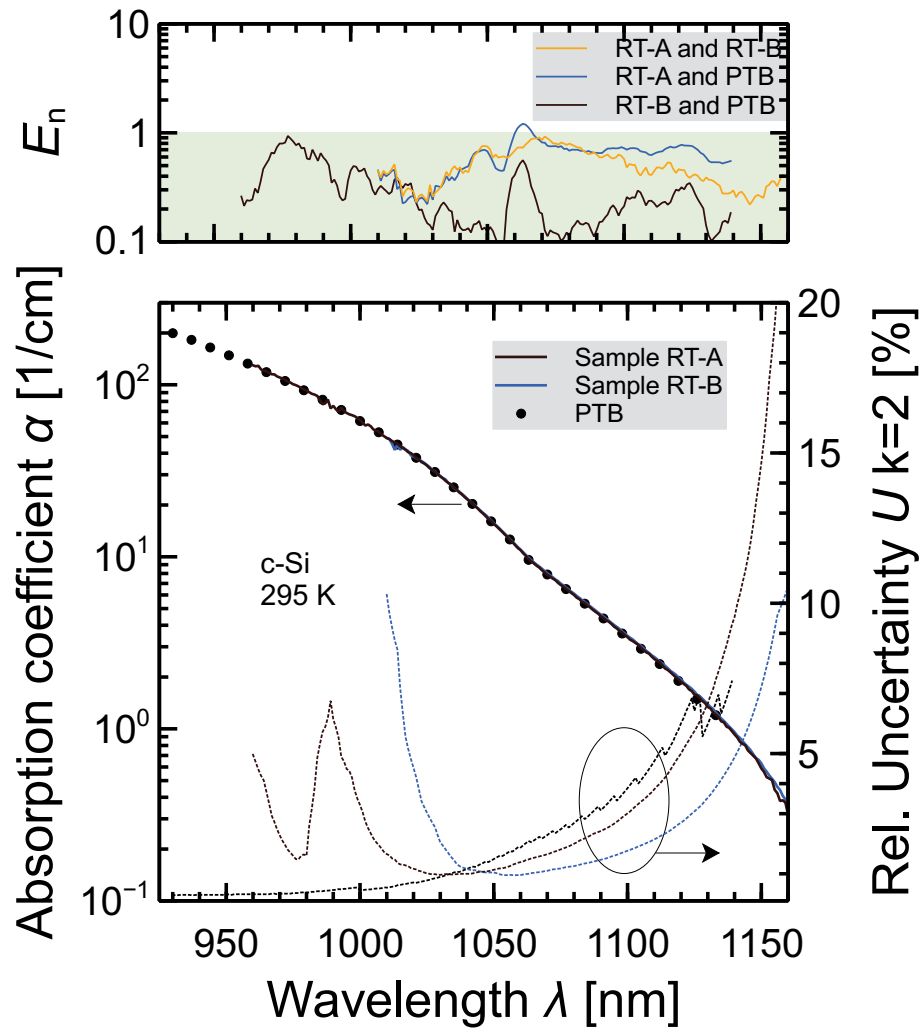


Figure 2.16: Absorption coefficient α_{bb} of crystalline silicon at 295 K as determined from RT measurements (bottom) and E_n number for the data (top).

Figure 2.16 shows the resulting absorption coefficient data and its uncertainty for both samples investigated in this work. Additionally, absorption coefficient data measured by the PTB on samples from the same wafers at (295.45 ± 0.1) K is included for comparison. In these investigations, the reflectance is determined by a combination of the results obtained using a commercial Varian Cary spectrophotometer as well as using a special setup with increased angle of acceptance in the primary national reference system for spectral reflectance. As for the data obtained in this work, a temperature correction is applied to these data as well due to the deviation from the nominal temperature of 295 K. Tabulated data for Fig. 2.16 is given in appendix D. The top graph of Fig. 2.16 shows the E_n number (see section 1.3.6) for the data. As can be seen, the data measured by the PTB are in agreement with the data obtained in this work. The finding $E_n < 1$ shows that the small deviations between the data are explained by their measurement uncertainty. Above 1150 nm, the uncertainty of the data increases strongly, indicating that scaling of relative absorption coefficient data (e.g., from luminescence measurements) to data from RT measurements should be done at wavelengths below 1150 nm.

2.2 Spectrally resolved luminescence measurements

Inter-band luminescence emission originates from the radiative recombination of electrons in the conduction band and holes in the valence band. This is the inverse process of absorption of photons with excitation of an electron from the valence to the conduction band. Both processes are related by Kirchhoff's law [71]. The luminescence spectrum thus contains information about the absorption coefficient.

Inter-band luminescence emission of silicon is emitted in the near-infrared wavelength range near the band gap (approximately between 950 and 1300 nm). As opposed to absorptance measurements, luminescence measurements feature a good signal-to noise ratio at wavelengths beyond the band gap. On the other hand, luminescence measurements determine the absorption coefficient in relative units. Accurate data of the absorption coefficient in absolute units (e.g., from RT measurements) is therefore required for scaling. Luminescence measurements are usually referred to as photoluminescence (PL) measurement when using optical excitation or electroluminescence (EL) measurements when using electrical excitation. In this work, EL and PL measurements are carried out in the wavelength range between 1100 and 1450 nm.

2.2.1 Principle of measurement

For a laterally homogeneous sample, the contribution to the luminescence emission at wavelength λ is given by the product of the spectral photon generation rate r_{ph} and the photon escape probability f_{esc} for each position z within the sample. By summing up all contributions over the thickness W of the sample, the emitted luminescence photon flux per wavelength interval and surface area $\Phi(\lambda)$ is obtained [79–81]:

$$\Phi(\lambda) = \int_0^W dz r_{\text{ph}}(\lambda, z) f_{\text{esc}}(\lambda, z). \quad (2.36)$$

The spectral photon generation rate r_{ph} per wavelength interval is defined by the generalized Planck radiation law for luminescence [72]:

$$r_{\text{ph}}(\lambda, z) = \alpha(\lambda) 8\pi c n_{\text{Si}}^2(\lambda) \lambda^{-4} \left[\exp\left(\frac{hc}{\lambda} - \mu_{\text{ph}}(z)\right) - 1 \right]^{-1}, \quad (2.37)$$

where c is the speed of light in vacuum, α is the absorption coefficient, n_{Si} is the refractive index of silicon, h is the Planck constant and μ_{ph} is the chemical potential of the photons given by the splitting ΔE_{F} of the quasi-Fermi levels. Under typical luminescence measurement conditions, where charge carriers are generated optically or injected electrically, the exponential term in Eq. (2.37) is some orders of magnitude larger than 1, allowing to approximate Eq. (2.37) by

$$r_{\text{ph}}(\lambda, z) \approx \alpha(\lambda) 8\pi c n_{\text{Si}}^2(\lambda) \lambda^{-4} \exp\left(-\frac{hc}{\lambda kT}\right) \exp\left(\frac{\mu_{\text{ph}}(z)}{kT}\right). \quad (2.38)$$

The main absorption processes at room temperature are band-to-band (inter-band) absorption and free carrier (intra-band) absorption (FCA). The absorption coefficient α is thus the sum of the coefficient of band-to-band absorption α_{bb} and the coefficient of free carrier absorption α_{fc} , $\alpha = \alpha_{\text{bb}} + \alpha_{\text{fc}}$. Importantly, the exponential term $\exp(\mu_{\text{ph}}(z)/kT)$ in Eq. (2.38) refers to the splitting of the quasi-Fermi levels and thus to inter-band transitions. Hence, this term only refers to the coefficient of band-to-band absorption α_{bb} and Eq. (2.38) can be written as [31, 82]

$$r_{\text{ph}}(\lambda, z) \approx 8\pi c n_{\text{Si}}^2(\lambda) \lambda^{-4} \exp\left(-\frac{hc}{\lambda kT}\right) \left[\alpha_{\text{fc}} + \alpha_{\text{bb}} \exp\left(\frac{\mu_{\text{ph}}(z)}{kT}\right) \right]. \quad (2.39)$$

Under typical charge carrier injection conditions, $\exp(\mu_{\text{ph}}(z)/kT)$ is of the order of 10^7 or larger. Consequently, the generation of luminescence photons is completely dominated by inter-band transitions, which means that generation of luminescence photons by intra-band recombination is negligible and $\alpha \approx \alpha_{\text{bb}}$. Taking this approximation into account and combining the latter equations shows that the emitted luminescence photon flux is proportional to the coefficient of band-to-band absorption α_{bb} ,

$$\Phi(\lambda) \approx \alpha_{\text{bb}}(\lambda) \frac{8\pi c n_{\text{Si}}^2(\lambda)}{\lambda^4} \exp\left(-\frac{hc}{\lambda kT}\right) \int_0^W dz f_{\text{esc}}(\lambda, z) \exp\left(\frac{\mu_{\text{ph}}(z)}{kT}\right). \quad (2.40)$$

In two special cases, the relation between the absorption coefficient and the luminescence spectrum simplifies [23]:

1. If the charge carrier concentration within the sample is homogeneous, μ_{ph} is independent from z and the exponential term can be pulled out of the integral. The remaining integral over f_{esc} equals the absorptance of the sample, as can be seen by carrying out the integration and comparing the result to the expression for the absorptance of the sample. Thus, in case of a homogenous charge carrier concentration, the luminescence spectrum is proportional to the absorptance of the sample.
2. If the absorption coefficient is small, f_{esc} becomes independent from z and can be pulled out of the integral. The remaining integral is then a constant with respect to wavelength. Thus, in case of a small absorption coefficient, the luminescence spectrum is directly proportional to the absorption coefficient itself. For wafer samples as used in this work, the approximation holds for wavelengths above 1200 nm.

In both cases, the absorption coefficient can be determined from relative measurements of the luminescence intensity. However, the determination of the scaling factor requires previously determined absolute values of the absorptance or absorption coefficient, respectively.

2.2.2 Samples for measurements

Spectrally resolved PL measurements are carried out on double side textured silicon samples with an area of $3 \times 3 \text{ cm}^2$ from the same wafers as for the absorptance measurements described in section 2.1.3. The samples for PL are electrically passivated on both sides by 15 nm thick layers of atomic-layer-deposited Al_2O_3 . The surface passivation increases the ratio of radiative recombination and non-radiative recombination. However, the presence of the passivation layers might affect the luminescence spectrum. Thus, for the correct determination of the absorption coefficient, the impact of the Al_2O_3 layer on the resulting luminescence spectrum must be examined. Figure 2.17 shows the absorption coefficient of Al_2O_3 , measured using spectroscopic ellipsometry on a 50 nm thick layer which was deposited onto a glass substrate. Above 850 nm, the absorption coefficient is too small to be measured accurately. However, the measurement shows that it is smaller than $3 \times 10^{-8} \text{ nm}^{-1}$. The dashed line represents the absorption length $L_\alpha = 1/\alpha$ within the coating. Considering the layer thickness of only 15 nm, it is obvious that absorption within the passivation layer is completely negligible. However, the reflectance of the surfaces is altered by the passivation layers. The effective surface reflectance of the passivated wafers is thus determined experimentally and used for the calculation of the absorption coefficient.

Moreover, spectrally resolved EL measurements are carried out on specially designed lab-type solar cells with an area of $2 \times 2 \text{ cm}^2$. These solar cells, made of p -type Czochralski grown silicon with a thickness of 711 μm and a resistivity of 2.5 Ωcm , feature a chemo-mechanically polished front and rear surface. The surface metallization is achieved by evaporating a 10 μm thick layer of aluminium on the rear side and a grid structure (also 10 μm thick aluminium) on the front side. The solar cells do not have a back surface field nor an antireflection coating in order to preserve the polished surfaces. Additionally, a reference sample without front surface metallization is available, as well as a reference sample which is not metallized and where the emitter diffusion is applied to both sides of the sample.

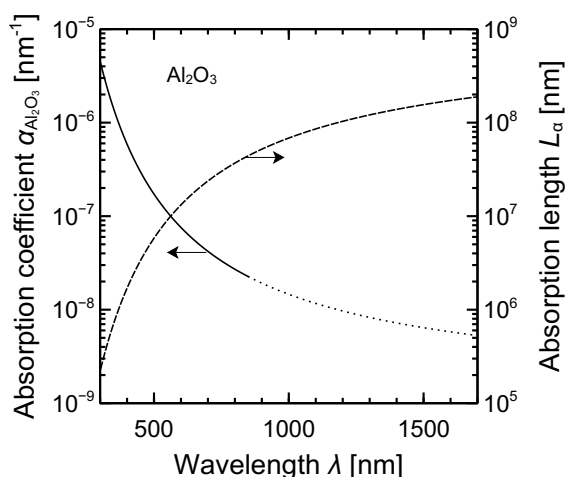


Figure 2.17: Absorption coefficient of Al_2O_3 and corresponding absorption length L_α obtained from ellipsometric measurements. Above 850 nm, the absorption coefficient is too low to be measured accurately.

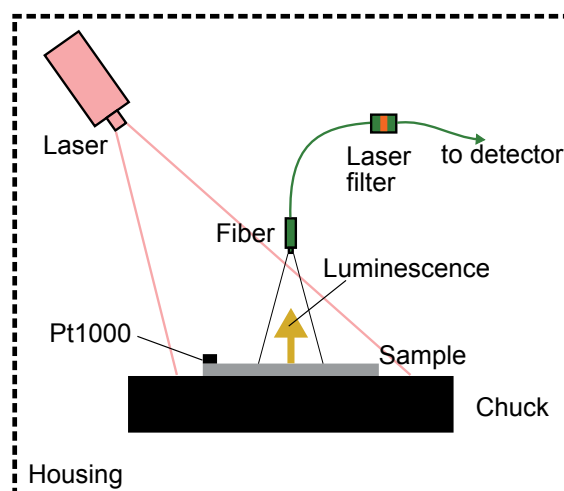


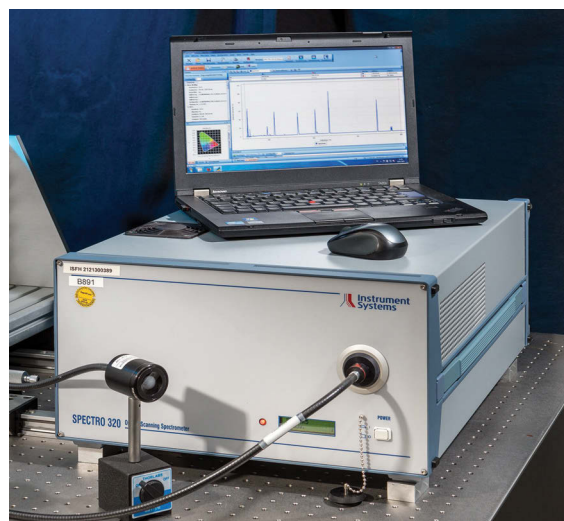
Figure 2.18: Sketch of the setup used for spectrally resolved photoluminescence measurements.

2.2.3 Setup for measurements

Although luminescence measurements provide a rather simple approach for the determination of the absorption coefficient beyond the bandgap in principle, the correct measurement of the luminescence spectrum itself requires an elaborate measurement procedure and comprehensive knowledge about the components and devices involved. The setup for the spectrally resolved luminescence measurements carried out in this work is sketched in Fig. 2.18. The core component of the setup is a commercially available spectrometer system. Two different systems are evaluated: A diode-array spectrometer system (*tec5 CompactSpec 1.7 CT*) capable of recording data at all wavelengths simultaneously, and a scanning spectrometer system featuring a single monochromator (*Instrument Systems Spectro 320 R5*). Both systems are in-house calibrated with respect to wavelength and irradiance as described in the next section. The luminescence emission is collected perpendicular from above and transmitted into the spectrometer by a multi-core fiber cable. Figure 2.19 shows photographs of the spectrometer systems. The sample stage is temperature controlled and the sample temperature is continuously monitored by a Pt1000 temperature sensor attached to the front surface of the sample. PL emission is excited by laser illumination from above. The laser (Jenoptik unique-mode, JUM30k/400/20) emits light at a center wavelength of 809 nm. Underground illumination at other wavelengths is filtered by an optical bandpass filter. The laser spot is widened by an array of micro lenses (custom-made product, Bayerisches Laserzentrum GmbH) and homogeneously illuminates an area of $5 \times 5 \text{ cm}^2$ with an intensity of about 70 mW/cm^2 . The lateral irradiance variation is below 10% rel. During PL measurements, the sample stage is a black anodized brass plate with a reflectance of below 10% within the wavelength range of interest. Ray tracing simulations (see appendix B) show that the presence of the brass plate does not affect the shape of the luminescence spectrum compared to the case that the sample is surrounded by air. EL emission is excited by attaching a power supply and contacting the front busbar of the solar cell with Kelvin probes. The rear contact is made by the brass plate (not anodized in case of EL) on which the sample is placed. Since the solar cells feature a rear surface metalization, the reflectance of the brass plate is irrelevant. The brass plate contains an additional Pt1000 temperature sensor which is attached to the rear surface of the solar cell.



(a)



(b)

Figure 2.19: Photographies of the spectrometers evaluated in this work. (a) Diode array spectrometer system *tec5 CompactSpec 1.7 CT*. (b) Scanning spectrometer system *Instrument Systems Spectro320 R5*.

2.2.4 In-house calibration of spectrometers

The detection system consists of several optical components such as mirrors, diffusers, fibre cables, gratings and detectors, each of which having its own wavelength characteristic. The whole system therefore needs to be calibrated with respect to wavelength and irradiance in order to measure the luminescence spectrum correctly. Basically, the irradiance calibration of a spectrometer consists of comparing the measured spectrum of the sample to the measured spectrum of a calibration light source, whose true spectrum is known. In this work, a 250 W halogen lamp (Gigahertz LN-250-BC) is used as calibration standard. The lamp is primarily calibrated at the *Physikalisch-Technische Bundesanstalt* (PTB). Moreover, a mercury vapor lamp is used for the calibration of the spectrometer with respect to wavelength prior to the intensity calibration. For an appropriate irradiance calibration of the spectrometer, it is necessary to ensure that

1. the calibration lamp is operated at exactly the same current as during the primary calibration,
2. that the same polarity as during the primary calibration is retained,
3. that the spectrum of the calibration lamp has not changed since the primary calibration,
4. that only direct light from the calibration lamp is measured, which means that sufficient stray light blocking is ensured,
5. that calibration lamp and entrance optics of the spectrometer are precisely aligned on the optical axis without tilt,
6. that the spectrometer is accurately calibrated with respect to wavelength and
7. that the distance between calibration lamp and entrance optics of the spectrometer is adjusted to exactly the same distance as during the primary calibration (300 mm).

The last requirement does not hold if only a relative intensity calibration is performed, i.e., the measured data is in relative units as for the luminescence measurements carried out in this work.

In order to meet the given requirements, a new setup for the irradiance calibration of spectrometers was built up during this work. Figure 2.20 shows a schematic drawing of the setup. The setup consists of an optical table on which the calibration lamp and the spectrometer can be mounted and adjusted precisely. A three-axis stage is used for mounting the lamp. The entrance optic of the spectrometer

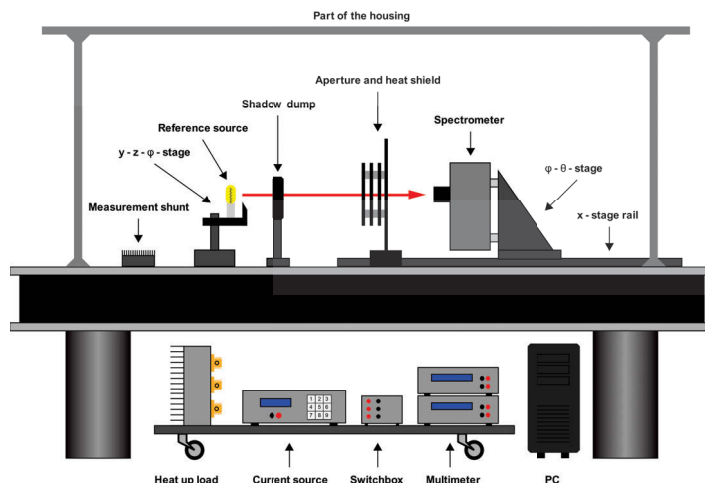


Figure 2.20: Schematic of the setup for radiometric calibrations of spectrometer systems built up during this work.

is mounted on a two-axis stage. An additional linear stage allows the distance between lamp and entrance optic to be adjusted. A housing made of black molton fabric reduces stray light from the ambience. A high-precision power supply provides stable current for the operation of the calibration lamp. The lamp current is monitored by a high-precision multimeter measuring the voltage drop over a calibrated measurement shunt, which is equipped with a Pt11000 temperature sensor attached to its heat sink in order to compensate for the temperature-induced change of resistivity. The calibration lamp is operated in current-regulated mode at a set point of 9.7 A. A connected computer is used to log the lamp current and also to regulate the power supply upon detection of a deviation from the set point. The setup is capable of regulating the lamp current to the set point of 9.7 A with a maximum deviation of not more than $400 \mu\text{A}$ (0.004% rel.). The calibration lamp is operated with a power of approximately 185 W, which is about 75% of the nominal power (250 W). Turn-on and turn-off procedures are realized by linear current ramps with a duration of 50 s. The reduced operation power and the ramping improve the stability of the lamp and enhance its lifetime to typically more than 1000 h of operation. A second multimeter is used to log the voltage between the terminals of the calibration lamp, which serves as an indicator of spectral stability. Deviations of more than 50 mV from the calibration voltage indicate that the spectrum of the lamp has changed and that a recalibration of the lamp is necessary. A pre-aging procedure is carried out by operating the lamp at its operation current for 60 h before the lamp is used as a calibration lamp. During this procedure, the lamp voltage is required to stabilize at a saturation value. If it does not, i.e., the lamp voltage fluctuates by more than 50 mV after the pre-aging procedure, the lamp is discarded. An aperture positioned between calibration lamp and spectrometer reduces stray light and also acts as a heat shield. The remaining stray light is measured and subtracted during the calibration measurement by placing a shadow dump between lamp and spectrometer which only blocks the direct light from the lamp. Calibration lamp and entrance optic of the spectrometer are aligned on the optical axis using a bidirectional adjustment laser. For this purpose, the calibration lamp is equipped with an adjustment aid. The distance between lamp and spectrometer is then precisely measured by a calibrated digital two-point inside micrometer with an accuracy of $\pm 1 \mu\text{m}$. Figure 2.21 shows photographs taken during the alignment procedure and the calibration measurement.

2.2.5 Procedure for measuring luminescence spectra

Prior to the measurement of luminescence spectra, an irradiance calibration of the spectrometer is performed. For this purpose, the spectrum of the calibration lamp is measured. The detector signal



Figure 2.21: Setup for radiometric calibrations of spectrometer built up during this work. Figure (a) shows the alignment of calibration lamp and entrance optic of the spectrometer using a bidirectional adjustment laser. Figure (b) shows the adjusted setup during the irradiance calibration of the spectrometer.

$N_{\text{ill}}(\lambda)$ consists of the component due to direct illumination by the lamp $N_{\text{imp}}(\lambda)$, the component due to background illumination from the ambience and dark signal of the detector $N_{\text{d}}(\lambda)$ and eventually an artificial signal offset $N_{\text{o}}(\lambda)$ (which is sometimes added to the signal in order to prevent negative values due to noise):

$$N_{\text{ill}}(\lambda) = N_{\text{imp}}(\lambda) + N_{\text{d}}(\lambda) + N_{\text{o}}(\lambda) . \quad (2.41)$$

Next, the shadow bump is mounted such that direct light from the calibration lamp is blocked. The resulting spectrum is measured. The detector signal $N_{\text{drk}}(\lambda)$ now consists of the component due to background illumination from the ambience and dark signal of the detector $N_{\text{d}}(\lambda)$ and the artificial signal offset $N_{\text{o}}(\lambda)$:

$$N_{\text{drk}}(\lambda) = N_{\text{d}}(\lambda) + N_{\text{o}}(\lambda) . \quad (2.42)$$

If dark signal N_{d} and signal offset N_{o} are constant over measurement time scales, the detector signal due to direct illumination by the lamp N_{imp} follows from Eqs. (2.41) and (2.42) as

$$N_{\text{imp}}(\lambda) = N_{\text{ill}}(\lambda) - N_{\text{drk}}(\lambda) . \quad (2.43)$$

In practice, several subsequent measurements of N_{ill} and N_{drk} are averaged in order to reduce the impact of measurement noise on the result. Since Eq. (2.44) is linear, it remains valid for the averaged values of the quantities \bar{N}_{ill} and \bar{N}_{drk} . Hence,

$$\bar{N}_{\text{imp}}(\lambda) = \bar{N}_{\text{ill}}(\lambda) - \bar{N}_{\text{drk}}(\lambda) . \quad (2.44)$$

After measuring the spectrum of the calibration lamp, the luminescence spectrum of the sample $N_{\text{lum}}(\lambda)$ is measured using the same procedure. The background signal N_{drk} is measured by turning off the excitation source. The detected luminescence intensity $I_{\text{lum}}(\lambda)$ in relative units finally follows from the comparison of the measured spectra of calibration lamp and luminescence:

$$I_{\text{lum}}(\lambda) \propto \frac{N_{\text{lum}}(\lambda)/t_{\text{int,lum}}}{N_{\text{imp}}(\lambda)/t_{\text{int,imp}}} I_{\text{imp}}(\lambda) \quad (2.45)$$

where $t_{\text{int,lum}}$ and $t_{\text{int,imp}}$ are the integration times used for the corresponding measurements and I_{imp} is the known spectral irradiance of the calibration lamp. The Spectro 320 system outputs data which

has already been normalized to scan speed. Hence, $t_{\text{int,lum}} = t_{\text{int,imp}}$ is used in the latter equation when evaluating data measured by this system. Note that the factor $t_{\text{int,imp}}/t_{\text{int,lum}}$ can also be included in the proportionality constant for relative measurements. Also, note that the proportionality in Eq. (2.45) can be replaced by equality if the spectrum of the calibration lamp is measured exactly at the same distance r_0 as used during the primary calibration of the lamp. If a small deviation $\Delta r \ll r_0$ occurs, a correction can be made. From the inverse-square law, $I(r) = I_0/r^2$, the relation

$$I(r) \approx I_0 \left[\frac{1}{r_0^2} - \frac{2\Delta r}{r_0^3} \right] \quad (2.46)$$

is obtained by Taylor series expansion. In the latter equations, I_0 is the emitted intensity and r the distance from the source. Hence, a small distance deviation can be taken into account by a distance correction factor

$$f_r = \frac{I(r)}{I(r_0)} = 1 - \frac{2\Delta r}{r_0} \quad (2.47)$$

in Eq. (2.45). However, for the determination of the absorption coefficient using the procedure described in section 2.2.1, no benefit can be drawn from a precise adjustment of the distances.

2.2.6 Correction of systematic effects

Several effects can lead to systematic deviations with respect to spectrally resolved irradiance measurements. Often, a major issue is the occurrence of stray light, i.e., signal contributions due to light which should actually not be measured. Two types of stray light effects are usually distinguished:

- Spectrally resolved irradiance measurements as carried out in this work aim at the detection of light that is emitted by the measurement object directly towards the detector. Light from the ambience of the measurement object might also be detected by mistake, e.g., due to reflections at other objects. This would lead to an overestimation of the direct irradiance. Stray light from the ambience is commonly denoted as *external* stray light and can often be corrected by using a suitable measurement procedure that determines the amount of external stray light. The procedure for measuring the irradiance of calibration lamps described above is of this kind. For measurements of luminescence emission, reflections from the ambience (except the sample stage) are negligible due to the low intensity of the luminescence emission, the weak reflectance of the surrounding, the narrow detection angle of the entrance optic and the geometry of the measurement setup. Optical ray tracing simulations (see appendix B) show that reflections at the sample stage do not affect the spectral shape of the measured luminescence spectrum and the subsequent determination of the absorption coefficient either.
- Light scattering can also occur inside the spectrometer system. Such reflections may lead to a signal contribution at wavelengths different from that of the incident light. For this reason, this type of stray light is commonly denoted as *spectral* (or *internal*) stray light. Spectral stray light can lead to large deviations in the measured spectrum [83]. The significance of this effect is a property of the specific spectrometer system. Unlike external stray light, spectral stray light effects cannot be compensated by the measurement procedure. The contribution N_{stray} to the detector signal at wavelength λ_i due to spectral stray light from other wavelengths λ_j can be expressed as

$$N_{\text{stray}}(\lambda_i) = \sum_{\lambda_j \neq \lambda_i} N_x(\lambda_j) f_{\text{stray}}(\lambda_j, \lambda_i) \quad (2.48)$$

where $N_x(\lambda_j)$ is the signal due to incident light at wavelength λ_j and $f_{\text{stray}}(\lambda_j, \lambda_i)$ is the stray light rejection factor. $f_{\text{stray}}(\lambda_j, \lambda_i)$ is typically of the order of 10^{-2} to 10^{-8} , depending on the specific

device. Note that stray light from the ambience is not considered here as it is compensated by the measurement procedure as outlined above. The impact of spectral stray light can be quantified and corrected rigorously if the stray light matrix $f_{\text{stray}}(\lambda_j, \lambda_i)$ is known [83, 84]. The stray light matrix, which is a unique property of the spectrometer system, is determined by subsequently illuminating the spectrometer with monochromatic light of several wavelengths and measuring the signal at all other wavelengths. Such measurements require equipment like tunable laser sources, which is not available at ISFH and could not be used during this work. However, the manufacturers indicate the typical level of stray light rejection achieved by their systems. These values are verified by measuring the apparent transmittance of a longpass filter with a cut-off wavelength of 1450 nm, which is inserted between the spectrometer and a calibration lamp. The transmittance of the filter is also determined using the Varian Cary 5000 described in section 2.1.2 and the expected signal is thereby calculated. The Varian Cary 5000 features a double monochromator and very good stray light rejection (of the order of 10^{-7} or better) can be assumed. The results of these measurements are shown in Fig. 2.22. All data is normalized to the maximum signal for each instrument. The expected signal (black line) is given by the detector signal obtained without longpass filter, multiplied with the measured transmittance of the filter. Below 10^{-4} , the filter transmittance is too small to be measured accurately. The line is therefore grayed out. The measured dark signal noise (standard deviation of dark signal) of the spectrometer systems is visualized by the dashed lines. Signals below these limits cannot be resolved by the systems. As can be seen in Fig. 2.22, the CompactSpec system achieves a maximum stray light rejection of the order of 2×10^{-3} for wavelengths below 1050 nm. The scanning system Spectro 320 achieves a maximum stray light rejection of the order of 2×10^{-4} . The stray light rejection increases with increasing distance from the cut-off wavelength. This is probably a consequence of the broad spectral distribution of the incident radiation shown in Fig. 2.23, which extends into the infrared. Hence, there are stray light contributions from a large wavelength region above 1450 nm. It is reasonable to assume that the impact of spectral stray light from a given wavelength λ_j decreases with increasing distance from λ_j . Thus, the overall stray light rejection should increase with increasing spectral distance from the cut-off wavelength, as observed in Fig. 2.22. The observed maximum stray light rejection levels are in agreement with the levels of stray light rejection indicated by the manufacturers (visualized by the dotted lines). Instrument Systems determined the stray light rejection level to be 10^{-4} by illuminating the spectrometer system with monochromatic laser light at 1152 nm and measuring the signal at a wavelength distance which is eight times the spectral bandwidth [85]. For the luminescence measurements with the Spectro 320 system, a spectral bandwidth of 10 nm is used. The stray light rejection thus refers to a spectral distance of 80 nm. Moreover, the stray light rejection was determined to be 2×10^{-4} at 950 nm using a black body radiator with a temperature of 2856 K and a longpass filter with a cut-off wavelength of 1200 nm. For the CompactSpec system, details about the measurement of the stray light rejection level by the manufacturer are not available, but a similar approach can be assumed.

As can be seen from Fig. 2.23, the intensity of the calibration lamp radiation is high and comparable for all wavelengths between 1100 and 1450 nm, where data from luminescence measurements is used. According to the observed levels of stray light rejection, the intensity of spectral stray light is lower by at least two orders of magnitude. The impact of spectral stray light for the calibration is thus negligible. The luminescence spectrum consists of a rather narrow peak compared to the spectrum of the calibration lamp (FWHM ≈ 50 nm). For luminescence measurements, the maximum amount of spectral stray light at wavelength λ can be estimated as a first approximation by

$$N_{\text{stray}}(\lambda) \approx N_{\text{max}} \times f_{\text{stray}} \quad (2.49)$$

where N_{max} is the peak signal and

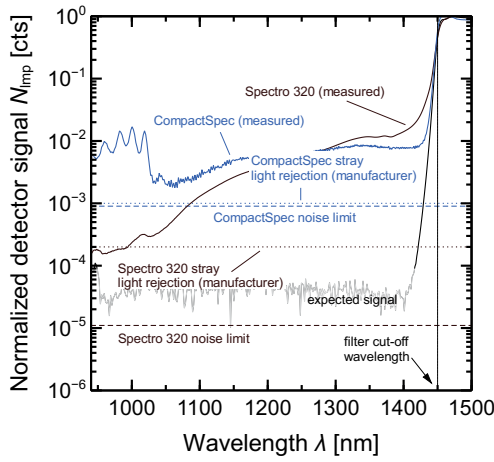


Figure 2.22: Estimation of the order of magnitude of spectral stray light within the two spectrometer systems used in this work.

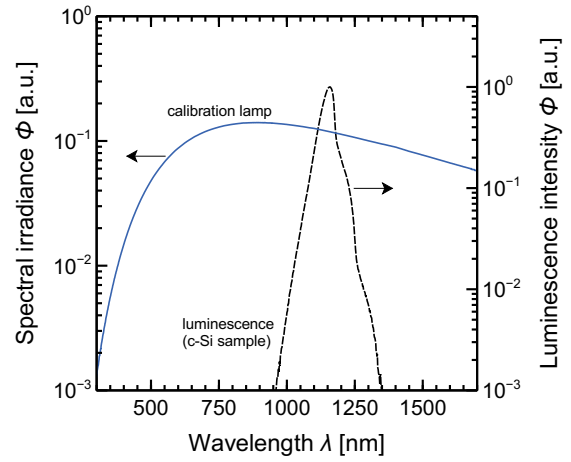


Figure 2.23: Spectral irradiance of the calibration lamp (solid line) and a typical luminescence spectrum of a silicon wafer sample (dashed line).

$$f_{\text{stray}} = \begin{cases} 2 \times 10^{-3} & \text{for the CompactSpec system,} \\ 2 \times 10^{-4} & \text{for the Spectro 320 system} \end{cases}$$

is the stray light rejection factor which is assumed to be constant for all wavelengths. The latter assumption is also supported by the measurement results indicated by the manufacturers. Intuitively, it is clear from Fig. 2.23 that the impact of spectral stray light may only be significant at the edges of the luminescence spectrum, where the detector signal is small. At these wavelengths, a large uncertainty is caused by the low signal-to-noise ratio (see section 2.2.8). Compared to the uncertainty, the deviations caused by spectral stray light are small. According to the GUM, corrections are thus not necessary and are therefore omitted. Neglecting corrections for spectral stray light is also supported by the finding that, although the stray light rejection of both systems differs by two orders of magnitude, no differences are visible in the measured luminescence spectra as shown in Fig. 2.26.

Other effects such as an angle-dependent sensitivity of the entrance optic can also lead to systematic deviations with respect to spectrally resolved irradiance measurements in principle. However, unlike spectral stray light, these effects do not alter the shape of the measured spectrum and thus do not affect the determination of the absorption coefficient. In the context of this work, corrections are thus not necessary.

2.2.7 Uncertainty contributions

Contributions to $u^2(I_{\text{lum}})$ result from the uncertainty of N_{lum} , the uncertainty of N_{Imp} and the uncertainty of I_{Imp} , according to Eq. (2.45). This section describes the uncertainty contributions and their determination.

Uncertainty contributions by N_{lum} and N_{Imp} The uncertainties of N_{lum} and N_{Imp} are determined in the same way. Therefore, in the following, N_x is used where “x” stands for “lum” and “Imp”.

According to Eqs. (2.41) to (2.44), N_x is given by the measurands N_{ill} and N_{drk} :

$$N_x = N_{\text{ill}} - N_{\text{drk}} . \quad (2.50)$$

Hence,

$$u^2(N_x) = u^2(N_{\text{ill}}) + u^2(N_{\text{drk}}). \quad (2.51)$$

The uncertainty contributions $u^2(N_{\text{ill}})$ and $u^2(N_{\text{drk}})$ contain photon noise, thermal noise and noise of the amplifier electronics and are thus statistically distributed (*type A* uncertainties). They are given by the variance $\sigma^2 = 1/(n-1) \sum_{i=1}^n (x_i - \bar{x})^2$ of subsequent measurements. Hence,

$$u^2(N_x) = \sigma^2(N_{\text{ill}}) + \sigma^2(N_{\text{drk}}). \quad (2.52)$$

Beside these *type A* uncertainty contributions, there are other effects which contribute to the uncertainty of N_x :

Spectral bandwidth: The spectral bandwidth of a monochromator characterizes the wavelength interval around the nominal wavelength within which the transmittance is not zero. It is determined, e.g., by the slit width and the geometry of the grating. Spectral bandwidth generates an additional detector signal due to light incident at adjacent wavelengths. In principle, this effect is taken into account by the irradiance calibration. However, if the shape of the sample spectrum (e.g., a luminescence spectrum) differs from that of the calibration lamp, the spectral bandwidth may cause an additional signal N_{bw} . Several approaches for a correction of this effect can be found in the literature, e.g., Refs. 86–89.

An upper limit for the signal contribution N_{bw} due to spectral bandwidth is obtained by using a second-order Taylor series expansion of the spectral irradiance around the bandpass central wavelength λ and assuming a rectangular bandpass function of width $\Delta\lambda$. According to the derivation given in appendix C.2, N_{bw} is given by

$$N_{\text{bw}} = \frac{N_x(\lambda - \Delta\lambda/2) - 2N_x(\lambda) + N_x(\lambda + \Delta\lambda/2)}{6}. \quad (2.53)$$

As shown in section 2.2.8, this contribution is small compared to other uncertainty components. Since assuming a rectangular bandpass function is a worst case estimation and typical bandpass functions are rather triangularly, N_{bw} can be assumed to be even smaller in reality. For this reason, a correction is not performed. Spectral bandwidth is instead taken into account by assuming a rectangularly distributed uncertainty contribution u_{bw}^2 of width N_{bw} . This leads to the estimation formula

$$u_{\text{bw}}^2 = \frac{1}{3} \left[\frac{N_x(\lambda - \Delta\lambda/2) - 2N_x(\lambda) + N_x(\lambda + \Delta\lambda/2)}{6} \right]^2. \quad (2.54)$$

For practical calculations, $N_x(\lambda \pm \Delta\lambda/2)$ is obtained from interpolation. The spectral bandwidth is taken from the technical data sheet for both systems. It is $\Delta\lambda = 3$ nm for the CompactSpec system and $\Delta\lambda = 10$ nm for the Spectro 320 system.

Accuracy of the wavelength calibration: Wavelength deviations can affect the signal attributed to the nominal wavelength. This may result in an additional signal contribution N_{wl} . Both spectrometers are calibrated with respect to wavelength using a mercury vapor lamp with known peak positions [90, 91]. After calibration of the wavelength scale, the deviation of nominal and measured peak wavelength is smaller than ± 0.15 nm for both systems and a systematic deviation is not observed. The possible signal contribution due to wavelength deviations is estimated by

$$N_{\text{wl}} \approx \max \left(\left| N_x(\lambda + \Delta\lambda) - N_x(\lambda) \right|, \left| N_x(\lambda - \Delta\lambda) - N_x(\lambda) \right| \right). \quad (2.55)$$

This possible signal contribution is taken into account by assuming a rectangularly distributed uncertainty contribution of width N_{wl} for N_x :

$$u_{\text{wl}}^2 = \frac{N_{\text{wl}}^2}{3}. \quad (2.56)$$

For practical calculations, $N_x(\lambda \pm \Delta\lambda)$ is obtained from interpolation.

Drift of the dark signal over time: The calculation of the dark signal corrected spectrum given by Eq. (2.44) assumes that the dark signal of the detector is constant during the measurements of sample signal and background signal. This assumption holds for the CompactSpec system, for which drifting of the dark signal is not measurable compared to its uncertainty (noise) on time scales of typical measurements (of the order of minutes). Hence,

$$u_{\text{drift,drk}}^2 = 0 \quad \text{for the CompactSpec system.} \quad (2.57)$$

The situation is different for the Spectro 320 system. Here, measurable deviations of the dark signal before and after the sample measurement can occur. This is a consequence of the lower dark signal noise limit (see Fig. 2.22) of this system. The observed signal change due to the drift is about five orders of magnitude smaller than the signal during the calibration of the spectrometer. For calibration measurements, drifting of the dark signal is thus neglected, i.e.,

$$u_{\text{drift,drk}}^2 = 0 \quad \text{for calibration measurements with the Spectro 320 system.} \quad (2.58)$$

However, the signal change due to drift of the dark signal and the signal due to luminescence radiation are of the same order of magnitude. For luminescence measurements, the drift can thus have a significant impact on the measurement results. For this reason, the dark signal is measured before and after the luminescence measurement ($N_{\text{drk}}(t_1)$ and $N_{\text{drk}}(t_2)$). From these values, the average dark signal

$$\bar{N}_{\text{drk}} = \frac{N_{\text{drk}}(t_1) + N_{\text{drk}}(t_2)}{2} \quad (2.59)$$

is obtained and used for the calculation of the luminescence spectrum by Eq. (2.44). Since drifting of the dark signal originates from temperature variations of the detector and the amplifier electronics, the dark signal is assumed to vary rather slowly between the limits $N_{\text{drk}}(t_1)$ and $N_{\text{drk}}(t_2)$. The uncertainty due to drifting of the dark signal is therefore estimated by

$$u_{\text{drift,drk}}^2 = \frac{1}{3} \left| \frac{N_{\text{drk}}(t_1) - N_{\text{drk}}(t_2)}{2} \right|^2 \quad \text{for luminescence measurements with the Spectro 320 system.} \quad (2.60)$$

In summary, the uncertainty of the dark signal is estimated by

$$u_{\text{drk}}^2 = \begin{cases} \sigma^2(N_{\text{drk}}) & \text{CompactSpec system (all measurements),} \\ \sigma^2(N_{\text{drk}}) & \text{Spectro 320 system (calibration measurements),} \\ \left[\sigma^2(N_{\text{drk}}(t_1)) + \sigma^2(N_{\text{drk}}(t_2)) \right] / 4 + u_{\text{drift,drk}}^2 & \text{Spectro 320 system (luminescence measurements).} \end{cases}$$

Nonlinearities of the detector regarding the irradiance: The irradiance levels during the measurements of the calibration lamp spectrum and the luminescence spectrum differ significantly. Thus, the responsivity of the detector with respect to the irradiance levels must be evaluated, since any deviations from a linear characteristic cause a signal deviation which must be taken into account. There are several possibilities for the determination of nonlinearities, e.g., using the inverse square law and varying the distance between light source and detector or using filters with different attenuation factors. The most accurate determination of nonlinearities is facilitated by using a superposition method [92]. Figure 2.24 shows a sketch and a photography of the setup used in this work. It consists of two stable light sources which illuminate the detector one after the other. Afterwards, both light sources illuminate the detector simultaneously. The procedure is carried out at different distances from the light sources in order to obtain variations of the irradiance.

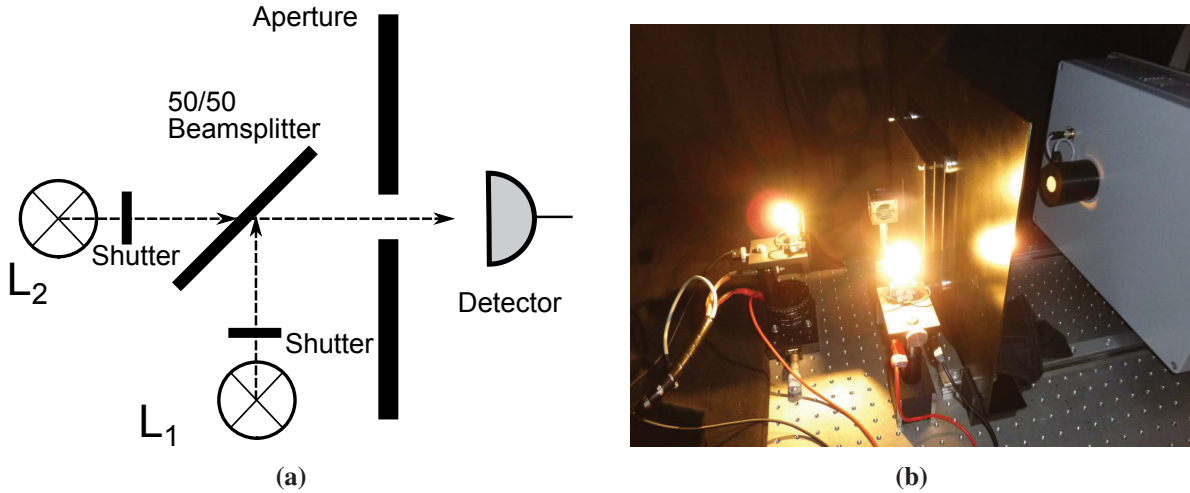


Figure 2.24: Sketch (a) and photography (b) of the setup for the determination of detector nonlinearities by the superposition method.

The irradiance level on the detector is I_1 for the first lamp, I_2 for the second lamp and $I_3 = I_1 + I_2$ for both lamps together. The corresponding detector signals are S_1 , S_2 and S_3 . Ideally, S_3 should be equal to $S_1 + S_2$. Deviations from this characteristic can be interpreted as nonlinearities of the detector with respect to irradiance. Figure 2.25 (a) shows the measured deviations for the InGaAs detectors of both CompactSpec and Spectro 320 as a function of the detector signal S_3 . The measured deviations do not show a clear trend, which would allow them to be parametrized and used as a correction. Moreover, the deviations are generally small ($\pm 0.87\%$ for the CompactSpec system and $\pm 0.066\%$ for the Spectro 320 system). For this reason, the maximum measured deviation is included into the uncertainty budget instead of applying a nonlinearity correction. Assuming a rectangular distribution for the uncertainty contribution $u_{\text{lin},i}^2$ due to nonlinearity regarding the irradiance, the contribution is

$$u_{\text{lin},i}^2 = \frac{(N_{\text{lin},i})^2}{3} \quad (2.61)$$

with

$$N_{\text{lin},i} = \begin{cases} 0.0087 \times N_x & \text{for the CompactSpec system,} \\ 0.00066 \times N_x & \text{for the Spectro 320 system.} \end{cases}$$

Note that in the literature, a parametrization method is found which makes use of a polynomial approximation of the nonlinearity [92, 93]. The application of this method requires the inversion of matrices and can be subject to numerical instabilities, as these matrices may be ill-conditioned. The calculated correction may then introduce a significant error. This is the case for the measurements carried out in this work. Appendix A contains a more detailed discussion of this issue.

Nonlinearities regarding the integration time: The CompactSpec system is operated with different integration times during the calibration and the luminescence measurement (700 ms and 6500 ms, respectively) in order to prevent the saturation of the detector and to achieve the maximum possible signal-to-noise ratio. Therefore, a linear characteristic of the system with respect to integration time must be ensured. The Spectro 320 system is operated with a scan speed of 350 ms/nm during both calibration and luminescence measurements since the signal-to-noise ratio cannot be improved by further reducing the scan speed. Figure 2.25 (b) shows the relative deviation of various measurements of a calibration lamp spectrum, carried out with the CompactSpec system using different integration

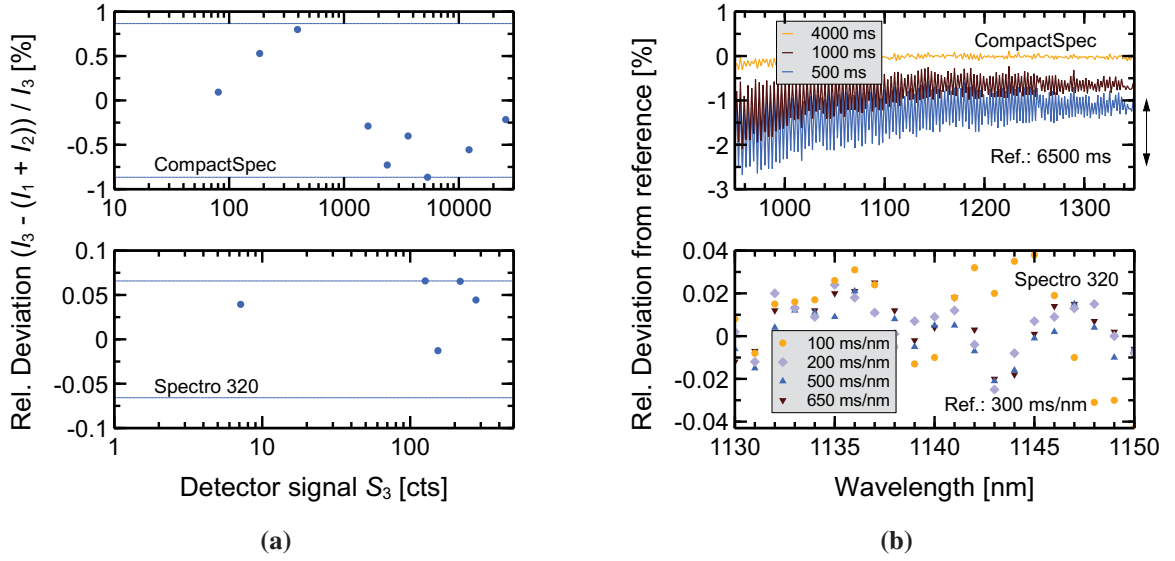


Figure 2.25: Nonlinearity of the spectrometer detectors with respect to intensity (a) and integration time or scan speed, respectively (b).

times. The data is normalized to integration time and divided by a reference measurement (6500 ms). The observed deviations are of the order of up to 2% rel. However, the luminescence measurements are carried out in relative units and scaled, so that absolute changes of the measured intensity cancel out. Hence, only the difference of the deviations with respect to wavelength, which is visualized by the vertical arrow in Fig. 2.25, must be taken into account. As for the Spectro 320, the measured deviations seem to be affected by measurement noise. The observed deviations are therefore not corrected but taken into account as an uncertainty contribution $u_{\text{lin,t}}^2 = (N_x \times 0.015)^2/3$.

For the sake of completeness, nonlinearities of the Spectro 320 system with respect to scan speed are also investigated and shown in Fig. 2.25 (b). The reference measurement uses a scan speed of 300 ms/nm. The deviations do not exceed $\pm 0.04\%$ and a systematic effect is not observed. Using the observed deviations as an estimate of the uncertainty contribution $u_{\text{lin,t}}^2$ due to nonlinearity with respect to scan speed yields $u_{\text{lin,t}}^2 = (N_x \times 0.0004)^2/3$. For the measurements presented in this work, however, this uncertainty contribution does not need to be considered as the same scan speed is used for calibration and luminescence measurements. Hence,

$$u_{\text{lin,t}}^2 = \begin{cases} (0.015 \times N_x)^2/3 & \text{for the CompactSpec system,} \\ 0 & \text{for the Spectro 320 system.} \end{cases} \quad (2.62)$$

Spectral stray light: As discussed in section 2.2.6, the impact of spectral stray light for luminescence measurements is small and corrections are not applied. The amount of spectral stray light obtained from the first order approximation is taken into account as a rectangularly distributed uncertainty component

$$u_{\text{stray}}^2 = \frac{(N_{\text{max}} \times f_{\text{stray}})^2}{3} \quad (2.63)$$

for both the measurement of the calibration lamp and the measurement of the luminescence spectrum.

Long term reproducibility: All other uncertainty contributions that have not been taken into account so far and lead to deviations in the reproducibility over time are summed into this contribution.

The relative deviation q between measurements using an identical setup is taken into account as a rectangularly distributed uncertainty component u_{rep}^2 . From experience, $q \leq 0.005$ holds. The uncertainty contribution is then

$$u_{\text{rep}}^2 = \frac{(N_x \times 0.005)^2}{3}. \quad (2.64)$$

Overall uncertainty of N_x : Taking into account the uncertainty contributions listed above, the overall uncertainty of N_x is given by

$$u^2(N_x) = \sigma^2(N_{\text{ill}}) + u_{\text{drk}}^2 + u_{\text{stray}}^2 + u_{\text{bw}}^2 + u_{\text{wl}}^2 + u_{\text{lin,i}}^2 + u_{\text{lin,t}}^2 + u_{\text{rep}}^2. \quad (2.65)$$

Uncertainty contribution by I_{Imp} : The uncertainty $u^2(I_{\text{Imp}})$ is given by the uncertainty of the primary calibration carried out at PTB. The uncertainty of the data is of the order of 2% rel. ($k = 2$).

Overall uncertainty of I_{lum} : The overall uncertainty of I_{lum} is calculated from Eq. (2.45). It is given by

$$\begin{aligned} u^2(I_{\text{lum}}) &= \left(\frac{I_{\text{Imp}} t_{\text{int,Imp}}}{N_{\text{Imp}} t_{\text{int,lum}}} \right)^2 u^2(N_{\text{lum}}) + \left(- \frac{N_{\text{lum}} I_{\text{Imp}} t_{\text{int,Imp}}}{(N_{\text{Imp}})^2 t_{\text{int,lum}}} \right)^2 u^2(N_{\text{Imp}}) \\ &+ \left(\frac{N_{\text{lum}} t_{\text{int,Imp}}}{N_{\text{Imp}} t_{\text{int,lum}}} \right)^2 u^2(I_{\text{Imp}}). \end{aligned} \quad (2.66)$$

Note that for the Spectro 320 system, $t_{\text{int,Imp}} = t_{\text{int,lum}}$ holds (see notes to Eq. (2.45)).

2.2.8 Performance of scanning vs. diode array spectrometer system

Based on the uncertainty analysis described above, the performance of both the scanning Spectro 320 system and the diode array CompactSpec system for luminescence measurements is evaluated. For this purpose, an electroluminescence spectrum of a polished solar cell is exemplarily measured with both systems and the uncertainty of the data is determined. Figure 2.26 shows the resulting data. The data is normalized to maximum for comparison. The relative uncertainty ($k = 2$) of the data is indicated by the lines. The uncertainty of the spectrum data is about 5-10% rel. ($k = 2$) at the peak wavelength (1140 nm) and increases to 100% or above at wavelengths above 1250 nm. The increase of the relative uncertainty is mainly due to a constant noise level of the detector and the decrease of the luminescence emission intensity by two orders of magnitude. For the sample under investigation, measurements with uncertainties below 10% are possible in the wavelength range from 1060 to 1170 nm.

The relative measurement uncertainty that is achieved is of the same order of magnitude for both systems. The major part of the uncertainty originates from the measurement of the luminescence spectrum. The measurement of the calibration lamp spectrum is subject to uncertainties of the order of 1% relative. Figure 2.27 visualizes the uncertainty budgets for the measurements of the luminescence spectrum at 1140 and 1200 nm. The figure shows the summands of Eq. (2.65) normalized to their sum $u^2(N_x)$. The uncertainty of the measured spectra is in all cases limited by the type A contributions due to photon noise, dark signal (thermal) noise and measurement amplifier noise, represented by $\sigma^2(N_{\text{ill}})$ and u_{drk}^2 . This is a reasonable result as the intensity of the luminescence emission is very small ($\lesssim 10^{-5} \text{ W}/(\text{m}^2\text{nm})$), which implies a low signal-to-noise ratio. Beside this finding, it can be seen that nonlinearities of the detector are much more significant for the CompactSpec system than for the Spectro 320 system. However, the impact of nonlinearities, spectral bandwidth, wavelength deviations and spectral stray light is small in general. Note that the ordinate is scaled logarithmically. It is thereby verified that these systematic effects are small compared to the overall uncertainty and that corrections of these effects can be omitted. Interestingly, the relative significance of wavelength

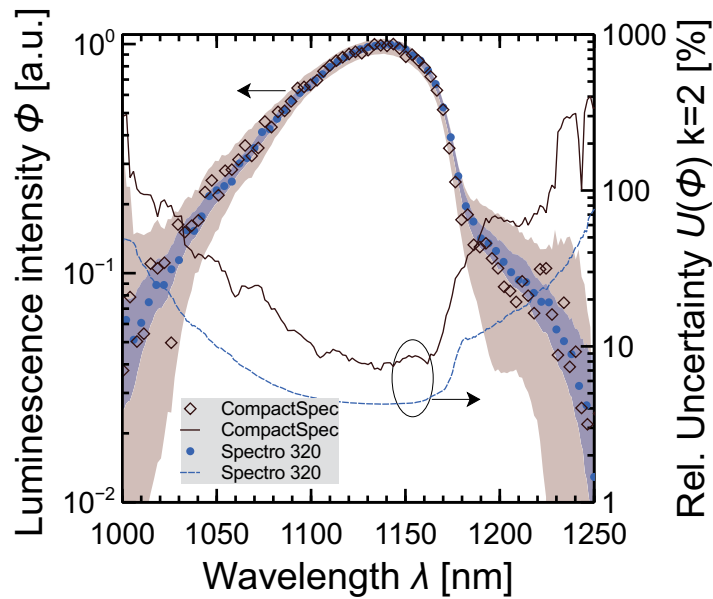


Figure 2.26: Comparison of electroluminescence spectra measured with both Spectro 320 and CompactSpec. The spectra are normalized to maximum for comparison. The lines indicate the relative uncertainty of the data. The absolute uncertainty is visualized by the shaded areas.

accuracy and long term reproducibility is larger for the Spectro 320 system than for the CompactSpec system. This finding is surprising at first sight, but it is a simple consequence of the fact that the type A uncertainty contributions due to noise are smaller for the Spectro 320 than for the CompactSpec system. In turn, this means that the relative significance of all other uncertainty contributions is increased. It is important to note that in the configuration used in this work, the Spectro 320 is equipped with a diffuser head as entrance optic (see Fig. 2.19). The diffuser decreases the intensity on the detector by a factor of about 10. The CompactSpec system is equipped with a bare fiber as entrance optic and does not suffer from this loss of intensity. Bare fibers are not suitable for irradiance measurements due to their strong angle dependence, but can be used unproblematically for relative measurements as done in this work. When using the Spectro 320 with a bare fiber or a mirror as entrance optic, a decreased relative uncertainty due to the increased signal-to-noise ratio is expected. A bare fiber for the Spectro 320 was not available during this work. Despite of the decreased intensity due to the diffuser optic, the Spectro 320 already achieves uncertainties that are smaller by a factor of about 2. An advantage of the CompactSpec system is the reduced data acquisition time compared to the Spectro 320 (about 5 min for 25 averages, compared to about 10 min for 5 scans). A second advantage is the stability of the wavelength calibration under exposure to vibrations (e.g., during transport), as the system does not contain any moving components.

As a conclusion, it can be stated that the scanning Spectro 320 system allows for luminescence measurements with reduced uncertainty compared to the diode array CompactSpec system. It is therefore used for all measurements concerning the determination of the absorption coefficient. The uncertainty could be further reduced by increasing the signal-to-noise ratio, e.g., by using a bare fiber as entrance optic. However, in the present configuration of the systems, the uncertainties achieved by both systems are of the same order of magnitude.

2.2.9 Electroluminescence vs. photoluminescence measurements

In general, the absorption coefficient can be determined by both electroluminescence (EL) and photoluminescence (PL) measurements. In practice, however, both methods have their advantages and

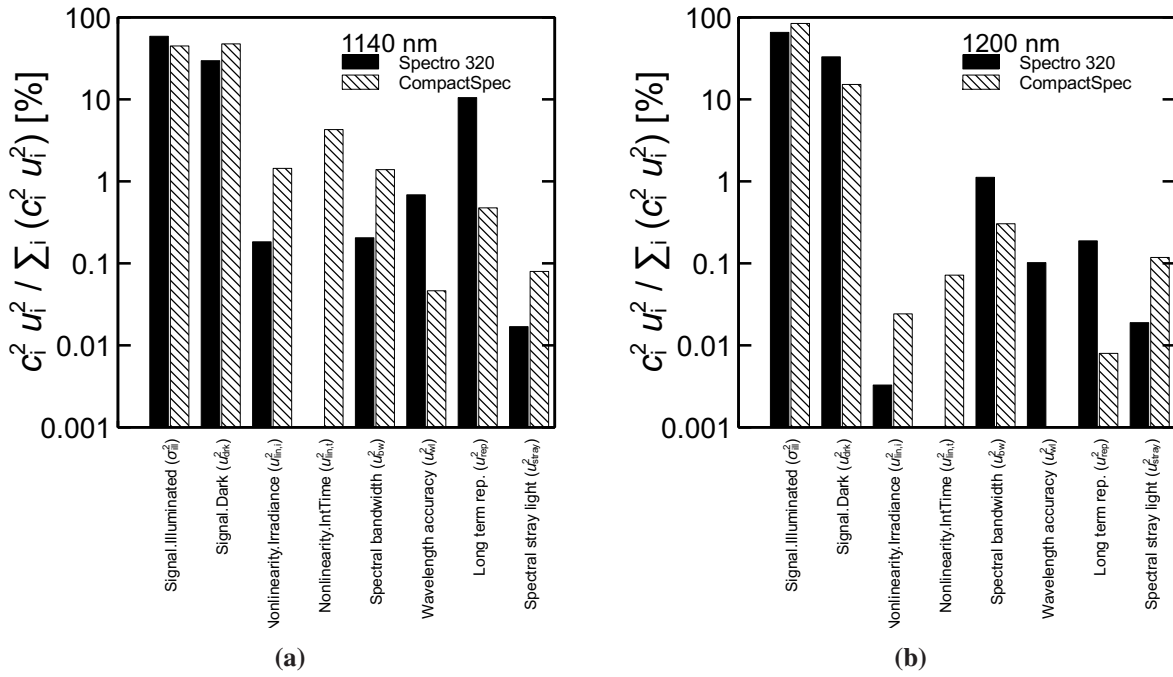


Figure 2.27: Uncertainty budget of the data shown in Fig. 2.26 at 1140 nm and 1200 nm.

disadvantages. A careful choice of the method is therefore necessary.

PL measurements can be carried out on wafer samples without the need of making an electrical contact to the sample. Thereby, also weakly doped or intrinsic samples can be used. As intense laser light sources for excitation have become available, very high injection levels can be achieved within the sample, which results in strong luminescence emission and high signal-to-noise ratios during the measurement. However, PL measurements have to deal with some issues of major impact. First of all, optical excitation causes significant heating of the sample. When local excitation is used (e.g., in order to achieve very high injection levels), large temperature gradients are induced. Considering the temperature dependence of the luminescence spectrum, it is obvious that it is important to measure and control the sample temperature precisely during illumination. Moreover, sufficient time must be allowed for the sample temperature to stabilize after powering up the laser. This increases the required delay between measurements of the sample spectrum and the dark signal of the detector and may lead to increased uncertainties. A second issue PL measurements have to deal with is spectral stray light within the detection system caused by the laser radiation. The exciting laser radiation is usually many orders of magnitude more intense than the luminescence radiation that is to be detected. Laser light that is accidentally coupled into the detection system can easily cause stray light artifacts. Also, many lasers (especially laser diodes, which are often used) feature a narrow peak but also a broad underground, which extends to wavelengths where the luminescence emission is located. Hence, adequate optical filters must be used in order to ensure that only luminescence radiation is detected. A third issue with PL measurements is an apparent dependence of the luminescence spectrum on the detection angle and the distance between sample and entrance optic of the spectrometer which has been observed for polished silicon wafer samples. Figure 2.28 shows PL spectra measured with various distances between sample and detector. The excitation conditions and the sample temperature are constant for all measurements. For comparison, the data is normalized. Variation of the distance leads to an apparent relative increase of luminescence intensity in the region around 1200 nm. However, the shape of the luminescence spectrum is not expected to show such variations, only the overall intensity should depend on the detection distance. The effect is not observed for textured wafer samples

as also shown in Fig. 2.28, and its origin is not yet understood. The effect might eventually originate from luminescence emission from the edges of the sample. Another possibility is stray light from the excitation laser. This assumption is supported by the finding that the effect is neither observed for PL measurements on textured samples nor for EL measurements in general. Nevertheless, these measurements show that PL measurements on polished samples may introduce potential uncertainties for the determination of the absorption coefficient at wavelengths around 1200 nm, which is evaluated from the shape of the luminescence spectrum. Critically, it is exactly this wavelength range, where luminescence data from textured samples is scaled.

EL measurements require an electrical contact to the sample and a *pn*-junction for the injection of charge carriers. This implies that the sample contains metallized surfaces as well as highly doped layers, in which free carrier absorption may be the dominant absorption mechanism. Free carrier absorption does not affect the generation but the escape probability of luminescence photons and may therefore affect the shape of the luminescence spectrum. The conductivity of the electrical contacting imposes restrictions on the injection levels that can be achieved. These are generally lower than for PL measurements and lead to lower signal-to-noise ratios during the measurement. For the calculation of the absorption coefficient from a luminescence spectrum, required optical properties of the sample such as surface reflectance are not as easily determined as for bare wafer samples. However, EL measurements solve the three major issues of PL measurements addressed above. The sample temperature under current injection is very stable. During the measurements carried out in this work, sample heating of only 0.5 K was observed under injection of 150 mA/cm² (corresponding to an illumination intensity of approximately 400 mW/cm² regarding the injection level, which would increase the sample temperature by about 40 K). Short time delays between acquisition of sample spectrum and dark spectrum can thus be realized. As no exciting laser illumination is involved, stray light effects are excluded. Furthermore, a dependence of the luminescence spectrum on the angle and distance of detection is not observed for EL measurements.

On the basis of these findings, the following procedure is applied in this work: In the wavelength range from 1100 to 1250 nm, EL measurements are carried out on the polished solar cells described in section 2.2.2. The data obtained by these measurements is scaled to measured values of the absorptance of the solar cell. Above 1250 nm, PL measurements are carried out on textured wafer samples. These samples feature an enhanced luminescence photon escape probability compared to polished samples, which leads to an increased signal-to-noise ratio. Also, the optical excitation allows for an enhanced luminescence emission intensity compared to electrical excitation. The PL data is scaled to the data from EL. The procedure is described in detail in the following.

2.2.10 Results

Figure 2.29 shows the measured electroluminescence spectrum of a polished solar cell and the photoluminescence spectrum of a textured wafer. The spectra are calculated using Eq. (2.45). The dashed lines show the relative expanded uncertainty of the data for $k = 2$ given by Eq. (2.66). The top graph shows the corresponding coverage probability for a t-distribution with an effective degrees of freedom (see section 1.3.5) following from the uncertainty analysis. Between 1100 and 1300 nm, the coverage probability for $k = 2$ is larger than 95.2%. Beyond 1300 nm, the coverage probability decreases to about 92%. This is a consequence of the dominant type A uncertainty of the luminescence measurement in this wavelength range and the small number of repeated measurements ($N = 3$). Obtaining a coverage probability of 95.45% would require to increase the coverage factor k to about 2.5.

The absorption coefficient is obtained from the luminescence data by scaling. The scaling procedures for EL and PL data are different.

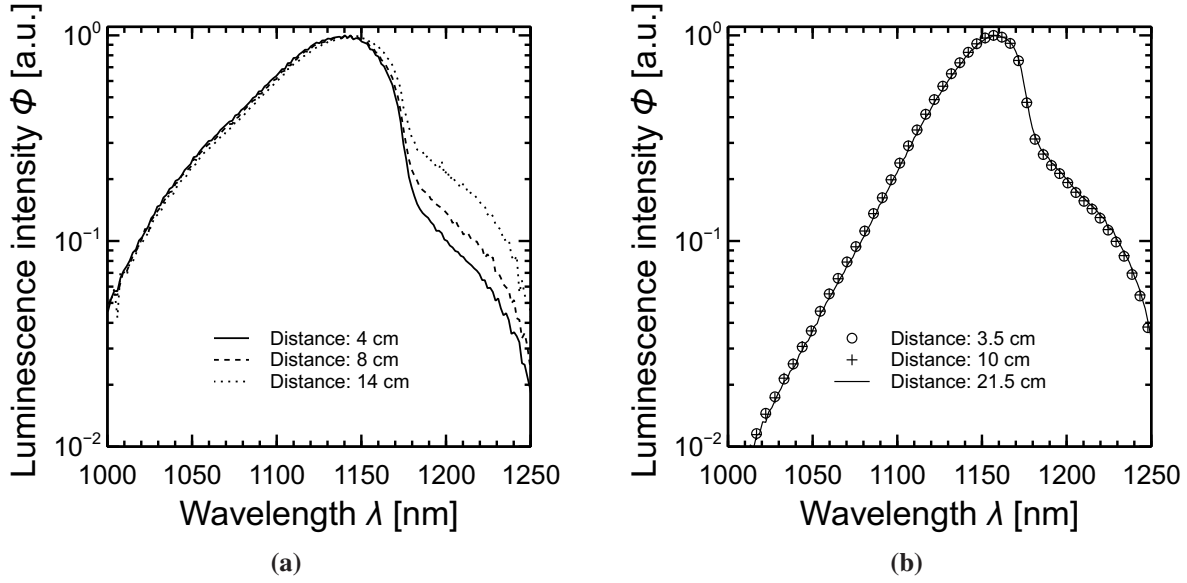


Figure 2.28: PL measurements on Czochralski grown silicon wafers under identical excitation conditions but different distances between sample and detector. The sample temperature is constant for all measurements. (a) Double side polished sample. (b) Double side textured sample.

Scaling of EL data As described in section 2.2.1, the luminescence data is proportional to the absorptance of the sample if the minority charge carrier distribution within the sample is homogeneous. A homogeneous minority charge carrier distribution can be assumed for wafer samples with passivated surfaces. The polished solar cells feature a fully metallized rear surface without surface passivation, which causes a high charge carrier recombination velocity S_r of the order of 10^4 cm/s. The assumption of a homogeneous minority charge carrier distribution within the solar cell is thus not fulfilled. On the contrary, the charge carrier concentration decreases linearly from $z = 0$ (where the minority charge carriers are injected) to $z = W$ (the rear surface) [94]. Inserting a linearly decreasing minority charge carrier concentration $n(z) = n_0(W - z)/W$ into Eq. (2.40) yields

$$\Phi(\lambda) \propto F(\alpha, W) \times A(\lambda), \quad (2.67)$$

where A is the absorptance of the sample and F is a factor which depends on α and W . For $\alpha \rightarrow 0$, F becomes constant, which means that the shape of the luminescence spectrum does not depend on the charge carrier distribution within the sample. This is a consequence of the negligible reabsorption of luminescence photons at long wavelengths. Figure 2.30 shows the ratio of $F(\alpha, W)$ and $F(\alpha \rightarrow 0, W)$ for $R_b = 0.8$ and $R_b = 1$, which approaches unity for $\alpha \rightarrow 0$ independent from the thickness of the sample. The ratio increases with decreasing rear surface reflectance and increasing sample thickness. For the sample thickness of $711 \mu\text{m}$ and $\alpha \leq 4 \text{ cm}^{-1}$, which corresponds to $\lambda \geq 1100 \text{ nm}$, the deviation from the saturation value $F(\alpha \rightarrow 0, W)$ is 1.2% for a rear surface reflectance R_b of 0.8. As shown below, $R_b > 0.8$ holds within the wavelength range of interest. Hence, this value represents an upper limit for the deviation at $\lambda > 1100 \text{ nm}$. For comparison, the dashed line visualizes the ratio for a sample thickness of $782 \mu\text{m}$ (+10% rel.), which increases slightly to 1.4% at $\alpha = 4 \text{ cm}^{-1}$. The variation of F of 1.2% is small compared to the variation of α_{bb} of several orders of magnitude. Despite the inhomogeneous minority charge carrier concentration, the proportionality of absorptance and luminescence spectrum is thus approximately given for wavelengths above 1100 nm and can be used for scaling of the EL data.

The luminescence spectrum is proportional to the absorptance of the silicon slab A_{Si} . In contrast to wafer samples, the directly measurable absorptance of the solar cell A_{sample} is not equal to A_{Si} due to

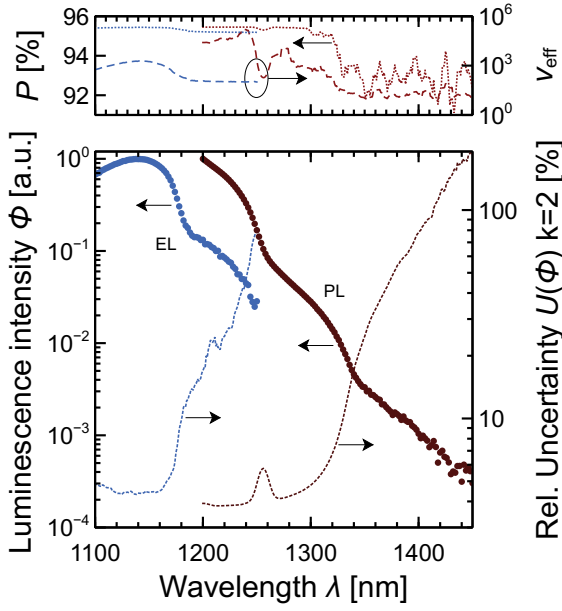


Figure 2.29: EL spectrum of the polished solar cell and PL spectrum of the textured wafer. Both spectra are normalized.

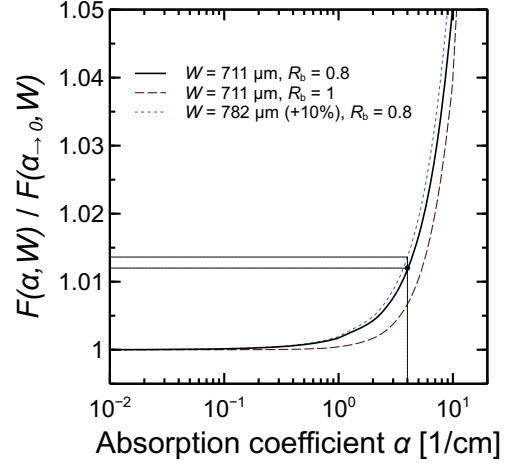


Figure 2.30: Dependence of F on the absorption coefficient α , the sample thickness W and the rear surface reflectance R_b .

the metallization of the rear surface. In order to scale the EL data, the absorptance of the silicon slab must first be determined. It is given by

$$A_{\text{Si}} = (1 - R_f) \frac{1 + (R_b - 1) \exp(-\alpha W) - R_b \exp(-2\alpha W)}{1 - R_b R_f \exp(-2\alpha W)}. \quad (2.68)$$

The reflectance of the front surface R_f is altered by the highly doped emitter layer compared to lowly doped silicon. It is thus obtained from reflectance and transmittance measurements on a reference sample, where the emitter diffusion and surface passivation has been applied to both surfaces, and Eq. (2.5). Further details are given in appendix C.3.

The measurable reflectance of the solar cell R_{sample} can be interpreted as the reflectance of the silicon slab with front surface reflectance R_f and an effective rear surface reflectance R_b which describes the reflection of light at the silicon-aluminium interface. Hence,

$$R_{\text{sample}} \stackrel{!}{=} R_{\text{Si}} = R_f + \frac{(1 - R_f)^2 R_b \exp(-2\alpha W)}{1 - R_f R_b \exp(-2\alpha W)}. \quad (2.69)$$

From the latter equation, R_b follows as

$$R_b = \frac{R_{\text{sample}} - R_f}{(R_{\text{sample}} R_f - 2R_f + 1) \exp(-2\alpha W)}. \quad (2.70)$$

In the wavelength range from 1100 to 1140 nm, α is known from the measurements described in section 2.1. For wavelengths above 1200 nm, the exponential term in Eq. (2.70) is approximately unity. Hence, R_b can be calculated between 1100 and 1140 nm and above 1200 nm and interpolated in the intermediate region. In order to avoid errors due to the metallization grid on the front surface, the sample reflectance R_b is measured on a reference sample without front surface metallization. Figure 2.31 shows the resulting surface reflectances R_f and R_b and their relative uncertainties ($k = 2$) using the combined absorption coefficient data described in section 3.1.2. Equation (2.68) is then used to calculate the absorptance of the silicon slab at wavelengths between 1100 and 1140 nm, to

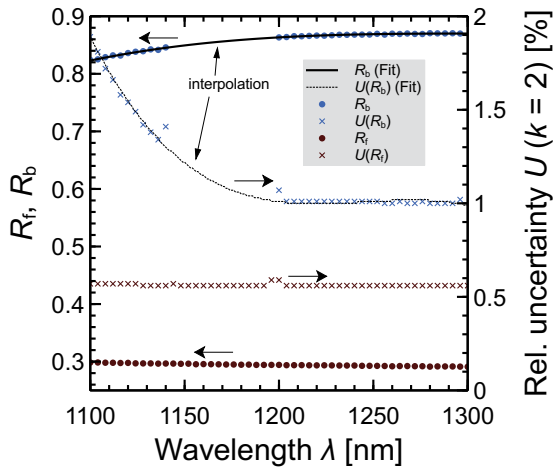


Figure 2.31: Front surface reflectance R_f and rear surface reflectance R_b of the polished solar cell.

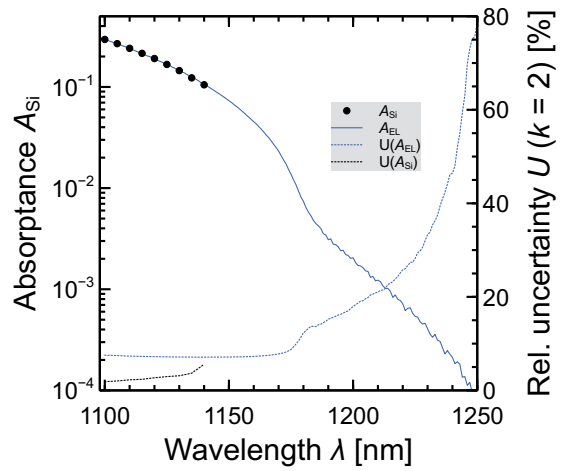


Figure 2.32: Calculated absorbance of the silicon slab and scaled EL data.

which the EL data is scaled. The resulting data is visualized in Fig. 2.32, showing the absorbance of the silicon slab A_{Si} as obtained from reflectance and transmittance measurements together with the scaled EL data A_{EL} . The scaling factor C_{scale} is obtained as a weighted average over the data in the wavelength range from 1100 to 1140 nm (see Eq. (1.32)):

$$C_{scale} = \frac{\sum_{i=1}^N C_i / u^2(C_i)}{\sum_{i=1}^N 1 / u^2(C_i)} \quad (2.71)$$

with

$$C_i = \frac{A_{Si}(\lambda_i)}{\Phi(\lambda_i)}, \quad (2.72)$$

$$u^2(C_i) = \frac{u^2(A_{Si}(\lambda_i))}{(\Phi(\lambda_i))^2} + \left(\frac{A_{Si}(\lambda_i)}{(\Phi(\lambda_i))^2} \right)^2 u^2(\Phi(\lambda_i)) \quad (2.73)$$

and $1100 \text{ nm} \leq \lambda_i \leq 1140 \text{ nm}$. The relative uncertainty of the C_i is of the order of 5%. Due to the small wavelength range used for scaling, the C_i are assumed to be fully correlated. Correspondingly, the uncertainty of C_{scale} is

$$u^2(C_{scale}) = \left(\frac{\sum_{i=1}^N 1 / u(C_i)}{\sum_{i=1}^N 1 / u^2(C_i)} \right)^2 \quad (2.74)$$

according to Eq. (1.34). The relative uncertainty $u(C_{scale})$ of the scaling factor is 2.8%. Assuming uncorrelated data would yield a relative uncertainty of 0.9%. From the scaled EL data, the absorption coefficient α is calculated using the solution of Eq. (2.68) for α .

Scaling of PL data PL measurements are applied at wavelengths above 1200 nm. In this wavelength region, the PL spectrum is proportional to the absorption coefficient α_{bb} , as described in section 2.2.1. Neither the particular optical properties of the sample nor the particular charge carrier concentration within the sample need to be taken into account. The PL data is scaled to the absorption coefficient data α_{EL} from EL at wavelengths between 1200 and 1250 nm. The scaling factor is obtained analogously to Eqs. (2.71) through (2.74) with A_{Si} replaced by α_{EL} . The relative uncertainty of the C_i ranges from 20 to 70%. The resulting relative uncertainty $u(C_{scale})$ of the scaling factor is 12.5%. Again, fully correlated C_i are assumed. By assuming uncorrelated C_i , the relative uncertainty

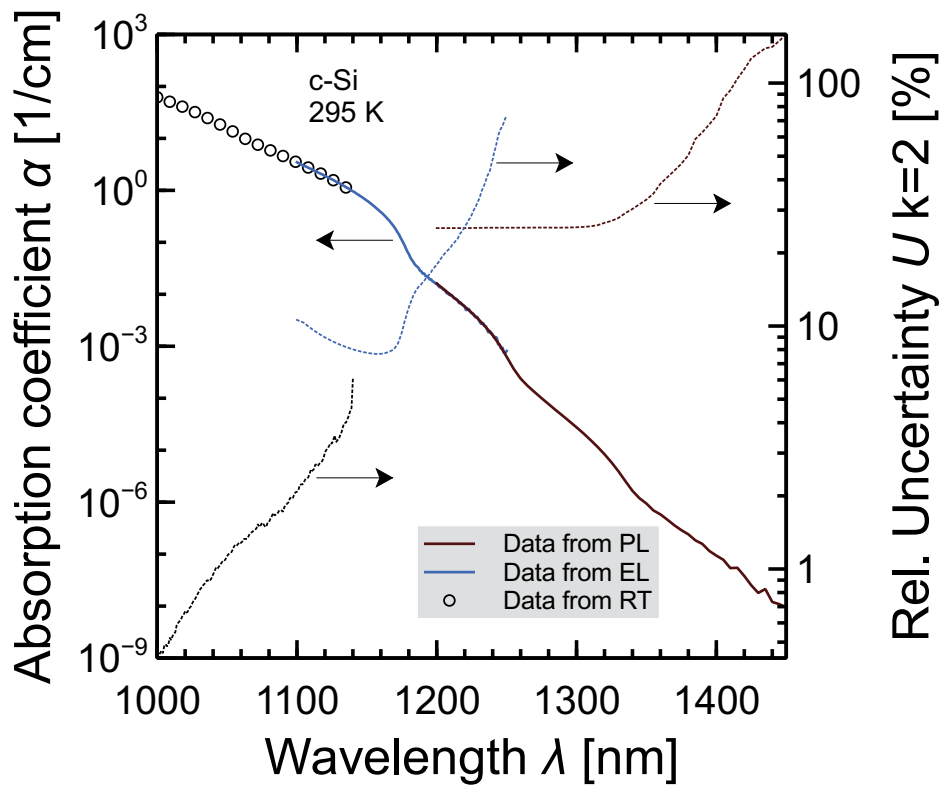


Figure 2.33: Absorption coefficient of crystalline silicon at 295 K as determined from spectrally resolved luminescence measurements.

of the scaling factor would be 4.1%. The uncertainty of the PL data would then be smaller than that of the EL data, to which it is scaled, which would be an unreasonable result and substantiates the assumption of fully correlated C_i for the calculation of the uncertainty of the scaling factor.

Resulting absorption coefficient data Figure 2.33 shows the absorption coefficient data and its uncertainty following from the EL and PL measurements described above. The data is scaled to the absorption coefficient data obtained from reflectance/transmittance measurements (see section 2.1). Tabulated values of the data shown in Fig. 2.33 are given in appendix D. The absorption coefficient decreases about eight orders of magnitude in the wavelength range from 1100 to 1450 nm. The relative uncertainty of the data ($k = 2$) is around 10% between 1100 and 1300 nm and increases approximately exponentially to about 200% at 1450 nm.

2.3 Spectral responsivity measurements

The spectral responsivity SR of a detector or solar cell, which is defined as the ratio of output short circuit current and incident intensity, depends on the collection probability for generated charge carriers and on the absorptance of the device. Hence, the spectral response of a silicon detector contains information about the absorption coefficient. Spectral responsivity measurements are applicable in the region around the band gap wavelength where the absorptance is not saturated. The SR measurements presented in this work are carried out by the Physikalisch-Technische Bundesanstalt (PTB) in Braunschweig, Germany.

2.3.1 Principle of measurements

The spectral responsivity $SR(\lambda)$ at wavelength λ is defined as short circuit current per incident intensity of light. From the spectral responsivity, the external quantum efficiency EQE is calculated via

$$EQE(\lambda) = SR(\lambda) \frac{hc}{q\lambda} \quad (2.75)$$

where h is the Planck constant, c is the speed of light, q is the elementary charge and λ is the wavelength. By an optical reciprocity theorem [73], the EQE and consequently the SR are connected to the electroluminescence photon flux Φ_{EL} of the solar cell by

$$\Phi_{EL}(\lambda, \Omega) d\lambda d\Omega = \Phi_{bb}(\lambda, \Omega) d\lambda d\Omega EQE(\lambda, \Omega) \exp\left(\frac{V}{V_T}\right), \quad (2.76)$$

where Ω is the solid angle into which the photons are emitted, V is the junction voltage, $V_T = kT/q$ is the thermal voltage at temperature T , k is the Boltzmann constant and

$$\Phi_{bb}(\lambda, \Omega) d\lambda d\Omega = \frac{2c}{\lambda^4} \exp\left(-\frac{hc}{\lambda kT}\right) d\lambda d\Omega. \quad (2.77)$$

Electroluminescence spectrum and SR can thus be transformed vice versa and the same theory as for the determination of the absorption coefficient from luminescence spectra (see section 2.2) applies to SR data. Note that an extended reciprocity relation also holds for EQE and PL spectrum [74]. Also note that in Ref. 73, the quantities EQE , Φ_{EL} and Φ_{bb} are given as functions of energy. The quantities are differential with respect to energy or wavelength. The transformations to functions of wavelength thus require the application of the chain rule. The derivation is outlined in appendix E.

2.3.2 Setup for measurements

Figure 2.34 shows a schematic drawing and a photography of the spectral responsivity measurement setup at the PTB. The measurement setup basically consists of light sources and a double monochromator, which provide light of the desired wavelength. The monochromatic light is modulated by a chopper wheel. A lock-in amplifier keeps the device under test at short circuit conditions and measures the short circuit current caused by the monochromatic illumination. Additionally, the device can be illuminated with white light (*bias light*) in order to operate the device at a specific working point. Additional components such as spectrometers and monitor photodiodes ensure a stable operation of the monochromator and the light source. The setup at the PTB is described in more details in Refs. 95 and 96.

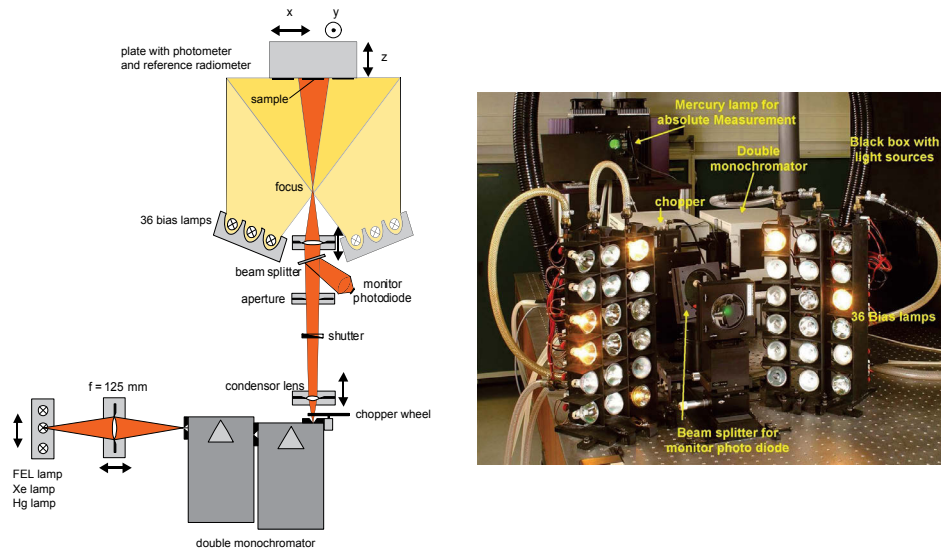


Figure 2.34: Schematic drawing and photography of the spectral responsivity measurement setup at the PTB which is used for the measurements in this work.

2.3.3 Samples for measurements

Different samples are used for *SR* measurements in this work. Industrial *p*-type silicon solar cells, cut down to an area of $2 \times 2 \text{ cm}^2$, are used for *SR* measurements in the wavelength range from 1200 to 1350 nm. The polished solar cells described in section 2.2.2 are also used for *SR* measurements in the wavelength range from 1100 to 1250 nm.

2.3.4 Results and measurement uncertainty

Figure 2.35 shows the measured *SR* of the polished solar cell and the industrial solar cell at 295 K. The data is normalized. The relative uncertainty of the data is indicated by the dashed lines. The uncertainty analysis for the *SR* measurements presented in this work is described in Ref. 96. From the *SR* data, the absorption coefficient is calculated analogously to the EL/PL data. The uncertainty of the scaling factor C_{scale} is calculated assuming full correlation of the data, as discussed for the evaluation of the EL/PL data. Figure 2.36 shows the resulting absorption coefficient data. Tabulated data for Fig. 2.36 is given in appendix D. The absorption coefficient obtained from *SR* measurements covers six orders of magnitude. The relative uncertainty of the data is of the order of 10 % at 1200 nm and increases to over 200 % at 1320 nm. Above 1200 nm, the confidence limits for $k = 2$ are visualized by the dashed lines, showing that the deviation between the data from the polished and textured sample at 1220 – 1250 nm is smaller than the uncertainty of the deviation, i.e., $E_n < 1$. Hence, compatibility of the two measurements is accepted. The relative uncertainty of the scaling factor for the data from the polished sample is 2.2 % and 6.5 % for the data from the textured sample.

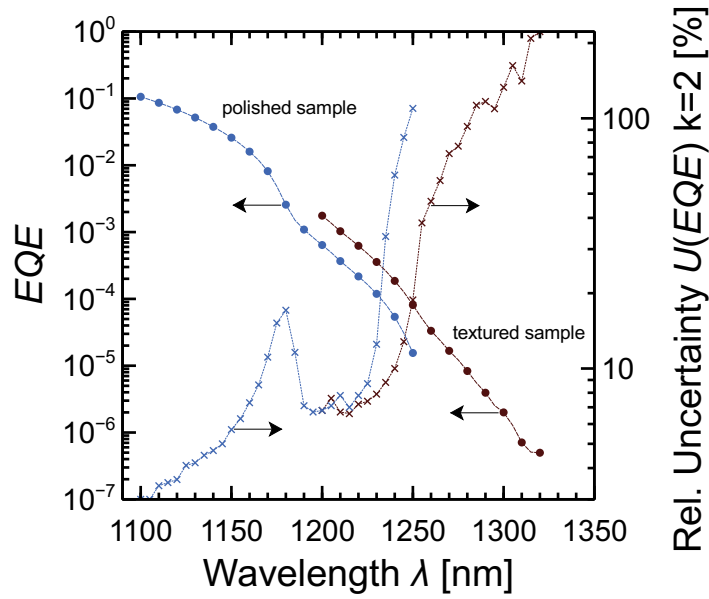


Figure 2.35: *EQE* data of the polished solar cell and an industrial solar cell (textured sample).

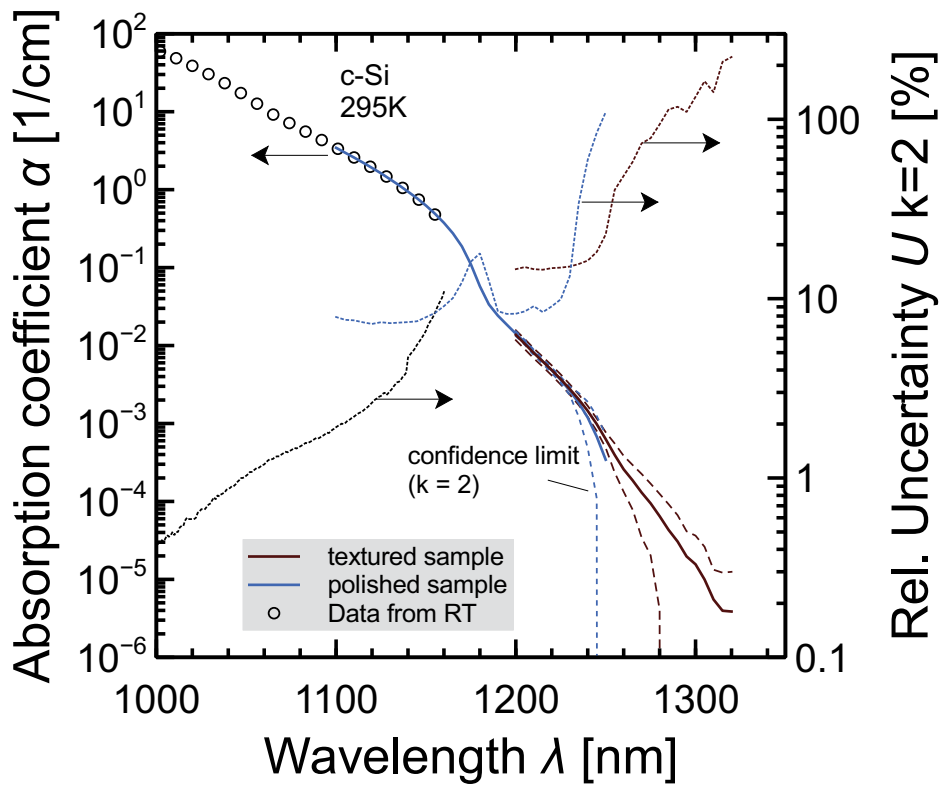


Figure 2.36: Absorption coefficient of crystalline silicon at 295 K as determined from spectral responsivity measurements carried out by the PTB.

2.4 Spectroscopic ellipsometry

Ellipsometric measurements determine the change of polarization of light that undergoes a reflection at a surface. Such measurements have been widely used as a method for the characterization of surfaces and thin layers. Although not called “ellipsometry”, this technique was already practiced in 1891 [97]. The complex index of refraction is obtained from the measured polarization data by fitting with a suitable model. Ellipsometry thus determines the extinction coefficient κ , which is related to the absorption coefficient by Eq. (1.10). The method is applicable in the wavelength range where the extinction coefficient is large enough to be measured. For silicon, this corresponds to wavelengths below approximately 950 nm. In this work, ellipsometric measurements are used for the determination of the absorption coefficient in the wavelength range from 250 to 930 nm.

2.4.1 Principle of measurements

A plain wave incident onto a surface can be divided into a component $E_{p,i}$ parallel to the plane of incidence and a component $E_{s,i}$ perpendicular to the plane of incidence, as visualized in Fig. 2.37. The phase difference between the components of the incoming wave $E_{p,i}$ and $E_{s,i}$ is δ_i , the phase difference between the components of the outgoing wave $E_{p,o}$ and $E_{s,o}$ is δ_o . A parameter

$$\Delta = \delta_i - \delta_o . \quad (2.78)$$

can be defined as the change in phase difference due to the reflection at the surface.

The reflection coefficient for the parallel component of the wave is $r_p = E_{p,o}/E_{p,i}$. For the perpendicular component, the reflection coefficient r_s is defined analogously. A quantity Ψ can be defined such that

$$\tan \Psi = \frac{|r_p|}{|r_s|} . \quad (2.79)$$

Using the quantities Δ and Ψ as defined above, the fundamental equation of ellipsometry is given by [98]

$$\frac{r_p}{r_s} = \tan \Psi \exp(i\Delta) \quad (2.80)$$

where i is the imaginary number. The spectroscopic ellipsometer used in this work measures Ψ and Δ as a function of wavelength λ and the angle of incidence γ . The coefficients r_p and r_s are related to the complex index of refraction by the specific optical model of the sample (layer stack) that is assumed. The model parameters are determined by fitting the model to the measured data of $\Psi(\gamma)$ and $\Delta(\gamma)$ for each wavelength λ_i , which yields the complex index of refraction $\hat{n}(\lambda_i)$. The absorption coefficient then follows from Eq. (1.10). In order to obtain smooth, Kramers-Kronig consistent data curves, a dispersion relation parameterizing the dielectric function of the sample can be fitted to these values. The fit can be extended to longer wavelengths by also taking transmittance data into account. Further details on ellipsometric measurements are found in the standard literature, e.g., Ref. 99.

The model of the layer stack which is used in this work is visualized in Fig. 2.37. It assumes a planar silicon slab of thickness W which is covered by a thin layer of silicon oxide of thickness W_{SiO_2} (which is of the order of 2 nm [100]). The oxide layer is assumed since the samples are handled in air and the formation of an oxide layer cannot be prevented. The model further assumes that no light is reflected at the rear surface of the sample (which is equal to the assumption that only light which is reflected at the front surface of the sample is collected by the detector). This assumption is justified within the wavelength range analyzed by ellipsometric measurements, since all light entering the sample is absorbed. The thickness W is measured using a dial gauge and assuming $W_{\text{SiO}_2} \approx 0$. The oxide

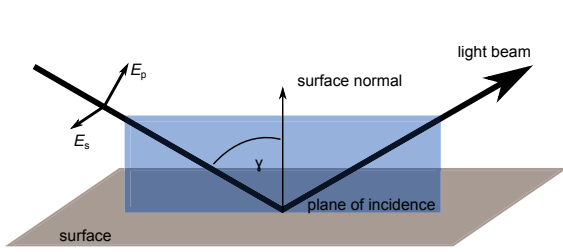


Figure 2.37: Schematic of the reflection of a planar wave at a surface.

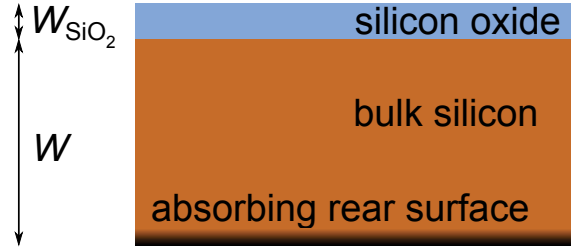


Figure 2.38: Optical model of the samples which is used in this work (not to scale).

thickness is determined from a fit of the data at wavelengths between 1200 and 1400 nm, where the absorptance of the silicon bulk is approximately zero. Measurements are taken at angles of incidence of 60° , 65° , 70° , 75° and 80° . The dispersion relation which is used to obtain a smooth Kramers-Kronig consistent data curve consists of a superposition of 5 Tauc-Lorentz oscillators and 2 gaussian shaped oscillators [101, 102].

2.4.2 Setup and samples for measurements

The measurements presented in this work are carried out with a commercially available M-2000 UI ellipsometer manufactured by J. A. Woolam Co., Inc. This instrument is capable of measuring Ψ and Δ under various angles of incidence. It is equipped with two detectors (silicon and InGaAs) and allows for measurements within the wavelength range from 240 to 1700 nm. The sample is placed on a temperature controlled sample stage. It is illuminated with white light from a halogen lamp which is spectrally decomposed after interaction with the sample by a diffraction grating. The instrument is calibrated with respect to wavelength and polarization using the standard procedure recommended by the manufacturer. The acquisition and evaluation of the measured data is performed using the software VWASE [102]. The evaluation procedure consists of fitting the measured angle dependent data ($\Psi(\gamma_j)$ and $\Delta(\gamma_j)$) with a model of the dielectric function separately for each wavelength. This fit is referred to as *wavelength-by-wavelength fit*. In a second step, the values of the dielectric function at each wavelength so obtained can be fitted with a dispersion relation (referred to as *function fit*). The measurements are carried out on the samples which are used for reflectance/transmittance measurements (see section 2.1.3). For the measurements, the samples are placed on a temperature controlled chuck. The sample temperature for the ellipsometric measurements is (295 ± 1) K.

2.4.3 Evaluation procedure

The measurements yield the parameters Ψ and Δ as a function of wavelength and for various angles of incidence. From this data, the dielectric function is obtained by nonlinear parameter estimation for each wavelength λ_i . Specifically, the fit procedure used in VWASE consists of minimizing

$$\chi^2(\lambda_i) = \frac{1}{2N - m} \sum_{j=1}^N \left[\frac{(\Psi_{\text{exp}}(\lambda_i, \gamma_j) - \Psi_{\text{mod}}(\lambda_i, \gamma_j, \vec{p}))^2}{u^2(\Psi_{\text{exp}}(\lambda_i, \gamma_j))} + \frac{(\Delta_{\text{exp}}(\lambda_i, \gamma_j) - \Delta_{\text{mod}}(\lambda_i, \gamma_j, \vec{p}))^2}{u^2(\Delta_{\text{exp}}(\lambda_i, \gamma_j))} \right] \quad (2.81)$$

using the Levenberg-Marquard algorithm [103]. In the latter equation, N is the number of angles γ , m is the number of parameters obtained from the fit, Ψ_{exp} and Δ_{exp} are the experimental data points and Ψ_{mod} and Δ_{mod} are the corresponding calculated data points which depend on the angle γ_j and the model parameters indicated by the vector \vec{p} . For the measurements in this work, $N = 5$ and $m = 2$ holds. By default, VWASE uses type A uncertainties determined from repeated measurements of Ψ and Δ for $u^2(\Psi_{\text{exp}})$ and $u^2(\Delta_{\text{exp}})$. For the data presented in this work, other (type B) contributions

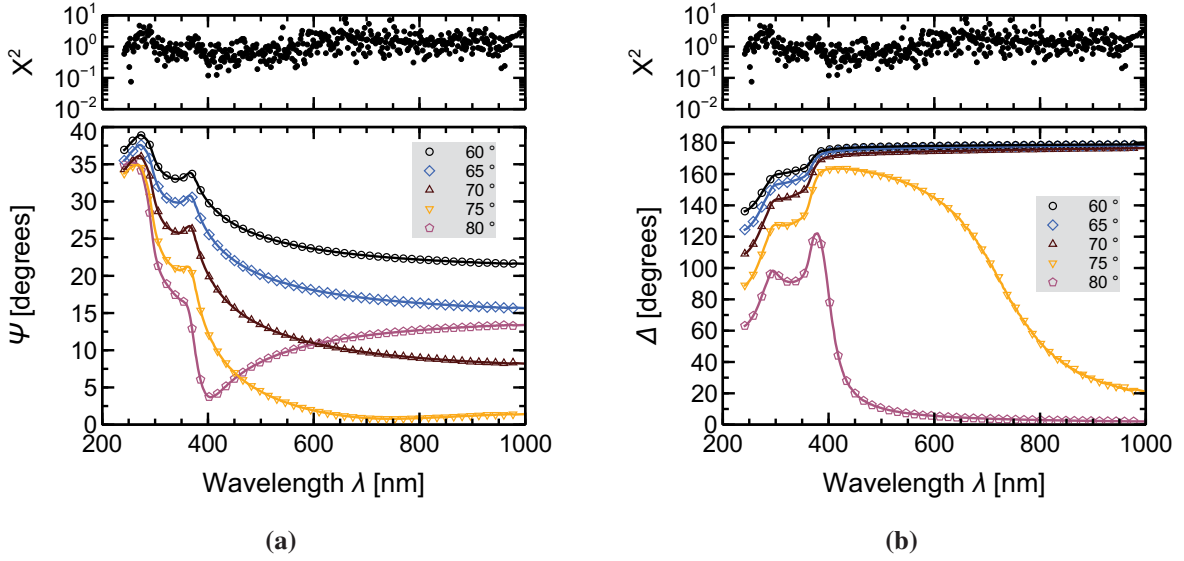


Figure 2.39: Measured and modeled data of Ψ (a) and Δ (b) as a function of wavelength and for different angles of incidence. The solid lines represent the calculated values. The top graphs show χ^2 calculated according to Eq. (2.81) using $N = 5$ and $m = 2$.

are also taken into account by the analysis outlined in the following sections. The quantities Ψ_{mod} and Δ_{mod} are calculated from the model of the dielectric function $\epsilon(\lambda_i, \vec{p})$. Figure 2.39 shows the measured data of Ψ and Δ together with the corresponding model curves as a function of wavelength. From $\epsilon(\lambda_i, \vec{p})$, the extinction coefficient κ is calculated using Eq. (??). The extinction coefficient is related to the absorption coefficient by Eq. (1.10).

2.4.4 Monte-Carlo simulation for the analysis of measurement uncertainty

The evaluation of the absorption coefficient from measured data of Ψ and Δ involves a fitting procedure. Therefore, uncertainties of Ψ and Δ cannot be propagated into the uncertainty of the absorption coefficient by using the analytical approach described in section 1.3. A *Monte-Carlo simulation* as described in the GUM [66, supplement 1] is a numerical approach for solving this task. Basically, it consists of many recalculations of the output quantity. On each iteration, all input quantities are randomly varied according to their probability distribution and a specific value of the output quantity is obtained. By calculation of the average and standard deviation of the output quantity, its value and uncertainty are determined. The Monte-Carlo approach has the advantage that it does not require an analytical process equation, which is not possible in case of fitting algorithms. Moreover, it easily allows to take correlations between input quantities into account and directly yields the probability distribution of the output quantity. On the other hand, Monte-Carlo simulations can be time-consuming and the significance of the single uncertainty contributions is not as easily evaluated as with the analytical approach. For the purpose of propagating the uncertainties of Ψ and Δ into the uncertainty of the absorption coefficient, however, only the Monte-Carlo approach is feasible.

The software WVASE is not capable of conducting such an analysis. The Monte-Carlo simulation is thus realized by generating the simulated (randomly varied) input data Ψ_{exp} and Δ_{exp} in Excel, loading the data into WVASE, executing the fit procedure in WVASE and exporting the resulting n and κ data to Excel again, where the standard deviations for n and κ are finally calculated. This procedure is quite slow, one iteration takes about 30 s. For this reason, the simulation is terminated after 10000 iterations, which corresponds to about five days of calculation time. On each iteration, WVASE returns 1162 values (n and κ at 581 wavelengths). In order to handle this large amount of

data, only the sums $\sum x_i$ and $\sum x_i^2$, $x = \{n, \kappa\}$, are stored for each wavelength. From these values, the standard deviation is obtained by using the relation

$$\sum_{i=1}^N (x_i - \bar{x})^2 = \left(\sum_{i=1}^N x_i^2 \right) - \frac{1}{N} \left(\sum_{i=1}^N x_i \right)^2, \quad (2.82)$$

which does not require the average \bar{x} to be known in advance.

2.4.5 Uncertainty contributions

Uncertainties of the absorption coefficient data resulting from spectroscopic ellipsometry arise from the type A uncertainties of the measurands Ψ and Δ , which are routinely calculated by WVASE, but also from other contributions which are not taken into account by the standard procedure in WVASE. In the following, other uncertainty contributions are discussed and quantitative estimates are given. Afterwards, the inclusion of these contributions in the uncertainty analysis is described.

Inappropriate model of the sample: A key component for the evaluation of an ellipsometric measurement is the optical model of the sample that is assumed. This model must reflect the real physical properties of the sample under investigation. An inappropriate model leads to systematic deviations of the parameters obtained from the fit. If only statistically distributed deviations occur during the measurement, χ^2 as defined in Eq. (2.81) will tend to unity or below. Hence, a value of $\chi^2 \gg 1$ indicates that systematic effects like an inappropriate model disturb the evaluation. In this case, the values obtained from the evaluation should be discarded.

The structure of the samples investigated for the determination of the absorption coefficient is simple. It consists of the bulk material (silicon) and a thin cover layer (SiO_2). This structure is reflected by the optical model. The thickness of the cover layer is obtained from the fit. Due to the simplicity of the optical model, it is assumed that the model is correct and that there are no uncertainty contributions due to the model. This assumption is supported by the finding $\chi \approx 1$, whereas χ would be expected to be much larger if the model was an inappropriate description of the sample.

Optical properties of SiO_2 : Handling of silicon samples in air leads to the formation of a SiO_2 layer on the surfaces of the silicon sample. This layer changes the optical properties of the sample and must therefore be included in the optical model which is used for the evaluation of the data. For this purpose, optical constants of SiO_2 are retrieved from the literature [30, 104, 105]. This data is visualized in Fig. 2.40 and shows deviations of the order of 0.4 % relative. The uncertainty of the extinction coefficient κ due to the choice of literature data of SiO_2 is estimated by performing the evaluation procedure with each of the data sets for SiO_2 mentioned above. The standard deviation of the resulting extinction coefficient data, which is shown in Fig. 2.41, is taken as the uncertainty contribution due to the choice of literature data of SiO_2 .

Wavelength accuracy: Deviations $\delta\lambda$ between nominal and actual wavelength affect the resulting Ψ and Δ data. For the ellipsometer used in this work, the wavelength accuracy cannot be measured easily, but from experience, $\delta\lambda \leq 0.5$ nm after calibration of the instrument. The uncertainty due to wavelength accuracy is estimated by Eq. (2.14).

Spectral bandwidth: Limited spectral bandwidth affects the measured data of Ψ and Δ . As for the wavelength accuracy, the spectral bandwidth cannot be measured precisely. From experience with other, similar detectors, it is therefore estimated to be 5 nm for the silicon detector and 10 nm for the InGaAs detector. The uncertainty contribution is estimated using Eq. (2.13) and included into the Monte-Carlo simulation (see below) in order to obtain the resulting uncertainty of the absorption coefficient.

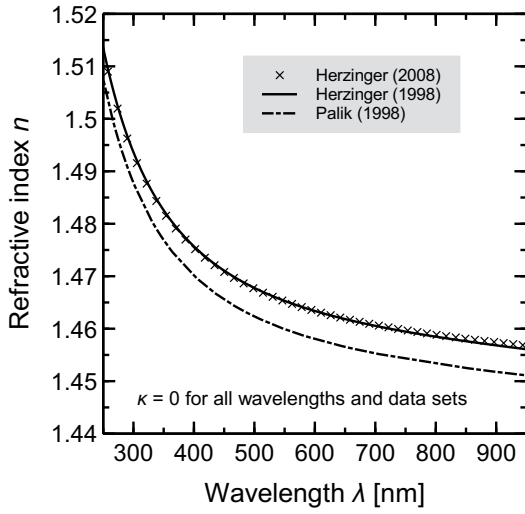


Figure 2.40: Optical constants of SiO₂ given by Refs. 30, 104, 105.

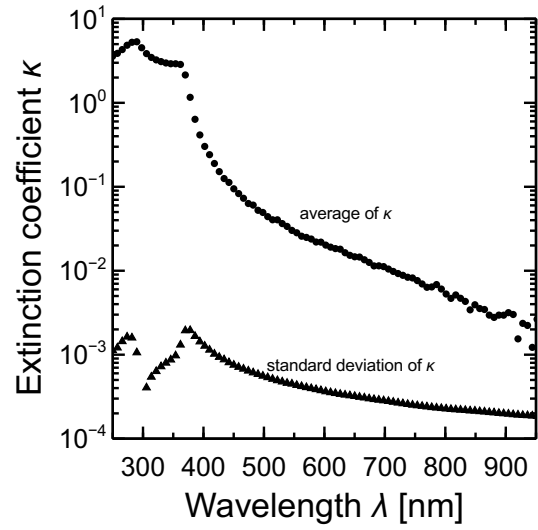


Figure 2.41: Resulting extinction coefficient κ of silicon using the different SiO₂ data from Fig. 2.40.

Angle of incidence: Ψ and Δ are measured for different angles of incidence γ_i . Deviations between the nominal value of γ_i and the real value during the measurement affect the evaluation of the data according to Eq. (2.81). The angle of incidence is controlled using a micrometer gauge. The different angles γ_i may be correlated, since an offset of the micrometer gauge would cause all angles to deviate in the same direction. In contrast, limited accuracy of the micrometer gauge may cause random deviations for each angle γ_i . Both effects are taken into account by including the uncertainty of the angle of incidence into the Monte-Carlo simulation. For this purpose, γ_i is varied according to

$$\gamma_i = \gamma_{i,0} + O + \delta(\gamma_{i,0}) \quad (2.83)$$

where $\gamma_{i,0}$ is the nominal value of γ_i ,

$$-0.02^\circ \leq O \leq 0.02^\circ \quad (2.84)$$

is an offset equal for all angles γ_i and

$$-0.01^\circ \leq \delta(\gamma_{i,0}) \leq 0.01^\circ \quad (2.85)$$

is a random deviation for each angle γ_i that represents the limited accuracy of the micrometer gauge. Both O and $\delta(\gamma_{i,0})$ are assumed to be rectangularly distributed. The choice of the boundaries for O and $\delta(\gamma_{i,0})$ follows from Ref. 106, stating that the angle of incidence can usually not be controlled to better than 0.02° . Moreover, fits of the data are carried out where the angle of incidence is used as a fit parameter. The angles returned by the fit deviate from the nominal angle by about 0.01° on average.

Other setup or sample dependent effects: Additional uncertainty can be introduced by specific properties of the sample and the measurement instrumentation, e.g., due to the alignment of optical components, nonlinearities of the detector or depolarization of light by the sample. These effects cannot be measured or quantified rigorously for the instrument used in this work. Depolarization effects are unlikely to occur since the sample's surfaces are polished. The proper alignment of the optical components is ensured by the mechanical construction and the calibration procedure of the instrument. As for typical detectors, nonlinearities of the instrument's detectors are expected to be of the order of 0.25 % rel. of the measurand [76, 106]. In order to take these systematic, setup and

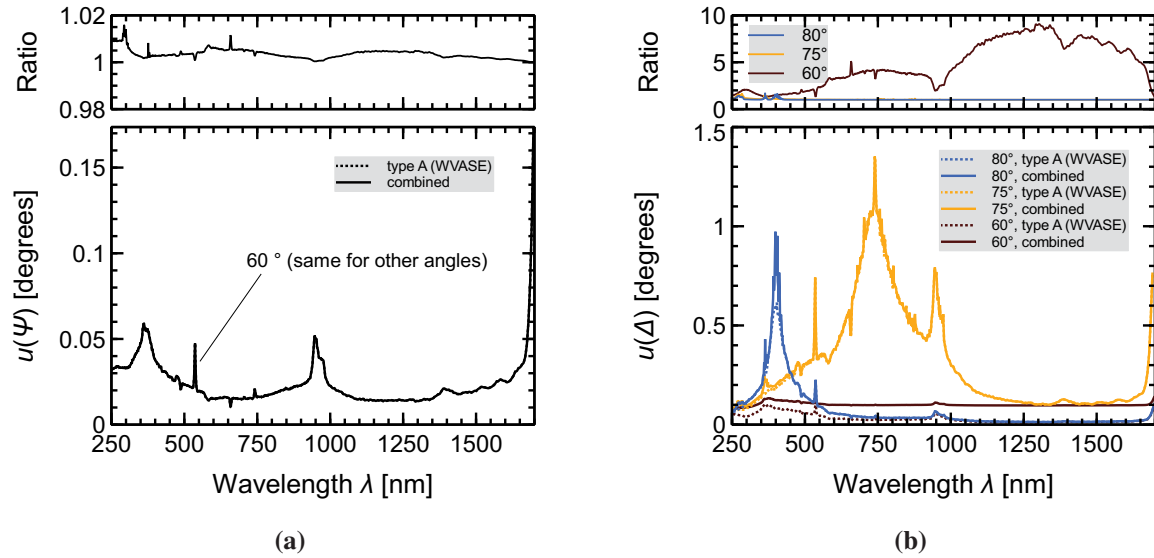


Figure 2.42: Comparison of type A and combined type A and B uncertainties for Ψ and Δ . To improve readability, figure (b) does not show the curves for 65° and 70° , which coincide with the curves for 60° .

sample dependent effects into account, they are subsumed into a rectangularly distributed uncertainty contribution

$$u_{\text{rep}}^2 = \frac{(M \times 0.003)}{3} \quad (2.86)$$

which is globally applied and describes the reproducibility of measurements. In the latter equation, M is the measurand (Ψ or Δ). This uncertainty contribution is included into the Monte-Carlo simulation in order to obtain the resulting uncertainty of the absorption coefficient.

The mentioned type B uncertainty contributions are combined with the type A uncertainties returned from WVASE according to Eq. (1.25), except for the contribution due to the angle of incidence. These combined uncertainties $u_c(\Psi)$ and $u_c(\Delta)$ are used as input for the Monte-Carlo simulation. The uncertainty of the angle of incidence is directly taken into account by the Monte-Carlo simulation as described above. Figure 2.42 compares the type A uncertainties of Ψ and Δ as returned from WVASE to the combined uncertainties $u_c(\Psi)$ and $u_c(\Delta)$ for both quantities. For Ψ , the combined uncertainties are not significantly increased, independent from the angle of incidence. For this reason, only the curves for 60° are shown, which coincides with the curves for the other angles. For Δ , the combined uncertainty is notably larger for angles of 60° , 65° and 70° . As these curves coincide, Fig. 2.42 (b) only shows the curves for 60° .

2.4.6 Results

Figure 2.43 shows the extinction coefficient κ (represented by the black dots) which is the average of the data generated by the Monte-Carlo simulation. The blue dots visualize the contribution to the uncertainty of κ resulting from the Monte-Carlo simulation. This data includes contribution from measurement noise (type A), wavelength accuracy (type B), spectral bandwidth (type B), angle of incidence (type B) and reproducibility (type B). The brown dots visualize the contribution due to the uncertainty of the SiO_2 literature data. As can be seen, the uncertainty contribution due to SiO_2 input data is about a factor 4 smaller than the uncertainty contribution resulting from the Monte-Carlo

simulation and thus does not dominate the overall uncertainty. Together with Fig. 2.42, it can be concluded that the uncertainty of κ is dominated by the type A uncertainty due to measurement noise, as adding the other type B contributions does not lead to a large increase of the uncertainties of Ψ and Δ for most of the data.

Figure 2.44 shows the resulting absorption coefficient and its uncertainty. The blue dots represent the data obtained from the Monte-Carlo simulation, the brown triangles represent the data returned by WVASE (wavelength-by-wavelength fit). For comparison, reflectance/transmittance data is visualized by the black squares. The yellow line visualizes the function fit of the brown triangles returned by WVASE. The uncertainty of the data for $k = 2$ obtained from the Monte-Carlo simulation is represented by the dotted line and also visualized by the colored area. It increases from 0.2 % at 300 nm to 12 % at 600 nm and 100 % at 900 nm.

The analysis shows that the ellipsometric determination of the absorption coefficient between 800 and 1000 nm is subject to uncertainties notably above 10 % relative. This is directly visible by the scattering of the data (blue dots/brown triangles), indicating a low signal-to-noise ratio. Fitting the data with a dispersion relation (yellow line) leads to a smooth data curve, which, however, does not agree with the data resulting from reflectance/transmittance measurements. The latter data is very accurate at wavelengths around 930 nm. The result of the function fit is thus questionable in this region. Moreover, the Monte-Carlo data differs slightly from that returned by the wavelength-by-wavelength fit, showing that the standard procedure tends to overestimate the absorption coefficient. Note that this issue is correctly reflected by the large uncertainty of the data in this region. In order to resolve the mismatch between the function fit and the reflectance/transmittance data, another parametrization is applied by fitting both ellipsometer and reflectance/transmittance data with Eq. (1.16) in the wavelength range from 650 to 1050 nm. This parametrization is represented by the red line in Fig. 2.44 and shows good agreement with the function fit at 650 nm and the reflectance/transmittance data at 930 nm. Therefore, it seems reasonable to use this parametrization as the best estimate of the absorption coefficient between 650 and 930 nm. The uncertainty of this parametrization cannot be determined rigorously. The fit procedure returns confidence limits for the fit parameters, but these cannot be interpreted in terms of realistic uncertainty estimates of the absorption coefficient obtained from the parametrization, as they only refer to deviations between model and data. The calculation of confidence limits for fit parameters and their interpretation is described in more details in the standard literature [99, 103]. It is reasonable to assume that the uncertainty of the parametrization is equal to the uncertainty of the data at 650 and 930 nm. In the intermediate region, the uncertainty should be a continuous function of the wavelength. Since no further information is available, a linear interpolation between the uncertainties at 650 and 930 nm is performed and used as an estimate for the uncertainty of the absorption coefficient. This curve is represented by the red dotted line in Fig. 2.44. At wavelengths below 930 nm, free carrier absorption can be neglected (see Fig. 1.5). The absorption coefficient determined by spectroscopic ellipsometry is therefore equal to the coefficient of band-to-band absorption α_{bb} and corrections for FCA are not necessary (see chapter 3). Figure 2.45 shows the resulting data for the coefficient of band-to-band absorption of crystalline silicon at 295 K and its uncertainty. Tabulated data is given in appendix D.

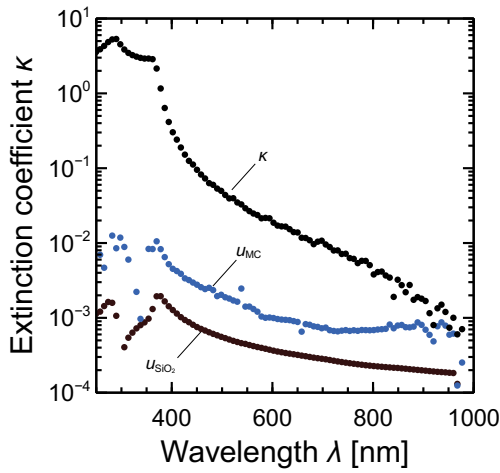


Figure 2.43: Extinction coefficient κ as obtained from the Monte-Carlo simulation and contributions to its uncertainty resulting from the Monte-Carlo simulation and from the uncertainty of the SiO_2 input data.

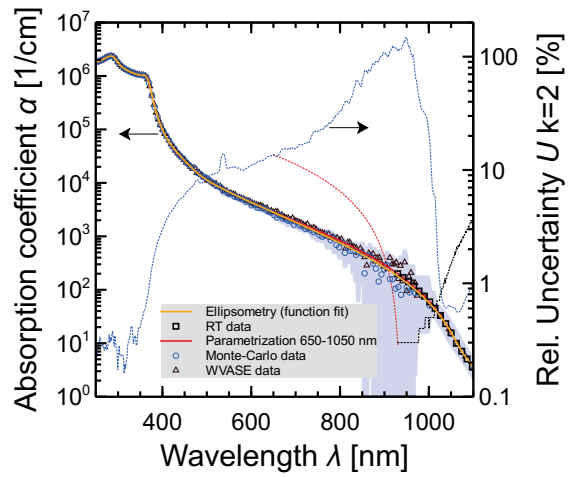


Figure 2.44: Absorption coefficient α_{bb} and uncertainty resulting from the data of Fig. 2.43. For comparison, the data resulting from reflectance/transmittance measurements is also shown.

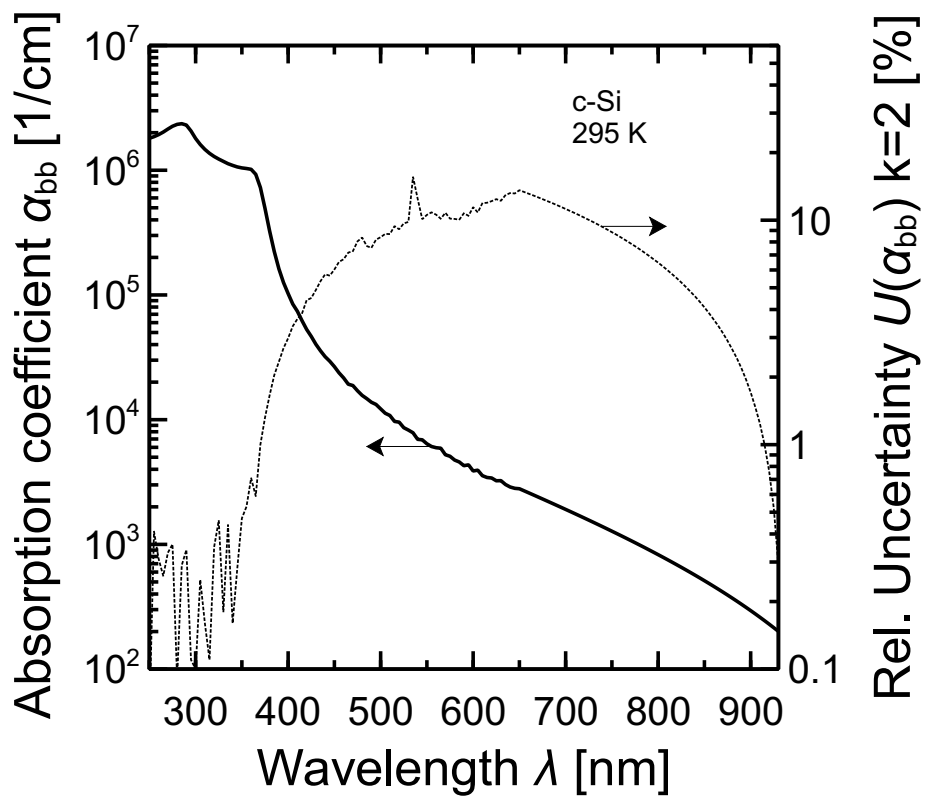


Figure 2.45: Coefficient of band-to-band absorption α_{bb} of crystalline silicon at 295 K as determined from spectroscopic ellipsometry.

Analysis of measured data

This chapter describes the calculation of a combined data set for the coefficient of band-to-band absorption and its uncertainty from the results of the preceding chapter. Corrections for free carrier absorption are discussed for the different samples and measurement approaches. Experimental evidence is given that luminescence and spectral responsivity measurements yield the same results. The final data of the coefficient of band-to-band absorption of crystalline silicon at 295 K is presented. Deviations to the most recent data from literature which is available for this temperature are of the order of 10 to 30% rel. The deviations are only partly explainable by the uncertainty of the data determined in this work, pointing towards systematic effects as the origin of the deviations.

The data of the absorption coefficient presented in the preceding chapter is obtained not only from different methods, but also from measurements on different samples and using different measurement setups at different institutions. It is desirable to combine these data into one set of data. The standard approach for combining different measurements of the same quantity is the calculation of a weighted average, the weights being given by the inverse squared uncertainty of the single measurement results. The uncertainty of the weighted average is usually calculated as the inverse sum of these weights, based on the assumption that the single results are uncorrelated. This assumption is questionable, for instance, if different data sets which are to be averaged are obtained using the same measurement setup, as is the case for some of the measurements carried out in this work. The first part of this chapter therefore discusses the calculation of a weighted average from the results of the different measurements with respect to the possibility of correlations between the measurements. Moreover, in order to determine the coefficient of band-to-band absorption, the correction of the data for free carrier absorption is discussed. The second part of this chapter is concerned with the temperature dependence of the absorption coefficient. Due to temperature dependent band gap narrowing, the temperature dependence is pronounced especially in the near-band gap region around 1150 nm and beyond. Uncertainties of the sample temperature during the measurements increase the uncertainty of the absorption coefficient. Temperature coefficients for the data resulting from ellipsometric measurements at different sample temperatures carried out in this work as well as data from literature are given and discussed. The uncertainty of the absorption coefficient due to sample temperature is evaluated. On the basis of the derived combined data and the uncertainty due to variations of temperature, the last part of this chapter presents the final data set of the coefficient of band-to-band absorption and its uncertainty at 295 K and summarizes the formulas and temperature coefficients required for the transformation of the data to other temperatures. It compares the results of this work to data from literature and discusses deviations.

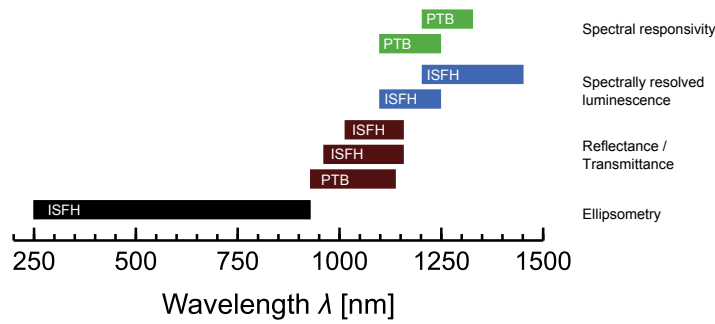


Figure 3.1: Overview of the different methods for measuring the absorption coefficient that are applied in this work.

3.1 Combined data of the coefficient of band-to-band absorption

The absorption coefficient varies by about 15 orders of magnitude between 250 and 1450 nm. Since no method is capable of covering this wavelength range completely, different methods must be used for measuring the absorption coefficient. Figure 3.1 shows an overview of the methods used in this work and the wavelength range where they are applied. The data between 250 and 930 nm result from ellipsometric measurements. In the wavelength range from 930 to 1160 nm, data from reflectance and transmittance measurements at ISFH as well as at the PTB is available. The wavelength range above 1100 nm is covered by spectrally resolved luminescence measurements at ISFH as well as spectral responsivity measurements at the PTB. From the different data, one combined data set of the absorption coefficient is determined by calculating a weighted average of the measured data, taking the possibility of correlations between the data into account. Moreover, corrections for free carrier absorption are applied.

3.1.1 Ellipsometry data

Ellipsometry data is available from measurements carried out at ISFH in the wavelength range from 250 to 930 nm. For the samples used in this work, the coefficient of free carrier absorption α_{fc} following from the FCA parametrization introduced in section 1.2.4 is below 10^{-2} cm^{-1} in this wavelength range, whereas the absorption coefficient is of the order of 10^2 to 10^6 cm^{-1} . Hence, $\alpha \approx \alpha_{bb}$ and corrections for FCA are not applied, since they are of the order of 0.01% rel. at most.

3.1.2 Reflectance/Transmittance data

Reflectance/transmittance measurements at ISFH are carried out on two different samples of different thickness. Additionally, measurements on two samples from the same wafers are carried out and combined into one data set by the PTB. Hence, a weighted average of three data sets (see Fig. 2.16) needs to be calculated. The two data sets measured at ISFH might contain hidden correlations, since the same setup is used for the measurements. The procedure for obtaining a weighted average thus consists of first calculating a weighted average of the two data sets measured at ISFH, which takes the hidden correlations into account. In a second step, the averaged data is combined with that measured at the PTB.

The approach for incorporating hidden correlations into the uncertainty of the weighted average is described in section 1.3.7. Figure 3.2 shows the uncertainty of the weighted average obtained by assuming uncorrelated data (lower limit), fully correlated data (upper limit) and hidden correlations. The limits are visualized by the dotted lines, the uncertainty assuming hidden correlations is represented by the open circles. The crosses show the value of χ^2 . For wavelengths below 1110 nm, only

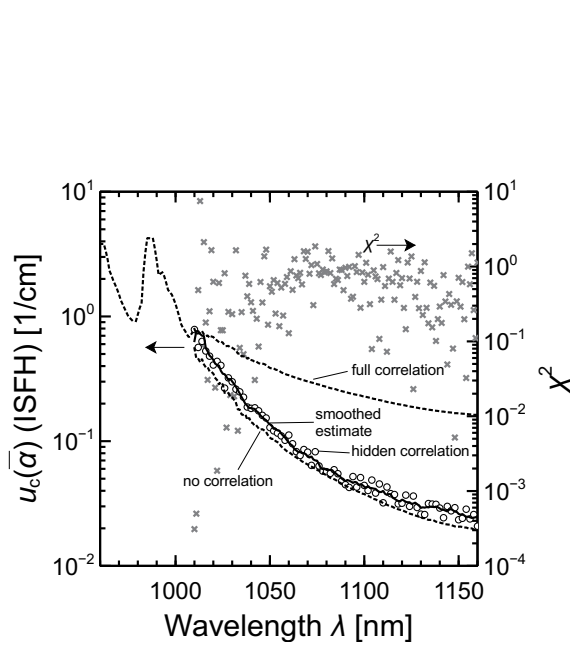


Figure 3.2: Uncertainty of the weighted average assuming hidden correlations compared to the uncertainties assuming no correlation and full correlation of the data. Below 1110 nm, only data of the thinner wafer is available (indicated by the dotted lines).

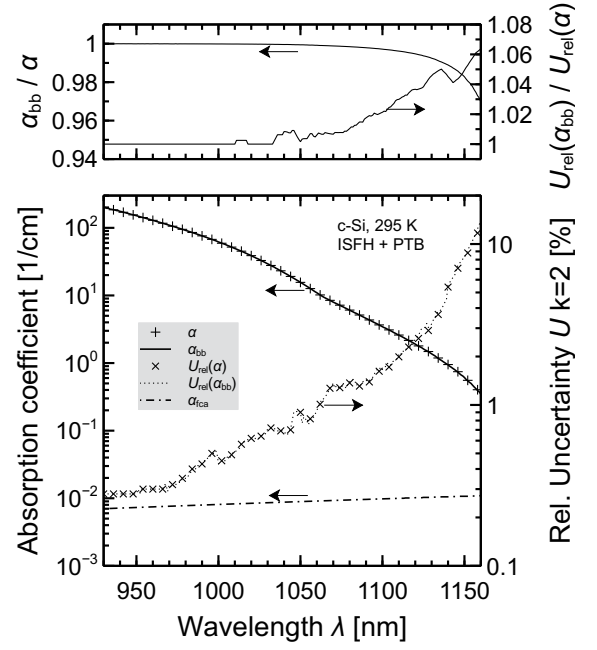


Figure 3.3: Final data of the coefficient of band-to-band absorption of crystalline silicon at 295 K as resulting from measurements of reflectance and transmittance carried out by ISFH and PTB.

data of the thinner wafer is available (visualized by the dotted lines). For the majority of the data, $\chi^2 < N - 1 = 1$ holds. This supports the assumption that the uncertainties of both data sets are partly correlated. However, the analysis shows that the uncertainty assuming hidden correlations is still close to the lower limit. Assuming full correlation of the data would thus lead to a significant overestimation of the uncertainty. The scattering of the data is due to the scattering of χ^2 , which is caused by the small number of data $N = 2$. The assumption that the uncertainty varies smoothly as a function of wavelength suggests the calculation of a smoothed estimate, which is visualized by the solid line in Fig. 3.2. Using this estimate and the data provided by PTB, the final data of the absorption coefficient is obtained using Eqs. (1.32) and (1.33).

Measurements of reflectance and transmittance yield the absorption coefficient α , which contains contributions of both band-to-band absorption and free carrier absorption (FCA), as described in section 1.2.1. The coefficient of band-to-band absorption is thus given by $\alpha_{bb} = \alpha - \alpha_{fca}$. In order to determine the coefficient of band-to-band absorption α_{bb} , the FCA parametrization introduced in section 1.2.4 is used for a doping concentration of $3 \times 10^{15} \text{ cm}^{-3}$, which follows from the resistivity of the samples. The resulting data for α_{bb} is shown in Fig. 3.3. The top graph visualizes the ratio α_{bb}/α , showing that the relative correction below 1150 nm, where data from RT measurements is used, is below 2% and hardly visible on the logarithmic scale. As the accuracy of the FCA parametrization is unknown, the uncertainty of the correction is assumed to equal the correction itself and a rectangular distribution is assumed. The relative uncertainty of α_{bb} is thereby increased by about 0.2% absolute at 1140 nm. Hence, for the samples investigated by reflectance/transmittance measurements, the impact of FCA is not significant.

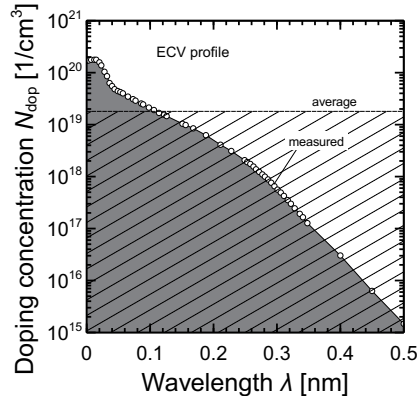


Figure 3.4: ECV profile of the emitter diffusion applied to the planar solar cells.

3.1.3 Luminescence/Spectral responsivity data

Luminescence and spectral responsivity measurements are carried out on various planar and textured samples. In general, both methods determine the coefficient of band-to-band absorption α_{bb} (see section 2.2.1). However, the measurands (photon flux or short circuit current) are affected by additional absorption due to free charge carriers. The incorporation of FCA into the evaluation of the data depends on the structure and doping concentration of the samples and is therefore discussed separately for the different samples investigated in this work.

FCA corrections

EL/SR measurements on planar solar cells: As luminescence and spectral responsivity data can be transformed vice versa by applying the reciprocity theorem (see section 2.3.1), the following discussion focuses on luminescence data but is also applicable for spectral responsivity data. The solar cells contain a highly doped emitter layer at the front surface, within which FCA is significantly increased compared to the bulk. This leads to an enhanced reabsorption of luminescence photons in the emitter and thereby to a reduction of the emitted photon flux. (In case of spectral responsivity measurements, this leads to a reduction of the generated short circuit current.) Figure 3.4 shows the doping concentration in the emitter as determined by electrochemical capacitance-voltage (ECV) measurements [107–110].

According to section 2.2.10, the absorption coefficient is evaluated by determining the absorbance of the silicon slab A_{Si} and scaling the luminescence data. In a second step, the absorption coefficient is then calculated from the scaled luminescence data. The determination of A_{Si} requires the determination of the rear surface reflectance R_b , which is obtained from the measured reflectance of the sample according to Eqs. (2.69) and (2.70). These equations do not account for additional reabsorption in the emitter due to FCA. However, as shown in appendix C.3, FCA in the emitter can be incorporated into the equations by adding multiplicative FCA terms A_{fc} . It is also shown that these extended equations are formally equal to the original equations (2.69) and (2.70) when replacing R_b by an effective rear surface reflectance $R_{b,eff}$ that contains the FCA terms A_{fc} . The meaning of this formal equality is that measurements of reflectance cannot distinguish between additional absorption in the emitter (due to FCA) and a decreased rear surface reflectance. On the other hand, evaluating the measured reflectance using Eqs. (2.69) and (2.70) means that as soon as additional absorption in the emitter is present, an effective rear surface reflectance is determined which accounts for the additional absorption in the emitter. FCA in the emitter is thus already taken into account by the evaluation procedure described in section 2.2.10 and further corrections are not necessary.

In order to evaluate the necessity of a correction of FCA in the bulk of the solar cell, the principle

of the determination of the absorption coefficient outlined in section 2.2.1 needs to be reviewed in more detail. The determination of the absorption coefficient from luminescence data is based on the luminescence integral Eq. (2.40),

$$\Phi(\lambda) \approx \alpha_{\text{bb}}(\lambda) \frac{8\pi c n_{\text{Si}}^2(\lambda)}{\lambda^4} \exp\left(-\frac{hc}{\lambda kT}\right) \int_0^W dz f_{\text{esc}}(\lambda, z) \exp\left(\frac{\mu_{\text{ph}}(z)}{kT}\right).$$

The photon escape probability f_{esc} for a planar sample of thickness W is (see appendix E.1)

$$f_{\text{esc}}(\lambda, z) = \frac{\Omega}{4\pi n_{\text{Si}}^2} (1 - R_{\text{f}}) \frac{R_{\text{b}} \exp(-\alpha(2W - z)) + \exp(-\alpha z)}{1 - R_{\text{b}} R_{\text{f}} \exp(-2\alpha W)}. \quad (3.1)$$

Ω denotes the solid angle into which the luminescence photons are emitted. In order to improve readability, the wavelength dependence of n_{Si} , R_{f} , R_{b} and α is not explicitly written. The reabsorption terms $\exp(-\alpha z)$ in the latter equation refer to both band-to-band and free carrier absorption and thus contain $\alpha = \alpha_{\text{bb}} + \alpha_{\text{fc}}$. Note that, as discussed above, FCA in the emitter is contained in the values of the rear surface reflectance R_{b} . In case of a homogeneous charge carrier distribution within the sample, the factor $\exp(\mu_{\text{ph}}(z)/kT)$ is independent from z and can be pulled out of the integral. As shown in section 2.2.10, this also holds for the solar cells. The remaining integral equals the absorptance A of the sample (Eq. (2.68)) divided by the absorption coefficient, giving

$$\Phi(\lambda) \propto \Phi_{\text{bb}}(\lambda) \alpha_{\text{bb}}(\lambda) \frac{A(\alpha, \lambda)}{\alpha(\lambda)}. \quad (3.2)$$

where

$$\Phi_{\text{bb}}(\lambda, \Omega) = \frac{2c}{\lambda^4} \exp\left(-\frac{hc}{\lambda kT}\right)$$

is the black body photon flux defined in Eq. (4.22). The proportionality factor is determined by dividing Φ by Φ_{bb} and scaling this data to the absorptance data in the wavelength range of overlap of reflectance/transmittance and luminescence data (1100 to 1140 nm). The scaled luminescence data Φ divided by Φ_{bb} is referred to as A_{lum} in the following. Using this definition, Eq. (3.2) reads

$$A_{\text{lum}}(\lambda) = \alpha_{\text{bb}}(\lambda) \frac{A(\alpha, \lambda)}{\alpha(\lambda)}. \quad (3.3)$$

The absorption coefficient is determined from A_{lum} by the solution of the latter equation for the absorption coefficient. For this solution, three regimes can be distinguished:

1. Below 1140 nm, where the luminescence data is scaled to the reflectance/transmittance data, the coefficient of free carrier absorption in the bulk is about two orders of magnitude smaller than the coefficient of band-to-band absorption (see Fig. 3.3). Hence, the approximation

$$\frac{\alpha_{\text{bb}}}{\alpha} \approx \text{const} \quad (3.4)$$

holds, as the variation of α_{fc} with respect to λ is negligible compared to the variation of α_{bb} . With this, Eq. (3.3) becomes

$$A_{\text{lum}}(\lambda) \propto A(\alpha, \lambda). \quad (3.5)$$

The proportionality factor is contained in the experimentally determined scaling factor. Consequently, A_{lum} depends on both band-to-band and free carrier absorption. From the luminescence data A_{lum} , the absorption coefficient α then follows from the solution of Eq. (2.68),

$$\alpha = \frac{1}{W} \ln\left(\frac{-\sqrt{4R_{\text{b}}(R_{\text{f}}A_{\text{lum}}^2 + R_{\text{f}}^2A_{\text{lum}} - A_{\text{lum}}) + (R_{\text{f}} - 1)^2(R_{\text{b}} + 1)^2 - R_{\text{b}}R_{\text{f}} + R_{\text{f}} + R_{\text{b}} - 1}}{2(A_{\text{lum}} + R_{\text{f}} - 1)}\right), \quad (3.6)$$

and the coefficient of band-to-band absorption is given by $\alpha_{bb} = \alpha - \alpha_{fc}$. This is an intuitive result: In the wavelength range where the scaled luminescence and reflectance/transmittance data are equal, the same correction must be applied. Note that, as already discussed in the preceding section, this is a small correction due to $\alpha_{fc} \ll \alpha_{bb}$. Also, note that directly inserting the approximation $\alpha_{fc} \ll \alpha_{bb} \Rightarrow \alpha_{bb}/\alpha \approx 1$ (which is rougher than the approximation $\alpha_{bb}/\alpha \approx \text{const}$) into Eq. (3.3) yields $A_{lum} \approx A(\alpha_{bb})$. This reflects the fact that the FCA correction is small.

2. Above 1165 nm, the absorptance $A(\alpha)$ becomes proportional to α . This can be seen by a first order Taylor series expansion of Eq. (2.68) at $\alpha = 0$, giving

$$A \stackrel{\alpha \rightarrow 0}{\approx} \alpha W \frac{(R_b + 1)R_f - R_b - 1}{R_b R_f - 1}. \quad (3.7)$$

Figure 3.5 compares the approximation to the correct expression for the absorptance Eq. (2.68) and shows that above 1165 nm, the deviation of the approximation becomes invisible on the logarithmic scale. For the calculation, the experimentally determined values of R_b and R_f shown in Fig. 2.31 are used. Combining Eq. (3.7) and Eq. (3.2) leads to

$$A_{lum} \stackrel{\alpha \rightarrow 0}{\approx} \alpha_{bb} W \frac{(R_b + 1)R_f - R_b - 1}{R_b R_f - 1}. \quad (3.8)$$

Hence, above 1165 nm, A_{lum} depends on α_{bb} instead of α and Eq. (3.6) directly yields the coefficient of band-to-band absorption α_{bb} . Corrections for FCA are not required.

3. In the transition region between 1140 and 1165 nm, α as determined varies smoothly between the two regimes. In this region, the increasing correction factor of the first regime is compensated by the decreasing dependence of A_{lum} on α . Hence, a correction is necessary, but an analytic expression for the calculation of the correction cannot be obtained.

The three regimes described above are visualized in Fig. 3.6. In summary, the discussion shows that a correction for FCA in the emitter is not necessary as FCA in the emitter is taken into account by the experimentally determined rear surface reflectance. FCA in the bulk is corrected for wavelengths below 1140 nm by determining α_{fc} from the parametrization introduced in section 1.2.4 and subtracting α_{fc} from α as determined. Above 1165 nm, the data is not corrected. Between 1140 and 1165 nm, the correction cannot be calculated rigorously. For this reason, it is linearly interpolated between the correction at 1140 nm and zero at 1165 nm. Since the accuracy of the FCA parametrization is unknown, the correction itself is taken into account as a rectangularly distributed uncertainty component. The relative uncertainty of the corrected data is thereby increased by not more than 2% absolute compared to the uncorrected data for both EL and SR.

PL measurements on textured wafer: The evaluation of the PL data is based on Eq. (2.40), using that $f_{esc} \approx \text{const}$ with respect to the position of photon generation within the sample. This approximation holds if the absorption coefficient becomes small enough such that photon reabsorption is negligible. For the samples investigated in this work, this condition is fulfilled if $\alpha \leq 5 \times 10^{-2} \text{ cm}^{-1}$ which corresponds to $\lambda \geq 1200 \text{ nm}$. The remaining integral is then a constant with respect to wavelength, yielding $\Phi(\lambda)/\Phi_{bb}(\lambda) \propto \alpha_{bb}(\lambda)$. The proportionality factor is determined by scaling the PL data to α_{bb} as obtained from EL/SR measurements on planar solar cells between 1200 and 1250 nm and is thus not affected by FCA. Photon reabsorption within the sample is not affected by FCA either, since the coefficient of free carrier absorption α_{fc} is below $3 \times 10^{-2} \text{ cm}^{-1}$ for all wavelengths that are covered by PL and the condition mentioned above is always fulfilled. The PL measurements on textured wafers therefore yield α_{bb} directly and do not require any corrections for FCA.

SR measurements on textured solar cells: As for the PL measurements on textured wafers, the evaluation of SR measurements on textured solar cells is based on the approximation $SR(\lambda) \propto \alpha_{bb}(\lambda)$. However, the solar cells contain a highly doped emitter, within which FCA is strongly enhanced

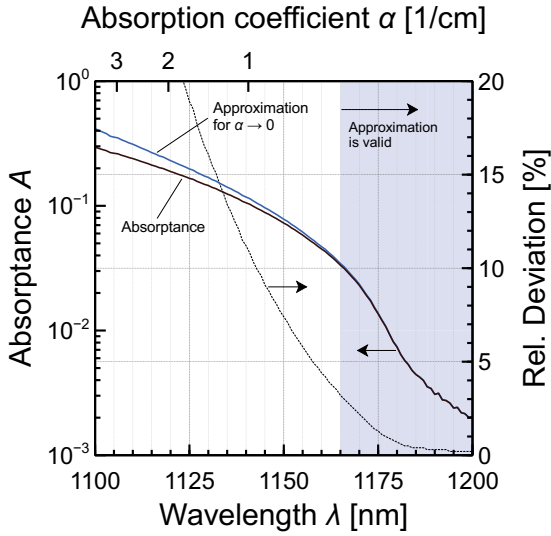


Figure 3.5: Comparison of the absorptance of the planar solar cell calculated from Eq. (2.68) and the approximation for $\alpha \rightarrow 0$ according to Eq. (3.7).

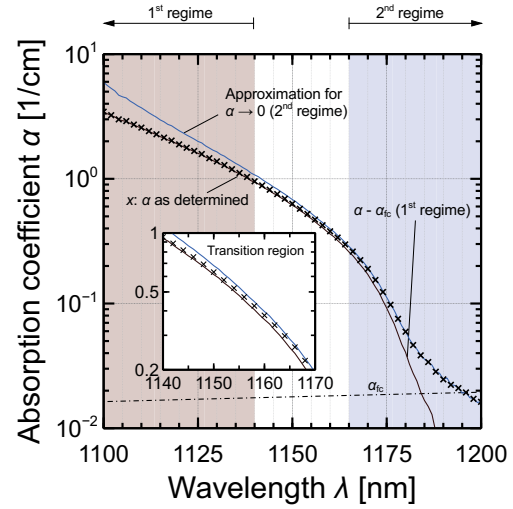


Figure 3.6: Comparison of the two correction regimes applicable for the absorption coefficient as determined from EL measurements.

compared to the bulk. Moreover, the solar cells feature a *back surface field* (BSF), which is a layer at the rear surface where the doping concentration is increased compared to the bulk. The purpose of a BSF is the shielding of minority charge carriers, which reduces recombination at the rear surface and thereby increases the energy conversion efficiency of the solar cell. FCA within the emitter and BSF decreases the short circuit current of the solar cell, which is the quantity actually measured, and thereby affects the absorption coefficient calculated from the SR data. This implies that unlike for the PL measurements on wafers, the scaling factor is not constant but must be increased towards longer wavelengths in order to compensate the increasing free carrier absorption, as outlined in appendix C.3. The required change of the scaling factor is estimated by using an analytical model for charge carrier generation from Ref. 111 (also see appendix C.3) and assuming an emitter with an average doping concentration of $5 \times 10^{19} \text{ cm}^{-3}$ and a thickness of $0.5 \mu\text{m}$, which are typical values for industrial solar cells. For the BSF, an average doping concentration of $4.5 \times 10^{18} \text{ cm}^{-3}$ and a thickness of $8 \mu\text{m}$ is assumed, which also represent typical values for industrial solar cells [112–114]. Figure 3.7 shows the result of this calculation (solid line). As only the change of the scaling factor is relevant, the data is normalized to the value at 1200 nm. The ratio of $C_{\text{scale}}(\lambda)$ and $C_{\text{scale}}(1200 \text{ nm})$ stays below 1.025 in the scaling region and increases to 1.07 at 1350 nm. Hence, assuming a constant scaling factor with respect to wavelength would imply an underestimation of α_{bb} by about 7% at 1350 nm. The wavelength dependence is approximately linear, which is shown by the dashed line, visualizing a linear fit of the data.

A correction of FCA in the emitter and BSF can be performed by multiplying the *EQE* with a wavelength dependent correction factor

$$f_{\text{fca}}(\lambda) = \frac{C_{\text{scale}}(\lambda)}{C_{\text{scale}}(1200 \text{ nm})}. \quad (3.9)$$

before calculating the scaling factor. This scaling factor will be denoted as C'_{scale} in the following in order to distinguish from the scaling factor C_{scale} which is obtained if the correction is not applied. The value of the correction factor f_{fca} is approximately

$$f_{\text{fca}}(\lambda) \approx 1 + (\lambda/\text{nm} - 1200) \times 0.00041035. \quad (3.10)$$

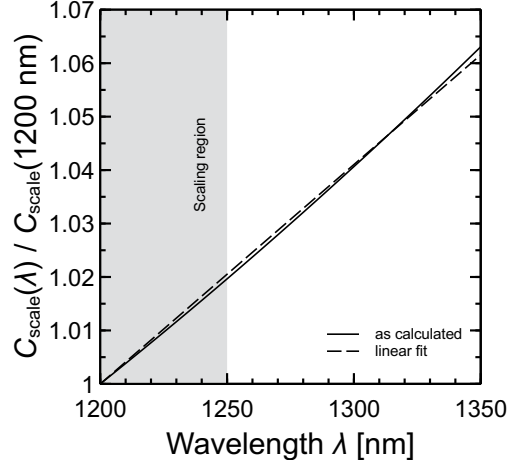


Figure 3.7: Increase of the scaling factor C_{scale} due to FCA in the emitter and BSF.

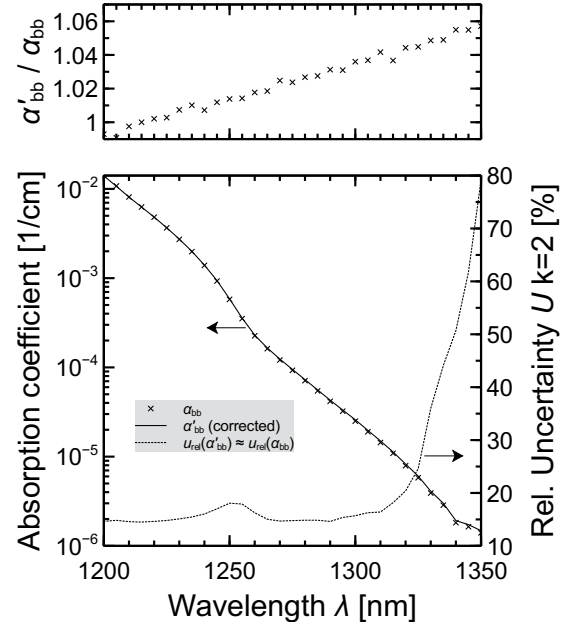


Figure 3.8: Impact of FCA correction for the SR data of the textured solar cell.

The corrected coefficient of band-to-band absorption α'_{bb} is then obtained by

$$\alpha'_{\text{bb}}(\lambda) = C'_{\text{scale}} \text{EQE}(\lambda) f_{\text{fca}}(\lambda) \approx \alpha_{\text{bb}}(\lambda) f_{\text{fca}}(\lambda). \quad (3.11)$$

The approximation $C'_{\text{scale}} \text{EQE}(\lambda) \approx \alpha_{\text{bb}}(\lambda)$ holds because $C'_{\text{scale}} \approx C_{\text{scale}}$ and $C_{\text{scale}} \text{EQE} = \alpha_{\text{bb}}$. The uncertainty of the correction is conservatively estimated by a rectangularly distributed contribution

$$u^2(f_{\text{fca}}) = \frac{(\alpha_{\text{bb}}(f_{\text{fca}} - 1))^2}{3}. \quad (3.12)$$

The contribution to the uncertainty of α'_{bb} due to $u(f_{\text{fca}})$ is about three orders of magnitude smaller than the contribution due to the uncertainty of the absorption coefficient $u(\alpha_{\text{bb}})$. The former is therefore neglected. The uncertainty of the corrected coefficient of band-to-band absorption is then

$$u(\alpha'_{\text{bb}}) \approx f_{\text{fca}} u(\alpha_{\text{bb}}). \quad (3.13)$$

Since $f_{\text{fca}} \approx 1$, the uncertainties of the corrected and uncorrected absorption coefficient are approximately equal. Figure 3.8 shows the impact of the FCA correction on the resulting absorption coefficient data. As can be seen, the correction is hardly visible on a logarithmic scale.

Verification of equality of luminescence/spectral response data

As described in section 2.3.1, luminescence and spectral response data are related to each other via a reciprocity theorem [73]. Therefore, both methods are expected to yield the same results for the absorption coefficient. The uncertainty analysis for the data presented in the preceding chapter allows this assumption to be verified quantitatively by considering the E_n criterion. Figure 3.9 shows the different data for the absorption coefficient obtained from EL and SR measurements on planar solar cells as well as PL measurements on a textured wafer and SR measurements on a textured solar cell. FCA corrections are applied to the data as described above. The top graph visualizes the E_n criterion

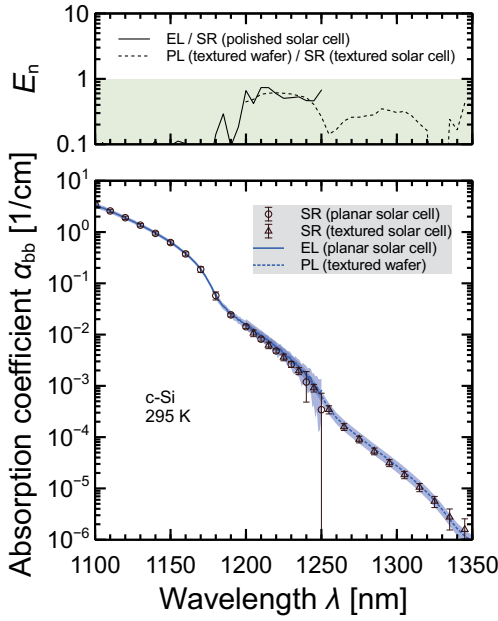


Figure 3.9: Comparison of absorption coefficient data obtained from EL/PL/SR measurements on planar and textured samples.

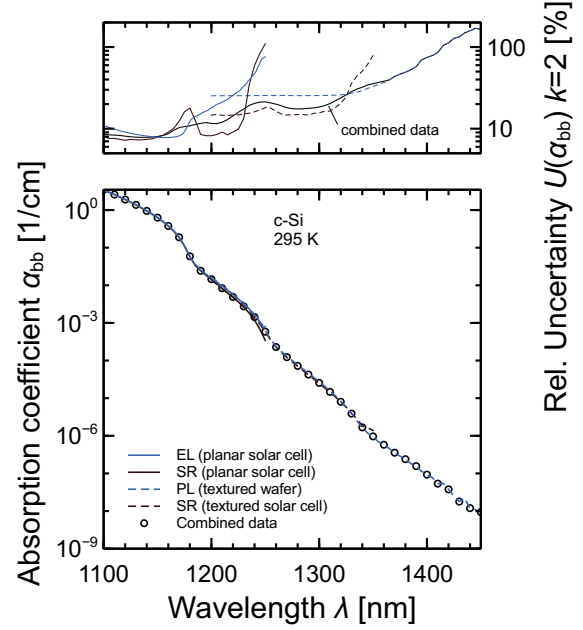


Figure 3.10: Combined data of the coefficient of band-to-band absorption obtained from luminescence and spectral responsivity measurements.

(see section 1.3.6), which is below unity for all wavelengths. Hence, the deviation between the data which is visible in Fig. 3.9 is explained by the uncertainty of the measurements. This provides experimental evidence that both methods yield the same results, although samples with different optical and electrical properties are used.

Combined luminescence/spectral response data

Having verified the equality of the data resulting from luminescence and spectral response measurements, the calculation of a weighted average is feasible. Both luminescence and spectral response data are scaled to the same data obtained from reflectance/transmittance measurements. The uncertainty of the weighted average is therefore calculated using Eq. (1.34), which assumes full correlation of the data. Figure 3.10 shows the averaged data. The relative uncertainty of the data is visualized in the top graph. It is of the order of 10% at 1200 nm, 20% at 1300 nm and 60% at 1400 nm.

3.2 Temperature dependence of the absorption coefficient

The sample temperature has an impact on the coefficient of band-to-band absorption, especially in the band gap region, due to the temperature dependence of the band gap energy as described in section 1.2.5. The uncertainty of the sample temperature during the measurement therefore causes an additional uncertainty contribution. In the vicinity of the nominal measurement temperature T_0 of 295 K, the absorption coefficient approximately obeys a linear relationship [32]

$$\alpha_{bb}(\lambda, T) \approx \alpha_{bb}(\lambda, T_0) [1 + c_T(\lambda) (T - T_0)], \quad (3.14)$$

where c_T is the temperature coefficient defined as

$$c_T(\lambda) = \frac{1}{\alpha_{bb}(\lambda, 295 \text{ K})} \left. \frac{d\alpha_{bb}(\lambda, T)}{dT} \right|_{295 \text{ K}}. \quad (3.15)$$

Several data of the temperature dependence have been published in the literature, e.g., Refs. 6, 13, 14 and 16. Based on these data, Green [32] calculated the temperature coefficient for the wavelength range from 250 to 1450 nm. Recently, new data of the temperature dependence in the near-band gap region (990-1300 nm) obtained by PL was published by the ANU [35]. In this work, the temperature coefficient is measured in the wavelength range from 250 to 990 nm using spectroscopic ellipsometry at different sample temperatures ranging from 295 K to 570 K. During these measurements, the sample is placed on a temperature controlled sample stage and the usual measurement and evaluation procedure as outlined in section 2.4 is carried out. For the determination of the temperature coefficient, absorption coefficient data from the wavelength-by-wavelength fit is used. Data from the function fit cannot be used since it incorporates transmittance measurements, which are, however, only carried out at room temperature in this work. The resulting temperature coefficient is shown in Fig. 3.11 together with the data from Refs. 32 and 35. Around 1200 nm, the shifting of the phonon structure is visible in the data from Ref. 35. The solid line represents the average of the measured data, which is used for further calculations in this work. The shaded area represents the standard deviation of the data. Tabulated data of the temperature coefficient is given in appendix D.

The estimation of the uncertainty contribution due to the temperature dependence of the absorption coefficient is based on Eq. (3.14). The nominal measurement temperature is $T_0 = 295$ K. The uncertainty of the sample temperature during the measurements is ± 0.5 K for luminescence and spectral responsivity measurements and ± 1 K for ellipsometry and reflectance/transmittance measurements. A rectangular distribution is assumed for the sample temperature. The resulting uncertainty contribution u_T^2 due to uncertainty of the temperature is

$$u_T^2 = (\alpha_{bb} c_T)^2 u^2(T_0) \quad (3.16)$$

with

$$u^2(T_0) = \begin{cases} \frac{(1 \text{ K})^2}{3} & \text{for ellipsometry/reflectance/transmittance,} \\ \frac{(0.5 \text{ K})^2}{3} & \text{for luminescence/spectral responsivity.} \end{cases} \quad (3.17)$$

3.3 Final data of the coefficient of band-to-band absorption and its uncertainty at 295 K

The final data of the coefficient of band-to-band absorption of crystalline silicon at 295 K and its uncertainty as determined in this work is shown in Fig. 3.12. Tabulated data is given in Tab. 3.1. This data contains corrections for FCA where necessary, as well as the uncertainty contribution due to uncertainty of the sample temperature during measurements. Over a wide wavelength range, the uncertainty of the data is of the order of 1% rel. Near the band gap (≈ 1150 nm), it increases to about 10% at 1200 nm. From 1200 to 1450 nm, the absorption coefficient decreases by about six orders of magnitude, leading to a decreasing signal-to-noise ratio during the measurements and an uncertainty of about 60% at 1400 nm and about 180% at 1450 nm.

For comparison, the figure includes the most recent data from literature which is available for the temperature of 295 K [23, 32, 35]. For the data of Ref. 32 (Green, 2008), “error limits” are specified for three wavelengths (250, 460, 1200 nm). In order to take these data into account, it appears reasonable to interpret the error limits as an estimation of measurement uncertainty for $k = 2$. Note that the exact meaning of “error limit” is not specified in Ref. 32. Between the three given values, the uncertainty is linearly interpolated due to the lack of information about its behavior at other wavelengths. Beyond 1200 nm, the uncertainty is linearly extrapolated (which probably corresponds to an underestimation of the uncertainty, as shown by the uncertainty determined in this work). The top graphs shows the

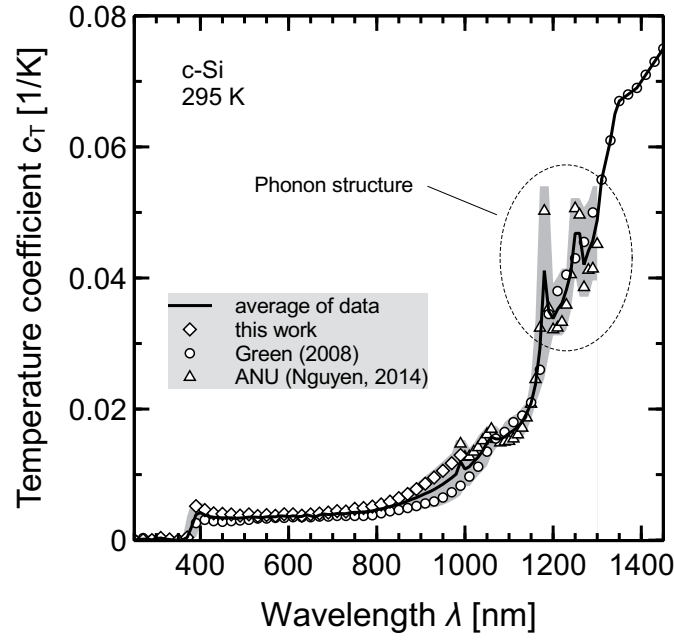


Figure 3.11: Temperature dependence of the coefficient of band-to-band absorption of crystalline silicon at 295 K. The shaded area represents the standard deviation of the data.

ratio of the data and the E_n number for the data determined in this work and Green’s data. For the other data, the “pseudo E_n number”

$$E'_n = \frac{|\alpha_{bb} - \alpha_{bb,lit}|}{U(\alpha_{bb})} \quad (3.18)$$

is shown, which is defined in analogy to the E_n number introduced in section 1.3.6 but neglects the unknown uncertainty of the literature data. In the latter equation, α_{bb} is the absorption coefficient determined in this work, $U(\alpha_{bb})$ is its uncertainty ($k = 2$) and $\alpha_{bb,lit}$ is the absorption coefficient from literature. If $E'_n < 1$, the difference between the data is explainable by the uncertainty of the data determined in this work. $E'_n > \sqrt{2}$ indicates that the difference of the data is larger than twice the uncertainty of the data determined in this work. Hence, $E'_n > \sqrt{2}$ would also occur if the uncertainty of the literature data would be equal to the uncertainty of the data determined in this work. In this case, the deviations are likely due to systematic effects. Additionally, the ratio of the data from this work and the data from literature is visualized.

Figure 3.12 shows deviations of the data of Green [32] around 500 and 1200 nm which are of the order of 10 to 30% rel. Compared to the data of Daub [23], deviations of the order of 10% rel. are found. Above 1250 nm, the deviation increases. As can be seen, the deviations are hardly visible on the logarithmic scale of Fig. 3.12 (except for the deviations around 1300 nm). The data by Nguyen [35], which is the most recent data published in the literature, is in good agreement with the data determined in this work, as can be seen by $E'_n < 1$ for almost all wavelengths.

For practical devices, the deviations in the short wavelength region are irrelevant as the absorption coefficient is so large that all light entering the device is absorbed anyway. However, in the region around 1200 nm, problems with the data from literature have been reported concerning the modeling and analysis of luminescence spectra of silicon wafers and solar cells [81, 115]. Using the data of Green [32] was found to lead to an overestimation of the luminescence intensity of the order of 20%, while the data of Daub [23] led to better agreement between model and experiment. This issue is discussed in more detail in chapter 4.

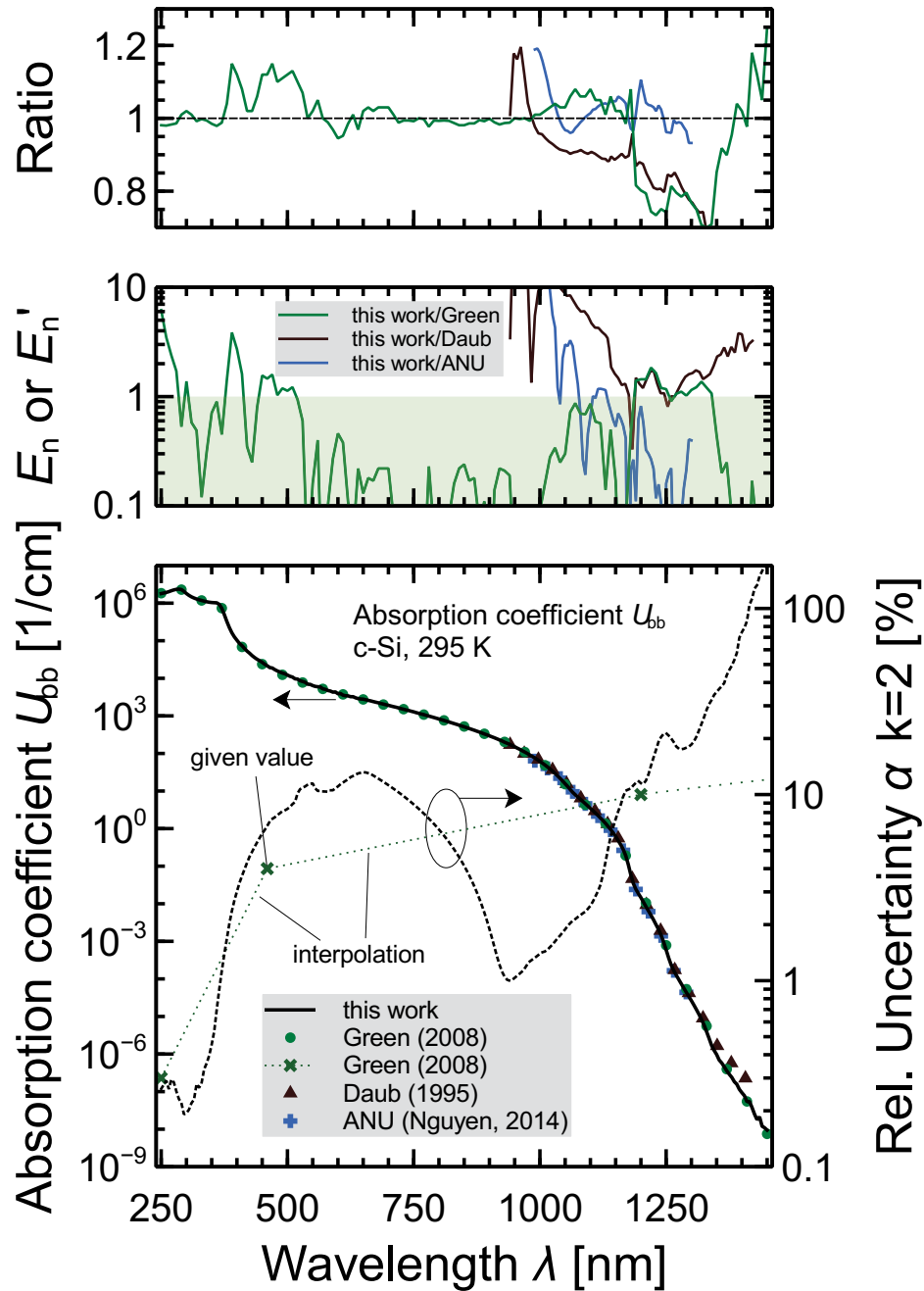


Figure 3.12: Final data of the coefficient of band-to-band absorption of crystalline silicon at 295 K and its uncertainty as determined in this work. For comparison, literature data which is also available for 295 K is shown [23, 32, 35]. For the data of Ref. 32 (Green, 2008), “error limits” are specified for three wavelengths (250, 460, 1200 nm) and visualized by the crosses. Between these given values, the uncertainty is linearly interpolated due to the lack of information about its behavior at other wavelengths (see discussion in the text). Beyond 1200 nm, the uncertainty is extrapolated.

Table 3.1: Final data of the coefficient of band-to-band absorption of crystalline silicon at 295 K and its relative uncertainty as determined in this work. The uncertainty is specified for a coverage factor $k = 2$ and rounded to two significant digits.

λ [nm]	α_{bb} [cm^{-1}]	$\frac{U(\alpha_{bb})}{\alpha_{bb}}$ [%]	λ [nm]	α_{bb} [cm^{-1}]	$\frac{U(\alpha_{bb})}{\alpha_{bb}}$ [%]	λ [nm]	α_{bb} [cm^{-1}]	$\frac{U(\alpha_{bb})}{\alpha_{bb}}$ [%]
250	1.804×10^6	0.26	455	2.374×10^4	6.4	660	2.591×10^3	13
255	1.859×10^6	0.26	460	2.161×10^4	6.8	665	2.495×10^3	13
260	1.930×10^6	0.28	465	1.925×10^4	7.2	670	2.402×10^3	13
265	2.023×10^6	0.34	470	1.878×10^4	7.5	675	2.313×10^3	12
270	2.139×10^6	0.27	475	1.704×10^4	7.7	680	2.226×10^3	12
275	2.253×10^6	0.26	480	1.566×10^4	7.8	685	2.142×10^3	12
280	2.332×10^6	0.28	485	1.475×10^4	8.0	690	2.061×10^3	12
285	2.362×10^6	0.24	490	1.380×10^4	8.0	695	1.983×10^3	11
290	2.302×10^6	0.18	495	1.325×10^4	8.1	700	1.907×10^3	11
295	2.064×10^6	0.22	500	1.220×10^4	8.3	705	1.834×10^3	11
300	1.797×10^6	0.19	505	1.125×10^4	8.7	710	1.763×10^3	11
305	1.608×10^6	0.15	510	1.080×10^4	8.9	715	1.695×10^3	11
310	1.469×10^6	0.20	515	9.684×10^3	9.1	720	1.629×10^3	10
315	1.367×10^6	0.27	520	9.553×10^3	9.3	725	1.565×10^3	10
320	1.289×10^6	0.25	525	8.625×10^3	11	730	1.503×10^3	9.8
325	1.229×10^6	0.31	530	8.252×10^3	11	735	1.443×10^3	9.6
330	1.178×10^6	0.32	535	7.849×10^3	12	740	1.386×10^3	9.3
335	1.129×10^6	0.30	540	6.957×10^3	12	745	1.330×10^3	9.1
340	1.093×10^6	0.30	545	6.894×10^3	12	750	1.276×10^3	8.9
345	1.063×10^6	0.37	550	6.406×10^3	11	755	1.224×10^3	8.6
350	1.044×10^6	0.43	555	6.093×10^3	10	760	1.173×10^3	8.4
355	1.032×10^6	0.51	560	5.958×10^3	11	765	1.125×10^3	8.1
360	1.017×10^6	0.66	565	5.906×10^3	11	770	1.078×10^3	7.9
365	9.275×10^5	0.83	570	5.235×10^3	10	775	1.032×10^3	7.7
370	7.269×10^5	1.1	575	5.087×10^3	10	780	9.882×10^2	7.4
375	4.941×10^5	1.3	580	4.744×10^3	10	785	9.458×10^2	7.2
380	3.254×10^5	1.7	585	4.580×10^3	10	790	9.049×10^2	7.0
385	2.231×10^5	2.0	590	4.276×10^3	11	795	8.653×10^2	6.7
390	1.621×10^5	2.4	595	4.343×10^3	11	800	8.271×10^2	6.5
395	1.257×10^5	2.7	600	3.879×10^3	11	805	7.902×10^2	6.3
400	1.025×10^5	3.0	605	3.937×10^3	11	810	7.546×10^2	6.0
405	8.455×10^4	3.3	610	3.555×10^3	12	815	7.203×10^2	5.8
410	7.395×10^4	3.7	615	3.440×10^3	12	820	6.871×10^2	5.5
415	6.220×10^4	4.0	620	3.407×10^3	12	825	6.552×10^2	5.3
420	5.294×10^4	4.3	625	3.237×10^3	12	830	6.243×10^2	5.1
425	4.651×10^4	4.6	630	3.245×10^3	13	835	5.946×10^2	4.8
430	4.023×10^4	5.0	635	3.020×10^3	13	840	5.659×10^2	4.6
435	3.564×10^4	5.2	640	2.885×10^3	13	845	5.383×10^2	4.4
440	3.199×10^4	5.5	645	2.815×10^3	13	850	5.116×10^2	4.1
445	2.942×10^4	5.9	650	2.793×10^3	13	855	4.859×10^2	3.9
450	2.663×10^4	6.1	655	2.691×10^3	13	860	4.612×10^2	3.7

Table continues on next page.

Continued from previous page.

λ [nm]	α_{bb} [cm^{-1}]	$\frac{U(\alpha_{bb})}{\alpha_{bb}}$ [%]	λ [nm]	α_{bb} [cm^{-1}]	$\frac{U(\alpha_{bb})}{\alpha_{bb}}$ [%]	λ [nm]	α_{bb} [cm^{-1}]	$\frac{U(\alpha_{bb})}{\alpha_{bb}}$ [%]
865	4.374×10^2	3.4	1065	9.216×10^0	2.1	1265	1.674×10^{-4}	18
870	4.145×10^2	3.2	1070	7.965×10^0	2.2	1270	1.258×10^{-4}	18
875	3.925×10^2	3.0	1075	6.946×10^0	2.2	1275	9.627×10^{-5}	17
880	3.713×10^2	2.8	1080	6.070×10^0	2.2	1280	7.391×10^{-5}	17
885	3.509×10^2	2.5	1085	5.285×10^0	2.3	1285	5.686×10^{-5}	18
890	3.313×10^2	2.3	1090	4.585×10^0	2.3	1290	4.364×10^{-5}	18
895	3.125×10^2	2.1	1095	3.985×10^0	2.4	1295	3.395×10^{-5}	18
900	2.945×10^2	1.9	1100	3.452×10^0	2.5	1300	2.632×10^{-5}	18
905	2.771×10^2	1.7	1105	3.011×10^0	2.6	1305	2.006×10^{-5}	19
910	2.605×10^2	1.5	1110	2.594×10^0	2.8	1310	1.521×10^{-5}	20
915	2.446×10^2	1.3	1115	2.237×10^0	3.0	1315	1.144×10^{-5}	21
920	2.293×10^2	1.2	1120	1.915×10^0	3.2	1320	8.301×10^{-6}	24
925	2.147×10^2	1.1	1125	1.627×10^0	3.5	1325	5.949×10^{-6}	26
930	1.994×10^2	1.0	1130	1.377×10^0	4.1	1330	3.972×10^{-6}	28
935	1.871×10^2	0.98	1135	1.136×10^0	4.9	1335	2.620×10^{-6}	31
940	1.746×10^2	0.98	1140	9.503×10^{-1}	5.8	1340	1.700×10^{-6}	33
945	1.623×10^2	1.0	1145	7.755×10^{-1}	6.9	1345	1.247×10^{-6}	34
950	1.507×10^2	1.0	1150	6.215×10^{-1}	7.8	1350	9.707×10^{-7}	36
955	1.393×10^2	1.1	1155	4.812×10^{-1}	8.3	1355	6.927×10^{-7}	37
960	1.286×10^2	1.1	1160	3.713×10^{-1}	8.8	1360	5.813×10^{-7}	38
965	1.184×10^2	1.1	1165	2.779×10^{-1}	9.3	1365	4.590×10^{-7}	39
970	1.089×10^2	1.2	1170	1.896×10^{-1}	10	1370	3.580×10^{-7}	42
975	9.995×10^1	1.2	1175	1.109×10^{-1}	11	1375	2.897×10^{-7}	47
980	9.147×10^1	1.3	1180	5.917×10^{-2}	11	1380	2.401×10^{-7}	50
985	8.327×10^1	1.3	1185	3.473×10^{-2}	12	1385	1.843×10^{-7}	53
990	7.570×10^1	1.4	1190	2.445×10^{-2}	12	1390	1.571×10^{-7}	58
995	6.856×10^1	1.4	1195	1.868×10^{-2}	11	1395	1.146×10^{-7}	63
1000	6.160×10^1	1.4	1200	1.456×10^{-2}	11	1400	9.360×10^{-8}	75
1005	5.540×10^1	1.4	1205	1.114×10^{-2}	11	1405	7.799×10^{-8}	81
1010	4.929×10^1	1.4	1210	8.398×10^{-3}	12	1410	5.385×10^{-8}	88
1015	4.385×10^1	1.5	1215	6.437×10^{-3}	12	1415	5.468×10^{-8}	95
1020	3.873×10^1	1.5	1220	4.938×10^{-3}	13	1420	3.796×10^{-8}	120
1025	3.390×10^1	1.6	1225	3.739×10^{-3}	15	1425	2.514×10^{-8}	120
1030	2.934×10^1	1.6	1230	2.772×10^{-3}	17	1430	1.791×10^{-8}	140
1035	2.532×10^1	1.7	1235	2.068×10^{-3}	20	1435	2.133×10^{-8}	150
1040	2.170×10^1	1.8	1240	1.451×10^{-3}	22	1440	1.203×10^{-8}	170
1045	1.847×10^1	1.8	1245	9.596×10^{-4}	23	1445	1.089×10^{-8}	170
1050	1.561×10^1	1.9	1250	5.911×10^{-4}	22	1450	9.447×10^{-9}	180
1055	1.315×10^1	2.0	1255	3.610×10^{-4}	21			
1060	1.096×10^1	2.0	1260	2.329×10^{-4}	20			

Application of derived data for photovoltaics

This chapter presents an analysis of the uncertainty of silicon solar cell energy conversion efficiency predictions by means of device simulations due to the uncertainty of the absorption coefficient. Moreover, the impact of deviations between the data determined in this work and data from literature is discussed. It is shown that the uncertainty of energy conversion efficiency predictions caused by the uncertainty of the absorption coefficient data is of the order of 0.1% relative, as well as the deviations when using absorption coefficient data from literature. The uncertainty of the absorption coefficient data is thus not expected to limit the accuracy of device simulations. The second part of this chapter presents a comprehensive analytical model for the spectral luminescence emission of silicon solar cells and wafers, which facilitates a detailed understanding of optical and electrical device properties on the luminescence spectrum. It is shown that models of spectral luminescence emission require accurate absorption coefficient data as input. Based on the model, a simple method for the determination of the rear surface reflectance of solar cells from the luminescence spectrum is outlined.

The optimization of solar cells and the evaluation of new concepts for further increasing the energy conversion efficiency or reducing production costs are supported by numerical device simulations, aiming at the prediction of the energy conversion efficiency. Such simulations require several device and material properties as input. One of these input quantities is the absorption coefficient, which describes the fundamental ability of the material to absorb light under generation of electrical charge carriers. The accuracy of energy conversion efficiency predictions by means of simulations depends on the accuracy of the available input data. The first part of this chapter discusses the uncertainty of energy conversion efficiency predictions with respect to the uncertainty of the absorption coefficient as determined in this work. Moreover, the impact of deviations between the data determined in this work and the data from literature is analyzed. The second part of this chapter describes the application of the derived absorption coefficient data for the modeling and analysis of spectrally resolved luminescence measurements. A detailed understanding of the spectral distribution of the luminescence emission forms the basis for a quantitative interpretation of luminescence images, which have become a versatile and routinely used tool for the characterization of silicon solar cells [116]. The applications range from qualitative characterization such as detection of cracks or broken contact fingers to quantitative methods such as the determination of series resistances or the determination of the charge carrier lifetime [79, 117–125]. For this purpose, a comprehensive analytical model for the spectral luminescence emission of silicon solar cells and wafers is presented. In the wavelength region around 1200 nm, deviations between measurements and models have been reported [81, 115]

when using the absorption coefficient data of Green [32], which is currently most widely used in the photovoltaic community. These deviations are shown to be resolved by the data determined in this work. Based on the model of spectral luminescence emission, the chapter closes by presenting an approach for the determination of the rear surface reflectance of silicon solar cells by means of spectrally resolved luminescence measurements.

4.1 Uncertainty of silicon solar cell energy conversion efficiency predictions

The accuracy of energy conversion efficiency predictions by means of device simulations depends on the accuracy of the input parameters. One of the required input parameters is the absorption coefficient. It is therefore reasonable to analyze the impact of the uncertainty of the absorption coefficient data on the accuracy of conversion efficiency simulations. The discussion starts with the consideration of ideal solar cells. This analysis can be carried out analytically, thus providing insights into the general relations. In a second step, specific devices and solar cell concepts are considered by means of numerical device simulations with the solar cell simulator PC1D [126].

4.1.1 Ideal solar cells

The energy conversion efficiency η is defined as the ratio of generated electrical power P_{out} and incident optical power P_{in} , both normalized to the area A_{cell} of the solar cell:

$$\eta = \frac{P_{\text{out}}}{P_{\text{in}}} = \frac{V_{\text{mpp}} I_{\text{mpp}}}{P_{\text{in}} A_{\text{cell}}}, \quad (4.1)$$

where V_{mpp} and I_{mpp} denote the output voltage and current at the *maximum power point* (MPP). For an ideal solar cell, current I and voltage V are related by Shockley's diode equation [40, 127], which leads to

$$I_{\text{mpp}} = I_{\text{sc}} - I_0 \left[\exp(V_{\text{mpp}}/V_T) - 1 \right]. \quad (4.2)$$

In the latter equation, I_{sc} is the short circuit current, I_0 is the junction saturation current and $V_T = kT/q$ is the thermal voltage, which is about 25.6 mV at room temperature. The saturation current density of an ideal silicon solar cell is 0.27 fA/cm² [128]. Figure 4.1 visualizes an exemplary ideal current-voltage and power-voltage characteristic for a solar cell with an area of 15.6 × 15.6 cm², which implies a saturation current of 65.7 fA. The short circuit current I_{sc} of a laterally homogeneous solar cell is

$$I_{\text{sc}} = A_{\text{cell}} q \int_0^\infty d\lambda \int_0^W dz G(\lambda, z) f_c(z). \quad (4.3)$$

In the latter equation, q is the elementary charge, G is the charge carrier generation rate per area at position z due to the absorption of photons of wavelength λ and f_c is the probability that generated charge carriers are collected by the junction and contribute to the terminal current. In the absence of parasitic absorption processes, each absorbed photon generates an electron-hole pair. The generation rate G is then given by the change of the photon flux per area Φ multiplied with -1 :

$$G(\lambda, z) = -\frac{d\Phi(\lambda, z)}{dz}. \quad (4.4)$$

The photon flux within the solar cell is given by the Lambert-Beer law Eq. (1.7). The charge carrier generation rate can thus be expressed as

$$G(\lambda, z) = \Phi(\lambda, 0) g(\lambda, z) \quad (4.5)$$

where g is a normalized generation rate and $\Phi(\lambda, 0)$ is the photon flux per area entering the solar cell. For simplicity, an infinitesimally thin emitter is assumed here. In an ideal solar cell, $f_c(z) = 1$, i.e., all generated charge carriers contribute to the terminal current. With this, Eq. (4.3) becomes

$$I_{sc} = A_{cell} q \int_0^{\infty} d\lambda \Phi(\lambda, 0) \int_0^W dz g(\lambda, z). \quad (4.6)$$

The integral of the normalized generation rate g over z equals the absorptance $A(\lambda)$ (see appendix C.4). With this, the short circuit current is finally expressed as

$$I_{sc} = A_{cell} q \int_0^{\infty} d\lambda \Phi(\lambda) A(\lambda). \quad (4.7)$$

This result is also expected intuitively: In the absence of parasitic absorption, all absorbed photons of wavelength λ generate charge carriers that contribute to the short circuit current. The short circuit current is then the sum of the contributions from all wavelengths.

Equations (4.1) through (4.7) describe the dependence of the conversion efficiency on the absorptance. The absorptance is, among others, determined by the absorption coefficient. In order to calculate the uncertainty of the conversion efficiency, in a first step the uncertainty of the absorptance must be determined from the uncertainty of the absorption coefficient. This requires a model for the absorptance as a function of the absorption coefficient. In a second step, the resulting uncertainty of the short circuit current is obtained by applying the GUM formalism to Eq. (4.7). In a last step, the uncertainty of the conversion efficiency is obtained by combining Eqs. (4.1) and (4.2), giving

$$\frac{u(\eta)}{\eta} = \frac{u(I_{mpp})}{I_{mpp}} = \frac{u(I_{sc})}{I_{mpp}} = f \frac{u(I_{sc})}{I_{sc}} \quad (4.8)$$

where

$$f = \frac{I_{sc}}{I_{mpp}} \approx 1.03 \quad (4.9)$$

for ideal solar cells with the mentioned saturation current density of 0.27 fA/cm^2 . Hence, the relative uncertainty of the energy conversion efficiency is approximately equal to the relative uncertainty of the short circuit current. For real solar cells, I_{sc}/I_{mpp} is typically of the order of 1.1. In order to obtain conservative uncertainty estimates, $f = 1.1$ is thus used in the following.

Model of the absorptance

The absorptance of a solar cell depends not only on the absorption coefficient and the thickness of the sample, but also on the optical properties of the surfaces. Usually, solar cells feature a textured front surface which randomizes the direction of transmitted or reflected light. This leads to a trapping of light rays^a within the sample, i.e., the optical path length is enhanced and absorptance thus increases. The rear surface of solar cells is usually “optically rough”, i.e., the direction of reflected light is at least partly randomized. The maximum optical path enhancement is achieved by lambertian light trapping schemes [130, 131] where both surfaces exhibit a lambertian reflection characteristic for light that is internally reflected at the surfaces. A comprehensive optical model for silicon solar cells was published by Basore [129] in 1993 and later extended by Brendel et al. [111] for application to thin-film solar cells. This extended model can be used for samples with planar or textured front surfaces and contains samples with two specular reflecting or two lambertian reflecting surfaces as

^aLight trapping denotes the enhancement of absorption by randomizing the direction of light undergoing an internal reflection at the surfaces, which leads to subsequent total internal reflections.

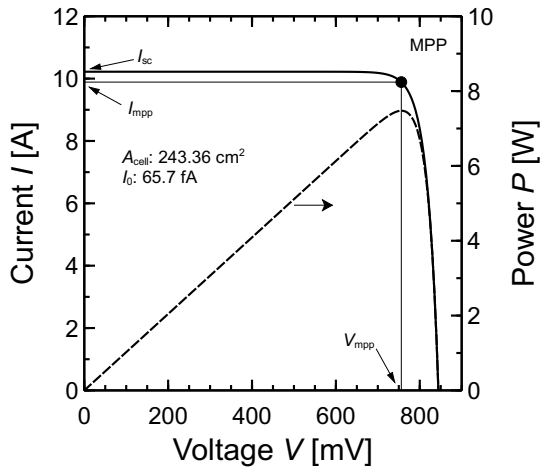


Figure 4.1: Sample current-voltage characteristic of an ideal silicon solar cell.

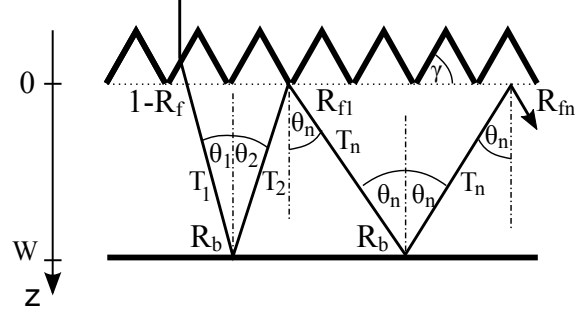


Figure 4.2: Optical model for solar cells, adapted from Refs. 129 and 111.

special cases. It can thus be used for the examination of the lambertian limit, but it can also be adapted in order to describe typical silicon solar cells. The model assumes that light is fully randomized after three internal reflections at rough surfaces. The reflection of a rough rear surface is modeled as an intermediate case of specular and lambertian reflection, thereby taking all kinds of arbitrary rough surfaces into account. The degree of lambertian reflection is described by a “lambertian factor” Λ which is unity for lambertian reflection and zero for specular reflection. The reflectance of a textured front surface is obtained by numerical ray tracing. The extended model is designed for thin-film solar cells and therefore explicitly considers charge carrier generation in the emitter and substrate region. This is not necessary when considering ideal silicon solar cells with an infinitesimally thin emitter. Therefore, the model is simplified as described in section 4.3. According to this simplified model, the absorptance can be expressed by

$$A(\lambda) = (1 - R_f) \left[1 - T_1 + T_1 R_b (1 - T_2) + T_1 R_b T_2 R_{f1} (1 - T_n) \frac{1 + T_n R_b}{1 - T_n^2 R_b R_{fn}} \right] \quad (4.10)$$

where the parameters are defined according to Fig. 4.2 and Ref. 111. The transmittances T_1 , T_2 and T_n depend on the angle of light propagation within the sample and the absorption coefficient. They are given by

$$T_i = \exp\left(\frac{-\alpha W}{\cos \theta_i}\right), \quad i = \{1, 2, n\}. \quad (4.11)$$

The angles θ_2 and θ_n depend on the wavelength. Further details on the calculation of the model parameters are given in section 4.3. Figure 4.3 shows the absorptance calculated according to Eq. (4.10) for different thicknesses of the solar cell. For the calculation, a textured front surface with a facet angle $\theta_1 = 41.8^\circ$ is assumed according to Ref. 129. Furthermore, the calculation assumes a perfect anti-reflection coating, for which $R_{f1} = R_{fn} = 0.921$ [111]. The rear surface is assumed to have a lambertian reflection characteristic. As for an ideal solar cell, the rear surface is a perfect reflector, i.e., $R_{b1} = R_{bn} = 1$.

Equation (4.10) provides the link between absorptance and absorption coefficient. If only the uncertainty of the absorption coefficient $u(\alpha)$ is considered, the uncertainty $u(A)$ of the absorptance is obtained from this equation by

$$u(A) = \frac{dA}{d\alpha} u(\alpha). \quad (4.12)$$

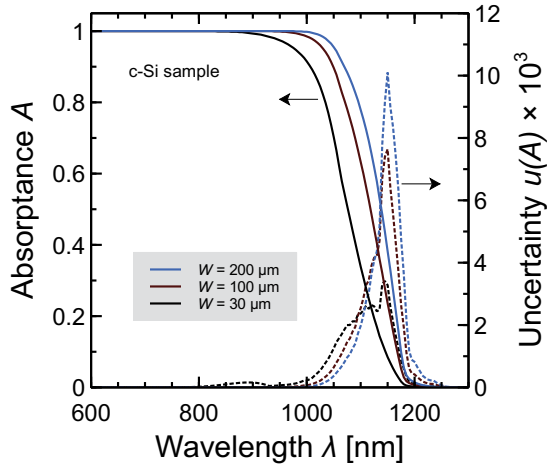


Figure 4.3: Absorbance of ideal silicon solar cells with different thicknesses according to Eq. (4.10). The dotted lines show the uncertainty of the absorbance ($k = 1$) following from the uncertainty of the absorption coefficient as determined in this work.

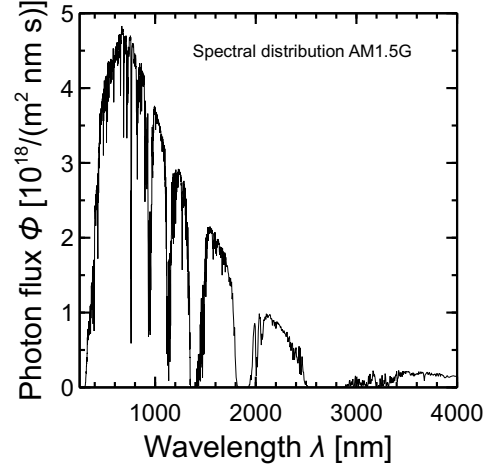


Figure 4.4: Spectral distribution *AM1.5G* according to standard testing conditions for solar cells as defined in IEC 60904.

It is visualized in Fig. 4.3 by the dotted lines. The calculation incorporates $u(\alpha)$ as determined in this work. An obvious finding from Fig. 4.3 is that the uncertainty of the absorbance is only significant in the wavelength region where the absorbance varies between its two saturation values. This can be understood by recognizing that at short wavelengths, the absorption coefficient is large and the absorption length $L_\alpha = 1/\alpha$ is short compared to the thickness of the sample. In this region, all light is absorbed anyway and small variations of the absorption coefficient do not affect the absorbance. Formally this is reflected in the uncertainty calculation by $dA/d\alpha = 0$, i.e., the sensitivity coefficient is zero. In the long wavelength region, the sensitivity coefficient is larger than zero, but due to the small absorption coefficient, $u(\alpha) \approx 0$ and consequently $u(A) \approx 0$.

Uncertainty calculation for the short circuit current

The short circuit current depends not only on the absorbance $A(\lambda)$, but also on the spectral distribution of the incident photons. For solar cells, measurements and simulations usually refer to standard testing conditions (STC) as defined in the standard IEC 60904. This standard also defines a spectral distribution of light which is referred to as *AM1.5G* [48]. The following considerations refer to this spectrum as shown in Fig. 4.4 in units of photons per time, area and wavelength interval.

Figure 4.5 shows the number of absorbed photons, which is given by $\Phi(\lambda) \times A(\lambda)$. As can be seen, significant contributions to the number of totally absorbed photons arise only from the wavelength interval 300 – 1200 nm. For the calculation of the short circuit current, Eq. (4.7) can therefore be approximated by considering the wavelength range from 300 to 1450 nm, for which data of the absorption coefficient are determined in this work and tabulated data of the *AM1.5G* spectral distribution are available:

$$I_{sc} \approx A_{cell} q \int_{300 \text{ nm}}^{1450 \text{ nm}} d\lambda \Phi(\lambda) A(\lambda), \quad (4.13)$$

Since Φ is a tabulated quantity at discrete values, the integral in the latter equation is actually calcu-

lated numerically using the trapezium rule

$$F = \int_a^b dx f(x) \approx \sum_{i=1}^{N-1} (x_{i+1} - x_i) \frac{f(x_i) + f(x_{i+1})}{2} = \Delta x \left(\frac{f(x_1)}{2} + \sum_{i=2}^{N-1} f(x_i) + \frac{f(x_N)}{2} \right) \quad (4.14)$$

where f is an arbitrary function of x , a and b are the lower and upper bound of the integration interval, N is the number of discrete (tabulated) values of f , $a \leq x \leq b$ and $\Delta x = x_{i+1} - x_i$. The uncertainty of the integrated quantity follows by applying the standard formalism to the right hand side of the latter equation.

In order to provide a conservative estimation of the uncertainty of the energy conversion efficiency, the maximum uncertainty of I_{sc} must be considered. According to Eq. (1.25), the combined uncertainty of an output quantity is maximized if all input quantities are fully correlated, i.e., all correlation coefficients r are equal to unity, and all sensitivity coefficients are positive. For the calculation of $u(I_{sc})$, this corresponds to the assumption of full correlation between the absorption coefficient data at all wavelengths. (Practically spoken, this means that an overestimation of α in the short wavelength region implies an overestimation also in the sub-band gap region.) The sensitivity coefficients are given by Φ and thus positive. For fully correlated quantities, Eq. (1.25) simplifies to [66]

$$u_c^2(y) = \left[\sum_{i=1}^N \frac{\partial f}{\partial x_i} u(x_i) \right]^2, \quad (4.15)$$

i.e., the uncertainty of the output quantity is simply the sum of the uncertainties of the input quantities, each multiplied with the corresponding sensitivity coefficient. Application of the latter equation to the calculation of the uncertainty of I_{sc} using the trapezium rule yields

$$\begin{aligned} u(I_{sc}) &= A_{cell} q \Delta \lambda \left(\frac{\Phi(\lambda_1) u(A(\lambda_1))}{2} + \sum_{i=2}^{N-1} \Phi(\lambda_i) u(A(\lambda_i)) + \frac{\Phi(\lambda_N) u(A(\lambda_N))}{2} \right) \\ &\approx A_{cell} q \int_{300 \text{ nm}}^{1450 \text{ nm}} d\lambda \Phi(\lambda) u(A(\lambda)). \end{aligned} \quad (4.16)$$

Resulting uncertainty of the energy conversion efficiency

Figure 4.6 shows the relative uncertainty ($k = 2$) of the energy conversion efficiency of an ideal silicon solar cell $u(\eta)/\eta$ according to Eqs. (4.10) through (4.16) and (4.8) with $f = 1.1$ as a function of the device thickness W . The solid line visualizes the uncertainty following from the uncertainty of the absorption coefficient as determined in this work. The dashed line represents the uncertainty following from Green's absorption coefficient data [32], which is the data most widely used in the photovoltaic community. Note that in Ref. 32, the uncertainty of the data is only specified for 250, 460 and 1200 nm. For the calculation, it is thus linearly interpolated or extrapolated as shown in Fig. 3.12. For comparison, the theoretical efficiency limit η_{lim} for p -type crystalline silicon solar cells with a resistivity of $1 \Omega\text{cm}$ according to Ref. 132 is shown on the right axis. For the thickness of typical industrial silicon solar cells, $W \approx 180 \mu\text{m}$, the relative uncertainty of the conversion efficiency is about 0.08%. For current silicon solar cells with an efficiency of about 20%, this corresponds to an uncertainty of about 0.02% absolute. Compared to the uncertainty following from Green's data, $u(\eta)/\eta$ is reduced by a factor of about 2. The uncertainty increases slightly with increasing device thickness. This is due to an enhanced absorptance at sub-band gap wavelengths, which leads to an enhanced uncertainty contribution from these wavelengths. It is interesting to note that the relative uncertainty of the short circuit current also increases with decreasing device thickness. The reason for this is a combination of the shape of the AM1.5G distribution, which shows a dip around 950 nm, and the minimum of the uncertainty of the absorption coefficient at 930 nm. For thick solar cells ($W \geq$

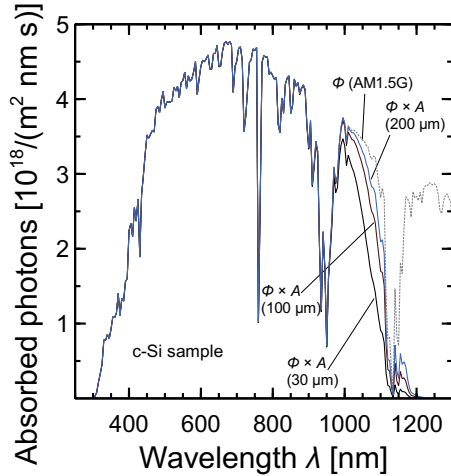


Figure 4.5: Number of absorbed photons per wavelength interval for silicon samples with different thicknesses.

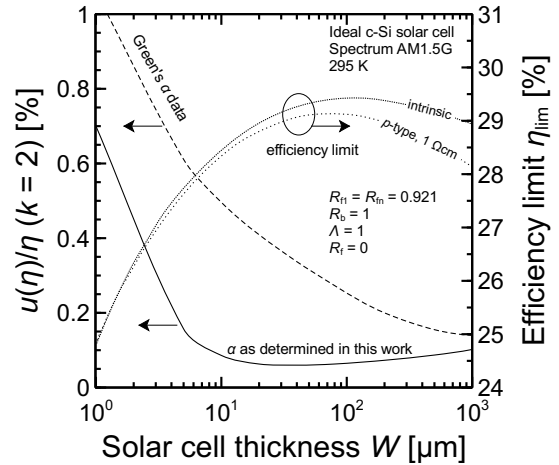


Figure 4.6: Relative uncertainty ($k = 2$) of the energy conversion efficiency of an ideal crystalline silicon solar cell as a function of the device thickness W . For comparison, the theoretical efficiency limits for intrinsic silicon and p -type silicon with a resistivity of $1 \Omega\text{cm}$ according to Ref. 132 are shown on the right axis.

180 μm), only the uncertainty of the absorption coefficient at wavelengths above 900 nm contributes to the uncertainty of I_{sc} and η , as shown in Fig. 4.3. For very thin solar cells, contributions also arise from the data at wavelengths around 800 nm, where the uncertainty of the absorption coefficient data is larger (see dotted black line in Fig. 4.3).

From the analysis outlined above, it can be concluded that the uncertainty of energy conversion efficiency predictions due to the uncertainty of the absorption coefficient data determined in this work is of the order of 0.1% relative for ideal silicon solar cells with a typical device thickness of about 180 μm . For thin film solar cells, the relative uncertainty is comparable as long as the device thickness exceeds 10 μm . Below, the uncertainty increases but stays below 1% relative for realistic devices. Other simulation input parameters are expected to have larger uncertainties. The accuracy of the absorption coefficient data determined in this work is thus sufficient for simulation purposes. Moreover, the analysis shows that, for typical solar cells, it is essential to have very accurate absorption coefficient data in the wavelength range from about 950 to 1200 nm since the contributions to the uncertainty of the energy conversion efficiency arise solely from this wavelength range (see Fig. 4.3). The absorption coefficient data determined in this work obviously fulfills this requirement.

4.1.2 Realistic solar cells

The current-voltage characteristic of realistic solar cells is influenced by parallel and series resistances and non-ideal diode characteristics. These effects have an impact on the maximum power point but are usually negligible under short circuit conditions. Thus, the ratio of I_{mpp} and I_{sc} (represented by f in Eq. (4.8)) may be different for realistic solar cells. However, for industrial solar cells with conversion efficiencies around 20%, $f \approx 1.1$ still holds. Realistic solar cells do not have a perfect lambertian reflector at the rear surface. In the analytical model of the absorptance, this can be described by $R_b < 1$ and $\Lambda < 1$. However, the lambertian factor Λ shows to have a minor impact on the estimated uncertainty of the energy conversion efficiency. Figure 4.7 therefore shows the relative uncertainty of the energy conversion efficiency as a function of the rear surface reflectance R_b calculated with the analytical model using $\Lambda = 1$ and $f = 1.1$. The solid line represents the uncertainty for silicon

solar cells with a thickness of 170 μm , the dashed line shows the corresponding uncertainty for thin solar cells with a thickness of 30 μm . For comparison, the conversion efficiency is simulated for different types of solar cells using the simulation tool PC1D. In order to obtain the uncertainty of the conversion efficiency calculated with PC1D, a Monte-Carlo simulation is performed. The circle represents the calculated uncertainty for a PERC solar cell with a conversion efficiency of 20.5%. The diamond represents the uncertainty for an industrial silicon solar cell featuring a back surface field with a thickness of 250 μm and a conversion efficiency of 16%. The cross shows the uncertainty for the same solar cell but thinned to 30 μm .

As for the ideal solar cell discussed above, the order of magnitude of uncertainty introduced by the absorption coefficient is generally small. The results are in agreement concerning the order of magnitude of uncertainty resulting from the calculations. It should be noted that PC1D contains an analytical optical model for the calculation of the charge carrier generation profile which is different from that introduced above, so that small deviations from the results of the analytical model presented above are expected simply due to deviations between these optical models.

4.2 Impact of deviations between absorption coefficient data

To date, the absorption coefficient data set published by Green [32] is most widely used in the photovoltaic community. This data is specified for a sample temperature of 300 K and includes temperature coefficients which allow to calculate the absorption coefficient also for different temperatures. As shown in the top graph of Fig. 3.12, the data of Green at 295 K deviates from the data determined in this work by up to $\pm 20\%$ depending on the wavelength. These deviations lead to slight differences in the short circuit current predicted using the absorption coefficient data and thus also affect the predicted conversion efficiency. According to Eqs. (4.1) and (4.2), the conversion efficiency η of an ideal solar cell changes approximately proportional to the change of the short circuit current ΔI_{sc} for small changes of I_{sc} :

$$\Delta\eta \approx \frac{V_{\text{mpp}} \Delta I_{\text{mpp}}}{P_{\text{in}} A_{\text{cell}}} . \quad (4.17)$$

The reason for this is that the change in V_{mpp} is small for small changes of I_{sc} . The relative change of the conversion efficiency is thus

$$\frac{\Delta\eta}{\eta} \approx \frac{\Delta I_{\text{mpp}}}{I_{\text{mpp}}} = \frac{\Delta I_{\text{sc}}}{I_{\text{sc}}} . \quad (4.18)$$

It is calculated using the analytical model described in the preceding section. Again, the calculation refers to the spectral distribution AM1.5G as shown in Fig. 4.4.

Figure 4.8 shows the resulting relative change $\Delta\eta/\eta$ as a function of the rear surface reflectance R_b and for different sample thicknesses. The relative change refers to the deviation of Green's data from the data determined in this work, i.e., $\Delta\eta = \eta_{\text{Green}} - \eta_{\text{this work}}$. In general, the relative change of the conversion efficiency is of the order of 0.1%. This value is in agreement with the results of an analysis conducted with PC1D [133]. For typical solar cells with $R_b > 0.5$, the data determined in this work lead to a slightly higher conversion efficiency than the data of Green. This is mainly due to the absorption coefficient data between 1000 and 1200 nm, where the data of Green is about 5 to 10% lower than the data determined in this work. For very thin solar cells, deviations of the data between 800 and 1000 nm become noticeable in the calculation of the short circuit current, whereas the impact of the data between 1000 and 1200 nm is reduced. The latter effect is enhanced for small values of R_b , since internal reflections facilitate the absorption of light at long wavelengths, whereas light at short wavelengths is already absorbed during the first pass through the sample. Between 800 and 1000 nm, Green's data is slightly larger than that determined in this work, which explains the sign change of $\Delta\eta/\eta$ when going to thin solar cells and $R_b < 0.5$.

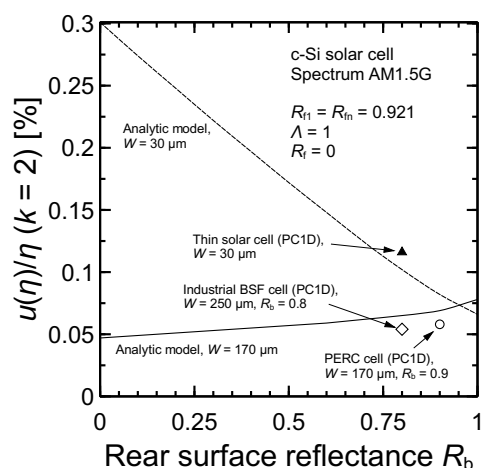


Figure 4.7: Relative uncertainty ($k = 2$) of the conversion efficiency η calculated with the analytical model (lines) and with the simulation tool PC1D (markers).

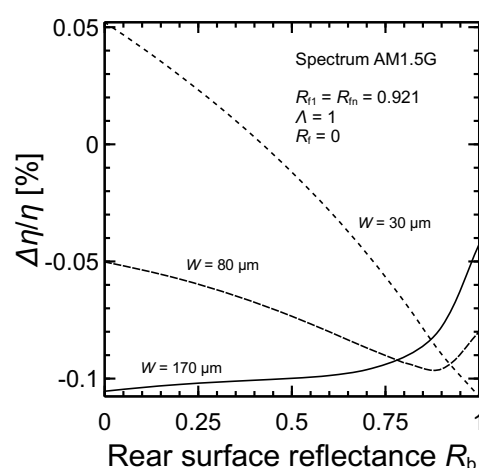


Figure 4.8: Relative change of the conversion efficiency when using the absorption coefficient data of Green [32] instead of the data determined in this work.

4.3 Modeling luminescence spectra of silicon solar cells and wafers

The analysis of luminescence emission is a powerful tool for the characterization of crystalline silicon solar cells [116]. Charge carriers, generated optically or injected electrically, recombine radiatively and give rise to luminescence emission detectable outside the sample. Luminescence measurements are usually referred to as photoluminescence (PL) when using optical excitation or electroluminescence (EL) when using electrical excitation. For both cases, the emitted luminescence photon flux depends on the rate of luminescence photon generation and on the photon escape probability, i.e. the probability that a photon which is spontaneously emitted within the sample can escape and contribute to the measurable luminescence emission. The first is determined by the rate of radiative recombination, which is in turn determined by the charge carrier distribution and the absorption coefficient. The latter is defined by photon reabsorption, which is also determined by the absorption coefficient, and the optical properties of the solar cell's surfaces, namely reflectance and light scattering. A comprehensive model of the luminescence emission should be able to describe electrical and optical excitation, photon reabsorption, reflectance and light scattering at the surfaces appropriately.

Different approaches for modelling the spectral distribution of the detected luminescence emission can be found in the literature [23, 31, 79, 120, 134–137]. However, each of them is valid only for a certain excitation mode (EL or PL) and describes samples with either two planar (specular reflecting) or two completely rough (lambertian reflecting) surfaces. This work outlines a generalized model of the spectral luminescence emission of silicon solar cells and wafers. The model consists of an electrical and an optical part and thus separates the electrical from the optical modelling. Starting with an overview of models of luminescence emission found in the literature, it is shown that these models can be generalized for use with both EL and PL independent from the excitation mode for which they were designed. The spectra predicted by these models are compared to spectrally resolved PL measurements carried out on specially prepared samples. Finally, an expression for the photon escape probability of samples with any combination of planar or textured surfaces is derived. Combining this optical model with expressions for the specific charge carrier distribution yields a model of the spectral luminescence emission which is valid for both EL and PL and for samples with planar and rough surfaces under both electrical and/or optical excitation.

4.3.1 General model of spectral luminescence emission

In general, the emitted luminescence photon flux is given by the product of the spectral photon generation rate r_{ph} and the photon escape probability f_{esc} , as described in section 2.2.1. To simplify matters, the following considerations assume laterally homogenous device properties, allowing a one-dimensional description of the spectral luminescence emission. The derivation focuses on low-level injection and detection of the luminescence emission perpendicular to the sample's surface. These assumptions are usually fulfilled for typical measurement conditions. High injection conditions are normally expected only in high efficiency devices and high lifetime wafers, in which the charge carrier distribution can usually be expected to be uniform. In this case, only small changes in the shape of the spectrum are observed between low and high injection conditions. However, a significant change in the spectrum can occur if some parts of the sample are in low injection while other parts are in medium or high injection. For instance, this may be the case in lowly doped samples or under local excitation by a focussed laser beam.

As already mentioned in chapter 2.2, the emitted luminescence photon flux is given by (see Eq. (2.36))

$$\Phi(\lambda) = \int_0^W dz r_{\text{ph}}(\lambda, z) f_{\text{esc}}(\lambda, z), \quad (4.19)$$

where r_{ph} (given by Eq. (2.37)) is determined by the generalized Planck law for luminescence emission [72]. It can be shown that for typical luminescence measurement conditions, Eq. (2.37) can be approximated by (see appendix E.4)

$$r_{\text{ph}}(\lambda, z) \approx b_{\text{rad}}(\lambda) n(z) p(z) \quad (4.20)$$

where b_{rad} is the coefficient of spectral radiative recombination given by [82, 134, 138, 139]

$$b_{\text{rad}}(\lambda) = \frac{n_{\text{Si}}^2(\lambda)}{n_i^2} \alpha(\lambda) 4\pi \Phi_{\text{bb}}(\lambda, \Omega). \quad (4.21)$$

In Eqs. (4.20) and (4.21), n_i is the intrinsic charge carrier concentration, α is the absorption coefficient, n and p are the concentrations of electrons and holes, respectively, and

$$\Phi_{\text{bb}}(\lambda, \Omega) = \frac{2c}{\lambda^4} \exp\left(-\frac{hc}{\lambda kT}\right) \quad (4.22)$$

is the black body photon flux per wavelength interval $d\lambda$ and solid angle $d\Omega$ ([140], see appendix E.3). The factor 4π in Eq. (4.21) results from the integration of Φ_{bb} over all solid angles. The integral of b_{rad} over all solid angles and all wavelengths yields the familiar coefficient of radiative recombination $B_{\text{rad}} = \int_0^\infty d\lambda b_{\text{rad}}(\lambda)$. Combining Eqs. (2.36) and (4.20) allows the emitted luminescence photon flux Φ of wavelength λ per wavelength interval and surface area to be written as the integral of the coefficient of spectral radiative recombination b_{rad} , the electron and hole concentrations n and p and the photon escape probability f_{esc} over the thickness W of the solar cell [79, 80, 141, 142]:

$$\Phi(\lambda) = \int_0^W dz b_{\text{rad}}(\lambda) n(z) p(z) f_{\text{esc}}(\lambda, z). \quad (4.23)$$

Note that Eq. (2.36) consists of an electrical and an optical part. The term $b_{\text{rad}}(\lambda) n(z) p(z)$ accounts for the rate of radiative recombination, which depends on the electrical properties, whereas the photon escape probability $f_{\text{esc}}(\lambda, z)$ depends on photon reabsorption and surface reflectances.

The refractive index n_{Si} is approximately constant in the wavelength range of luminescence emission [37]. b_{rad} is in good approximation independent of z [143]. In a p -type sample, the hole concentration

p at room temperature and under low-level injection conditions is in good approximation equal to the doping concentration N_{dop} and thus independent of z for practical cases. The electron concentration n is then obtained as a solution of the diffusion equation and depends on the excitation conditions [40]. Equation (4.23) can thus be written as

$$\Phi(\lambda) = \frac{n_{\text{Si}}^2}{n_i^2} N_{\text{dop}} \alpha 4\pi \Phi_{\text{bb}}(\lambda, \Omega) \int_0^W dz n(z) f_{\text{esc}}(\lambda, z). \quad (4.24)$$

(The latter equation holds analogously for n -type samples.) Explicit solutions of the diffusion equation for all excitation modes are given in Refs. [80] and [142]. They depend on the bulk diffusion length L_b , the rear surface recombination velocity S_r , the effective front surface recombination velocity $S_{f,\text{eff}}$ and on the absorption length $L_\alpha = \alpha^{-1}$ of the incident light used for the excitation of the luminescence emission.

The remaining unknown quantity is the luminescence photon escape probability f_{esc} which depends on both depth position and wavelength. The following section reviews analytical expressions for f_{esc} which can be found in the literature and hold for samples with two specular or two lambertian reflecting surfaces.

4.3.2 Review of models for the photon escape probability

Several models describing the spectral luminescence emission of solar cells and wafers can be found in the literature. The models are designed for the description of samples with either two specular reflecting or two lambertian reflecting surfaces and consider detection of the emitted luminescence perpendicular to the sample's surface. A comparison of the model equations to Eq. (4.24) allows to extract the underlying optical model which defines the photon escape probability f_{esc} . This optical model can then be combined with the appropriate charge carrier distribution for electrical and/or optical excitation to calculate the spectral distribution of the emitted luminescence photon flux. The resulting photon escape probabilities are listed in appendix E.1.

Overview of models from literature

- Schick et al. [134] (1992) derive an expression for the spectral luminescence emission of p - n junctions in planar wafers. Multiple internal reflections of luminescence photons at the surfaces are considered. The surfaces are assumed to reflect specular. Thus, photons emerging towards the detector must travel perpendicular to the surfaces inside the sample. The photon escape probability follows from Lambert-Beer's law and decays exponentially with the distance of the photon from the front surface.
- Daub et al. [23] (1995) use the generalized Planck law for indirect transitions [72] to derive an expression for the spectral luminescence emission of planar wafers. The optical model is equal to the one used by Schick et al. Note that in the work of Daub et al., a different coordinate system is used. The transformation to the coordinate system used in this work is carried out by replacing z by $(W - z)$.
- Trupke et al. [31] (1998) address the modelling of luminescence spectra of planar wafers by application of the generalized Planck law and also analyze the impact of surface texture on the emission spectrum. Their model is equal to the one used by Daub et al. Thus, again a coordinate transformation $z \rightarrow (W - z)$ is necessary to compare the photon escape probability to the one derived in this work.
- Würfel et al. [79] (2007) also use the generalized Planck law for indirect transitions [72] to derive an expression for the spectral luminescence emission of planar solar cells. Their model is designed to evaluate EL images taken with a Si-CCD camera at wavelengths below 1050 nm. The result

is similar to the one obtained by Daub et al., but only one internal reflection at the rear surface is taken into account since photon reabsorption is considerably strong in the considered wavelength range.

- Rüdiger et al. [135] (2007) also apply the generalized Planck law to model the spectral luminescence emission of textured wafers. They consider multiple internal lambertian reflections at the surfaces, i.e. the directions of reflected photons are completely randomized and each photon travels under a specific angle θ to the surface afterwards. Since measurements of luminescence spectra yield the average of many luminescence photons, for the modelling of luminescence spectra it is sufficient to consider an averaged escape probability. Due to the isotropic distribution of photon directions, the latter is *not* simply given by an exponential decay. It can, however, be approximated by an exponential decay using an effective optical path which is not perpendicular but under an angle θ_n to the surfaces and thus extended by a factor $1/\cos(\theta_n)$. If reabsorption is negligible, θ_n approaches 60° (see appendix E.2) which corresponds to a doubling of the optical path length. This approximation is used throughout the model for all wavelengths.
- Kirchartz et al. [120] (2008) apply the reciprocity relation [73] between the spectral external quantum efficiency and the spectral EL emission to model the spectral luminescence emission of planar and textured solar cells. In both cases, an infinite number of internal reflections at the surfaces is taken into account. For the description of the planar case, specular internal reflections at the surfaces are assumed. The resulting photon escape probability is equal to the one calculated by Daub et al. For the textured case, this model also assumes lambertian reflection at the surfaces. However, the non-exponential decay of the escape probability which results from the lambertian reflections is explicitly calculated instead of using the approximation of a doubled optical path length for all wavelengths as in the model of Rüdiger et al.
- Brüggemann [136] (2009) uses the generalized Planck law for indirect transitions [72] to model the spectral luminescence emission of planar wafers. The escape probability is equal to the escape probability calculated by Schick et al.
- Green [137] (2011) derives analytical expressions for the photoluminescence of silicon bricks and wafers. The photon escape probability is equal to the one used by Schick et al.

Comparison of models to experiment

In order to compare the models from literature with measurements, spectrally resolved PL measurements are carried out on a $379\ \mu\text{m}$ thick silicon wafer with both surfaces polished (sample A) and a $362\ \mu\text{m}$ thick silicon wafer with both surfaces textured with random pyramids (sample B). Both samples are FZ-Si (*n*-type) with a resistivity of $2\ \Omega\text{cm}$. The surfaces are passivated by a $15\ \text{nm}$ thick layer of Al_2O_3 . The measurements are carried out using the setup described in section 2.2.3. Data acquisition is performed using the tec5 CompactSpec spectrometer. A relative intensity calibration of the spectrometer is performed as described in section 2.2.4. The luminescence emission is stimulated by monochromatic laser light at a wavelength of $808\ \text{nm}$ incident onto the front surface. The laser spot is widened to homogeneously illuminate an area of $15 \times 15\ \text{cm}^2$ (larger than the sample) with an intensity of $10\ \text{mW}/\text{cm}^2$. Calculations with PC1D [126] show that the concentration of minority charge carriers in the sample is then one order of magnitude below that of the majority charge carriers which means that low-level injection conditions are fulfilled. The emitted luminescence radiation is collected by a fiber mounted perpendicular to the front surface at a distance of $3\ \text{cm}$.

Figure 4.9 shows the measured spectra together with the simulated spectra according to the models discussed above. For the simulations, the general description of luminescence spectra given by Eq. (4.24) is used together with the specific photon escape probabilities (see appendix E.1) and the charge carrier distribution under illumination according to Ref. 80. Simulations show that the charge carrier distribution within the sample hardly affects the shape of the resulting normalized lumines-

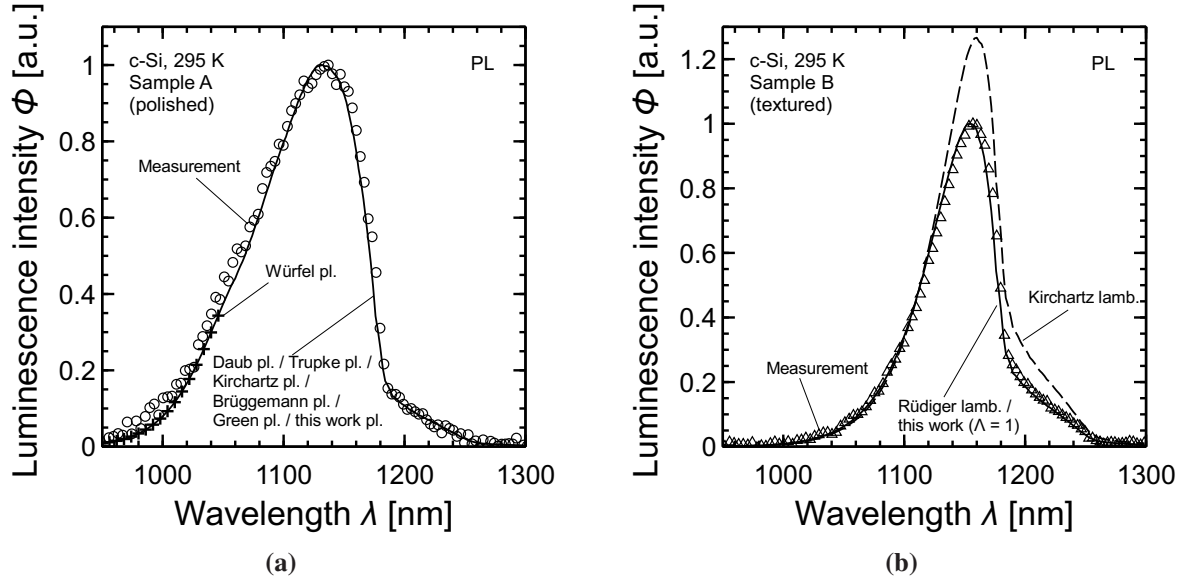


Figure 4.9: Measured luminescence spectra of a polished (a) and a textured (b) float zone (FZ) silicon wafer (markers) and spectral luminescence emission according to the models discussed in the text (lines).

cence spectrum (see Fig. 4.16). Only in the case of $L_b < W$, small deviations become visible in the short-wave part of the spectrum. For the samples described above, $L_b > W$ holds. Thus, for the simulations shown here, $L_b = 500 \mu\text{m}$ and $S_r = S_{f,\text{eff}} = 10 \text{ cm/s}$ is used. The absorption coefficient as determined in this work is used for the simulations. Front and rear surface reflectance R_f and R_b (see appendix E.1) are set to 0.31 for the planar models (according to the fresnel reflectance of a planar silicon-air interface) and 0.928 (according to calculations in Ref. 111) for the lambertian model of Kirchartz. For the refractive index of silicon, a value of $n_{\text{Si}} = 3.6$ is used. Within the wavelength range of interest, the relative deviation of $n_{\text{Si}}(\lambda)$ from this value stays below 3% and is therefore neglected. The data shown is normalized at the short wavelength part of the spectrum (wavelengths below 1050 nm). The model of Würfel et al. is designed for wavelengths below 1050 nm and is therefore only plotted for these wavelengths.

In general, the models allow to reproduce the measured spectra. Both measurements and simulations show a strong dependence of the luminescence spectrum on the topography of the surfaces. The spectrum of the textured sample peaks around 1160 nm, while the peak of the spectrum of the polished sample is located around 1130 nm. The peak shift can be explained as follows: In the polished sample, the majority (about 92%) of the long-wavelength photons is trapped inside the sample due to total internal reflection and cannot contribute to the measured luminescence signal. In the textured sample, the direction of these photons is randomized which means that part of these photons is not trapped anymore and escapes from the sample. This leads to an enhanced emission of long-wavelength photons and consequently to a peak shift of the spectrum towards longer wavelengths.

4.3.3 Spectral luminescence emission of samples with a textured front surface and an arbitrary rough rear surface

The preceding section discussed the spectral luminescence emission of samples with either two planar or two lambertian surfaces. However, solar cells usually feature a textured front surface and an arbitrary rough rear surface and thus represent an intermediate case. Therefore, we turn to the question if the existing models are also suitable for the description of luminescence spectra of samples with only one textured (lambertian) surface.

Experimental findings

Figure 4.10 shows the measured photoluminescence spectrum of the sample with two textured surfaces already shown in Fig. 4.9 (sample B, circles) together with the spectra of a sample with one textured and one polished surface (sample C, triangles, same material, $W = 362 \mu\text{m}$). Both spectra are again normalized at the short wavelength part of the spectrum. For sample C, there is no significant difference between the normalized spectra with the textured or the polished surface facing the detector. Thus, for reasons of clarity only the latter spectrum is shown. For wavelengths above 1100 nm, the luminescence emission of sample B (two textured surfaces) is enhanced compared to sample C (one textured and one planar surface). This is a consequence of the different surface topographies: As has already been stated, the randomisation of photon directions enhances the luminescence emission in the long-wave part of the spectrum. Randomization of photon directions and thus also photon emission in the long-wave part of the spectrum are increased if two textured surfaces are present.

Derivation of an optical model for samples with arbitrary rough surfaces

So far, it was shown that the surface topography of the sample strongly affects the luminescence photon escape probability and thus the luminescence spectrum. If both surfaces are polished, the spectrum peaks around 1130 nm. If both surfaces are textured, the emission of long-wavelength photons is enhanced. This causes a peak shift of about 30 nm towards longer wavelengths. If one surface is textured and one is polished, the peak is also located around 1160 nm, but the enhancement of long-wavelength photon emission is not as strong as for two textured surfaces. In the following, a general optical model is introduced which accounts for all of the mentioned effects. It is derived by applying the reciprocity relation between the electroluminescence spectrum and the spectral quantum efficiency of a solar cell [73]. This allows to take advantage of an optical model originally introduced to analyze quantum efficiency measurements on random pyramide textured solar cells with rough rear surfaces.

The optical reciprocity theorem of Rau [73] which has already been mentioned in section 2.3 relates the spectral electroluminescence (EL) emission Φ_{EL} of a solar cell per photon energy interval dE into a solid angle $d\Omega$ to its external quantum efficiency EQE per photon energy interval dE under illumination from the solid angle $d\Omega$. It reads

$$\Phi_{\text{EL}}(E, \Omega) dE d\Omega = \Phi_{\text{bb}}(E, \Omega) dE d\Omega EQE(E, \Omega) \left[\exp\left(\frac{V}{V_T}\right) - 1 \right] \quad (4.25)$$

where V denotes the junction voltage and V_T the thermal voltage. Incidence and emission of the photons are both assumed to be perpendicular to the sample's surface. In terms of wavelengths and for detection of Φ_{EL} perpendicular above the front surface from a certain solid angle Ω , it can be transformed (see appendix E.5) into

$$\Phi_{\text{EL,det}}(\lambda) d\lambda \approx \Omega \Phi_{\text{bb}}(\lambda) d\lambda EQE(\lambda) \exp\left(\frac{V}{V_T}\right) \quad (4.26)$$

where $\Phi_{\text{EL,det}}$ is the detected luminescence photon flux. Following Kirchartz et al. [120], this theorem is used to derive a model for the spectral distribution of the EL emission from a model for the external quantum efficiency.

For the purpose of modelling EL spectra using the optical reciprocity theorem (Eq. (4.26)), it is instructive to recall the definition of the EQE via the normalized generation rate under illumination g and the collection probability f_c [129], which can be written as

$$EQE(\lambda) = \int_0^W dz g(\lambda, z) f_c(z) . \quad (4.27)$$

z denotes the distance of a volume element inside the solar cell from the front surface at a given position (x_0, y_0) on the solar cell. A detailed model of the generation rate g under illumination for solar cells with planar or textured front surfaces was introduced by Basore [129] and later extended by Brendel et al. [111] for application to arbitrary wavelengths and use with thin-film solar cells. By introduction of a lambertian factor Λ , the extended model accounts for the degree of lambertian reflection at the rear surface. The idealized cases of a planar (specular reflecting) and a completely rough (lambertian reflecting) rear surface are described by $\Lambda = 0$ and $\Lambda = 1$, respectively. The model is designed to describe thin-film solar cells and therefore considers optical generation of charge carriers in the emitter, space charge region and substrate region. As shown in Ref. 124, over 95% of the luminescence radiation emitted by common crystalline silicon solar cells is generated in the base. For the purpose of modeling luminescence spectra, it is thus reasonable to restrict the analysis to the base contributions, i.e. $g(\lambda, z) = 0$ outside the base region. For this case, the simplified model reads

$$g(\lambda, z) = (1 - R_f) \left[\frac{\alpha}{\cos \theta_1} \exp\left(\frac{-\alpha z}{\cos \theta_1}\right) + \frac{\alpha}{\cos \theta_2} T_1 R_{b1} \exp\left(\frac{-\alpha(W-z)}{\cos \theta_2}\right) + \frac{\alpha}{\cos \theta_n} \frac{T_1 R_{b1} T_2 R_{f1}}{1 - T_n^2 R_{fn} R_{bn}} \times \left(\exp\left(\frac{-\alpha z}{\cos \theta_n}\right) + T_n R_{bn} \exp\left(\frac{-\alpha(W-z)}{\cos \theta_n}\right) \right) \right]. \quad (4.28)$$

The parameters are defined according to Fig. 4.2 and Ref. 111. The model assumes that the direction of light is completely randomized after three internal reflections at the surfaces. T_1 , T_2 and T_n denote the transmittance of the solar cell for light propagating under an angle θ_1 , θ_2 and θ_n , respectively, and follow from Lambert-Beer's law. R_f is the reflectance of the front surface for light incident onto the sample from above. R_{f1} and R_{fn} account for the first and subsequent internal reflections of light at the front surface. Correspondingly, R_{b1} and R_{bn} account for internal reflections at the rear surface. R_{b1} and R_{bn} are assumed to equal a rear surface reflectance R_b in order to reduce the number of model parameters. The roughness of the rear surface, described by the lambertian factor Λ , is included in the parameters θ_2 , T_2 and R_{f1} . The determination of these parameters is explained in detail in Ref. 111 and is also briefly summarized in appendix E.1. Additionally, the calculation of the effective path angle θ_n of randomized light is outlined in appendix E.2.

In order to model the *EQE* according to Eq. (4.27), an expression for the collection probability f_c must be derived as a last step. Again, the analysis can be restricted to the base region. The validity of the optical reciprocity theorem implies the applicability of Donolato's theorem [144], stating that the collection efficiency $f_c(z)$ under illumination equals the normalized minority charge carrier density $\tilde{n}_d(z)$ in the dark:

$$f_c(z) = \tilde{n}_d(z). \quad (4.29)$$

$\tilde{n}_d(z)$ is obtained as a solution of the diffusion equation [40] and reads

$$\tilde{n}_d(z) = \frac{n_d(z)}{n_d(0)} = \cosh\left(\frac{z}{L_b}\right) - \frac{L_b}{L_{\text{eff}}} \sinh\left(\frac{z}{L_b}\right). \quad (4.30)$$

It depends on the bulk diffusion length L_b of the minority charge carriers and the effective diffusion length L_{eff} , which is a function of L_b and the rear surface recombination velocity S_r . Note that

$$n_d(0) = \frac{n_i^2}{N_{\text{dop}}} \left[\exp\left(\frac{V}{V_T}\right) - 1 \right] \approx \frac{n_i^2}{N_{\text{dop}}} \exp\left(\frac{V}{V_T}\right). \quad (4.31)$$

Inserting Eqs. (4.27) to (4.31) into Eq. (4.26) yields an expression for the spectral distribution of the EL emission which is valid for pyramide textured solar cells with partly rough rear surfaces and holds for the whole wavelength range of luminescence emission originating from radiative band-to-band

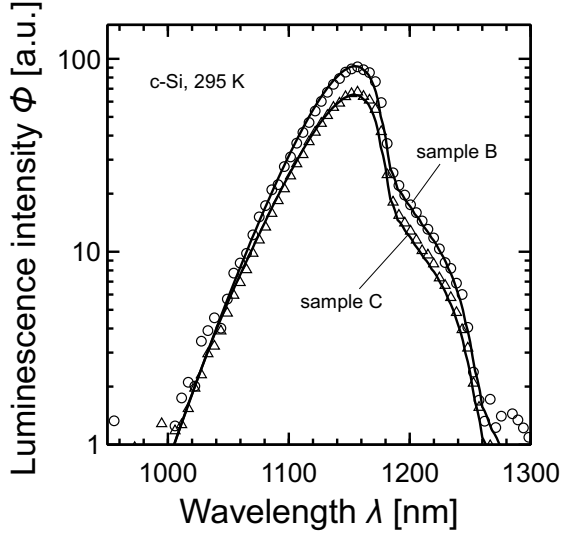


Figure 4.10: Measured photoluminescence spectra of samples with two textured surfaces (sample B, circles) and one textured and one polished surface (sample C, triangles). The model introduced in this work (Eq. (4.34), see next paragraph) is visualized by the solid lines.

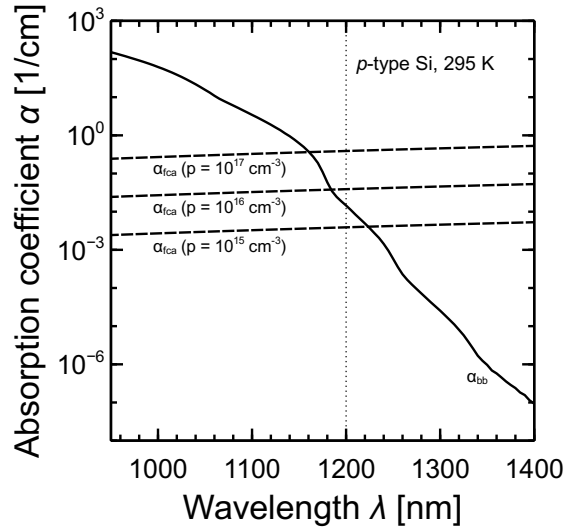


Figure 4.11: Absorption coefficient α_{bb} as determined in this work and α_{fc} from Ref. 37 as a function of wavelength for a p -type sample with different doping concentrations.

recombination. This model of the spectral electroluminescence emission,

$$\Phi_{EL,det}(\lambda) = \Omega \Phi_{bb}(\lambda) \exp\left(\frac{V}{V_T}\right) \times \int_0^W dz g(\lambda, z) \tilde{n}_d(z), \quad (4.32)$$

can now be compared to Eq. (4.24), yielding the general relation

$$f_{esc}(\lambda, z) = \frac{\Omega}{4\pi n_{Si}^2} \frac{g(\lambda, z)}{\alpha(\lambda)} \quad (4.33)$$

and, in particular, for the photon escape probability,

$$f_{esc}(\lambda, z) = \frac{\Omega}{4\pi n_{Si}^2} \frac{1 - R_f}{\cos \theta_1} \left[\frac{1}{\cos \theta_1} \exp\left(\frac{-\alpha z}{\cos \theta_1}\right) + \frac{1}{\cos \theta_2} T_1 R_{b1} \exp\left(\frac{-\alpha(W-z)}{\cos \theta_2}\right) \right] + \frac{1}{\cos \theta_n} \frac{T_1 R_{b1} T_2 R_{f1}}{1 - T_n^2 R_{fn} R_{bn}} \times \left(\exp\left(\frac{-\alpha z}{\cos \theta_n}\right) + T_n R_{bn} \exp\left(\frac{-\alpha(W-z)}{\cos \theta_n}\right) \right). \quad (4.34)$$

This expression is valid for samples with any configuration of textured and arbitrary rough surfaces. For example, $\theta_1 = \theta_2 = \theta_n = 0$ holds for a sample with two planar surfaces since both surfaces reflect specular and the light is not randomized. For this case, Eq. (4.34) simplifies to the expression given by Schick, Daub, Trupke, Kirchartz, Brüggemann and Green (Eq. (E.1)) and thus contains these models as a special case. For two textured surfaces, $\Lambda = 1$ holds and θ_1 is determined by the geometry of the front surface. For one textured and one planar surface, θ_1 is again determined by the geometry of the front surface and $\Lambda = 0$.

Extension of the model to account for free carrier absorption

Free carrier absorption (FCA) occurs due to inter-band or intra-band transitions of free charge carriers. Unlike band-to-band absorption, where a charge carrier is excited from the valence band into the

conduction band, FCA does not generate additional free charge carriers. In general, FCA depends on the wavelength of the photon and on the charge carrier density within the sample. Green [37] states an empirical parametrization of the absorption coefficient for FCA α_{fc} which holds for carrier densities around 10^{18} cm^{-3} (see section 1.2.4):

$$\alpha_{fc} [\text{cm}^{-1}] = n K_n \lambda^a + p K_p \lambda^b \quad (4.35)$$

where n and p are the densities of electrons and holes in units of cm^{-3} , λ is the wavelength in units of nm, $K_n = 2.6 \times 10^{-27}$, $K_p = 2.7 \times 10^{-24}$, $a = 3$ and $b = 2$. In Fig. 4.11, a comparison of α_{fc} and the band-to-band absorption coefficient α_{bb} is exemplarily shown for a p -type sample with different doping densities. For doping densities below 10^{16} cm^{-3} , as used in the bulk of typical solar cells and wafers, the total absorption coefficient $\alpha = \alpha_{bb} + \alpha_{fc}$ is dominated by α_{bb} for wavelengths below approximately 1200 nm, where the majority of luminescence emission is located. Consequently, the spectral luminescence photon generation rate r_{ph} in the bulk (Eq. (2.37)) is determined by the coefficient of band-to-band absorption α_{bb} which means $\alpha \approx \alpha_{bb}$. Note that literature data of the absorption coefficient as widely used in the photovoltaic community (e.g. [23, 37]) usually refers to the coefficient of band-to-band absorption. Using this data for the simulation of luminescence spectra, for instance, means using the approximation $\alpha \approx \alpha_{bb}$ in Eq. (4.24). In highly doped front and rear regions (e.g. emitter and BSF), where typical doping densities are of the order of 10^{18} to 10^{20} cm^{-3} , FCA cannot be neglected as shown in Fig. 4.11. In fact, FCA may substantially increase reabsorption, which decreases the photon escape probability and thereby affects the luminescence spectrum. In order to account for FCA in the front and rear region, the expression for the luminescence photon escape probability Eq. (4.34) can be extended with "FCA damping factors"

$$g_{f,i} = \exp\left(-\frac{\alpha_{fc} W_f}{\cos \theta_i}\right), \quad i = \{1, 2, n\} \quad (4.36)$$

and

$$g_{r,i} = \exp\left(-\frac{\alpha_{fc} W_r}{\cos \theta_i}\right), \quad i = \{1, 2, n\} \quad (4.37)$$

which are multiplied with the reabsorption (exponential) terms. W_f and W_r are the thickness of the front and rear region, respectively. α_{fc} refers to the averaged doping density in the corresponding region. Note that for textured samples, where the emitter layer is orientated parallel to the front surface, θ_1 in Eq. (4.36) should be replaced by $\gamma - \theta_1$, where γ is the facet angle of the front texture (see Fig. 4.2), to account for the orientation of the emitter layer. The change in θ_2 and θ_n due to FCA is usually negligible. With this extension, Eq. (4.34) takes the form

$$\begin{aligned} f_{esc}(\lambda, z) = & \frac{\Omega}{4\pi} \frac{1 - R_f}{n_{Si}^2} \left[\frac{g_{f,1}}{\cos \theta_1} \exp\left(\frac{-\alpha z}{\cos \theta_1}\right) + \frac{g_{r,2}}{\cos \theta_2} \tilde{T}_1 R_{b1} \exp\left(\frac{-\alpha(W-z)}{\cos \theta_2}\right) \right. \\ & \left. + \frac{1}{\cos \theta_n} \frac{\tilde{T}_1 R_{b1} \tilde{T}_2 R_{f1}}{1 - \tilde{T}_n^2 R_{fn} R_{bn}} \times \left(g_{f,n} \exp\left(\frac{-\alpha z}{\cos \theta_n}\right) + \tilde{T}_n R_{bn} g_{r,n} \times \exp\left(\frac{-\alpha(W-z)}{\cos \theta_n}\right) \right) \right] \end{aligned} \quad (4.38)$$

where

$$\tilde{T}_i = g_{f,i} g_{r,i} T_i, \quad i = \{1, 2, n\}. \quad (4.39)$$

Note that the approximation $\alpha \approx \alpha_{bb}$ may still be used in Eq. (4.38) for typical silicon solar cells and wafers. In order to take FCA in the bulk into account additionally (which might be necessary, for instance, for highly doped samples), $\alpha = \alpha_{bb} + \alpha_{fc}$ has to be used in Eqs. (4.38) and (E.10)

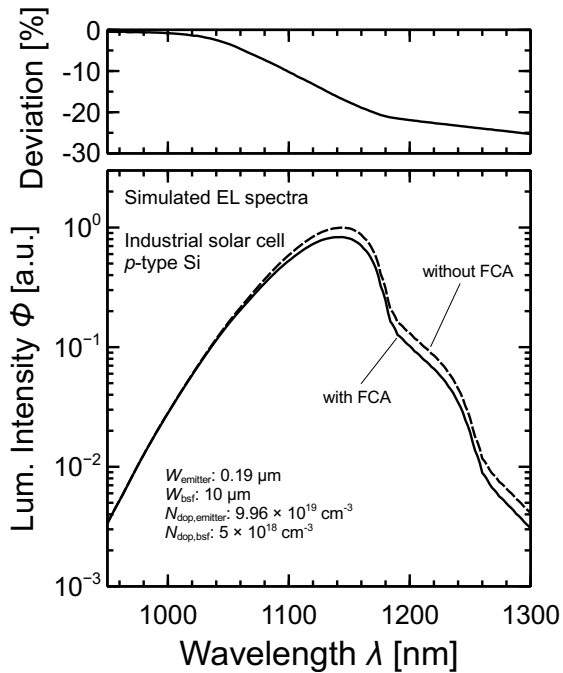


Figure 4.12: Simulation of EL spectra of a *p*-type silicon sample visualizing the impact of FCA in the emitter and BSF on the luminescence spectrum.

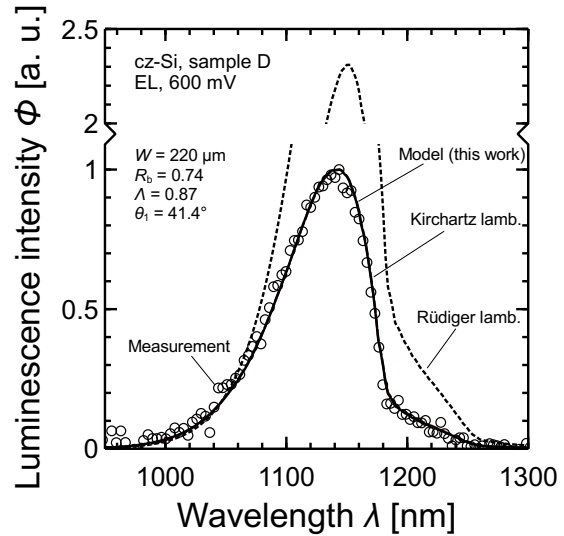


Figure 4.13: Measured and modeled EL spectrum of an industrial monocrystalline cz-Si solar cell at an applied voltage of 600 mV.

through (E.12). Figure 4.12 exemplarily visualizes the impact of FCA on the resulting luminescence spectrum. For the simulation, the same parameters as for the simulation of a typical electroluminescence spectrum in Fig. 4.13 are used (see next paragraph). As can be seen, FCA has a noticeable impact on the luminescence spectrum: Depending on the wavelength, relative deviations above 20% occur. Thus, FCA in the emitter and BSF region should be taken into account for practical cases. This holds especially when analyzing reflectance data of samples in order to quantify the rear surface reflectance R_b : Neglecting FCA may result in an underestimation of R_b of the order of 10% or even more, depending on the thickness and dopant concentration of the emitter and BSF layers.

Comparison to experiment and literature

The spectrum predicted by the model derived in this work for samples with two textured or two polished surfaces is visualized in Fig. 4.9 together with the measurements and models from literature. For the planar sample, θ_1 , θ_2 and θ_n are set to zero. As already mentioned, the model is equivalent to the planar models of Schick, Daub, Trupke, Kirchartz, Brüggemann and Green for the planar case. For the textured sample, $\theta_1 = 41.4^\circ$ and $\Lambda = 1$. The resulting spectrum equals the spectrum predicted by the model of Rüdiger. For the sample with one textured and one polished surface (shown in Fig. 4.10), the slightly decreased luminescence intensity in the long wavelength part of the spectrum compared to the sample with two textured surfaces is reproduced by the model (using $\Lambda = 0$). Figure 4.13 shows the normalized measured EL spectrum of a 250 μm thick industrial monocrystalline cz-Si solar cell (sample D, manufactured in 2008), which represents a sample with a textured front surface, anti-reflection coating and rough rear surface. The applied voltage is 600 mV. Calculations with PC1D show that the concentration of minority charge carriers in the sample is then one order of magnitude below that of the majority charge carriers which means that low-level injection conditions are fulfilled. The measurement (represented by the open circles) is shown together with a plot of the models for textured surfaces discussed in this paper (solid lines). All data is again normalized at the

short wavelength part of the spectrum since only relative luminescence intensities were measured. The model parameters are determined as follows: Assuming a thickness of the rear metallization of 30 μm , a bulk thickness W of 220 μm is obtained. Following the approach of Ref. [111], the parameters R_b and Λ are determined from a reflectance measurement (see appendix E.1) which is corrected for the metallization of the front surface. Resulting parameters are $R_b = 0.74$ and $\Lambda = 0.87$. R_f is assumed to be equal to the measured reflectance in the wavelength range of strong absorption (absorption length $L_\alpha \ll W$) and extrapolated for the wavelength range of weak absorption ($L_\alpha > W$). θ_1 follows from the geometry of the front surface and the law of defraction and is $\theta_1 = 41.4$. The values used for the calculation of the charge carrier distribution are determined from a fit to the measured EQE. A bulk diffusion length $L_b = 140 \mu\text{m}$ and a rear surface recombination velocity $S_r > 500 \text{ cm/s}$ is obtained. Note that the charge carrier distribution mainly affects the intensity of luminescence emission. The shape of the (normalized) spectrum is hardly affected when choosing other values for L_b and S_r . FCA in the emitter and in the BSF is taken into account using Eqs. (4.36) to (4.39) with $W_f = 0.19 \mu\text{m}$, $N_{\text{dop},f} = 9.96 \times 10^{19} \text{ cm}^{-3}$, $W_r = 10 \mu\text{m}$ and $N_{\text{dop},r} = 5 \times 10^{18} \text{ cm}^{-3}$. These values also result from the evaluation of the EQE measurement. Good agreement between measured electroluminescence spectrum and model is found. Note that R_f is not independent of the wavelength (as for the wafer samples discussed in this work) due to the presence of the anti-reflection coating (ARC). Also note that the deviations of Rüdiger's model from the measured data in Fig. 4.13 are due to the wavelength-independent surface reflectances assumed in the model ($R_f = R_b = 1 - 1/n_{\text{Si}}^2 \approx 0.92$, see Eq. (E.3); this is a valid approximation for wafer samples without ARC, for which the model was designed, but not for solar cells).

For comparison, Fig. 4.14 shows the *EQE* and total reflectance of the solar cell. Measurements and models are represented by the open circles and solid lines, respectively. The dashed line visualizes the base contribution to the *EQE* on which the model of the luminescence spectrum is based. The model uses the same parameters as for the model of the luminescence spectrum in Fig. 4.13. All curves refer to the intermediate which means that they are corrected for the front grid metallization. As expected, the *EQE* is also well described by the model. Above 950 nm, good agreement between measured *EQE* and modelled base *EQE* contribution is visible, which verifies the approximation of only using the base contribution in the model of the luminescence spectrum.

4.3.4 Impact of absorption coefficient data set on modeled luminescence spectra

As already mentioned in chapter 2.2, the luminescence spectrum is proportional to the absorption coefficient for long wavelengths, where photon reabsorption is negligible. The accuracy of modeled luminescence spectra therefore depends on the absorption coefficient data used as input, especially in the long wavelength region. The data set of the absorption coefficient which is probably most widely used in the photovoltaic community is the one published by Green [32, 40] (1995, updated 2008). Above 1200 nm, the data originates from spectral response measurements on high-efficiency solar cells. In Fig. 3.12, a comparison of Green's data and the data determined in this work is shown. Between 1200 and 1250 nm, the data of Green is larger by about 20%. The impact of the absorption coefficient data set used for the simulation is shown in Fig. 4.15. As can be seen, the data of Green leads to an overestimation of the luminescence intensity between 1200 and 1250 nm. This overestimation has been confirmed by other authors as well [115].

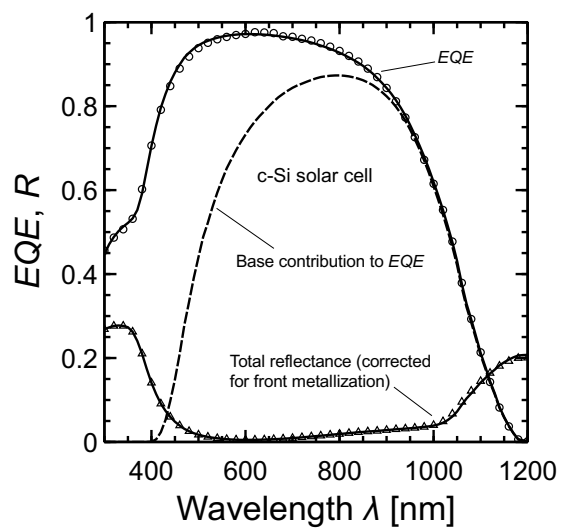


Figure 4.14: Measured (circles) and modeled (lines) EQE and total reflectance spectrum of the solar cell modeled in Fig. 4.13. The dashed line shows the base contribution to the EQE which is used in the model of the luminescence spectrum. All curves refer to the intermediate area which means that they are corrected for the front grid metallization.

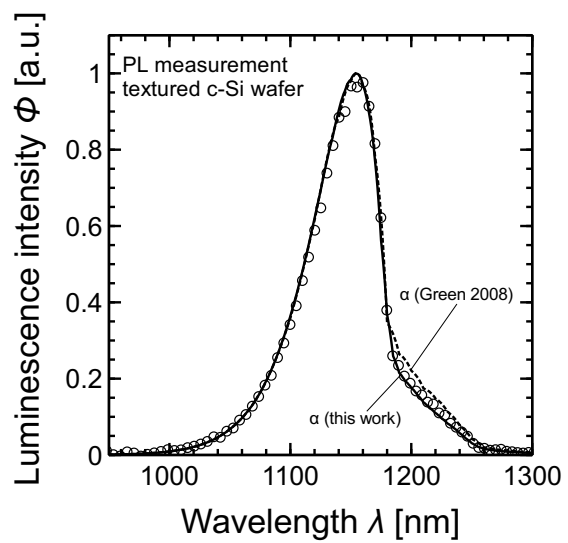


Figure 4.15: Measured c-Si wafer PL spectrum (circles) and model calculated with the absorption coefficient data as determined in this work and as published by Green [32] (solid/dotted line).

4.4 Determination of the rear surface reflectance of silicon solar cells from their luminescence spectrum

The rear surface reflectance of solar cells affects the light trapping capabilities of solar cells, which enhance the absorption of light at near-infrared wavelengths. This leads to an increased short circuit current and consequently an increased energy conversion efficiency. The experimental determination of the rear surface reflectance is thus an important characterization technique for the optimization of solar cells. It is routinely done by measuring the hemispherical reflectance of the sample with a spectrophotometer like the one used in this work (see chapter 2.1). The reflectance spectrum is then fitted with a model of the reflectance which contains the rear surface reflectance as a parameter. The model of the reflectance can be derived, for instance, from the optical model described in section 4.3.3. A disadvantage of this method for typical, double side contacted solar cells is the necessity of a correction of the reflectance spectrum for the front surface metallization of the solar cell unless the measurement spot is so small that it fits between two fingers. Moreover, the measurement of the reflectance spectrum with a typical scanning spectrophotometer involves the acquisition of several calibration baselines and is time consuming.

Based on the model of the spectral luminescence emission presented in the preceding section, it is possible to determine the rear surface reflectance also from a luminescence spectrum. The method only requires a luminescence spectrum measured in relative units, which can be done quickly. The experimental setup is simple as it consists only of a power supply or a laser for the excitation of luminescence emission and a spectrometer for the detection of the latter. The method is outlined in the following.

The analytical model of the spectral luminescence emission provides a simple option to analyze the impact of the various electrical and optical properties of a solar cell on the resulting luminescence spectrum. Figure 4.16 shows the dependence of the spectrum on the roughness of the rear surface (Λ), the bulk diffusion length of the minority charge carriers (L_b), the rear surface recombination velocity (S_r) and the front surface reflectance (R_f). The values of the parameters given in the top right corner of Fig. 4.16 are used for the simulation. For each curve, some parameters are varied according to the legend of the figure. It is obvious that all of these parameters affect the intensity of the luminescence emission (changes are of the order of 70% rel.). However, the shape of the spectrum is hardly affected. Relative measurements of the spectral luminescence emission thus cannot distinguish between these parameters.

The situation is different for the rear surface reflectance, as shown in Fig. 4.17. When varying R_b from 0 to 1, the intensity in the long-wave part of the spectrum increases about two orders of magnitude. This implies a change of the shape as well as a shift of the peak wavelength of about 30 nm as indicated. Hence, unlike the other parameters (Λ , L_b , S_r , R_f), the rear surface reflectance R_b affects the luminescence spectrum in a way that is accessible by relative measurements of the spectral luminescence emission. The effect is explained as follows: Due to negligible reabsorption at long wavelengths, long-wave luminescence photons can be subject to multiple internal reflections before they escape. For these photons, the escape probability is enhanced when R_b increases. In the short-wave part of the spectrum, however, photon reabsorption is significant. Hence, luminescence photons that are eventually emitted towards the rear surface and reflected there are reabsorbed before they can escape. The luminescence intensity in the short-wave part of the spectrum is thus hardly affected by R_b .

In summary, the analysis of the impact of the various model parameters on the luminescence spectrum shows that only the rear surface reflectance R_b causes a shift of the peak wavelength, whereas the other parameters slightly affect the emitted intensity but not the shape of the spectrum. However, only the latter is detectable by measuring relative luminescence intensity. Hence, the unambiguous relation between the peak wavelength λ_{peak} and the rear surface reflectance R_b can be used for the

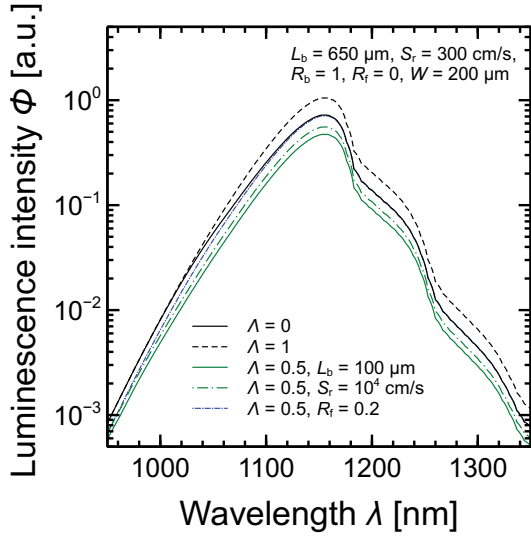


Figure 4.16: Dependence of the luminescence spectrum of a c-Si solar cell on the roughness of the rear surface (Λ), the bulk diffusion length of the minority charge carriers (L_b), the rear surface recombination velocity (S_r) and the front surface reflectance (R_f).

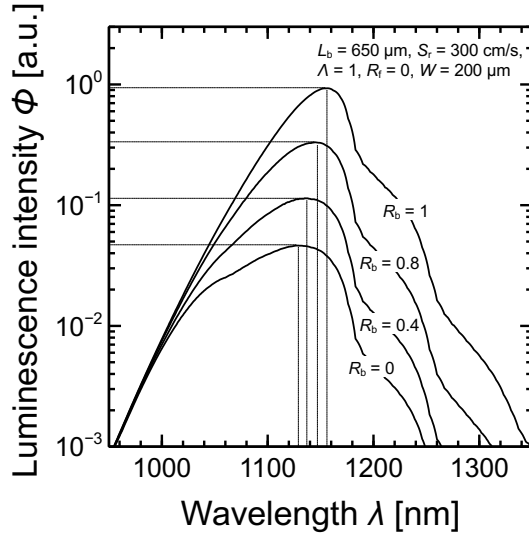


Figure 4.17: Dependence of the luminescence spectrum of a c-Si solar cell on the rear surface reflectance R_b .

determination of the latter. For this purpose, the following procedure is applied:

1. A look-up table for R_b as a function of the peak wavelength λ_{peak} is generated using the model. The thickness of the bulk is an input parameter for this calculation. Note that this also holds for the “classical” way of determining R_b from a fit of reflectance data [111]. For the generation of the look-up table, typical values for the roughness of the rear surface (Λ), the front surface reflectance (R_f) and for the charge carrier distribution can be used, as these parameters do not affect the peak wavelength (see Fig. 4.16).
2. The luminescence spectrum is measured in relative units. Since the peak wavelength of the spectrum is not affected by the charge carrier distribution within the sample, electrical or optical excitation can be used (EL or PL).
3. The peak wavelength of the spectrum is determined. This is done by fitting the data with a second order polynomial in the wavelength range from 1110 nm to 1170 nm.
4. As a last step, R_b is obtained from the look-up table using the measured peak wavelength.

The applicability of the method is experimentally confirmed by comparison of the rear surface reflectance $R_{b,\text{lum}}$ determined from luminescence measurements to the rear surface reflectance $R_{b,\text{sp}}$ as determined using the spectrophotometer described in section 2.1. For this purpose, different wafers and solar cells are selected, which exhibit different rear surface reflectances, e.g., due to variations of the dielectric rear surface passivation. For each sample, a reflectance spectrum $R(\lambda)$ is measured and the rear surface reflectance $R_{b,\text{sp}}$ is obtained by fitting the data with the model

$$R = 1 - (1 - R_f) \left[1 - T_1 R_{b,\text{sp}} T_2 (1 - R_{f1}) - \frac{T_1 R_{b,\text{sp}} T_2 R_{f1} R_{b,\text{sp}} (1 - R_{fn}) T_n^2}{1 - R_{b,\text{sp}} R_{fn} T_n^2} \right], \quad (4.40)$$

which follows from the optical model introduced in section 4.3.3. Moreover, the luminescence spectrum (EL for solar cells, PL for wafers) is measured and the peak wavelength λ_{peak} is determined following the procedure described above. The rear surface reflectance $R_{b,\text{lum}}$ is then calculated from a look-up table which is generated using the model. The measured reflectance curves and corresponding luminescence spectra are shown in Fig. 4.18. Figure 4.19 compares the values of $R_{b,\text{lum}}$ and $R_{b,\text{sp}}$

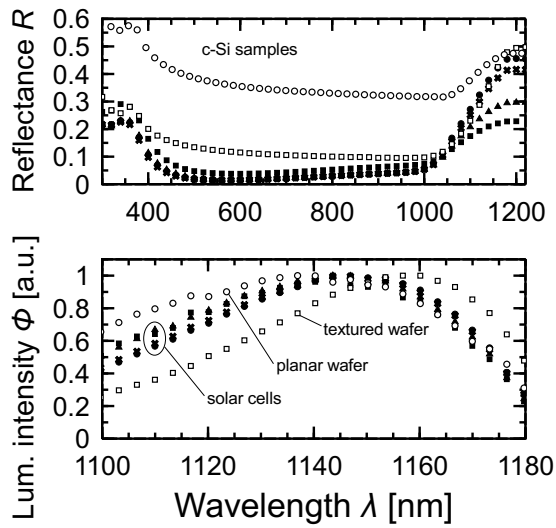


Figure 4.18: Measured reflectance curves and corresponding luminescence spectra of c-Si samples. Same symbols refer to the same sample in both plots.

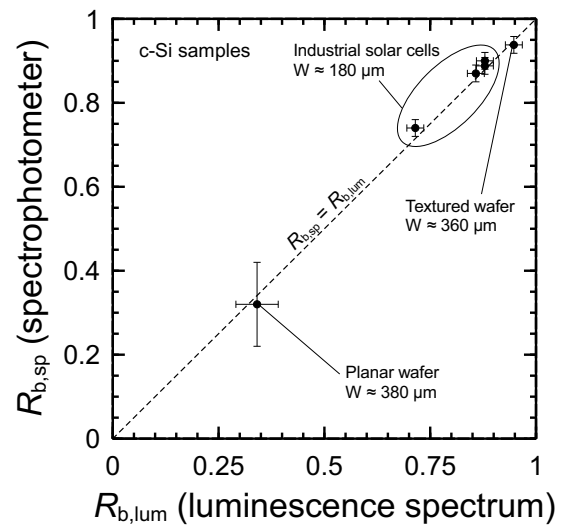


Figure 4.19: Comparison of the rear surface reflectances $R_{b,sp}$ and $R_{b,lum}$ of silicon samples determined using a spectrophotometer or using luminescence measurements, respectively.

for the different samples obtained from the measured data. The dashed line visualizes the situation $R_{b,sp} = R_{b,lum}$. The error bars do not represent a rigorously determined uncertainty, but rather a “guide to the eye” showing the order of magnitude of uncertainty which is expected from experience. Good agreement between $R_{b,sp}$ and $R_{b,lum}$ is obtained, verifying the applicability of the method.

For planar samples, the peak shift is generally small (about 4 nm only when going from $R_b = 0$ to $R_b = 1$). This is a consequence of the fact that in a planar sample, about 92% of the luminescence photons are trapped by total internal reflections at the surfaces. Only photons inside the escape cone can be emitted towards the detector. For a silicon/air interface, the critical angle of total reflection is $\approx 16.1^\circ$. For typical setups where the luminescence emission is detected perpendicular from above, as used in this work, this angle is even reduced by the solid angle of detection. Hence, the length of the optical path of all detectable luminescence photons within the sample is comparable and the effect of an enhanced emission of long wavelength photons is much less pronounced than for textured samples. The steep slope of the $R_b(\lambda_{peak})$ curve makes the determination of R_b very sensitive to small variations of the peak wavelength. A variation of λ_{peak} of 0.5 nm changes the value of R_b by about 10% absolute. For planar samples, the method can thus only be used for a rough estimation of R_b , but not for an accurate determination. This expectation is reflected by the large error bars for the planar wafer. However, in practice, planar samples are irrelevant due to their small absorptance. Practical solar cells feature a front surface texture in order to improve the absorptance at near-infrared wavelengths. For textured samples, the slope of the $R_b(\lambda_{peak})$ curve is smaller, enabling an accurate determination of R_b .

Summary and outlook

This work presents an extensive study of the coefficient of band-to-band absorption of crystalline silicon. It is motivated by the finding that, although the determination of the absorption coefficient of crystalline silicon is an ongoing subject of research since 1955, the published studies investigate the absorption coefficient only in a part of the wavelength range being of interest for specific applications. Moreover, different measurement methods are used. A comparison of literature data shows deviations of up to 20% between these data sets. It is unclear whether these deviations are only due to the specific properties of the investigated samples or whether they originate from systematic deviations or uncertainties due to the different measurement approaches. The accuracy of the literature data cannot be assessed since measurement uncertainties have not been determined systematically or, as for the major part of the studies, have not been indicated at all. This lack of information casts doubt on the correctness of combined data sets which have been calculated from different sources and cover a larger wavelength range.

In order to resolve the discrepancies, the coefficient of band-to-band absorption of crystalline silicon is determined under well-defined laboratory conditions using spectroscopic ellipsometry, measurements of reflectance and transmittance, spectrally resolved measurements of luminescence emission and measurements of the spectral responsivity of silicon solar cells. For the first time, different measurement approaches are thus combined in one study and allow the absorption coefficient to be measured over more than fifteen orders of magnitude. The new data cover the wavelength range from 250 to 1450 nm. Moreover, a systematic measurement uncertainty analysis is carried out for each measurement method. The analysis is based on an extensive characterization of the measurement setups and follows the *Guide to the expression of uncertainty in measurement* (GUM), which is the international standard for the evaluation of measurement uncertainties. Thereby, substantiated estimates of the uncertainty of the coefficient of band-to-band absorption of crystalline silicon are given for the first time. The data obtained during this work at the *Institute for Solar Energy Research Hamelin* (ISFH) are consolidated by comparison with measurement results obtained at the *Physikalisch-Technische Bundesanstalt* (PTB, the German National Metrology Institute) in Braunschweig, Germany, as well as at *The Australian National University* (ANU) in Canberra, Australia. It is shown that the data obtained in this work reduces the uncertainty of silicon solar cell energy conversion efficiency predictions by means of device simulations by a factor of 2 compared to literature data.

Spectroscopic ellipsometry determines the change of polarization of light that undergoes a reflection at a surface. The absorption coefficient is obtained by fitting the polarization data with a model for the dielectric function of the sample. In the literature, the uncertainty of absorption coefficient data re-

sulting from spectroscopic ellipsometry is either not considered at all or determined by varying single fit parameters according to their variance calculated by the fit algorithm. This approach may yield an estimation for the maximum error of the data so determined, but it neglects correlations between the fit parameters and is based on the covariance matrix determined by the fit algorithm, which can usually not be interpreted as an estimate of uncertainty in a rigorous sense. In this work, a *Monte-Carlo* simulation is used for the evaluation of the polarization data in order to perform a quantitative analysis of the measurement uncertainty in accordance with the GUM. This novel approach for the evaluation of ellipsometry data allows all relevant uncertainty contributions and correlations to be taken into account adequately. Moreover, the Monte-Carlo analysis shows that the standard evaluation approach tends to overestimate the absorption coefficient in the near-infrared region.

Measurements of reflectance and transmittance are a straight-forward method for the determination of the absorption coefficient near the band edge. The method can be used in the wavelength range where the transmittance varies between its saturation values. This implies that the measurement signal varies over several orders of magnitude. Especially for small signals, the measurement results can be subject to systematic deviations caused by the measurement setup. The measurements presented in this work are carried out with a commercially available Varian Cary two-channel spectrophotometer, which is widely used throughout the scientific community. However, measurement uncertainties caused by the instrument are not considered systematically in the literature. By the extensive characterization of the instrument, a systematic deviation due to inertia of the measurement amplifier is identified, which leads to deviations of the order of 50 to 100% relative for small measurement signals. A mathematical model of this effect is presented, allowing the deviations to be corrected and thereby to extend the useable dynamic range of the instrument by more than one order of magnitude. Moreover, measurement uncertainties caused by the instrument are quantified systematically for the first time. The resulting absorption coefficient data are compared to data determined at the PTB on samples from the same wafers. In these investigations, the reflectance is determined by a combination of the results obtained using a commercial Varian Cary spectrophotometer as well as using a special setup with increased angle of acceptance in the primary national reference system for spectral reflectance. The agreement of both absorption coefficient data sets with respect to their measurement uncertainty is shown by calculating the E_n criterion, which is used for the examination of conformity of measurement data in international key comparisons. It is shown that absorption coefficient data obtained from measurements of reflectance and transmittance are subject to large uncertainties (of the order of 100% rel. or above) at wavelengths beyond 1180 nm. Using these data for scaling of luminescence or spectral responsivity data, as demonstrated in the literature, thus leads to large uncertainties of the scaled data. Spectrally resolved luminescence measurements are used for the determination of the coefficient of band-to-band absorption beyond the band edge. For the accurate determination of the absorption coefficient, the spectrometer must be calibrated with respect to wavelength and irradiance. For this purpose, a new calibration facility was built up at ISFH during this work. Based on an extensive measurement uncertainty analysis, the performance of a scanning spectrometer system and a diode-array spectrometer system for measurements of luminescence spectra of crystalline silicon samples is evaluated. It is shown that the use of the scanning spectrometer system allows the uncertainty to be reduced by a factor of 2 to 3 compared to the use of the diode-array spectrometer system. Moreover, it is shown that photoluminescence measurements on planar (polished) wafer samples introduce potential uncertainties for the determination of the absorption coefficient due to an apparent dependence of the spectrum on the angle and distance of detection. The effect might originate from stray light of the excitation laser. This assumption is supported by the finding that the effect is neither observed for photoluminescence measurements on textured wafers nor for electroluminescence measurements in general. In order to circumvent possible problems with photoluminescence data, electroluminescence measurements are carried out on specially designed lab-type solar cells with polished surfaces and a novel procedure for the determination of the absorption coefficient from these data is developed.

The resulting absorption coefficient data are compared to absorption coefficient data originating from measurements of the spectral responsivity of silicon solar cells carried out at the PTB. By calculating the E_n criterion for both data sets, the agreement of the results of both methods is quantitatively verified for the first time. Moreover, this analysis provides the first rigorous experimental evidence for the correctness of an underlying optical reciprocity theorem, on which the expected equality of both measurement approaches is based.

In order to obtain a combined data set for the coefficient of band-to-band absorption from the different measurement results, the calculation of a weighted average with respect to hidden correlations in the data is discussed in detail. Moreover, an extensive discussion of the requirement of corrections for free carrier absorption within the samples is performed. It is shown that small corrections are necessary, which are, however, hardly visible on a logarithmic scale.

Based on the results of this work, the uncertainty of silicon solar cell energy conversion efficiency predictions by means of device simulations, which require the absorption coefficient as input, is analyzed rigorously for the first time. For this purpose, a new analytical model for the uncertainty is presented and verified by Monte-Carlo simulations using the solar cell simulator PC1D. It is shown that the uncertainty of energy conversion efficiency predictions by means of device simulations due to the uncertainty of the absorption coefficient data determined in this work is of the order of 0.1% relative. For current silicon solar cells with an energy conversion efficiency of about 20%, this corresponds to an uncertainty of about 0.02%. Compared to using literature data of the absorption coefficient, the uncertainty is thus reduced by a factor of 2.

As an application of the absorption coefficient data, a new analytical model of the spectral luminescence emission of silicon solar cells and wafers is presented. This model consists of an electrical and an optical part and thus separates the electrical from the optical modeling. It is valid for samples with any configurations of planar and arbitrary rough surfaces and can be used for both electrical and optical excitation. The methodology outlined in this work allows other models of the spectral luminescence emission from literature, which are valid only for the description of either electroluminescence or photoluminescence measurements, to be generalized for use with both types of excitation. Comparison of the models shows that the new model presented in this work is the first which correctly describes the luminescence spectrum of samples with one planar and one rough surface. Based on the analysis of the impact of the various sample properties on the luminescence spectrum, which is facilitated by the new model, a novel approach for the determination of the rear surface reflectance of industrial silicon solar cells from the peak wavelength of their luminescence spectrum is presented and experimentally validated. This approach can thus be implemented with a simple measurement setup and the measurement can be performed contactless.

Further work on the absorption coefficient of crystalline silicon could aim at the extension of the wavelength range into the infrared by using, for instance, photoluminescence measurements on textured wafer samples with increased excitation intensity. The wavelength range beyond 1450 nm is of interest, for instance, for optical communication technologies or fundamental physical research, both of which require the transparency of silicon. In this context, an important issue might be the investigation of the dependence of the luminescence spectrum on the angle and distance of detection, which is mentioned above. Moreover, the uncertainty of the temperature coefficient of the absorption coefficient could be analyzed. Device simulations, which require the absorption coefficient as input, are often performed for different device temperatures. However, the uncertainty along with the transformation of the absorption coefficient data to other temperatures is still unknown.

Instability of nonlinearity corrections obtained by the superposition method

In the literature, an approach for the correction of nonlinearities using the superposition method is found [92, 93]. This approach is based on the following considerations: For each wavelength, the detector signal N_x is proportional to the irradiance I :

$$N_x = k I \eta(N_x) \quad (\text{A.1})$$

where k is the proportionality constant and η is the sensitivity of the detector, which may depend on N_x in general. This dependence causes a nonlinear behavior of the detector. The sensitivity can be expressed as the sum of a linear part η_0 and a nonlinear part $\Delta\eta(N_x)$ which depends on the detector signal:

$$\eta(N_x) \approx \eta_0 - \Delta\eta(N_x) . \quad (\text{A.2})$$

Equations (A.1) and (A.2) lead to

$$N_x \left(1 + \frac{k I \Delta\eta(N_x)}{N_x} \right) = k I \eta_0 , \quad (\text{A.3})$$

where the term $k I \Delta\eta(N_x)/N_x$ represents the signal contribution due to the nonlinearity. In order to obtain a correction for this effect, the fraction is approximated by a polynomial,

$$\frac{k I \Delta\eta(N_x)}{N_x} = a N_x + b N_x^2 + c N_x^3 + d N_x^4 + \dots , \quad (\text{A.4})$$

yielding

$$N_x (1 + a N_x + b N_x^2 + c N_x^3 + d N_x^4 + \dots) = k I \eta_0 . \quad (\text{A.5})$$

The coefficients of the polynomial can be determined experimentally by using a superposition method, where the detector is consecutively illuminated by Lamp 1, Lamp 2 and both lamps together. The irradiance levels on the detector during these measurements are I_1 , I_2 and

$$I_3 = I_1 + I_2 . \quad (\text{A.6})$$

For this situation, Eq. (A.5) can be rewritten as

$$N_{x1} \left(1 + a N_{x1} + b N_{x1}^2 + c N_{x1}^3 + d N_{x1}^4 + \dots \right) = k I_1 \eta_0 , \quad (\text{A.7})$$

$$N_{x2} \left(1 + a N_{x2} + b N_{x2}^2 + c N_{x2}^3 + d N_{x2}^4 + \dots \right) = k I_2 \eta_0 , \quad (\text{A.8})$$

$$N_{x3} \left(1 + a N_{x3} + b N_{x3}^2 + c N_{x3}^3 + d N_{x3}^4 + \dots \right) = k I_3 \eta_0 . \quad (\text{A.9})$$

Summation of Eqs. (A.8) and (A.9) and subtraction of Eq. (A.9) yields

$$N_{x1}(\dots) + N_{x2}(\dots) - N_{x3}(\dots) = 0 \quad (\text{A.10})$$

because of Eq. (A.6). From this equation, the coefficients of the polynome can be factored out. For instance, for a fourth-order-polynome,

$$a(N_{x1}^2 + N_{x2}^2 - N_{x3}^2) + b(N_{x1}^3 + N_{x2}^3 - N_{x3}^3) + c(N_{x1}^4 + N_{x2}^4 - N_{x3}^4) + d(N_{x1}^5 + N_{x2}^5 - N_{x3}^5) = N_{x3} - N_{x2} - N_{x1} \quad (\text{A.11})$$

is obtained. Note that the procedure can easily be extended to polynomials of higher orders.

Using the definitions

$$\begin{aligned} x_1 &= N_{x1}^2 + N_{x2}^2 - N_{x3}^2 \\ x_2 &= N_{x1}^3 + N_{x2}^3 - N_{x3}^3 \\ &\dots \end{aligned}$$

and

$$y = N_{x3} - N_{x2} - N_{x1}, \quad (\text{A.12})$$

Eq. (A.11) can be compactly rewritten as

$$ax_1 + bx_2 + cx_3 + dx_4 = y. \quad (\text{A.13})$$

For the determination of the four unknown coefficients $a-d$, four measurements of the irradiance triples at different irradiance levels are carried out. In matrix notation, this reads

$$\begin{pmatrix} x_{1,1} & x_{1,2} & x_{1,3} & x_{1,4} \\ x_{2,1} & x_{2,2} & x_{2,3} & x_{2,4} \\ x_{3,1} & x_{3,2} & x_{3,3} & x_{3,4} \\ x_{4,1} & x_{4,2} & x_{4,3} & x_{4,4} \end{pmatrix} \times \begin{pmatrix} a \\ b \\ c \\ d \end{pmatrix} = \begin{pmatrix} y_1 \\ y_2 \\ y_3 \\ y_4 \end{pmatrix}. \quad (\text{A.14})$$

Solving of the latter equation for y yields the unknown coefficients and the signal contribution due to nonlinearity

$$\Delta N_x(N_x) = a N_x + b N_x^2 + c N_x^3 + d N_x^4. \quad (\text{A.15})$$

The calculation of the correction using the method described above always requires the solution of a system of equations that can be represented by

$$\mathbf{A} \vec{s} = \vec{y}$$

where \mathbf{A} is the matrix containing the $x_{i,j}$, \vec{s} is the solution vector containing the coefficients a, b, c, d, \dots of the polynomial and \vec{y} is the vector containing the y_i . The calculation of the solution \vec{s} requires the inversion of the matrix \mathbf{A} . From numerical mathematics, it is known that such a solution may be unstable, i.e., a small relative change in \mathbf{A} or \vec{y} may lead to a large relative change in \vec{s} [145]. In this case, using the solution \vec{s} for correction purposes can introduce significant errors. The relative changes of \vec{s} and \vec{y} are related by

$$\frac{\|\Delta \vec{s}\|}{\|\vec{s}\|} \leq \text{Cond}(\mathbf{A}) \times \frac{\|\Delta \vec{y}\|}{\|\vec{y}\|}, \quad (\text{A.16})$$

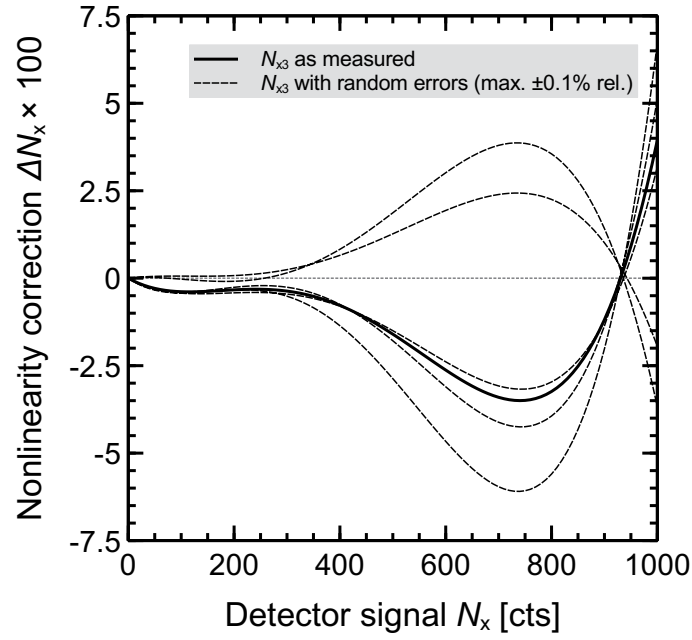


Figure A.1: Impact of random errors in N_{x3} of $\pm 0.1\%$ relative at most on the calculated correction.

where

$$\text{Cond}(A) = \|A\| \|A^{-1}\| \quad (\text{A.17})$$

is the *condition number* of the matrix A and $\|\cdot\|$ denotes the matrix norm. A condition number close to 1 indicates that the accuracy of \vec{y} and \vec{s} is of the same order of magnitude. In this case, the matrix is said to be *well-conditioned*. If the condition number is much larger than 1, a small relative change in \vec{s} can cause a much larger relative change in \vec{y} . The matrix is then said to be *ill-conditioned*. For the measurements carried out in this work, the condition number is of the order of 10^8 or larger. This means that small errors in the measured signals can already have a significant impact on the calculated solution. Figure A.1 exemplary shows the impact of a small relative error in N_{x3} on the calculated correction ΔN_x . The correction is calculated five times and a random error of $\pm 0.1\%$ rel. at most is added to N_{x3} for each calculation. The small variations in N_{x3} lead to very different results for the correction. Note that for experimentally determined quantities such as N_{x3} , errors of the order of 0.1% relative are likely to occur.

Impact of chuck reflectance on luminescence spectra

In order to ensure a laterally homogeneous distribution of the sample temperature during PL measurements and to facilitate a precise temperature control, the sample is placed on a black anodized brass plate. However, the models used for the evaluation of the PL data assume that the sample is surrounded by air. It is thus necessary to verify that the presence of the brass plate does not affect the resulting data. For this purpose, ray tracing simulations are carried out using the program *Daidalos* [146–148]. These simulations either assume a double side polished or a double side textured silicon sample with an antireflection coating (ARC) consisting of a 15 nm thick layer of Al_2O_3 on both sides. The simulation domains are shown in Fig. B.1. At the edges of the sample, reflecting boundaries are placed. On top of the sample, a photon counter is positioned which counts all emitted photons. A second counter at the same position only counts the photons which are emitted into an angle of 12° . This angle approximately corresponds to the detection angle of the spectrometer's entrance optic. The photons are generated by an area light source which is placed in the middle of the sample. The photons are distributed laterally homogeneous and emitted isotropically. The simulation is carried out for temperatures of 10°C and 60°C , which represent a lower and upper limit of the sample temperature during the measurements in this work. In order to take the roughness of the brass plate into account, a gap of $1\ \mu\text{m}$ is assumed between the surfaces of the sample and the brass plate. This reflects the fact that the sample is in touch with the plate only at distinct positions. The measured hemispherical reflectance of the brass plate as shown in Fig. B.2 is used as input for the simulation. The brass plate is assumed to have a specular reflection characteristic. This leads to a conservative estimation of its impact on the spectrum, as can be seen from the following considerations: The generation of luminescence photons inside the sample is isotropic. The probability for a photon to escape from or enter through the sample's surface is maximum in the direction perpendicular to the surface (corresponding to an emission angle of 0° in the usual definition) and decreases towards the direction parallel to the surface (corresponding to an emission angle of 90°). This is a consequence of increasing photon re-absorption and surface reflectance for larger emission angles. For a planar sample, specular reflection at the brass plate retains the angle of each photon and thereby the probability to re-enter the sample. In contrast, light scattering at the brass plate would lead to a randomization of angles and thereby to a reduced re-entry probability. Consequently, a smaller part of the photons which are reflected at the brass plate are able to emerge from the sample's surface and contribute to the detectable luminescence emission than in the case of a specular reflection. In a textured sample, the light is randomized by reflections at the (rough) surfaces. In this case, the photon directions are random anyway and it is irrelevant whether the reflection at the brass plate randomizes the photon directions or not. Figure B.3 exemplary shows the results of the simulation for a sample temperature of 10°C . At

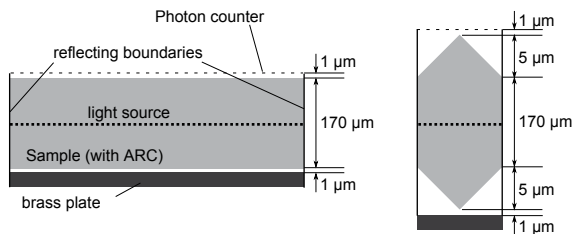


Figure B.1: Sketch of the domains for the ray tracing simulations (not to scale). Left: Planar sample, right: Textured sample.

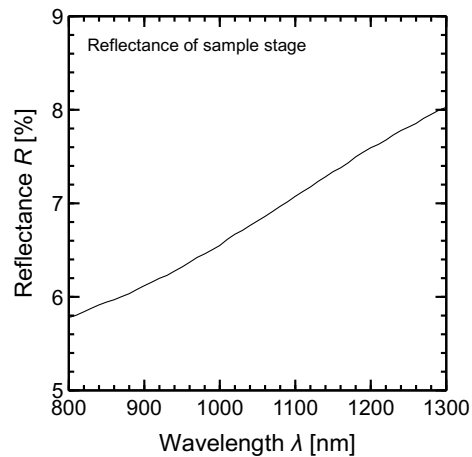


Figure B.2: Hemispherical reflectance of the black anodized brass plate.

60 °C, the conclusions drawn from the results are the same. The plots show the total number of emitted photons at the front surface as a function of wavelength. The uncertainty of the data is given by the Poisson distribution, which describes the detection probability for photons [149]. As can be seen, the number of photons is increased by the additional reflection at the brass plate. Between 800 and 1100 nm, the number of photons increases with respect to wavelength. This is a consequence of the decreasing photon reabsorption, which is negligible above 1200 nm. It is important to note that for the determination of the absorption coefficient, absolute changes of the number of emitted photons are irrelevant as only relative luminescence intensities are measured. The top graphs show the ratio of the numbers of emitted photons. The dashed lines visualize a linear fit of the data, serving as a guide to the eye. The ratio is approximately constant with respect to wavelength, which implies that the shape of the luminescence spectrum is not affected by the additional reflection at the brass plate. Note that PL measurements on planar samples are not used for the determination of the absorption coefficient due to the problems described in section 2.2.9. The results are only shown for the sake of completeness. For textured samples, the ratio varies by only 0.0021 %/nm (abs.) on average, which is negligible for the evaluation of the absorption coefficient.

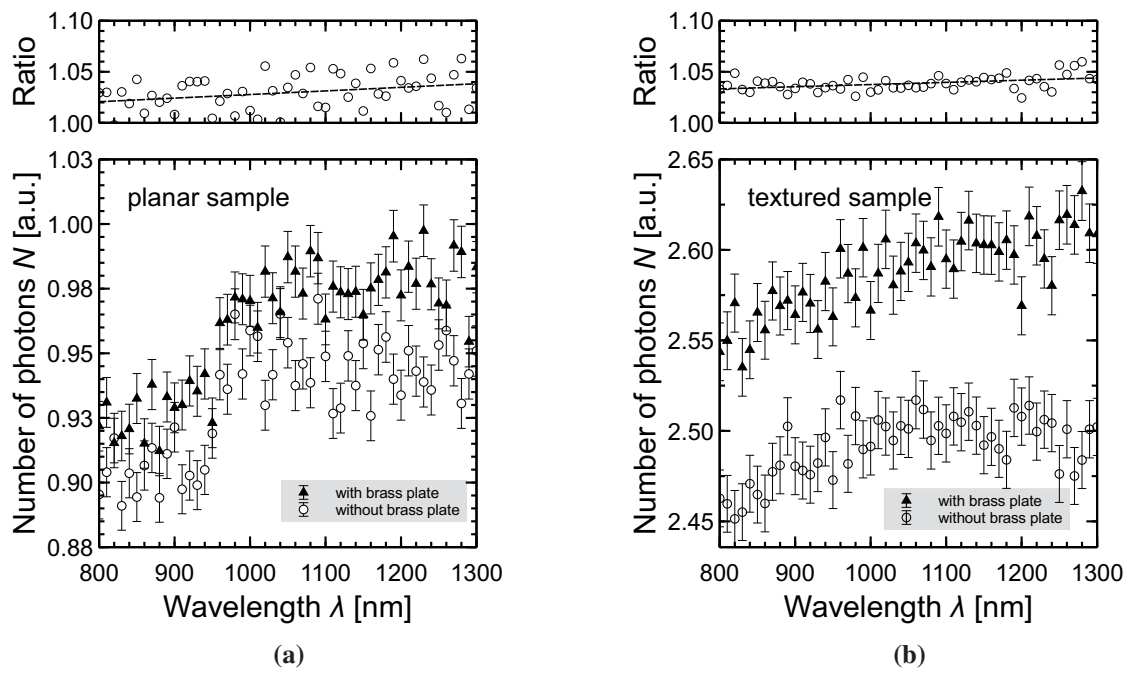


Figure B.3: Results of the ray tracing simulations for the investigation of the impact of the additional reflection at the brass plate on the luminescence spectrum.

C.1 Varian Cary 5000: Signal correction for reflectance/transmittance measurements with the PbS detector

In order to obtain a correction that determines

$$Y = \frac{Y_{\text{sample}} - Y_0}{Y_{\text{mon}} - Y_0}, \quad Y = \{S_{\text{sample}}, S_{100}, S_0\} \quad (\text{C.1})$$

as defined in Eq. (2.9) from the signal levels Y'_{mon} , Y'_{sample} and Y'_0 which are actually measured due to the inertia of the detector and/or measurement amplifier and give

$$Y' = \frac{Y'_{\text{sample}} - Y'_0}{Y'_{\text{mon}} - Y'_0}, \quad (\text{C.2})$$

a model of the detector signal as a function of time is required. Depending on the physical origin of the inertia effect, different functions can be assumed. At this point, it should be noted that the exact procedure for the determination of the detector signal is unknown. However, as shown below, the different corrections obtained by assuming different functions lead to the same results within $\pm 0.01\%$ absolute.

- A decay of the charge carrier concentration within the detector is a possible reason for the occurrence of the inertia effect. In this case, the signal decay would be expected to be exponentially. According to Fig. C.1, the time-dependent detector output signal $Y'(t)$ is then described by

$$Y'(t) = \begin{cases} Y_{\text{mon}} + (Y'(0) - Y_{\text{mon}}) e^{-kt}, & 0 \leq t \leq \tau \\ Y_{\text{sample}} + (Y'(\tau) - Y_{\text{sample}}) e^{-k(t-\tau)}, & \tau \leq t \leq 2\tau \\ Y_0 + (Y'(2\tau) - Y_0) e^{-k(t-2\tau)}, & 2\tau \leq t \leq 3\tau \end{cases} \quad (\text{C.3})$$

and

$$Y'(t) = Y'(t + n \times 3\tau), \quad n = 1, 2, 3, \dots \quad (\text{C.4})$$

In the latter equations, k is the (unknown) time constant of the signal decay and τ the length of the decay time. Y_{mon} , Y_{sample} and Y_0 denote the saturation levels of the signal as defined in Figs.

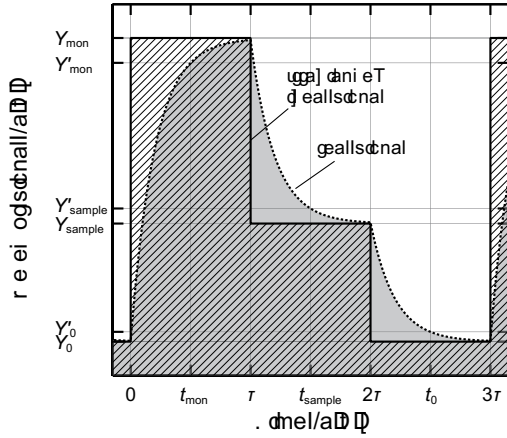


Figure C.1: Detector signal as a function of time assuming an exponential decay.

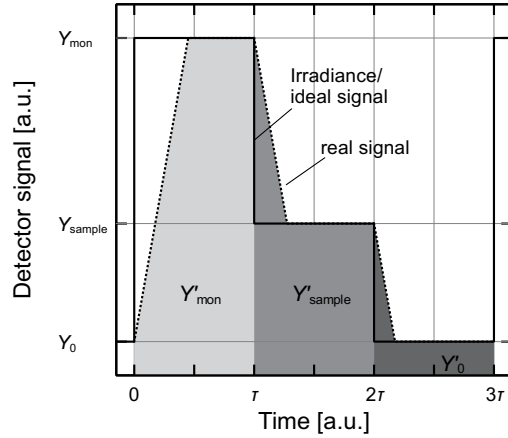


Figure C.2: Detector signal as a function of time assuming a linear decay with constant slope.

2.2 and C.1. The general solution to Eqs. (C.3) and (C.4) is

$$Y'(t) = \begin{cases} \left(Y_{\text{mon}} + Y_{\text{sample}} e^{k\tau} + Y_0 e^{2k\tau} \right) c e^{-kt} + Y_{\text{mon}} (1 - e^{-kt}), & 0 \leq t \leq \tau \\ \left(Y_{\text{sample}} + Y_0 e^{k\tau} + Y_{\text{mon}} e^{2k\tau} \right) c e^{-k(t-\tau)} + Y_{\text{sample}} (1 - e^{-k(t-\tau)}), & \tau \leq t \leq 2\tau \\ \left(Y_0 + Y_{\text{mon}} e^{k\tau} + Y_{\text{sample}} e^{2k\tau} \right) c e^{-k(t-2\tau)} + Y_0 (1 - e^{-k(t-2\tau)}), & 2\tau \leq t \leq 3\tau \end{cases} \quad (\text{C.5})$$

with

$$c = \frac{1}{1 + e^{k\tau} + e^{2k\tau}}. \quad (\text{C.6})$$

A reasonable assumption would be that there are points t_{mon} , t_{sample} and t_0 , which are equidistant in time, at which the signal levels

$$Y'_{\text{mon}} = Y'(t_{\text{mon}}), \quad (\text{C.7})$$

$$Y'_{\text{sample}} = Y'(t_{\text{sample}}), \quad (\text{C.8})$$

$$Y'_0 = Y'(t_0) \quad (\text{C.9})$$

are measured. We define a quantity x such that

$$t_{\text{mon}} = x\tau, \quad (\text{C.10})$$

$$t_{\text{sample}} = (1+x)\tau, \quad (\text{C.11})$$

$$t_0 = (2+x)\tau, \quad (\text{C.12})$$

i.e., x denotes the relative position during the decay time where the signal level is measured. Combining Eqs. (C.3) through (C.12) leads to

$$Y'_{\text{mon}} = \left(Y_{\text{mon}} + Y_{\text{sample}} e^{k\tau} + Y_0 e^{2k\tau} \right) c e^{-k\tau x} + Y_{\text{mon}} (1 - e^{-k\tau x}), \quad (\text{C.13})$$

$$Y'_{\text{sample}} = \left(Y_{\text{sample}} + Y_0 e^{k\tau} + Y_{\text{mon}} e^{2k\tau} \right) c e^{-k\tau x} + Y_{\text{sample}} (1 - e^{-k\tau x}), \quad (\text{C.14})$$

$$Y'_0 = \left(Y_0 + Y_{\text{mon}} e^{k\tau} + Y_{\text{sample}} e^{2k\tau} \right) c e^{-k\tau x} + Y_0 (1 - e^{-k\tau x}). \quad (\text{C.15})$$

By defining the abbreviation

$$\kappa = e^{-k\tau x} \quad (\text{C.16})$$

and assuming that the signal levels are measured in the middle of the decay period, i.e.,

$$x = 1/2, \quad (\text{C.17})$$

the latter equations simplify to

$$Y'_{\text{mon}} = \frac{\kappa Y_0 + \kappa^3 Y_{\text{sample}} + (\kappa^4 - \kappa^3 + \kappa^2 - \kappa + 1) Y_{\text{mon}}}{\kappa^4 + \kappa^2 + 1}, \quad (\text{C.18})$$

$$Y'_{\text{sample}} = \frac{\kappa^3 Y_0 + (\kappa^4 - \kappa^3 + \kappa^2 - \kappa + 1) Y_{\text{sample}} + \kappa Y_{\text{mon}}}{\kappa^4 + \kappa^2 + 1}, \quad (\text{C.19})$$

$$Y'_0 = \frac{(\kappa^4 - \kappa^3 + \kappa^2 - \kappa + 1) Y_0 + \kappa Y_{\text{sample}} + \kappa^3 Y_{\text{mon}}}{\kappa^4 + \kappa^2 + 1}. \quad (\text{C.20})$$

The assumption $x = 1/2$ is reasonable because it corresponds to a measurement in the middle of the interval defined by the rotation of the chopper wheel. Moreover, it allows a closed analytical solution to be calculated. The equations can further be simplified by recognizing that $Y_0 \leq Y_{\text{sample}} \leq Y_{\text{mon}}$ holds. Moreover, these signal levels are constant on relevant time scales. Therefore,

$$Y_0 = 0, \quad (\text{C.21})$$

$$Y_{\text{mon}} = 1 \quad (\text{C.22})$$

and

$$0 \leq Y_{\text{sample}} \leq 1 \quad (\text{C.23})$$

can be assumed without loss of generality, giving

$$Y'_{\text{mon}} = \frac{\kappa^3 Y_{\text{sample}} + \kappa^4 - \kappa^3 + \kappa^2 - \kappa + 1}{\kappa^4 + \kappa^2 + 1}, \quad (\text{C.24})$$

$$Y'_{\text{sample}} = \frac{(\kappa^4 - \kappa^3 + \kappa^2 - \kappa + 1) Y_{\text{sample}} + \kappa}{\kappa^4 + \kappa^2 + 1}, \quad (\text{C.25})$$

$$Y'_0 = \frac{\kappa Y_{\text{sample}} + \kappa^3}{\kappa^4 + \kappa^2 + 1}. \quad (\text{C.26})$$

Inserting Eqs. (C.24) through (C.26) into Eq. (C.2) leads to

$$Y' = \frac{(\kappa^3 + \kappa - 1) Y_{\text{sample}} - \kappa^2 - \kappa}{(\kappa^2 + \kappa) Y_{\text{sample}} + \kappa^3 - \kappa^2 - 1}. \quad (\text{C.27})$$

Note that for an instant change of the signal level, i.e., $\kappa \rightarrow 0$ according to Eq. (C.16), the latter equation yields $Y' = Y_{\text{sample}}$, which is the correct result for this case where a correction is not required.

Equation (C.27) contains two unknowns, namely κ , which describes the time constant of the signal decay, and Y_{sample} , which is to be determined. The quantity Y' is known from the measurement. In order to obtain Y_{sample} , a second measurement is required, namely a measurement of the 0 % baseline S_0 . For this situation, $Y_{\text{sample}} = Y_0$ holds and Eq. (C.27) becomes

$$Y' = S_0 = \frac{-\kappa^2 - \kappa}{\kappa^3 - \kappa^2 - 1}. \quad (\text{C.28})$$

Combining Eqs. (C.27) and (C.28) yields

$$Y_{\text{sample}} = \frac{Y' - S_0}{1 + S_0 (Y' - 1)}. \quad (\text{C.29})$$

Since we assumed $Y_0 = 0$ and $Y_{\text{mon}} = 1$,

$$Y = Y_{\text{sample}} \quad (\text{C.30})$$

holds according to Eq. (2.9), which finally leads to

$$Y = \frac{Y' - S_0}{1 + S_0 (Y' - 1)}, \quad (\text{C.31})$$

which is the correction formula Eq. (2.10).

- Another reasonable possibility would be that the decay is also exponentially, but the detector signal is integrated over the decay period instead of being measured at single distinct points. This case, which is visualized in Fig. C.1 by the shaded areas, can be investigated by integrating Eq. (C.5) over time. This corresponds to an integration of Eqs. (C.13) through (C.15) over x ($0 \leq x \leq 1$). Carrying out the integration, setting $Y_{\text{mon}} = 1$ and $Y_0 = 0$ as described above and inserting the results into Eq. (C.2) leads to

$$Y' = \frac{(\beta^2 + \beta + 1) \ln(\beta) Y_{\text{sample}} + (\beta + 1 - 2\beta^2) Y_{\text{sample}} + \beta^2 - 2\beta + 1}{(\beta^2 + \beta + 1) \ln(\beta) + (2\beta - \beta^2 - 1) Y_{\text{sample}} - \beta^2 - \beta + 2} \quad (\text{C.32})$$

with

$$\beta = e^{k\tau}. \quad (\text{C.33})$$

For the 0 % baseline measurement, this yields

$$Y' = S_0 = \frac{\beta^2 - 2\beta + 1}{(\beta^2 + \beta + 1) \ln(\beta) - \beta^2 - \beta + 2}. \quad (\text{C.34})$$

Combining the latter equations and solving for Y_{sample} leads to

$$Y = \frac{Y' - S_0}{1 + S_0 (Y' - 1)}, \quad (\text{C.35})$$

which is the same correction formula as already derived above. This shows that for an exponential decay, the correction formula does not depend on the method of data acquisition. However, it is reasonable to assume that the detector signal is integrated because this corresponds to a calculation of an average and thereby reduces measurement noise.

- Inertia of the measurement amplifier is another possible reason for the occurrence of the inertia effect. In this case, a linear signal decay with constant slope would be expected, as shown in Fig. C.2. The dependence of the measured 0 % baseline signal on the amplification factor points towards the measurement amplifier as the origin of the effect. Assuming that the detector signal is given by the integral over the period τ , as shown in Fig. C.2, the signal levels Y'_{mon} , Y'_{sample} and Y'_0 follow as

$$Y'_{\text{mon}} = Y_{\text{mon}} \tau + (Y_0 - Y_{\text{mon}}) \frac{\Delta t_1}{2}, \quad (\text{C.36})$$

$$Y'_{\text{sample}} = Y_{\text{sample}} \tau + (Y_{\text{mon}} - Y_{\text{sample}}) \frac{\Delta t_2}{2}, \quad (\text{C.37})$$

$$Y'_0 = Y_0 \tau + (Y_{\text{sample}} - Y_0) \frac{\Delta t_3}{2}. \quad (\text{C.38})$$

Since the signal decay is linearly with constant slope a ,

$$\Delta y = a \Delta t \quad (\text{C.39})$$

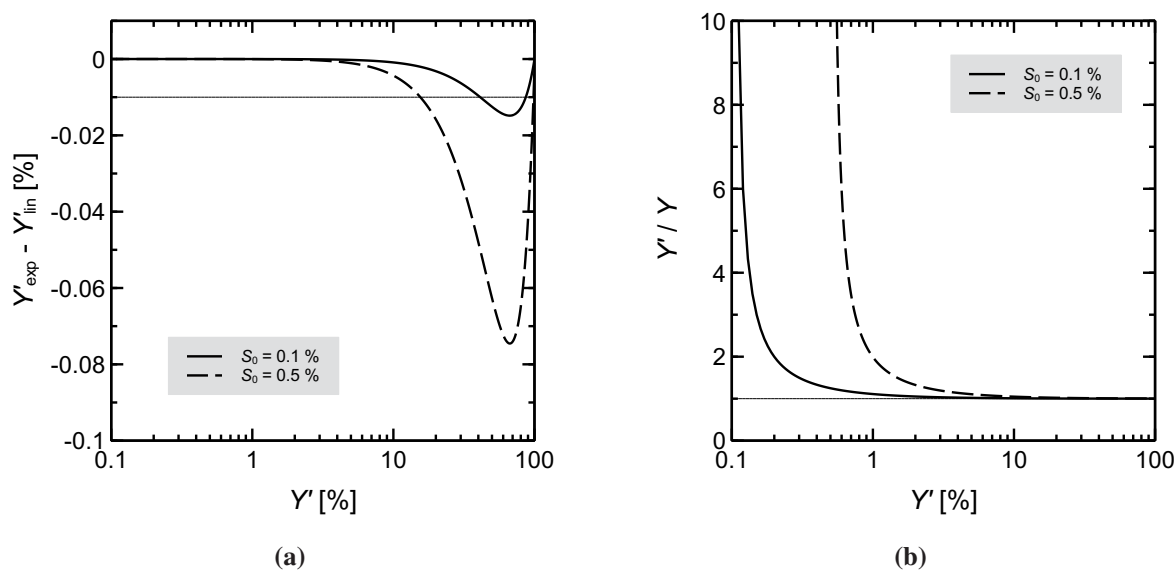


Figure C.3: Comparison of the correction formulas for exponential and linear decay. (a): Absolute deviation between both corrections. (b): Significance of the corrections with respect to the level of the uncorrected detector signal Y' .

holds where Δy denotes the amplitude of the signal change. Combining the latter equations yields

$$Y'_{\text{mon}} = Y_{\text{mon}} \tau - \frac{(Y_0 - Y_{\text{mon}})^2}{2a}, \quad (\text{C.40})$$

$$Y'_{\text{sample}} = Y_{\text{sample}} \tau + \frac{(Y_{\text{mon}} - Y_{\text{sample}})^2}{2a}, \quad (\text{C.41})$$

$$Y'_0 = Y_0 \tau + \frac{(Y_{\text{sample}} - Y_0)^2}{2a}. \quad (\text{C.42})$$

Inserting this result into Eq. (C.2) and following the derivation outlined above, the correction formula

$$Y = \frac{\sqrt{(1 - 4Y')S_0^2 + (4Y'^2 - 2)S_0 + 1} + S_0 - 1}{2Y'S_0} \quad (\text{C.43})$$

is obtained.

A comparison of the correction formulas Eq. (C.31) and Eq. (C.43) for exponential or linear decay, respectively, is shown in Fig. C.3. Figure C.3(a) shows the absolute deviation between the corrected values using the correction for exponential or linear decay, respectively, as a function of the measured (uncorrected) signal Y' . Figure C.3(b) visualizes the impact of the correction as a function of the measured (uncorrected) signal Y' by showing the ratio Y'/Y (Y is the corrected signal). As can be seen, the correction is only significant for small signals below approximately 10 %, depending on the 0 % baseline signal S_0 or the amplification factor g_{amp} , respectively. This confirms the experimental finding shown in Fig. 2.5. Signal levels above 0.5 % for S_0 do not occur during the measurements in this work. Moreover, it can be seen that the absolute deviation between both corrections is below 0.01 % for signal levels below 10 %, where the correction has a significant impact. Compared to the uncertainty of the measured data, this deviation can be neglected, i.e., both corrections yield the same results. For the purpose of simplicity, the correction formula for exponential decay is thus used in this work.

C.2 Uncertainty contribution due to spectral bandwidth

The detector signal N_x at the nominal wavelength λ_i is given by the spectral irradiance $I(\lambda)$ and the spectral sensitivity $S(\lambda)$ of the monochromator/detector system:

$$N_x(\lambda_i) = C \int_0^{\infty} d\lambda I(\lambda) S(\lambda). \quad (\text{C.44})$$

C is a scaling factor which depends on the detector and the read-out electronics. Ideally, $S(\lambda)$ would be given by a Dirac distribution, i.e., $S(\lambda) = \delta(\lambda_i)$. In this case, Eq. (C.44) would give $N_x(\lambda_i) = C I(\lambda_i)$. In reality, S will have a broader distribution. For a worst case estimation, a rectangular distribution for S can be assumed:

$$S(\lambda) = \begin{cases} \frac{1}{\Delta\lambda}, & \lambda_i - \Delta\lambda/2 \leq \lambda \leq \lambda_i + \Delta\lambda/2 \\ 0 & \text{elsewhere} \end{cases} \quad (\text{C.45})$$

Combining Eqs. (C.44) and (C.45) yields

$$N_x(\lambda_i) = \frac{C}{\Delta\lambda} \int_{\lambda_i - \Delta\lambda/2}^{\lambda_i + \Delta\lambda/2} d\lambda I(\lambda). \quad (\text{C.46})$$

If $I(\lambda)$ is constant on the interval $[\lambda_i - \Delta\lambda/2, \lambda_i + \Delta\lambda/2]$, it is easily seen that $N_x(\lambda_i) = C I(\lambda_i)$ still holds. However, if $I(\lambda)$ is not constant, $N_x(\lambda_i)$ will be affected. The change in $N_x(\lambda_i)$ can be calculated by the following consideration: Since $\Delta\lambda$ is small, $I(\lambda)$ can be approximated by a Taylor series expansion around λ_i :

$$I(\lambda) \approx I(\lambda_i) + \left. \frac{dI(\lambda)}{d\lambda} \right|_{\lambda_i} (\lambda - \lambda_i) + \left. \frac{d^2I(\lambda)}{d\lambda^2} \right|_{\lambda_i} \frac{(\lambda - \lambda_i)^2}{2}. \quad (\text{C.47})$$

Inserting Eq. (C.47) into Eq. (C.44) evaluates to

$$N_x(\lambda_i) = C \left[I(\lambda_i) + \frac{(\Delta\lambda)^2}{24} \left. \frac{d^2I(\lambda)}{d\lambda^2} \right|_{\lambda_i} \right] \quad (\text{C.48})$$

as the derivatives evaluated at λ_i are no function of λ and the integral over $(\lambda - \lambda_i)$ disappears. The first summand in the latter equation is the signal due to incident light at the nominal wavelength λ_i . The second summand is the additional signal N_{bw} due to light incident at neighbouring wavelengths. For a specific measurement, it can be calculated approximately by

$$\left. \frac{d^2I(\lambda)}{d\lambda^2} \right|_{\lambda_i} \approx \frac{I(\lambda_i - \Delta\lambda/2) - 2I(\lambda_i) + I(\lambda_i + \Delta\lambda/2)}{(\Delta\lambda/2)^2} \quad (\text{C.49})$$

which represents the approximation of the second derivative for discrete data. From Eqs. (C.48) and (C.49),

$$N_{\text{bw}}(\lambda_i) \approx \frac{N_x(\lambda_i - \Delta\lambda/2) - 2N_x(\lambda_i) + N_x(\lambda_i + \Delta\lambda/2)}{6} \quad (\text{C.50})$$

follows. Taking N_{bw} into account as a rectangularly distributed uncertainty component yields

$$u_{\text{bw}}^2 = \frac{N_{\text{bw}}^2}{3} = \frac{\left(N_x(\lambda_i - \Delta\lambda/2) - 2N_x(\lambda_i) + N_x(\lambda_i + \Delta\lambda/2) \right)^2}{108}. \quad (\text{C.51})$$

C.3 Evaluation of luminescence and spectral responsivity measurements

C.3.1 Incorporation of FCA in the emitter of solar cells into the optical model

The transmittance T_{em} of the emitter layer for a single light pass is given by the Lambert-Beer law Eq. (1.7),

$$T_{\text{em}} = e^{-\alpha W_{\text{em}}} , \quad (\text{C.52})$$

where W_{em} is the thickness of the emitter layer. The absorption coefficient α contains contributions due to band-to-band absorption and free carrier absorption and is thus given by

$$\alpha = \alpha_{\text{bb}} + \alpha_{\text{fc}} . \quad (\text{C.53})$$

Due to the high doping concentration in the emitter, $\alpha_{\text{fc}} \ll \alpha_{\text{bb}}$. Combining the latter equations and using the relation $e^{x+y} = e^x e^y$ yields

$$T_{\text{em}} = e^{-\alpha_{\text{bb}} W_{\text{em}}} e^{-\alpha_{\text{fc}} W_{\text{em}}} . \quad (\text{C.54})$$

In the bulk, $\alpha_{\text{fc}} \ll \alpha_{\text{bb}}$ holds due to the lower doping concentration compared to the emitter. FCA in the bulk can thus be neglected. The transmittance T' of the whole silicon slab for a single light pass is thus

$$T' = T_{\text{em}} e^{-\alpha_{\text{bb}}(W-W_{\text{em}})} = e^{-\alpha_{\text{fc}} W_{\text{em}}} e^{-\alpha_{\text{bb}} W} , \quad (\text{C.55})$$

where W is the thickness of the silicon slab. In the absence of a highly doped emitter layer, the transmittance would be

$$T = e^{-\alpha_{\text{bb}} W} . \quad (\text{C.56})$$

Comparing this to Eq. (C.55) and defining

$$A_{\text{fc}} = e^{-\alpha_{\text{fc}} W_{\text{em}}} \quad (\text{C.57})$$

leads to

$$T' = T A_{\text{fc}} . \quad (\text{C.58})$$

Hence, additional absorption due to FCA in the emitter can be incorporated into the optical model by adding multiplicative terms A_{fc} for each light pass.

C.3.2 Effective rear surface reflectance of solar cells

In the presence of a highly doped emitter layer at the front surface, the experimentally determined rear surface reflectance is actually an effective value which takes additional reabsorption in the emitter due to FCA into account. This is seen from the following considerations: The reflectance R of a silicon slab (without highly doped layer) is given by

$$\begin{aligned} R &= R_{\text{f}} \\ &+ (1 - R_{\text{f}}) e^{-2\alpha W} R_{\text{b}} (1 - R_{\text{f}}) \\ &+ (1 - R_{\text{f}}) e^{-2\alpha W} R_{\text{b}} R_{\text{f}} e^{-2\alpha W} R_{\text{b}} (1 - R_{\text{f}}) \\ &+ (1 - R_{\text{f}}) e^{-2\alpha W} R_{\text{b}} R_{\text{f}} e^{-2\alpha W} R_{\text{b}} R_{\text{f}} e^{-2\alpha W} R_{\text{b}} (1 - R_{\text{f}}) \\ &+ \dots \\ &= R_{\text{f}} + (1 - R_{\text{f}})^2 e^{-2\alpha W} R_{\text{b}} \sum_{i=0}^{\infty} (R_{\text{f}} R_{\text{b}} e^{-2\alpha W})^i \\ &= R_{\text{f}} + \frac{(1 - R_{\text{f}})^2 R_{\text{b}} e^{-2\alpha W}}{1 - R_{\text{f}} R_{\text{b}} e^{-2\alpha W}} . \end{aligned} \quad (\text{C.59})$$

The latter equation takes an infinite number of internal reflections into account and makes use of the relation

$$\sum_{i=0}^{\infty} q^i = \frac{1}{1-q}, \quad |q| \leq 1 \quad (\text{C.60})$$

for the infinite geometric series [150]. For a solar cell, it can be extended in order to take FCA in the emitter into account by using the results of section C.3.1:

$$\begin{aligned} R_{\text{cell}} &= R_f \\ &+ (1 - R_f) A_{\text{fc}}^2 e^{-2\alpha W} R_b (1 - R_f) \\ &+ (1 - R_f) A_{\text{fc}}^2 e^{-2\alpha W} R_b A_{\text{fc}}^2 R_f e^{-2\alpha W} R_b (1 - R_f) \\ &+ \dots \\ &= R_f + (1 - R_f)^2 A_{\text{fc}}^2 e^{-2\alpha W} R_b \sum_{i=0}^{\infty} (R_f R_b A_{\text{fc}}^2 e^{-2\alpha W})^i \\ &= R_f + \frac{(1 - R_f)^2 A_{\text{fc}}^2 R_b e^{-2\alpha W}}{1 - R_f R_b A_{\text{fc}}^2 e^{-2\alpha W}}. \end{aligned} \quad (\text{C.61})$$

With the definition

$$R_{\text{b,eff}} = R_b A_{\text{fc}}^2, \quad (\text{C.62})$$

this result can be rewritten as

$$R_{\text{cell}} = R_f + \frac{(1 - R_f)^2 R_{\text{b,eff}} e^{-2\alpha W}}{1 - R_f R_{\text{b,eff}} e^{-2\alpha W}}. \quad (\text{C.63})$$

A comparison of Eq. (C.63) to Eq. (C.59) shows that the expression for the reflectance of the solar cell is formally equal to the expression for the silicon slab without a highly doped layer. The meaning of this formal equality is that measurements of reflectance cannot distinguish between additional absorption in the emitter (due to FCA) and a decreased rear surface reflectance. Using Eq. (C.59) for the evaluation of the rear surface reflectance of a solar cell thus determines an effective value which contains additional absorption in the emitter due to FCA.

C.3.3 Determination of the surface reflectance of solar cells from reference samples with highly doped layers on both sides

As shown in section C.3.1, FCA in highly doped layers can be incorporated into the optical model by adding multiplicative terms A_{fc} to the absorption (exponential) terms. For a symmetric reference sample with highly doped layers on both sides, the expressions for the reflectance R and transmittance T of the sample (Eqs. (2.2) and (2.3)) thus become

$$R = R_s \left(1 + \frac{(1 - R_s)^2 A_{\text{fc}}^4 \exp(-2\alpha W)}{1 - R_s^2 A_{\text{fc}}^4 \exp(-2\alpha W)} \right) \quad (\text{C.64})$$

and

$$T = \frac{(1 - R_s)^2 A_{\text{fc}}^4 \exp(-\alpha W)}{1 - R_s^2 A_{\text{fc}}^4 \exp(-2\alpha W)}. \quad (\text{C.65})$$

Note that Eqs. (C.62) and (C.63) (containing a factor A_{fc}^2) refer to samples with only one highly doped layer. From Eqs. (C.64) and (C.65), it is seen that the FCA terms A_{fc} *cannot* be subsumed

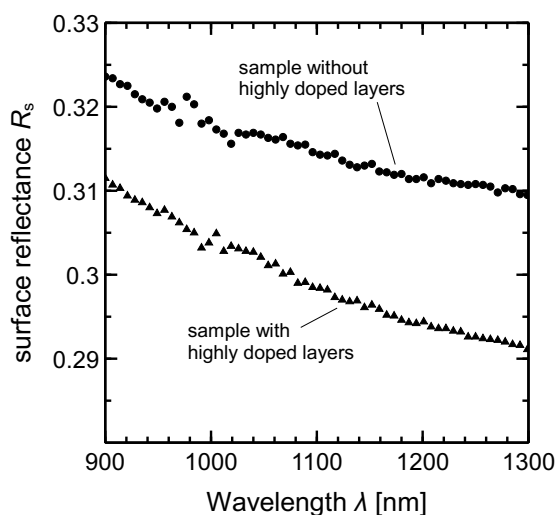


Figure C.4: Surface reflectance of the sample with highly doped layers. For comparison, the surface reflectance of a sample without highly doped layers is also shown.

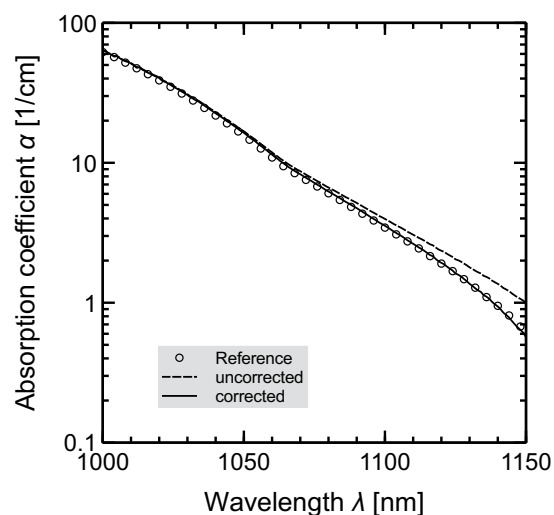


Figure C.5: Determination of the absorption coefficient from the sample with highly doped layers. The dashed line shows the result without FCA correction, the solid line visualizes the corrected results.

into effective surface reflectance terms $R_{s,\text{eff}}$. Rather, it is possible to define effective absorption terms which take both absorption in the bulk and additional free carrier absorption in the highly doped layers into account. Solving Eqs. (C.64) and (C.65) for R_s and α yields the unchanged relation Eq. (2.5) for the surface reflectance R_s , whereas for α , the modified relation

$$\alpha = -\frac{1}{W} \ln \left(\frac{C - R^2 + 2R + T^2 - 1}{2TA_{\text{fc}}^4} \right) \quad (\text{C.66})$$

is obtained. Hence, FCA affects the absorption coefficient which is determined from the RT measurements, but not the surface reflectance. Changes of the surface reflectance compared to samples without highly doped layers are thus due to a change of the refractive index, which also depends on the doping concentration. Figure C.4 compares the surface reflectances of a sample with highly doped layers and without highly doped layers.

The considerations outlined above can be verified experimentally by comparing the absorption coefficient determined from the sample with highly doped layers and from the sample without such layers. This is shown in Fig. C.5. The open circles visualize the reference data determined from a sample without highly doped layers. The dashed line visualizes the data determined using Eq. (2.4), which do not contain the FCA correction. As can be seen, omitting the FCA correction for the absorption coefficient (i.e., $A_{\text{fc}} = 1$) leads to an overestimation of α , as expected from a comparison of Eqs. (2.4) and (C.66). The solid line represents the data determined using Eq. (C.66), which contains a correction for FCA. The correction factor A_{fc} is calculated using Green's FCA parametrization (see section 1.2.4) with $W = 0.5 \mu\text{m}$, $N_{\text{dop}} = 3.5 \times 10^{19} \text{ cm}^{-3}$ and $\lambda = 1130 \text{ nm}$, which are realistic values for the sample. Although the wavelength dependence of the FCA correction is neglected, the corrected data are in qualitative agreement with the reference data. This experiment confirms that FCA in the highly doped layers affects the determination of the absorption coefficient.

C.3.4 Impact of FCA on the scaling factor for EQE data of textured solar cells

The external quantum efficiency EQE that results from the SR is given by the integral of the product of the normalized charge carrier generation rate g and the probability f_c that the generated charge

carriers are collected by the junction and contribute to the terminal current:

$$EQE(\lambda) = \int_0^W dz g(\lambda, z) f_c(z). \quad (C.67)$$

Assuming that each absorbed photon generates an electron-hole pair, the normalized charge carrier generation rate is given by the change of the normalized photon flux Φ/Φ_0 ,

$$g(\lambda, z) = -\frac{1}{\Phi_0(\lambda)} \frac{d\Phi(\lambda, z)}{dz}. \quad (C.68)$$

The change of the photon flux is determined by the Lambert-Beer law. For the simplest case of a single pass of light through the sample without reflections at the surfaces, $g(\lambda, z)$ is thus

$$g(\lambda, z) = \alpha_{bb}(\lambda) e^{-\alpha_{bb}(\lambda)z}. \quad (C.69)$$

SR measurements on textured solar cells are carried out at wavelengths above 1200 nm. At these wavelengths, photon absorption is weak because of $\alpha_{bb} \approx 0$. Hence, $e^{-\alpha_{bb}z} \approx 1$ and the charge carrier generation rate is approximately constant over the thickness of the sample. This means

$$g(\lambda, z) \approx \alpha_{bb}(\lambda) \quad (C.70)$$

and

$$EQE(\lambda) \approx \alpha_{bb}(\lambda) \int_0^W dz f_c(z). \quad (C.71)$$

If multiple internal reflections are taken into account, the charge carrier generation rate can be written as

$$g(\lambda, z) = \alpha_{bb}(\lambda) f_0(\lambda) \quad (C.72)$$

where the factor f_0 accounts for the reflectances of the surfaces, which may depend on the wavelength, and eventually for FCA in the emitter or back surface field. In this case,

$$EQE(\lambda) \approx \alpha_{bb}(\lambda) f_0(\lambda) \int_0^W dz f_c(z) \quad (C.73)$$

follows. The integral $\int_0^W dz f_c(z)$ is a constant with respect to wavelength. Hence, the EQE at wavelengths above 1200 nm can generally be expressed as

$$EQE(\lambda) \approx \alpha_{bb}(\lambda) f_0(\lambda) C \quad (C.74)$$

where C is a proportionality factor. Note that for the case of a single pass of light through the sample without reflections at the surfaces as described above, $f_0(\lambda) = 1$. In case of a negligible wavelength dependence of the charge carrier generation rate (i.e., $f_0 = \text{const}$), f_0 can be subsumed into the proportionality factor, giving

$$\alpha_{bb}(\lambda) = C_{\text{scale}} EQE(\lambda), \quad C_{\text{scale}} = \frac{1}{f_0 C}. \quad (C.75)$$

C_{scale} is determined by scaling the EQE data to known values of the absorption coefficient between 1200 and 1250 nm, as described in section 2.3. In a second step, α_{bb} is then obtained from the EQE at longer wavelengths.

FCA in the emitter or back surface field of a solar cell leads to an increasing absorption with respect to wavelength. However, this does not lead to an increased charge carrier generation rate, as FCA does not lead to the generation of electron-hole pairs. On the contrary, f_0 is decreased, which means that C_{scale} needs to be increased in order to compensate the impact of FCA. Assuming a constant scaling factor C_{scale} thus corresponds to an underestimation of α_{bb} .

The required change of the scaling factor C_{scale} is estimated using the analytical model for the charge carrier generation rate given in Eq. (4.38). This model is adapted from Ref. 111. For wavelengths above 1200 nm, the exponential terms describing the absorption are approximately unity. This yields

$$f_0(\lambda) \approx (1 - R_f) \left[\frac{g_{f,1}}{\cos \theta_1} + \frac{g_{r,2} g_{f,1} g_{r,1} R_b}{\cos \theta_2} + \frac{1}{\cos \theta_n} \frac{g_{f,1} g_{r,1} g_{f,2} g_{r,2} R_b R_{f1}}{1 - g_{f,n} g_{r,n} R_{fn} R_b} (g_{f,n} + g_{f,n} g_{r,n}^2 R_{bn}) \right]. \quad (\text{C.76})$$

The terms $g_{f,i}$ and $g_{r,i}$ take FCA in the emitter and back surface field into account and depend on the wavelength λ . The change of the scaling factor C' in Eq. (3.11) is calculated according to Eqs. (C.76), (4.36), (4.37) and (C.75) using $\theta_1 = 41^\circ$, $\theta_2 = 55^\circ$, $\theta_n = 60^\circ$, $R_b = 0.8$, $R_{fn} = 0.92$, $R_{f1} = 0.62$ and $R_f = 0.1$. The FCA correction factor f_{fca} then follows as

$$f_{\text{fca}}(\lambda) = \frac{C_{\text{scale}}(\lambda)}{C_{\text{scale}}(1200 \text{ nm})} = \frac{f_0(1200 \text{ nm})}{f_0(\lambda)}. \quad (\text{C.77})$$

C.4 Relation between absorptance and charge carrier generation rate

In an ideal solar cell, each absorbed photon generates an electron-hole pair. The normalized charge carrier generation rate $g(z)$ is thus given by the change of the normalized photon flux Φ (see Eq. (C.68)). The change of the photon flux is determined by the Lambert-Beer law and thus described by an exponential decay. In case of multiple internal reflections, each pass of light through the sample is also described by an exponential decay. For the purpose of simplicity, only a single pass is considered in the following. Without loss of generality, the surface reflectance is assumed to be zero. The consideration can easily be extended to the case of multiple internal reflections, which leads to the same conclusions. For a single pass of light, the normalized charge carrier generation rate is

$$g(z) = -\frac{d}{dz} \exp(-\alpha z) = \alpha \exp(-\alpha z). \quad (\text{C.78})$$

Integration of $g(z)$ over the thickness W of the sample yields the cumulated generation

$$G = \int_0^W dz g(z) = 1 - \exp(-\alpha W). \quad (\text{C.79})$$

The transmittance T of the sample is

$$T = \exp(-\alpha W). \quad (\text{C.80})$$

Considering the relation

$$A = 1 - T \quad (\text{C.81})$$

for the absorptance A and comparison with Eqs. (C.79) and (C.80) leads to

$$A = \int_0^W dz g(z), \quad (\text{C.82})$$

i.e., the cumulated charge carrier generation rate equals the absorptance of the sample.

Tabulated data

D.1 Absorption coefficient

Table D.1: Absorption coefficient as determined from measurements of reflectance and transmittance (Fig. 2.16). The uncertainty is specified for a coverage factor $k = 2$ and rounded to two significant digits. Note that the data is not corrected for FCA yet. For the corrections, see chapter 3.

λ [nm]	sample RT-A		sample RT-B		PTB	
	α [cm^{-1}]	$\frac{U(\alpha)}{\alpha}$ [%]	α [cm^{-1}]	$\frac{U(\alpha)}{\alpha}$ [%]	α [cm^{-1}]	$\frac{U(\alpha)}{\alpha}$ [%]
930					1.994×10^2	0.29
935					1.871×10^2	0.30
940					1.746×10^2	0.30
945					1.623×10^2	0.30
950					1.507×10^2	0.30
955					1.393×10^2	0.32
960	1.297×10^2	5.8			1.286×10^2	0.32
965	1.198×10^2	3.5			1.184×10^2	0.32
970	1.101×10^2	2.1			1.088×10^2	0.34
975	1.005×10^2	1.4			9.979×10^1	0.36
980	9.264×10^1	1.1			9.118×10^1	0.38
985	8.118×10^1	10			8.331×10^1	0.42
990	7.524×10^1	5.4			7.571×10^1	0.46
995	6.842×10^1	4.3			6.856×10^1	0.50
1000	6.230×10^1	3.6			6.153×10^1	0.46
1005	5.495×10^1	2.2			5.549×10^1	0.50
1010	4.895×10^1	1.8	4.906×10^1	16	4.940×10^1	0.54
1015	4.393×10^1	1.3	4.186×10^1	6.4	4.384×10^1	0.63
1020	3.887×10^1	1.2	3.821×10^1	3.8	3.863×10^1	0.71
1025	3.390×10^1	0.91	3.420×10^1	3.6	3.381×10^1	0.78
1030	2.927×10^1	0.89	2.953×10^1	2.2	2.937×10^1	0.90

Table continues on next page.

Continued from previous page.

λ [nm]	sample RT-A		sample RT-B		PTB	
	α [cm^{-1}]	$\frac{U(\alpha)}{\alpha}$ [%]	α [cm^{-1}]	$\frac{U(\alpha)}{\alpha}$ [%]	α [cm^{-1}]	$\frac{U(\alpha)}{\alpha}$ [%]
1035	2.536×10^1	0.86	2.522×10^1	1.1	2.533×10^1	1.0
1040	2.162×10^1	0.83	2.180×10^1	1.0	2.167×10^1	1.2
1045	1.837×10^1	0.89	1.859×10^1	0.91	1.839×10^1	1.3
1050	1.550×10^1	0.99	1.567×10^1	0.72	1.555×10^1	1.5
1055	1.310×10^1	1.2	1.318×10^1	0.83	1.308×10^1	1.7
1060	1.093×10^1	1.2	1.100×10^1	0.79	1.074×10^1	1.9
1065	9.143×10^0	1.3	9.271×10^0	0.89	9.051×10^0	2.1
1070	7.851×10^0	1.5	8.022×10^0	0.91	7.887×10^0	2.3
1075	6.861×10^0	1.7	6.988×10^0	1.0	6.864×10^0	2.5
1080	6.003×10^0	1.9	6.106×10^0	1.1	5.969×10^0	2.7
1085	5.228×10^0	2.2	5.312×10^0	1.2	5.192×10^0	2.9
1090	4.524×10^0	2.3	4.614×10^0	1.3	4.510×10^0	3.1
1095	3.926×10^0	2.5	4.011×10^0	1.4	3.907×10^0	3.6
1100	3.409×10^0	3.0	3.471×10^0	1.6	3.380×10^0	3.9
1105	2.965×10^0	3.2	3.033×10^0	1.8	2.923×10^0	4.1
1110	2.548×10^0	3.6	2.615×10^0	2.0	2.529×10^0	4.7
1115	2.202×10^0	4.3	2.253×10^0	2.3	2.165×10^0	5.1
1120	1.880×10^0	5.0	1.931×10^0	2.6	1.833×10^0	6.0
1125	1.579×10^0	5.7	1.647×10^0	2.9	1.558×10^0	6.4
1130	1.340×10^0	6.6	1.392×10^0	3.4	1.339×10^0	6.0
1135	1.106×10^0	8.2	1.149×10^0	4.0	1.107×10^0	6.3
1140	9.280×10^{-1}	9.4	9.563×10^{-1}	4.7		
1145	7.486×10^{-1}	12	7.824×10^{-1}	5.7		
1150	5.889×10^{-1}	14	6.304×10^{-1}	7.0		
1155	4.422×10^{-1}	19	4.903×10^{-1}	8.8		
1160	3.182×10^{-1}	26	3.695×10^{-1}	11		

Table D.2: Absorption coefficient as determined from spectrally resolved luminescence measurements (Fig. 2.33). The uncertainty is specified for a coverage factor $k = 2$ and rounded to two significant digits. Note that the data is not corrected for FCA yet. For the corrections, see chapter 3.

λ [nm]	RT		EL		PL	
	α [cm^{-1}]	$\frac{U(\alpha)}{\alpha}$ [%]	α [cm^{-1}]	$\frac{U(\alpha)}{\alpha}$ [%]	α [cm^{-1}]	$\frac{U(\alpha)}{\alpha}$ [%]
1100	3.452×10^0	1.6	3.476×10^0	11		
1105	3.011×10^0	1.7	2.960×10^0	10		
1110	2.594×10^0	2.0	2.589×10^0	9.6		
1115	2.237×10^0	2.1	2.208×10^0	9.2		
1120	1.915×10^0	2.5	1.899×10^0	8.8		
1125	1.627×10^0	2.9	1.625×10^0	8.5		
1130	1.377×10^0	3.1	1.387×10^0	8.3		
1135	1.136×10^0	3.6	1.156×10^0	8.0		
1140	9.503×10^{-1}	5.4	9.602×10^{-1}	7.9		
1145			7.860×10^{-1}	7.7		
1150			6.346×10^{-1}	7.6		
1155			5.003×10^{-1}	7.5		
1160			3.813×10^{-1}	7.5		
1165			2.789×10^{-1}	7.6		
1170			1.904×10^{-1}	7.9		
1175			1.111×10^{-1}	8.8		
1180			5.974×10^{-2}	12		
1185			3.585×10^{-2}	14		
1190			2.477×10^{-2}	16		
1195			1.923×10^{-2}	17		
1200			1.637×10^{-2}	17	1.616×10^{-2}	25
1205			1.211×10^{-2}	20	1.251×10^{-2}	25
1210			9.798×10^{-3}	21	9.716×10^{-3}	25
1215			7.617×10^{-3}	22	7.557×10^{-3}	25
1220			5.736×10^{-3}	25	5.824×10^{-3}	25
1225			4.300×10^{-3}	29	4.412×10^{-3}	25
1230			3.228×10^{-3}	33	3.269×10^{-3}	25
1235			2.433×10^{-3}	37	2.357×10^{-3}	25
1240			1.687×10^{-3}	46	1.633×10^{-3}	25
1245			1.092×10^{-3}	61	1.054×10^{-3}	25
1250			8.101×10^{-4}	72	6.290×10^{-4}	25
1255					3.682×10^{-4}	26
1260					2.386×10^{-4}	26
1265					1.736×10^{-4}	25
1270					1.313×10^{-4}	25
1275					1.003×10^{-4}	25
1280					7.713×10^{-5}	25
1285					5.937×10^{-5}	25
1290					4.625×10^{-5}	25
1295					3.573×10^{-5}	25

Table continues on next page.

Continued from previous page.

λ [nm]	RT		EL		PL	
	α [cm^{-1}]	$\frac{U(\alpha)}{\alpha}$ [%]	α [cm^{-1}]	$\frac{U(\alpha)}{\alpha}$ [%]	α [cm^{-1}]	$\frac{U(\alpha)}{\alpha}$ [%]
1300					2.750×10^{-5}	25
1305					2.100×10^{-5}	25
1310					1.571×10^{-5}	25
1315					1.163×10^{-5}	26
1320					8.358×10^{-6}	26
1325					5.822×10^{-6}	26
1330					3.910×10^{-6}	26
1335					2.518×10^{-6}	27
1340					1.650×10^{-6}	28
1345					1.186×10^{-6}	32
1350					9.394×10^{-7}	31
1355					6.927×10^{-7}	34
1360					5.813×10^{-7}	40
1365					4.590×10^{-7}	38
1370					3.580×10^{-7}	41
1375					2.897×10^{-7}	42
1380					2.401×10^{-7}	47
1385					1.843×10^{-7}	64
1390					1.571×10^{-7}	54
1395					1.146×10^{-7}	58
1400					9.360×10^{-8}	64
1405					7.799×10^{-8}	74
1410					5.385×10^{-8}	130
1415					5.468×10^{-8}	83
1420					3.796×10^{-8}	93
1425					2.514×10^{-8}	100
1430					1.791×10^{-8}	190
1435					2.133×10^{-8}	120
1440					1.203×10^{-8}	180
1445					1.089×10^{-8}	160
1450					9.447×10^{-9}	190

Table D.3: Absorption coefficient as determined from measurements of the spectral responsivity of solar cells (Fig. 2.36). The uncertainty is specified for a coverage factor $k = 2$ and rounded to two significant digits. Note that the data is not corrected for FCA yet. For the corrections, see chapter 3.

λ [nm]	RT		polished sample		textured sample	
	α [cm^{-1}]	$\frac{U(\alpha)}{\alpha}$ [%]	α [cm^{-1}]	$\frac{U(\alpha)}{\alpha}$ [%]	α [cm^{-1}]	$\frac{U(\alpha)}{\alpha}$ [%]
1100	3.442×10^0	1.6	3.465×10^0	7.4		
1105	2.997×10^0	1.7	3.001×10^0	7.1		
1110	2.586×10^0	2.0	2.593×10^0	7.1		
1115	2.227×10^0	2.2	2.231×10^0	6.9		
1120	1.904×10^0	2.5	1.914×10^0	6.8		
1125	1.617×10^0	2.9	1.626×10^0	7.0		
1130	1.371×10^0	3.1	1.371×10^0	6.9		
1135	1.132×10^0	3.7	1.145×10^0	7.0		
1140	9.495×10^{-1}	5.4	9.484×10^{-1}	7.1		
1145	7.745×10^{-1}	6.7	7.799×10^{-1}	7.1		
1150	6.206×10^{-1}	7.8	6.279×10^{-1}	7.6		
1155	4.791×10^{-1}	10	4.940×10^{-1}	8.0		
1160	3.582×10^{-1}	13	3.767×10^{-1}	8.8		
1165			2.763×10^{-1}	9.9		
1170			1.877×10^{-1}	12		
1175			1.103×10^{-1}	16		
1180			5.796×10^{-2}	18		
1185			3.393×10^{-2}	12		
1190			2.436×10^{-2}	8.3		
1195			1.856×10^{-2}	8.0		
1200			1.431×10^{-2}	8.0	1.413×10^{-2}	15
1205			1.103×10^{-2}	8.2	1.078×10^{-2}	15
1210			8.209×10^{-3}	8.9	8.127×10^{-3}	14
1215			6.300×10^{-3}	8.2	6.278×10^{-3}	14
1220			4.834×10^{-3}	8.8	4.821×10^{-3}	15
1225			3.651×10^{-3}	9.7	3.664×10^{-3}	15
1230			2.654×10^{-3}	13	2.726×10^{-3}	15
1235			1.848×10^{-3}	34	1.986×10^{-3}	15
1240			1.197×10^{-3}	59	1.389×10^{-3}	16
1245			6.839×10^{-4}	84	9.286×10^{-4}	17
1250			3.449×10^{-4}	110	5.785×10^{-4}	18
1255					3.522×10^{-4}	18
1260					2.267×10^{-4}	16
1265					1.622×10^{-4}	15
1270					1.215×10^{-4}	15
1275					9.281×10^{-5}	15
1280					7.107×10^{-5}	15
1285					5.456×10^{-5}	15
1290					4.163×10^{-5}	15
1295					3.233×10^{-5}	15

Table continues on next page.

Continued from previous page.

λ [nm]	RT		polished sample		textured sample	
	α [cm^{-1}]	$\frac{U(\alpha)}{\alpha}$ [%]	α [cm^{-1}]	$\frac{U(\alpha)}{\alpha}$ [%]	α [cm^{-1}]	$\frac{U(\alpha)}{\alpha}$ [%]
1300					2.505×10^{-5}	16
1305					1.902×10^{-5}	16
1310					1.445×10^{-5}	16
1315					1.089×10^{-5}	18
1320					7.921×10^{-6}	20
1325					5.806×10^{-6}	24
1330					3.914×10^{-6}	36
1335					2.864×10^{-6}	44
1340					1.822×10^{-6}	51
1345					1.644×10^{-6}	62
1350					1.399×10^{-6}	79

Table D.4: Absorption coefficient as determined from spectroscopic ellipsometry (Fig. 2.45). The uncertainty is specified for a coverage factor $k = 2$ and rounded to two significant digits. Note that this data represents the coefficient of band-to-band absorption α_{bb} since corrections for FCA are not necessary (see chapter 3).

λ [nm]	α_{bb} [cm^{-1}]	$\frac{U(\alpha_{bb})}{\alpha_{bb}}$ [%]	λ [nm]	α_{bb} [cm^{-1}]	$\frac{U(\alpha_{bb})}{\alpha_{bb}}$ [%]	λ [nm]	α_{bb} [cm^{-1}]	$\frac{U(\alpha_{bb})}{\alpha_{bb}}$ [%]
250	1.804×10^6	0.063	430	4.023×10^4	4.9	610	3.555×10^3	12
255	1.859×10^6	0.41	435	3.564×10^4	5.4	615	3.440×10^3	12
260	1.930×10^6	0.31	440	3.199×10^4	5.7	620	3.407×10^3	12
265	2.023×10^6	0.26	445	2.942×10^4	5.7	625	3.237×10^3	12
270	2.139×10^6	0.33	450	2.663×10^4	6.0	630	3.245×10^3	12
275	2.253×10^6	0.36	455	2.374×10^4	6.5	635	3.020×10^3	13
280	2.332×10^6	0.086	460	2.161×10^4	6.7	640	2.885×10^3	13
285	2.362×10^6	0.29	465	1.925×10^4	7.2	645	2.815×10^3	13
290	2.302×10^6	0.34	470	1.878×10^4	7.3	650	2.793×10^3	14
295	2.064×10^6	0.11	475	1.704×10^4	8.1	655	2.691×10^3	13
300	1.797×10^6	0.096	480	1.566×10^4	8.4	660	2.591×10^3	13
305	1.608×10^6	0.25	485	1.475×10^4	7.7	665	2.495×10^3	13
310	1.469×10^6	0.16	490	1.380×10^4	7.5	670	2.402×10^3	13
315	1.367×10^6	0.11	495	1.325×10^4	8.2	675	2.313×10^3	12
320	1.289×10^6	0.35	500	1.220×10^4	8.4	680	2.226×10^3	12
325	1.229×10^6	0.46	505	1.125×10^4	8.7	685	2.142×10^3	12
330	1.178×10^6	0.18	510	1.080×10^4	8.7	690	2.061×10^3	12
335	1.129×10^6	0.44	515	9.684×10^3	9.4	695	1.983×10^3	11
340	1.093×10^6	0.16	520	9.553×10^3	9.1	700	1.907×10^3	11
345	1.063×10^6	0.28	525	8.625×10^3	9.7	705	1.834×10^3	11
350	1.044×10^6	0.47	530	8.252×10^3	9.8	710	1.763×10^3	11
355	1.032×10^6	0.53	535	7.849×10^3	16	715	1.695×10^3	11
360	1.017×10^6	0.71	540	6.957×10^3	12	720	1.629×10^3	10
365	9.275×10^5	0.59	545	6.894×10^3	10	725	1.565×10^3	10
370	7.269×10^5	1.0	550	6.406×10^3	11	730	1.503×10^3	9.8
375	4.941×10^5	1.3	555	6.093×10^3	11	735	1.443×10^3	9.6
380	3.254×10^5	1.7	560	5.958×10^3	11	740	1.386×10^3	9.3
385	2.231×10^5	2.0	565	5.906×10^3	10	745	1.330×10^3	9.1
390	1.621×10^5	2.3	570	5.235×10^3	11	750	1.276×10^3	8.8
395	1.257×10^5	2.7	575	5.087×10^3	10	755	1.224×10^3	8.6
400	1.025×10^5	3.0	580	4.744×10^3	10	760	1.173×10^3	8.4
405	8.455×10^4	3.4	585	4.580×10^3	10	765	1.125×10^3	8.1
410	7.395×10^4	3.6	590	4.276×10^3	11	770	1.078×10^3	7.9
415	6.220×10^4	3.8	595	4.343×10^3	10	775	1.032×10^3	7.7
420	5.294×10^4	4.4	600	3.879×10^3	11	780	9.882×10^2	7.4
425	4.651×10^4	4.5	605	3.937×10^3	11	785	9.458×10^2	7.2

Table continues on next page.

Continued from previous page.

λ [nm]	α_{bb} [cm^{-1}]	$\frac{U(\alpha_{bb})}{\alpha_{bb}}$ [%]	λ [nm]	α_{bb} [cm^{-1}]	$\frac{U(\alpha_{bb})}{\alpha_{bb}}$ [%]	λ [nm]	α_{bb} [cm^{-1}]	$\frac{U(\alpha_{bb})}{\alpha_{bb}}$ [%]
790	9.049×10^2	6.9	840	5.659×10^2	4.6	890	3.313×10^2	2.2
795	8.653×10^2	6.7	845	5.383×10^2	4.3	895	3.125×10^2	1.9
800	8.271×10^2	6.5	850	5.116×10^2	4.1	900	2.945×10^2	1.7
805	7.902×10^2	6.2	855	4.859×10^2	3.9	905	2.771×10^2	1.5
810	7.546×10^2	6.0	860	4.612×10^2	3.6	910	2.605×10^2	1.2
815	7.203×10^2	5.8	865	4.374×10^2	3.4	915	2.446×10^2	1.0
820	6.871×10^2	5.5	870	4.145×10^2	3.1	920	2.293×10^2	0.76
825	6.552×10^2	5.3	875	3.925×10^2	2.9	925	2.147×10^2	0.52
830	6.243×10^2	5.0	880	3.713×10^2	2.7	930	2.007×10^2	0.29
835	5.946×10^2	4.8	885	3.509×10^2	2.4			

D.2 Temperature coefficient

Table D.5: Temperature coefficient c_T of α_{bb} at 295 K as used in this work (Fig. 3.11).

λ [nm]	c_T [K^{-1}]	λ [nm]	c_T [K^{-1}]	λ [nm]	c_T [K^{-1}]	λ [nm]	c_T [K^{-1}]
250	4.500×10^{-5}	560	3.565×10^{-3}	870	5.969×10^{-3}	1180	4.111×10^{-2}
260	7.500×10^{-5}	570	3.555×10^{-3}	880	6.246×10^{-3}	1190	3.494×10^{-2}
270	1.550×10^{-4}	580	3.702×10^{-3}	890	6.486×10^{-3}	1200	3.382×10^{-2}
280	1.650×10^{-4}	590	3.674×10^{-3}	900	6.789×10^{-3}	1210	3.520×10^{-2}
290	4.000×10^{-5}	600	3.570×10^{-3}	910	7.104×10^{-3}	1220	3.614×10^{-2}
300	2.352×10^{-4}	610	3.719×10^{-3}	920	7.382×10^{-3}	1230	3.820×10^{-2}
310	3.261×10^{-4}	620	3.581×10^{-3}	930	7.723×10^{-3}	1240	4.077×10^{-2}
320	1.818×10^{-4}	630	3.617×10^{-3}	940	8.126×10^{-3}	1250	4.680×10^{-2}
330	8.743×10^{-5}	640	3.883×10^{-3}	950	8.543×10^{-3}	1260	4.682×10^{-2}
340	2.794×10^{-5}	650	3.711×10^{-3}	960	9.022×10^{-3}	1270	4.204×10^{-2}
350	$0.000 \times 10^{+0}$	660	3.513×10^{-3}	970	9.513×10^{-3}	1280	4.411×10^{-2}
360	7.000×10^{-5}	670	3.830×10^{-3}	980	1.007×10^{-2}	1290	4.570×10^{-2}
370	4.102×10^{-4}	680	3.992×10^{-3}	990	1.199×10^{-2}	1300	4.883×10^{-2}
380	2.054×10^{-3}	690	3.902×10^{-3}	1000	1.084×10^{-2}	1310	5.500×10^{-2}
390	3.894×10^{-3}	700	3.945×10^{-3}	1010	1.122×10^{-2}	1320	5.800×10^{-2}
400	4.208×10^{-3}	710	4.062×10^{-3}	1020	1.199×10^{-2}	1330	6.100×10^{-2}
410	3.843×10^{-3}	720	4.035×10^{-3}	1030	1.267×10^{-2}	1340	6.500×10^{-2}
420	3.612×10^{-3}	730	4.032×10^{-3}	1040	1.360×10^{-2}	1350	6.700×10^{-2}
430	3.494×10^{-3}	740	4.198×10^{-3}	1050	1.481×10^{-2}	1360	6.750×10^{-2}
440	3.450×10^{-3}	750	4.238×10^{-3}	1060	1.572×10^{-2}	1370	6.800×10^{-2}
450	3.405×10^{-3}	760	4.262×10^{-3}	1070	1.545×10^{-2}	1380	6.850×10^{-2}
460	3.402×10^{-3}	770	4.299×10^{-3}	1080	1.543×10^{-2}	1390	6.900×10^{-2}
470	3.411×10^{-3}	780	4.349×10^{-3}	1090	1.575×10^{-2}	1400	7.000×10^{-2}
480	3.336×10^{-3}	790	4.461×10^{-3}	1100	1.630×10^{-2}	1410	7.100×10^{-2}
490	3.371×10^{-3}	800	4.636×10^{-3}	1110	1.674×10^{-2}	1420	7.200×10^{-2}
500	3.438×10^{-3}	810	4.774×10^{-3}	1120	1.730×10^{-2}	1430	7.300×10^{-2}
510	3.514×10^{-3}	820	4.925×10^{-3}	1130	1.806×10^{-2}	1440	7.400×10^{-2}
520	3.523×10^{-3}	830	5.138×10^{-3}	1140	1.934×10^{-2}	1450	7.500×10^{-2}
530	3.487×10^{-3}	840	5.314×10^{-3}	1150	2.089×10^{-2}		
540	3.442×10^{-3}	850	5.503×10^{-3}	1160	2.377×10^{-2}		
550	3.561×10^{-3}	860	5.705×10^{-3}	1170	2.919×10^{-2}		

Modeling of luminescence spectra

E.1 Photon escape probabilities

The following photon escape probabilities are extracted from the optical models from literature which are discussed in this work:

- **Schick et al. [134]:**

$$f_{\text{esc}} = \frac{\Omega}{4\pi n_{\text{Si}}^2} \left[1 - R_f \right] \frac{\exp(-\alpha z) + R_b \exp(-\alpha(2W - z))}{1 - R_f R_b \exp(-2\alpha W)}. \quad (\text{E.1})$$

- **Daub et al. [23]:** The escape probability is equal to the one calculated by Schick et al. (see Eq. (E.1)).
- **Trupke et al. [31]:** The escape probability is equal to the one calculated by Schick et al. (see Eq. (E.1)).
- **Würfel et al. [79]:**

$$f_{\text{esc}} = \frac{\Omega}{4\pi n_{\text{Si}}^2} \left[1 - R_f \right] \left[\exp(-\alpha z) + R_b \exp(-\alpha(2W - z)) \right] \quad (\text{E.2})$$

- **Rüdiger et al. [135]:**

$$f_{\text{esc}} = \frac{\Omega}{4\pi n_{\text{Si}}^2} \frac{1}{n_{\text{Si}}^2} \left[\exp(-2\alpha z) + \left(1 - \frac{1}{n_{\text{Si}}^2} \right) \exp(-2\alpha(2W - z)) \right] \times \sum_{i=0}^{\infty} \left[\left(1 - \frac{1}{n_{\text{Si}}^2} \right)^2 \exp(-4\alpha W) \right]^i \quad (\text{E.3})$$

- **Kirchartz et al. [120]:** For the planar case the escape probability is equal to the one calculated by Schick et al. (see Eq. (E.1)).

For the textured case the escape probability is taken from Ref. [151] and reads

$$f_{\text{esc}} = \frac{\Omega}{4\pi n_{\text{Si}}^2} 2 \left[1 - R_f \right] \frac{\text{Ei}_2(\alpha z) + R_b \text{Ei}_2(\alpha(2W - z))}{1 - t_{\text{cell}}(1 - t_{\text{lamb}})} \quad (\text{E.4})$$

with

$$t_{\text{lamb}} = \frac{1 - R_f}{n_{\text{Si}}^2}, \quad (\text{E.5})$$

where n_{Si} is the index of refraction of the sample,

$$t_{\text{cell}} = R_b \left[\exp(-2\alpha W)(1 - 2\alpha W) + (2\alpha W)^2 \text{Ei}(2\alpha W) \right], \quad (\text{E.6})$$

$$\text{Ei}(z) = \int_z^\infty dt \frac{\exp(-t)}{t} \quad (\text{E.7})$$

and

$$\text{Ei}_2(z) = z \int_z^\infty dt \frac{\exp(-t)}{t^2} = \exp(-z) - z \text{Ei}(z). \quad (\text{E.8})$$

- **Brüggemann [136]:** The escape probability is equal to the one calculated by Schick et al. (see Eq. (E.1)).
- **Green [137]:** The escape probability is equal to the one calculated by Schick et al. (see Eq. (E.1)).
- **This work:**

$$\begin{aligned} f_{\text{esc}}(z) = & \frac{\Omega}{4\pi} \frac{1 - R_f}{n_{Si}^2} \left[\frac{1}{\cos \theta_1} \exp\left(\frac{-\alpha z}{\cos \theta_1}\right) + \frac{1}{\cos \theta_2} T_1 R_{b1} \exp\left(\frac{-\alpha(W-z)}{\cos \theta_2}\right) \right. \\ & \left. + \frac{1}{\cos \theta_n} \frac{T_1 R_{b1} T_2 R_{f1}}{1 - T_n^2 R_{fn} R_{bn}} \left(\exp\left(\frac{-\alpha z}{\cos \theta_n}\right) + T_n R_{bn} \exp\left(\frac{-\alpha(W-z)}{\cos \theta_n}\right) \right) \right]. \quad (\text{E.9}) \end{aligned}$$

Details about the determination of the parameters of Eq. (E.9) can be found in Ref. 111. Only a short summary is given here:

T_1 is the transmission through the sample for photons propagating under an angle θ_1 , i.e.

$$T_1 = \exp(-\alpha W / \cos(\theta_1)) \quad (\text{E.10})$$

T_2 and T_n are the transmissions through the sample for photons propagating under an angle θ_2 or θ_n , respectively:

$$T_2 = \exp(-\alpha W / \cos(\theta_2)) \quad (\text{E.11})$$

$$T_n = \exp(-\alpha W / \cos(\theta_n)) \quad (\text{E.12})$$

The front surface reflectance R_f is taken equal to the measured reflectance in the wavelength range of strong absorption (absorption length of light $L_\alpha = \alpha^{-1} \ll W$) and linearly extrapolated for the wavelength range of weak absorption ($L_\alpha > W$).

θ_1 is calculated from the facet angle γ (see Fig. 4.2) using the law of defraction:

$$\theta_1 = \gamma - \arcsin\left(\frac{n_{\text{air}}}{n_{Si}} \sin(\gamma)\right) \quad (\text{E.13})$$

where $n_{\text{air}} \approx 1$ holds.

θ_n is calculated using the equations given in appendix E.2.

θ_2 follows as the solution of Eq. (E.11) with

$$T_2 = \frac{\Lambda R_{bd} T_n + (1 - \Lambda) R_{bs} T_1}{\Lambda R_{bd} + (1 - \Lambda) R_{bs}}. \quad (\text{E.14})$$

Here, T_2 is expressed as a weighted average of T_1 and T_n where the weighting factor Λ ($0 \leq \Lambda \leq 1$) determines the fraction of light reflected with a lambertian characteristic, such that its direction

is randomized by the reflection at the surface. R_{bd} is the rear surface reflectance for lambertian reflected light, R_{bs} is the rear surface reflectance for specularly reflected light. The denominator of Eq. (E.14) is the rear surface reflectance

$$R_b = (1 - \Lambda) R_{bs} + \Lambda R_{bd} \quad (\text{E.15})$$

which is a weighted average of the reflectance for specularly reflected light R_{bs} and the reflectance for diffusely (lambertian) reflected light R_{bd} . In a first approximation, R_{bs} and R_{bd} are assumed equal to R_b . Consequently, the rear surface reflectance R_b is independent of the lambertian factor Λ . However, Λ affects the effective path angle θ_2 as well as the front surface reflectance R_{f1} .

R_{f1} is

$$R_{f1} = \frac{\Lambda R_{bd} T_n R_{fn} + (1 - \Lambda) R_{bs} T_1 R_{fs}}{\Lambda R_{bd} T_n + (1 - \Lambda) R_{bs} T_1}, \quad (\text{E.16})$$

where $R_{fs} = 0.62$ is determined by numerical ray-tracing simulations for rays at a wavelength of 1000 nm which are isotropically incident onto the inner surface of regular inverted pyramids with 109 nm of SiO_2 as anti-reflection coating.

R_{fn} is also determined by numerical ray-tracing simulations to be $R_{fn} = 0.928 \pm 0.001$ for rays at a wavelength of 1000 nm which are isotropically incident onto the inner surface of regular inverted pyramids with 109 nm of SiO_2 as anti-reflection coating. It is stated that the value is similar for other wavelengths and anti-reflection coatings.

The parameters Λ and R_b are determined by a fit of the model of the total reflectance R (corrected for front grid metallization if present),

$$R = 1 - (1 - R_f) \left[1 - T_1 R_{b1} T_2 (1 - R_{f1}) - \frac{T_1 R_{b1} T_2 R_{f1} R_{bn} (1 - R_{fn}) T_n^2}{1 - R_{bn} R_{fn} T_n^2} \right], \quad (\text{E.17})$$

to a measured reflectance curve. Eq. (E.17) follows from the model for the optical path.

E.2 Effective path angle θ_n for lambertian diffused light

A lambertian radiator is characterized by an angle-dependent photon escape probability

$$f_{em,lamb} = C \cos(\theta),$$

where θ is the angle to the perpendicular of the radiator's surface and C is the proportionality factor. The probability for the emission of a photon into the half space is unity. Therefore,

$$C \int_0^{2\pi} d\varphi \int_0^{\pi/2} d\theta \sin \theta \cos \theta = 1 \quad (\text{E.18})$$

which yields

$$C = \frac{1}{\pi}. \quad (\text{E.19})$$

The total transmission of light T_n emitted by a lambertian radiator through a slab of thickness W follows as

$$\begin{aligned} T_n &= \int_0^{2\pi} d\varphi \int_0^{\pi/2} d\theta \sin \theta \frac{\cos \theta}{\pi} \exp\left(-\frac{\alpha W}{\cos \theta}\right) \\ &= 2 \int_0^{\pi/2} d\theta \sin \theta \cos \theta \exp\left(-\frac{\alpha W}{\cos \theta}\right). \end{aligned} \quad (\text{E.20})$$

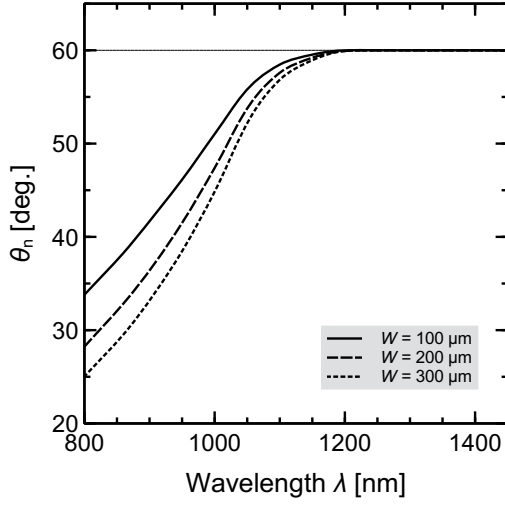


Figure E.1: Effective path angle following from Equations (E.20) and (E.21) for different thicknesses W of the sample.

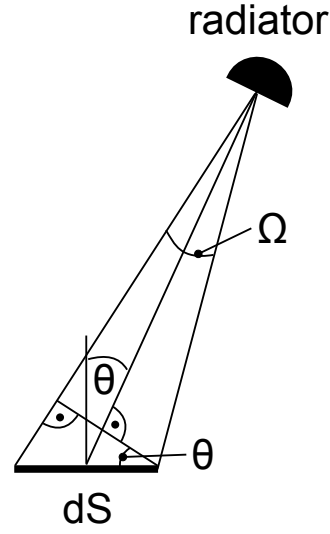


Figure E.2: Schematic of a surface element dS which is seen from the radiator under the solid angle Ω and orientated under an angle θ with respect to the optical axis.

Inserting T_n from Eq. (E.20) into the relation

$$T_n = \exp\left(-\frac{\alpha W}{\cos \theta_n}\right) \quad (\text{E.21})$$

allows to calculate the effective path angle θ_n which is shown in Fig. E.1 as a function of wavelength for different thicknesses W . For long wavelengths, it approaches 60° independent from the thickness of the sample.

E.3 Derivation of $\Phi_{bb}(\lambda)$

In 1901, Planck [152] showed that the energy of black body radiation u in the photon frequency interval $[\nu, \nu + d\nu]$ is

$$u(\nu)d\nu = \frac{8\pi h\nu^3}{c^3} \frac{1}{\exp\left(\frac{h\nu}{kT}\right) - 1} d\nu. \quad (\text{E.22})$$

The latter equation can be written in terms of photon energy by applying the well known energy relation of photons, $E = h\nu$. The radiation is emitted isotropically. The fraction $d\Omega/4\pi$ is emitted into the solid angle $d\Omega$. Hence, the emitted radiation per solid angle can be expressed as

$$u(\nu, \Omega)d\nu d\Omega = \frac{2h\nu^3}{c^3} \frac{1}{\exp\left(\frac{h\nu}{kT}\right) - 1} d\nu d\Omega. \quad (\text{E.23})$$

Note that $u(\nu) = 4\pi u(\nu, \Omega)$. From Eq. (E.23), the number N of photons per frequency interval is obtained by division by the energy of a photon $h\nu$:

$$N(\nu, \Omega)d\nu d\Omega = \frac{2\nu^2}{c^3} \frac{1}{\exp\left(\frac{h\nu}{kT}\right) - 1} d\nu d\Omega. \quad (\text{E.24})$$

The photon flux $\Phi_{\text{bb}}(\nu, \Omega, \theta)$ incident onto a surface element dS which is seen from the radiator under the solid angle Ω and orientated under an angle θ with respect to the optical axis (see Fig. E.2) follows from Eq. (E.24) by multiplication with the speed of photons c and a scaling factor $\cos(\theta)$:

$$\Phi_{\text{bb}}(\nu, \Omega, \theta) d\nu d\Omega = \frac{2\nu^2}{c^2} \frac{\cos(\theta)}{\exp\left(\frac{h\nu}{kT}\right) - 1} d\nu d\Omega. \quad (\text{E.25})$$

For perpendicular irradiation, which is typically used for quantum efficiency measurements, $\cos(\theta) = 1$ and

$$\Phi_{\text{bb}}(\nu, \Omega) d\nu d\Omega = \frac{2\nu^2}{c^2} \frac{1}{\exp\left(\frac{h\nu}{kT}\right) - 1} d\nu d\Omega \quad (\text{E.26})$$

follows. In order to write Eq. (E.26) as a function of wavelength, we note that $\Phi_{\text{bb}}(\nu, \Omega)$ is a differential quantity in terms of frequency, i.e. there is an antiderivative F for which

$$\Phi_{\text{bb}}(\nu, \Omega) = \frac{dF}{d\nu} \quad (\text{E.27})$$

holds. Thus, the differential quantity in terms of wavelengths $\Phi_{\text{bb}}(\lambda, \Omega) = dF/d\lambda$ is obtained either by calculating F , replacing ν by λ in F using the frequency-wavelength relation of photons

$$\nu = \frac{c}{\lambda} \quad (\text{E.28})$$

and differentiating F with respect to λ or, more easily, by replacing ν by λ in $\Phi_{\text{bb}}(\nu, \Omega)$ and using the chain rule:

$$\Phi_{\text{bb}}(\lambda, \Omega) = \frac{dF}{d\nu} \frac{d\nu}{d\lambda}. \quad (\text{E.29})$$

From Eq. (E.28), we get

$$\left| \frac{d\nu}{d\lambda} \right| = \frac{c}{\lambda^2}. \quad (\text{E.30})$$

Combining Eqs. (E.27) through (E.30) yields

$$\Phi_{\text{bb}}(\lambda, \Omega) d\lambda d\Omega = \frac{2c}{\lambda^4} \frac{1}{\exp\left(\frac{hc}{\lambda kT}\right) - 1} d\lambda d\Omega. \quad (\text{E.31})$$

For wavelengths below 1400 nm, where significant luminescence emission is located, the exponential term in Eq. (E.31) is always larger than 10^{14} . We can thus neglect the -1 in the denominator of Eq. (E.31) and finally end up with

$$\Phi_{\text{bb}}(\lambda, \Omega) d\lambda d\Omega = \frac{2c}{\lambda^4} \exp\left(-\frac{hc}{\lambda kT}\right) d\lambda d\Omega \quad (\text{E.32})$$

which is the result given in Eq. (4.22).

E.4 Approximation of the photon generation rate r_{ph}

The photon generation rate per wavelength interval and solid angle r_{ph} is determined by the generalized Planck radiation law for luminescence [72]:

$$r_{\text{ph}}(\lambda, z) d\lambda = \frac{2c \alpha(\lambda) n_{\text{Si}}^2(\lambda)}{\lambda^4 \left[\exp\left(\frac{hc}{\lambda} - \mu_{\text{ph}}(z)\right) - 1 \right]} d\lambda. \quad (\text{E.33})$$

For typical luminescence measurement conditions, the exponential term in the denominator of Eq. (E.33) is of the order of 10^6 . The -1 can thus be neglected. The chemical potential μ_{ph} of the photons is given by the splitting of the quasi-Fermi levels ΔE_{F} :

$$\mu_{\text{ph}} = \Delta E_{\text{F}}. \quad (\text{E.34})$$

Equation (E.33) can thus be reformulated as

$$r_{\text{ph}}(\lambda, z) d\lambda \approx 2 c \alpha(\lambda) n_{\text{Si}}^2(\lambda) \lambda^{-4} \exp\left(-\frac{\frac{hc}{\lambda} - \Delta E_{\text{F}}(z)}{kT}\right) d\lambda. \quad (\text{E.35})$$

Finally, considering the relation

$$n(z) p(z) = n_{\text{i}}^2 \exp\left(\frac{\Delta E_{\text{F}}(z)}{kT}\right) \quad (\text{E.36})$$

and the definition of the coefficient of spectral radiative recombination in Eq. (4.21) yields the expression given in Eq. (4.20).

E.5 Derivation of the optical reciprocity theorem in terms of wavelengths and for a specific detection cone

The reciprocity theorem of Rau [73] as given in Eq. (4.25),

$$\Phi_{\text{EL}}(E, \Omega) dE d\Omega = \Phi_{\text{bb}}(E, \Omega) dE d\Omega \text{EQE}(E, \Omega) \left[\exp\left(\frac{V}{V_{\text{T}}}\right) - 1 \right], \quad (\text{E.37})$$

holds for photon flux densities $\Phi_{\text{EL}}(E, \Omega)$ and $\Phi_{\text{bb}}(E, \Omega)$ per energy interval dE and solid angle $d\Omega$. Both photon incidence and emission are assumed to be perpendicular to the sample's surface. The term $dE d\Omega$ on both sides of the equation is added as an indication that we refer to an energy and solid angle interval, respectively. Φ_{bb} and thus also Φ_{EL} are differential quantities which means that the chain rule must be used together with the energy-wavelength relation of photons $E = hc/\lambda$ in order to obtain these quantities in terms of wavelength:

$$\Phi_{\text{EL}}(\lambda) = \Phi_{\text{EL}}(E) \frac{dE}{d\lambda}, \quad (\text{E.38})$$

$$\Phi_{\text{bb}}(\lambda) = \Phi_{\text{bb}}(E) \frac{dE}{d\lambda}. \quad (\text{E.39})$$

Inserting Eqs. (E.38) and (E.39) as well as the approximation

$$\exp\left(\frac{V}{V_{\text{T}}}\right) - 1 \approx \exp\left(\frac{V}{V_{\text{T}}}\right) \quad (\text{E.40})$$

into Eq. (E.37) leads to

$$\Phi_{\text{EL}}(\lambda, \Omega) d\lambda d\Omega = \Phi_{\text{bb}}(\lambda, \Omega) d\lambda d\Omega \text{EQE}(E, \Omega) \exp\left(\frac{V}{V_{\text{T}}}\right). \quad (\text{E.41})$$

Note that at room temperature, Eq. (E.40) is justified as soon as V exceeds about 120 mV. This assumption is always fulfilled under typical EL measurement conditions. For the quantum efficiency, the relation

$$\text{EQE}(E) = \text{EQE}(\lambda(E)) \quad (\text{E.42})$$

holds where

$$\lambda(E) = \frac{hc}{E} \quad (\text{E.43})$$

is the energy-wavelength relation of photons. Hence, with the abbreviation $EQE(\lambda(E)) = EQE(\lambda)$ and keeping in mind that Eq. (E.43) must be fulfilled, we can write Eq. (E.41) as

$$\Phi_{\text{EL}}(\lambda, \Omega) d\lambda d\Omega = \Phi_{\text{bb}}(\lambda, \Omega) d\lambda d\Omega EQE(\lambda, \Omega) \exp\left(\frac{V}{V_T}\right). \quad (\text{E.44})$$

In an experiment, the detector collects luminescence photons from a certain solid angle Ω which is defined by the numerical aperture of the detector and its distance from the sample. The measurable photon flux is thus given by the integral of Eq. (E.44) over Ω . Since Ω is typically very small ($\Omega \ll 4\pi$), we can approximate that the integrand is constant on this interval and obtain

$$\Omega \Phi_{\text{EL}}(\lambda) d\lambda = \Omega \Phi_{\text{bb}}(\lambda) d\lambda EQE(\lambda) \exp\left(\frac{V}{V_T}\right). \quad (\text{E.45})$$

Inserting the definition

$$\Phi_{\text{EL,det}}(\lambda) = \Omega \Phi_{\text{EL}}(\lambda), \quad (\text{E.46})$$

into Eq. (E.46), we obtain

$$\Phi_{\text{EL,det}}(\lambda) d\lambda = \Omega \Phi_{\text{bb}}(\lambda) EQE(\lambda) d\lambda \exp\left(\frac{V}{V_T}\right) \quad (\text{E.47})$$

which is the result given in Eq. (4.26). Note that from Eq. (E.39) and (E.43),

$$\Phi_{\text{bb}}(E) = \Phi_{\text{bb}}(\lambda) \frac{d\lambda}{dE} = \Phi_{\text{bb}}(\lambda) \frac{\lambda^2}{hc} \quad (\text{E.48})$$

follows. Combining the latter equation with Eq. (4.22) and using the energy-wavelength relation of photons (Eq. (E.43)) again, we obtain

$$\Phi_{\text{bb}}(E) dE = \frac{2E^2}{h^3 c^2} dE \exp\left(-\frac{E}{kT}\right) \quad (\text{E.49})$$

which is in agreement with the literature [73, 153].

Bibliography

- [1] R. Schnabel, M. Britzger, F. Brückner, O. Burmeister, K. Danzmann, J. Dück, T. Eberle, D. Friedrich, H. Luck, M. Mehmet, R. Nawrodt, S. Steinlechner, and B. Willke: *Building blocks for future detectors: Silicon test masses and 1550 nm laser light*. Journal of Physics: Conference Series, 228:012029, 2010.
- [2] W. C. Dash and R. Newman: *Intrinsic optical absorption in single-crystal Germanium and Silicon at 77°K and 300°K*. Phys. Rev., 99:1151–1155, 1955.
- [3] G. G. Macfarlane and V. Roberts: *Infrared absorption of Silicon near the lattice edge*. Phys. Rev., 98(6):1865, 1955.
- [4] C. D. Salzberg and J. J. Villa: *Infrared refractive indexes of Silicon, Germanium and modified Selenium glass*. J. Opt. Soc. Am., 47(3):244–246, 1957.
- [5] W. Spitzer and H. Y. Fan: *Infrared absorption in n-type silicon*. Phys. Rev., 108(2):268–271, 1957.
- [6] G. G. Macfarlane, T. P. McLean, J. E. Quarrington, and V. Roberts: *Fine structure in the absorption-edge spectrum of si*. Phys. Rev., 111:1245–1254, Sep 1958.
- [7] G. G. Macfarlane, T. P. McLean, J. E. Quarrington, and V. Roberts: *Exciton and phonon effect in the absorption spectra of Germanium and Silicon*. J. Phys. Chem. Solids, 8:388–392, 1959.
- [8] H.R. Phillip and E.A. Taft: *Optical constants of Silicon in the region 1 to 10 eV*. Phys. Rev., 120(1):37–38, 1960.
- [9] A. A. Vol’fson and V. K. Subashiev: *Fundamental absorption edge of silicon heavily doped with donor or acceptor impurities*. Sov. Phys. Semicond., 1(3):327–332, 1967.
- [10] C. Anagnostopoulos and G. Sadasiv: *Fine structure in the optical-absorption edge of silicon*. Phys. Rev., 7(2):733–739, 1973.
- [11] R. Hulthén: *Optical constants of epitaxial silicon in the region 1-3.3 eV*. Phys. Scr., 12(6):342–344, 1975.
- [12] D. K. Schroder, R. N. Thomas, and J. C. Swartz: *Free carrier absorption in silicon*. IEEE J. Solid-St. Circ., 13(1):180–187, 1978.
- [13] K. G. Svantesson and N. G. Nilsson: *Determination of the temperature dependence of the free carrier and interband absorption in silicon at 1,06 μm*. J. Phys. C: Solid State Phys., 12:3837–3842, 1979.

- [14] H. A. Weakliem and D. Redfield: *Temperature dependence of the optical properties of silicon*. J. Appl. Phys., 50(3):1491–1493, 1979.
- [15] P. E. Schmidt: *Optical absorption in heavily doped silicon*. Phys. Rev. B, 23(10):5531–5536, 1981.
- [16] G. E. Jellison and F. A. Modine: *Optical functions of silicon between 1.7 and 4.7 eV at elevated temperatures*. Phys. Rev. B, 27:7466–7472, 1983.
- [17] Edward S. Nartowitz and Alvin M. Goodman: *Evaluation of silicon optical absorption data for use in minority-carrier-diffusion-length measurements by the spv method*. J. Electrochem. Soc., 132(12):2992–2997, 1985.
- [18] J. Geist, A. Migdall, and H. P. Baltes: *Analytic representation of the silicon absorption coefficient in the indirect transition region*. Applied Optics, 27(18):3777–3779, 1988.
- [19] G.E. Jellison: *Optical functions of silicon determined by two-channel polarization modulation ellipsometry*. Optical Materials, 1:41–47, 1991.
- [20] A. Oschlies, R. W. Godby, and R. J. Needs: *First-principles self-energy calculations of carrier-induced band-gap narrowing in silicon*. Phys. Rev. B, 45(23):13741–13744, 1992.
- [21] J. M. Essick and R. T. Mather: *Characterization of a bulk semiconductor's band gap via a near-absorption edge optical transmission experiment*. Am. J. Phys., 61(7):646–649, 1993.
- [22] E. Daub: *Photolumineszenz von Silizium*. PhD thesis, University of Karlsruhe, Germany, 1995.
- [23] E. Daub and P. Würfel: *Ultralow values of the absorption coefficient of Si obtained from luminescence*. Phys. Rev. Letters, 74(6):1020–1023, 1995.
- [24] M. A. Green and M. J. Keevers: *Optical properties of intrinsic silicon at 300 K*. Prog. Photovolt: Res. Appl., 3:189–192, 1995.
- [25] M.J. Keevers and M.A. Green: *Absorption edge of silicon from solar cell spectral response measurements*. Appl. Phys. Lett., 66(2):174–176, 1995.
- [26] M. J. Keevers and M. A. Green: *Extended infrared response of silicon solar cells and the impurity photovoltaic effect*. Sol. Energ. Mat. Sol. C., 41(42):195–204, 1996.
- [27] A. Neisser and M.A. Green: *Very low absorption coefficients of silicon at low temperatures from spectral response measurements*. In Proc. 2nd WPVSC, Vienna, Austria, pages 136–139, 1998.
- [28] A. Neisser: *Spectral Response Measurements on Silicon Solar Cells in the Range of 1 eV to 5 eV Photon Energy at Different Temperatures*. Master's thesis, Technische Universität Berlin, Germany, 1998.
- [29] J. Geist: *Handbook Of Optical Constants Of Solids III*. Academic Press, 1998.
- [30] C. M. Herzinger, B. Johs, W. A. McGahan, J. A. Woollam, and W. Paulson: *Ellipsometric determination of optical constants for silicon and thermally grown silicon dioxide via a multi-sample, multi-wavelength, multi-angle investigation*. J. Appl. Phys., 83(6):3323–3336, 1998.
- [31] T. Trupke, E. Daub, and P. Würfel: *Absorptivity of silicon solar cells obtained from luminescence*. Sol. Energ. Mat. Sol. C., 53:103–114, 1998.

- [32] M.A. Green: *Self-consistent optical parameters of intrinsic silicon at 300 K including temperature coefficients*. Sol. Energ. Mat. Sol. C., 92:1305–1310, 2008.
- [33] T. R. Harris: *Optical Properties Of Si, Ge, GaAs, GaSb, InAs, And InP at Elevated Temperatures*. PhD thesis, Air Force Institute Of Technology, Ohio, USA, 2010.
- [34] C. Schinke, K. Bothe, P. C. Peest, J. Schmidt, and R. Brendel: *Uncertainty of the coefficient of band-to-band absorption of crystalline silicon at near-infrared wavelengths*. Appl. Phys. Lett., 104(081915), 2014.
- [35] H. T. Nguyen, F. E. Rougieux, B. Mitchell, and D. Macdonald: *Temperature dependence of the band-band absorption coefficient in crystalline silicon from photoluminescence*. J. Appl. Phys., 115:043710, 2014.
- [36] S. C. Baker-Finch, K. R. McIntosh, D. Yan, K. C. Fong, and T. C. Kho: *Near-infrared free carrier absorption in heavily doped silicon*. J. Appl. Phys., 116(063106), 2014.
- [37] M.A. Green: *Silicon Solar Cells - Advanced Priciples and Practice*. University of New South Wales, 1995.
- [38] H. Graßl, J. Kokott, M.E. Kulesa, J. Luther, F. Nuscheler, R. Sauerborn, H. J. Schellnhuber, R. Schubert, and E. D. Schulze: *Welt im Wandel: Energiewende zur Nachhaltigkeit*. Springer-Verlag, 2003.
- [39] C. Podewils: *Billiger als Braunkohle*. Photon, 4:40–44, 2007.
- [40] M. A. Green: *Solar Cells - Operating Priciples, Technology and System Application*. University of New South Wales, 1992.
- [41] J.R. Chelikowsky and M.L. Cohen: *Electronic structure of silicon*. Phys. Rev. B, 10(12):5095–5107, 1974.
- [42] J.R. Chelikowsky and M.L. Cohen: *Nonlocal pseudopotential calculations for the electronic structure of eleven diamond and zinc-blende semiconductors*. Phys. Rev. B, 14(2):556–582, 1976.
- [43] R. A. Smith: *Semiconductors*. Cambridge Univ. Press, 1961.
- [44] P. Würfel: *Physics of Solar Cells: From Priciples to New Concepts*. Wiley-VCH, 2005.
- [45] J.I. Pankove: *Optical Processes in Semiconductors*. Prentice-Hall, 1971.
- [46] K.W. Böer: *Survey of semiconductor physics*. Wiley, Ney York, 2nd edition, 1990.
- [47] J. Tauc, R. Grigorovici, and A. Vancu: *Optical properties and electronic structure of amorphous germanium*. Phys. Stat. Sol., 15:627–637, 1966.
- [48] International Electrotechnical Commission: *International Standard IEC 60904-3:2008*. Geneva, Switzerland, 2008.
- [49] H. Y. Fan: *Temperature dependence of the energy gap in monatomic semiconductors*. Phys. Rev., 78:808–809, 1950.
- [50] H. Y. Fan: *Temperature dependence of the energy gap in semiconductors*. Phys. Rev., 82:900–905, 1951.

- [51] T. Muto and S. Ôyama: *Theory of the temperature effect of electronic energy bands in crystals*. Progress of Theoretical Physics, 5(5):833–843, 1950.
- [52] E. Antoncik: *On the theory of temperature shift of the absorption curve in non-polar crystals*. Czech. J. Phys., 5(4):449–461, 1955.
- [53] H. D. Vasileff: *Electron self-energy and temperature-dependent effective masses in semiconductors: n-type ge and si*. Phys. Rev., 105:441–446, 1957.
- [54] E. N. Adams: *Vasileff's calculation of electronic self-energy in semiconductors*. Phys. Rev., 107:671–671, 1957.
- [55] F. Möglich and R. Rompe: *Über den Einfluß der Wärmedehnung auf das Absorptionsspektrum von Isolatoren*. Phys., 119(7-8):472–481, 1942.
- [56] J. Bardeen and W. Shockley: *Deformation potentials and mobilities in non-polar crystals*. Phys. Rev., 80:72–80, 1950.
- [57] Y.P. Varshni: *Temperature dependence of the energy gap in semiconductors*. Physica, 34:194–154, 1967.
- [58] K.P. O'Donnell and X. Chen: *Temperature dependence of semiconductor band gaps*. Appl. Phys. Lett., 58(25):2924–2926, 1991.
- [59] W. Bludau, A. Onton, and W. Heinke: *Temperature dependence of the band gap of silicon*. Journal of Applied Physics, 45(4):1846–1848, 1974.
- [60] Vassil Palankovski: *Simulation of Heterojunction Bipolar Transistors*. PhD thesis, Technische Universität Wien, Austria, 2000.
- [61] C.D. Thurmond: *The standard thermodynamic functions for the formation of electrons and holes in Ge, Si, GaAs, and GaP*. J. Electrochem. Soc., 122(8):1133–1141, 1975.
- [62] J. Singh: *Physics of Semiconductors and their Heterostructures*. McGraw Hill, 1993.
- [63] S. Sze: *Physics of Semiconductor Devices*. Wiley, 1981.
- [64] D. S. Lee and J. G. Fossum: *Energy-band distortion in highly doped silicon*. IEIEEE. Electron Dev., 30(6):626–634, 1983.
- [65] A. Schenk: *Finite-temperature full random-phase approximation model of band gap narrowing for silicon device simulation*. J. Appl. Phys., 84(7), 1998.
- [66] Joint Committee for Guides in Metrology: *Guide to the expression of uncertainty in measurement*. BIPM, Paris, 2008.
- [67] Joint Committee for Guides in Metrology: *International vocabulary of metrology - Basic and general concepts and associated terms (VIM)*. BIPM, Paris, 2008.
- [68] H. F. Inman and Jr. E. L. Bradley: *The overlapping coefficient as a measure of agreement between probability distributions and point estimation of the overlap of two normal densities*. Commun. Stat. Theory, 18(10):3851–3874, 1989.
- [69] W. Wöger: *Remarks on the en-criterion used in measurement comparisons*. PTB-Mitteilungen, 109:24–27, 1999.

- [70] M. Schmelling: *Averaging measurements with hidden correlations and asymmetric errors*. Technical Report 1, Max-Planck Institute for Nuclear Physics, Heidelberg, Germany, 2000.
- [71] G. Kirchhoff: *Ueber das Verhältniss zwischen dem Emissionsvermögen und dem Absorptionsvermögen der Körper für Wärme und Licht*. *Annalen der Physik*, 185(2):275–301, 1860.
- [72] P. Würfel: *Generalized planck's radiation law for luminescence via indirect transitions*. *Appl. Phys. A*, 60:67–70, 1995.
- [73] U. Rau: *Reciprocity relation between photovoltaic quantum efficiency and electroluminescent emission of solar cells*. *Phys. Rev. B*, 76, 2007.
- [74] U. Rau: *Superposition and reciprocity in the electroluminescence and photoluminescence of solar cells*. *IEEE J. Photovolt.*, 2(2):169–172, 2012.
- [75] W. Kern and D. Puotinen: *Cleaning solutions based on hydrogen peroxide for use in silicon semiconductor technology*. *RCA review*, 187, 1970.
- [76] W. Budde: *Multidecade linearity measurements on Si photodiodes*. *Applied Optics*, 18(10):1555–1558, 1979.
- [77] W. Demtröder: *Experimentalphysik 2: Elektrizität und Optik*. Springer-Verlag, 2006.
- [78] B. Edlén: *The refractive index of air*. *Metro*, 2(2):71–80, 1966.
- [79] P. Würfel, T. Trupke, and T. Puzzer: *Diffusion lengths of silicon solar cells from luminescence images*. *J. Appl. Phys.*, 101, 2007.
- [80] D. Hinken, K. Bothe, K. Ramspeck, S. Herlufsen, and R. Brendel: *Determination of the effective diffusion length of silicon solar cells from photoluminescence*. *J. Appl. Phys.*, 105(10):104516, 2009.
- [81] C. Schinke, D. Hinken, J. Schmidt, K. Bothe, and R. Brendel: *Modeling the spectral luminescence emission of silicon solar cells and wafers*. *IEEE J. Photovolt.*, 3(3):1038–1052, 2013.
- [82] P. Würfel: *The chemical potential of radiation*. *J. Phys. C: Solid State Phys.*, 15:3967–3985, 1982.
- [83] Yuqin Zong, Steven W. Brown, B. Carol Johnson, Keith R. Lykke, and Yoshi Ohno: *Simple spectral stray light correction method for array spectroradiometers*. *Applied Optics*, 45(6):1111–1119, 2006.
- [84] A. Sperling, O. Larionov, U. Grusemann, and S. Winter: *Stray-light correction of array spectroradiometers using tunable pulsed and cw lasers*. In *Proceedings of the 9th International Conference on New Developments and Applications in Optical Radiometry*, Davos, Switzerland, 2005.
- [85] Instrument Systems GmbH: *Spectro 320 (D) R5 Benutzerhandbuch*, 2010.
- [86] E. I. Stearns and R. E. Stearns: *An example of a method for correcting radiance data for bandpass error*. *Color Res. Appl.*, 13(4):257–259, 1988, ISSN 1520-6378.
- [87] J. L. Gardner: *Bandwidth correction for LED chromaticity*. *Color Res. Appl.*, 31(5):374–380, 2006.

- [88] E. R. Wooliams, R. Baribeau, A. Bialek, and M. G. Cox: *Spectrometer bandwidth correction for generalized bandpass functions*. *Metrologia*, 48:164–172, 2011.
- [89] S. Nevas, G. Wübbeler, A. Sperling, C. Elster, and A. Teuber: *Simultaneous correction of bandpass and stray-light effects in array spectroradiometer data*. *Metrologia*, 49:43–47, 2012.
- [90] C. J. Sansonetti, M. L. Salit, and J. Reader: *Wavelengths of spectral lines in mercury pencil lamps*. *Applied Optics*, 35(1):74–77, 1996.
- [91] C. Burgess and J. Hammond: *Wavelength standards for the near-infrared spectral region*. *Spectroscopy*, 22(4):40–48, 2007.
- [92] L. Coslovi and F. Righini: *Fast determination of the nonlinearity of photodetectors*. *Applied Optics*, 19(18):3200–3203, 1980.
- [93] J. Hohl-Ebinger: *Untersuchungen zur hochpräzisen Vermessung der elektrischen Parameter von Solarzellen*. PhD thesis, University of Konstanz, Germany, 2011.
- [94] C. Schinke, D. Hinken, K. Bothe, C. Ulzhöfer, A. Milsted, J. Schmidt, and R. Brendel: *Determination of the collection diffusion length by electroluminescence imaging*. *Energy Procedia*, 8:147, 2011.
- [95] S. Winter, T. Wittchen, and J. Metzendorf: *Primary reference cell calibration at the PTB based on an improved DSR facility*. In *Proc. 16th EUPVSEC, Glasgow, Great Britain*, pages 2198–2201, 2000.
- [96] S. Winter: *Analyse und Verbesserung der rückführbaren Kalibrierung von Solarzellen*. PhD thesis, Technische Universität Carolo-Wilhelmina, Braunschweig, Germany, 2004.
- [97] P. Drude: *Ueber die Reflexion und Brechung ebener Lichtwellen beim Durchgang durch eine mit Oberflächenschichten behaftete planparallele Platte*. *Ann. Phys.*, 279(5):126–157, 1891, ISSN 1521-3889.
- [98] H. G. Tompkins: *A User's Guide to Ellipsometry*. Academic Press, San Diego, 1993.
- [99] H. G. Tompkins: *Handbook of Ellipsometry*. William Andrew, Inc., 2005.
- [100] J.H. Mazur, R. Gronsky, and J. Washburn: *High resolution electron microscopy studies of native oxide on silicon*. *Proc. 3rd Oxford Conference on Microscopy of Semiconducting Materials*, pages 77–82, 1983.
- [101] Jr. G. E. Jellison and F. A. Modine: *Parameterization of the optical functions of amorphous materials in the interband region*. *Appl. Phys. Lett.*, 69(3):371–373, 1996.
- [102] J. A. Woollam Co.: *Guide to using WVASE32*. J. A. Woollam Co., Inc., 2010.
- [103] W. H. Press, S. A. Teukolsky, W. T. Vetterling, and B. P. Flannery: *Numerical Recipes in C*. Cambridge Univ. Press, 1992.
- [104] E. D. Palik: *Handbook of optical constants of solids*, volume 3. Academic press, 1998.
- [105] J. A. Woollam Co. Electronic data attachment for VWASE.
- [106] G. E. Jellison, Jr.: *Use of the biased estimator in the interpretation of spectroscopic ellipsometry data*. *Applied Optics*, 30(23), 1991.

- [107] T. Ambridge and M. M. Faktor: *An automatic carrier concentration profile plotter using an electrochemical technique*. J. Appl. Electrochem., 5:319–328, 1975.
- [108] P. Blood: *Capacitance-voltage profiling and the characterisation of III-V semiconductors using electrolyte barriers*. Semicond. Sci. Technol., pages 7–27, 1986.
- [109] E. Peiner, A. Schlachetzki, and D. Krüger: *Doping profile analysis in Si by electrochemical capacitance-voltage measurements*. J. Electrochem. Soc., 142(2):576–580, 1995.
- [110] R. Bock, P. P. Altermatt, and J. Schmidt: *Accurate extraction of doping profiles from electrochemical capacitance voltage measurements*. In *Proc. 23rd EUPVSEC, Valencia, Spain*, pages 1510–1513, 2008.
- [111] R. Brendel, M. Hirsch, R. Plieninger, and J.H. Werner: *Quantum efficiency analysis of thin-layer silicon solar cells with back surface fields and optical confinement*. IEEE T. Electron Dev., 43:1104–1113, 1996.
- [112] C.J.J. Tool, P. Manshanden, A.R. Burgers, and A.W. Weeber: *Higher efficiency for thin multi crystalline silicon solar cells by improving the rear surface passivation*. Proc. 29th IEEE PVSC, New Orleans, LA, USA, pages 304–307, 2002.
- [113] M. Becker, U. Gösele, A. Hofmann, and S. Christiansen: *Highly p-doped regions in silicon solar cells quantitatively analyzed by small angle beveling and micro-Raman spectroscopy*. J. Appl. Phys., 106(074515), 2009.
- [114] S. Steingrube, H. Wagner, H. Hannebauer, S. Gatz, R. Chen, S. T. Dunham, T. Dullweber, P. P. Altermatt, and R. Brendel: *Loss analysis and improvements of industrially fabricated Cz-Si solar cells by means of process and device simulations*. Energy Procedia, 8:263–268, 2011.
- [115] B. Mitchell, M.K. Juhl, M.A. Green, and T. Trupke: *Full spectrum photoluminescence lifetime analyses on silicon bricks*. IEEE J. Photovolt., 3(3):962–969, 2013, ISSN 2156-3381.
- [116] T. Trupke, R. A. Bardos, M. D. Abbott, P. Würfel, E. Pink, Y. Augarten, F. W. Chen, K. Fisher, J. E. Cotter, M. Kasemann, M. Rüdiger, S. Kontermann, M. C. Schubert, M. The, S. W. Glunz, W. Warta, D. Macdonald, J. Tan, A. Cuevas, J. Bauer, R. Gupta, O. Breitenstein, T. Buonassisi, G. Tarnowski, A. M. Lorenz, H. P. Hartmann, D. H. Neuhaus, and J. M. Fernandez: *Progress with luminescence imaging for the characterisation of silicon wafers and solar cells*. In *Proc. 22nd EUPVSEC, Milan, Italy*, pages 22–31, 2007.
- [117] T. Fuyuki, H. Kondo, T. Yamazaki, Y. Takahashi, and Y. Uraoka: *Photographic surveying of minority carrier diffusion length in polycrystalline silicon solar cells by electroluminescence*. Appl. Phys. Lett., 86, 2005.
- [118] M. Kasemann, M.C. Schubert, M. The, M. Köber, M. Hermle, and W. Warta: *Comparison of luminescence imaging and illuminated lock-in thermography on silicon solar cells*. Appl. Phys. Lett., 89, 2006.
- [119] D. Hinken, K. Ramspeck, K. Bothe, B. Fischer, and R. Brendel: *Series resistance imaging of solar cells by voltage dependent electroluminescence*. Appl. Phys. Lett., 91, 2007.
- [120] T. Kirchartz, A. Helbig, and U. Rau: *Note on the interpretation of electroluminescence images using their spectral information*. Sol. Energ. Mat. Sol. C., 92:1621–1627, 2008.
- [121] A. Helbig, T. Kirchartz, and U. Rau: *Quantitative information of electroluminescence images*. Proceedings of the 23rd EUPVSEC, Valencia, Spain, pages 426–429, 2008.

- [122] K. Bothe, K. Ramspeck, D. Hinken, C. Schinke, J. Schmidt, S. Herlufsen, R. Brendel, J. Bauer, J. M. Wagner, N. Zakharov, and O. Breitenstein: *Luminescence emission from forward- and reverse-biased multicrystalline silicon solar cells*. J. Appl. Phys., 106, 2009.
- [123] Y. Takahashi, Y. Kaji, A. Ogane, Y. Uraoka, and T. Fuyuki: *Luminoscopy-novel tool for the diagnosis of crystalline silicon solar cells and modules utilizing electroluminescence*. Proceedings of the 4th WPVSC, Waikoloa, Hawaii, 1:924–927, 2006.
- [124] K. Bothe, P. Pohl, J. Schmidt, T. Weber, P. Altermatt, B. Fischer, and R. Brendel: *Electroluminescence imaging as an in-line characterisation tool for solar cell production*. page 597, 2006.
- [125] T. Fuyuki, Y. Kaji, A. Ogane, and Y. Takahashi: *Analytic findings in the photographic characterization of crystalline silicon solar cells using electroluminescence*. Proceedings of the 4th World Conference on Photovoltaic Energy Conversion, Waikoloa, Hawaii, 1:905–907, may 2006.
- [126] University of New South Wales: *PCID*.
- [127] W. Shockley: *The theory of p-n-junctions in semiconductors and p-n-junction transistors*. Bell System Technical Journal, 28:435, 1949.
- [128] R.M. Swanson: *Approaching the 29% limit efficiency of silicon solar cells*. Proc. 31st IEEE PVSC, Lake Buena Vista, FL, USA, pages 889–894, 2005.
- [129] P.A. Basore: *Extended spectral analysis of internal quantum efficiency*. Proc. 23rd IEEE PVSC, Louisville, KY, USA, pages 147–152, 1993.
- [130] E. Yablonowitch: *Statistical ray optics*. J. Opt. Soc. Am., 72(7):899–907, 1982.
- [131] C. Battaglia, M. Boccard, F. J. Haug, and C. Ballif: *Light trapping in solar cells: When does a lambertian scatterer scatter lambertianly?* J. Appl. Phys., 112(094504), 2012.
- [132] A. Richter, M. Hermle, and S. W. Glunz: *Reassessment of the limiting efficiency for crystalline silicon solar cells*. IEEE J. Photovolt., 3(4):1184–1191, 2013.
- [133] P. C. Peest: *Bestimmung der Messunsicherheiten eines Photospektrometers für Reflexions- und Transmissionsmessungen an planaren Siliziumwafern*. Master’s thesis, Leibniz University of Hanover, Germany, 2014.
- [134] K. Schick, E. Daub, S. Finkbeiner, and P. Würfel: *Verification of a generalized planck law for luminescence radiation from silicon solar cells*. Appl. Phys. A, 54:109–114, 1992.
- [135] M. Rüdiger, T. Trupke, P. Würfel, R.A. Bardos, and T. Roth: *Influence of photon reabsorption on temperature dependent quasi-steady-state photoluminescence lifetime measurements on crystalline silicon*. In Proc. 22nd EUPVSEC, Milan, Italy, 2007.
- [136] R. Brüggemann: *Kirchhoff’s generalised law applied to amorphous silicon/crystalline silicon heterostructures*. Philos. Mag., 89:2519–2529, 2009.
- [137] M. A. Green: *Analytical expressions for spectral composition of band photoluminescence from silicon wafers and bricks*. Appl. Phys. Lett., 99(131112), 2011.
- [138] W. van Roosbroeck and W. Shockley: *Photon-radiative recombination of electrons and holes in germanium*. Phys. Rev., 94:1558–1560, 1954.

-
- [139] T. Trupke, M. A. Green, P. Würfel, P. P. Altermatt, A. Wang, J. Zhao, and R. Corkish: *Temperature dependence of the radiative recombination coefficient of intrinsic crystalline silicon*. J. Appl. Phys., 94(8):4930–4937, 2003.
- [140] M. Planck: *Vorlesungen über die Theorie der Wärmestrahlung*. Johann Ambrosius Barth, 1923.
- [141] K. Bothe, D. Hinken, K. Ramspeck, B. Fischer, and R. Brendel: *Combined quantitative analysis of electroluminescence images and lbc mappings*. In *Proc. 22nd EUPVSEC, Milan, Italy*, 2007.
- [142] D. Hinken: *Luminescence-based characterization of crystalline silicon solar cells*. PhD thesis, Gottfried Wilhelm Leibniz University of Hanover, 2012.
- [143] P. P. Altermatt, F. Geelhaar, T. Trupke, X. Dai, A. Neisser, and E. Daub: *Injection dependence of spontaneous radiative recombination in crystalline silicon: Experimental verification and theoretical analysis*. Appl. Phys. Lett., 88(26):261901, 2006.
- [144] C. Donolato: *A reciprocity theorem for charge collection*. Appl. Phys. Lett., 46:270–272, 1985.
- [145] E. W. Cheney and D. R. Kincaid: *Numerical mathematics and computing*. Brooks/Cole, 1999.
- [146] H. Holst, M. Winter, M. Vogt, K. Bothe, M. Köntges, R. Brendel, and P.P. Altermatt: *Application of a new ray tracing framework to the analysis of extended regions in Si solar cell modules*. Energy Procedia, 38:86–93, 2013.
- [147] M. Winter, H. Holst, and P. P. Altermatt: *Prediction of a double-antireflection coating made solely with SiNx in a single, directional deposition step*. Energy Procedia, 38(0):895 – 900, 2013, ISSN 1876-6102.
- [148] M. Winter, M. R. Vogt, H. Holst, and P. P. Altermatt: *Combining structures on different length scales in ray tracing: analysis of optical losses in solar cell modules*. Optical and Quantum Electronics, pages 1–7, 2014, ISSN 0306-8919.
- [149] C. Gerry and P. Knight: *Introductory quantum optics*. Cambridge Univ. Press, 2005.
- [150] I.N. Bronstein and K.A. Semendjaev: *Taschenbuch der Mathematik*. Verlag Harri Deutsch, 2001.
- [151] J. Mattheis: *Mobility and homogeneity effects on the power conversion efficiency of solar cells*. PhD thesis, Universität Stuttgart, Germany, 2008.
- [152] M. Planck: *Ueber das Gesetz der Energieverteilung im Normalspectrum*. Annalen der Physik, 4:553–563, 1901.
- [153] T. Kirchartz and U. Rau: *Detailed balance and reciprocity in solar cells*. phys. stat. sol. (a), 12:2737–2751, 2008.

- absorption
 - band-impurity, 11
 - free carrier, 11
 - inter-band, 11
 - intra-band, 11
- band gap
 - direct, 10
 - energy, 9
 - indirect, 10
 - narrowing, 14
- band structure, 9
- band tails, 14
- central limit theorem, 18
- coefficient of overlap, 18
- combined standard uncertainty, 17
- condition number of matrix, 113
- conduction band, 9
- correction, 16
- correlation
 - coefficient, 17
 - hidden, 19
- Coulomb screening, 14
- coverage factor, 18
- coverage probability, 18
- degree of freedom
 - effective, 34
- diamond lattice, 9
- diffusion length, 93
 - effective, 97
- dispersion relations, 9
- electroluminescence, 37
- Ellipsometry, 61
- En criterion, 19
- energy conversion efficiency, 84
- error, 16
- Fermi-Dirac distribution function, 10
- free carrier absorption, 98
- free carrier absorption, FCA, 14
- GUM, 15
- input quantity, 16
- Kramers-Kronig relations, 13
- Lambert-Beer absorption law, 12
- level of confidence, 18
- light trapping, 85
- Monte-Carlo simulation, 63
- optical reciprocity theorem, 58
- output quantity, 16
- photoluminescence, 37
- photon escape probability, 37
- photon generation rate, 37
- probability distribution function, 16
- process equation, 15
- Quasi-Fermi energy, 11
 - splitting, 11
- rear surface recombination velocity, 93
- recombination, 9
- sensitivity coefficient, 17
- spectral responsivity, 58
- stray light
 - external, 43
 - spectral, 43
- t-distribution, 18
- Tauc plot, 13
- type A/B uncertainty, 17
- uncertainty, 16
 - expanded, 18
- valence band, 9

weighted average, 19
uncertainty, 19

Refereed papers as first author

- C. Schinke, P. C. Peest, J. Schmidt, R. Brendel, K. Bothe, M. R. Vogt, I. Kröger, S. Winter, A. Schirmacher, S. Lim, H. Nguyen, and D. MacDonald: *Uncertainty analysis for the coefficient of band-to-band absorption of crystalline silicon*. AIP Advances, 5(067168), 2015.
- C. Schinke, K. Bothe, P. C. Peest, J. Schmidt, and R. Brendel: *Uncertainty of the coefficient of band-to-band absorption of crystalline silicon at near-infrared wavelengths*. Appl. Phys. Lett., 104(081915), 2014.
- C. Schinke, D. Hinken, J. Schmidt, K. Bothe, and R. Brendel: *Modeling the spectral luminescence emission of silicon solar cells and wafers*. IEEE J. Photovolt., 3(3):1038–1052, 2013.
- C. Schinke, F. Kiefer, M. Offer, D. Hinken, A. Schmidt, N. P. Harder, R. Bock, T. Brendemühl, J. Schmidt, K. Bothe, and R. Brendel: *Contacting interdigitated back-contact solar cells with four busbars for precise current–voltage measurements under standard testing conditions*. IEEE J. Photovolt., 2(3):247–255, 2012.

Conference papers as first author

- C. Schinke, P. C. Peest, J. Schmidt, R. Brendel, K. Bothe, M. R. Vogt, I. Kröger, S. Winter, A. Schirmacher, S. Lim, H. Nguyen, and D. MacDonald: *Experimental determination of the uncertainty of the absorption coefficient of crystalline silicon*. Proc. 5th SiliconPV, Konstanz, Germany, 2015.
- C. Schinke, N. Maris, I. Kunze, M. Köntges, and D. Tegtmeier: *Messunsicherheitsanalyse zur präzisen Bestimmung der lateralen Bestrahlungsstärkeverteilung von Sonnensimulatoren für PV-Module*. Proc. 30th Symposium Photovoltaische Solarenergie, Bad Staffelstein, Germany, 2015.
- C. Schinke, D. Hinken, K. Bothe, J. Schmidt, and R. Brendel: *Analyzing the spectral luminescence emission of silicon solar cells and wafers*. Proc. 39th IEEE PVSC, Tampa, FL, USA, pages 0203–0208, 2013.
- C. Schinke, D. Hinken, K. Bothe, C. Ulzhöfer, A. Milsted, J. Schmidt, and R. Brendel: *Determination of the collection diffusion length by electroluminescence imaging*. Energy Procedia, 8:147, 2011.

Refereed papers as co-author

- M. R. Vogt, H. Hahn, H. Holst, M. Winter, C. Schinke, M. Köntges, R. Brendel, and P. P. Altermatt: *Measurement of the optical constants of soda-lime glasses in dependence of iron*

content, and modeling of iron-related power losses in crystalline si solar cell modules. IEEE J. Photovolt., 2015. Submitted.

D. Hinken, C. Schinke, S. Herlufsen, A. Schmidt, K. Bothe, and R. Brendel: *Experimental setup for camera-based measurements of electrically and optically stimulated luminescence of silicon solar cells and wafers.* Rev. Sci. Instrum., 82(3):033706, 2011.

K. Bothe, K. Ramspeck, D. Hinken, C. Schinke, J. Schmidt, S. Herlufsen, R. Brendel, J. Bauer, J. M. Wagner, N. Zakharov, and O. Breitenstein: *Luminescence emission from forward- and reverse-biased multicrystalline silicon solar cells.* J. Appl. Phys., 106, 2009.

CURRICULUM VITAE

CARSTEN JONATHAN SCHINKE

Persönliche Daten

Carsten Jonathan Schinke
Potsdamer Str. 15
30952 Ronnenberg
Deutschland

Verheiratet, deutsch
Geboren am 31. Mai 1984 in Düsseldorf

Anstellung

seit 04/2010 Wissenschaftlicher Mitarbeiter, Charakterisierung von Solarzellen,
Institut für Solarenergieforschung Hameln

Studium

06/2010 *Diplom Physik*, Leibniz Universität Hannover
04/2009-03/2010 Diplomarbeit, Institut für Solarenergieforschung Hameln
04/2006-03/2010 Studium Physik (Studienrichtung Technische Physik), Leibniz Universität Han-
nover
10/2004-03/2006 Studium Physikalische Technik, Fachhochschule Münster

Wehrersatzdienst

11/2003-08/2004 Freizeit- und Begegnungsstätte Oese, Basdahl

Schulbildung

1994-2003 Humboldt-Gymnasium, Düsseldorf
1990-1994 Grundschule Sonnenstraße, Düsseldorf

Danksagung

Stellvertretend für alle, die zum Gelingen dieser Arbeit beigetragen haben, möchte ich mich bedanken bei

Prof. Dr. Jan Schmidt für die Betreuung der Arbeit und wertvolle Anregungen,

Prof. Dr. Michael Oestreich und *Prof. Dr. Daniel MacDonald* für die bereitwillige Übernahme der Koreferate,

Dr. Karsten Bothe für zahlreiche Diskussionen, hilfreiche Nachfragen und das unermüdliche Korrekturlesen der Arbeit,

Christian Peest für die gute Arbeit als Masterstudent,

Cornelia Marquardt und *Susanne Mau* für die schnelle und zuverlässige Herstellung und Prozessierung der Proben für diese Arbeit,

Dr. Matthias Offer und *Dr. David Hinken* für die Unterstützung beim Aufbau des Spektralradiometrie-Messplatzes am ISFH und zahlreiche hilfreiche Diskussionen zu Unsicherheitsanalysen und Lumineszenzmessungen,

Arne Schmidt und *Ingo Ahrens* für die vielfache technische Unterstützung an den Messplätzen,

Hendrik Holst für die Unterstützung bei Raytracing-Simulationen,

Dr. Erich Daub und *Dr. Bob Falster* für die Bereitstellung von polierten Silizium-Wafern,

meiner Familie, die mich vielfältig unterstützt hat, obwohl sie mich häufig entbehren musste.

Außerdem danke ich Gott für Bewahrung und Gesundheit während der Zeit, in der diese Arbeit entstanden ist.